Selected Topics of Semiconductor Physics and Technology

Ausgewählte Probleme der Halbleiterphysik und Technologie

Vol. 145

Thomas Zabel

Study on silicon-germanium nanoislands as emitters for a monolithic silicon light source

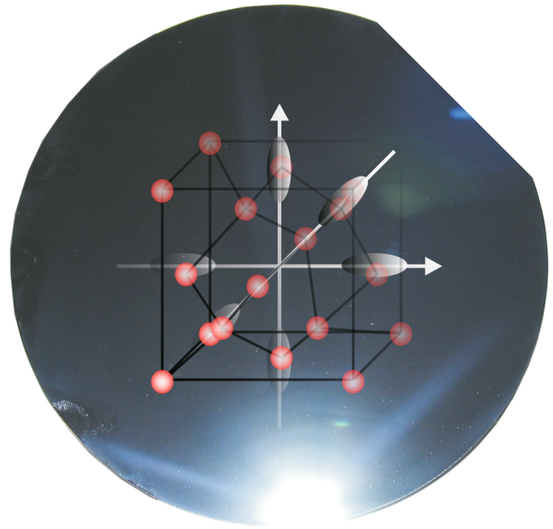

T. Zabel • Silicon-germanium nanoislands as emitters for a silicon light source

ISBN 978-3-941650-45-9

(€ 15,00)

145

Editors:

G. Abstreiter, M.-C. Amann, M. Stutzmann, P. Vogl

Walter Schottky Institut, Technische Universität München

TECHNISCHE UNIVERSITÄT MÜNCHEN
Lehrstuhl für Experimentelle Halbleiterphysik I E24
Walter Schottky Institut

Study on silicon-germanium nanoislands as emitters for a monolithic silicon light source

Thomas Zabel

Vollständiger Abdruck der von der Fakultät für Physik der Technischen Universität München zur Erlangung des akademischen Grades eines

Doktors der Naturwissenschaften

genehmigten Dissertation.

Vorsitzender: Univ.-Prof. Dr. Wilhelm Zwerger

Prüfer der Dissertation:
1. Univ.-Prof. Dr. Gerhard Abstreiter
2. Univ.-Prof. Jonathan J. Finley, Ph.D.
3. Univ.-Prof. Dr. Dominique Bougeard, Universität Regensburg

Die Dissertation wurde am 26.07.2012 bei der Technischen Universität München eingereicht und durch die Fakultät für Physik am 30.08.2012 angenommen.

1. Auflage Oktober 2012

Titelbild:

Photograph of a silicon wafer with the flash focused to the lower corner resembling the idea of light extraction. Dirt at the silicon wafer surface illustrates several methods of light generation either by impurities (dust particles) or defects (cracks at the left corner). The method of band structure engineering which is utilized within this thesis is illustrated by the transparent overlay of the diamond crystal structure and the Δ-valleys in silicon.

Druck: Printy Digitaldruck, München (http://www.printy.de)

ISBN: 978-3-941650-45-9

Abstract

There is a strong desire in modern communication technology to further improve the processing speed of silicon based integrated circuits by replacing the electrical interconnects with optical waveguides. This is a great challenge as light sources based on bulk silicon have a poor efficiency due to its indirect band gap.
A possible route towards a higher radiative recombination efficiency in silicon-based materials is the introduction of a spatial confinement provided by germanium heterostructures. Such confinements can lead to a strong spreading of the charge carrier wave functions in k-space circumventing the limitation of the indirect transition.
In this thesis, we present a systematic evaluation of building blocks for a silicon-based light source. In the first part we investigate the optical recombination properties of molecular beam epitaxy grown silicon-germanium based light emitters. In a second part such emitters are embedded in photonic crystals and P-I-N diode structures to asses the impact of potential photonic enhancement effects and of an electrical current injection.
Using molecular beam epitaxy we perform representative growth studies on various silicon-germanium based three dimensional nanostructures. A successive analysis of the optical recombination properties using a comparative study based on realistic band structure simulations, photoluminescence and electroluminescence spectroscopy then allows to conclude that the silicon-germanium alloy composition of the nanostructures and their dimensions dominate the radiative recombination efficiency. However, due to kinetic and thermodynamic considerations both parameters are correlated and compete in their influence on the radiative recombination rate. The strong correlation between the alloy content and the nanostructure dimensions results in the fact that it is either possible to optimize the real space properties by a large spatial electron-hole envelope wave function overlap or the reciprocal space properties by a large spreading of the hole wave function in k-space.

Zusammenfassung

Im Bereich moderner Telekommunikationstechnologie gibt es starke Bestrebungen dahingehend die elektrischen Verbindungen zwischen einzelnen Bauelementen durch optische Wellenleiter zu ersetzen. Dies ist eine große Herausforderung, da auf Silizium basierende Lichtquellen, durch dessen indirekte Bandlücke, eine sehr geringe Effizienz aufweisen.
Ein möglicher Ausweg, in Richtung höherer strahlender Rekombinationseffizienzen, ist die Kombination von Silizium-Volumenmaterial und Germanium Heterostrukturen, was eine räumliche Ladungslokalisierung erlauben würde. Diese Lokalisierung kann zu einem Verschmieren der Ladungsträgerwellenfunktionen im k-Raum führen, was es ermöglicht die Limitierung durch den indirekten Übergang zu umgehen.
Im Rahmen dieser Dissertation bewerten wir systematisch die Eignung verschiedener Bausteine einer Silizium-basierenden Lichtquelle. In einem ersten Teil untersuchen wir die optischen Rekombinationseigenschaften von molekularstrahlepitaktisch gewachsenen Silizium-Germanium Lichtemittern. In einem zweiten Teil werden solche Emitter in Photonische-Kristalle und P-I-N Dioden eingebaut. Dies erlaubt den Einfluß von auftretenden photonischen Verstärkungseffekten und von elektrischer Ladungsinjektion zu bewerten.
Wir benutzen Molekularstrahlepitaxie um repräsentative Wachstumsstudien, von verschiedenen Silizium-Germanium basierenden dreidimensionalen Nanostrukturen, durchzuführen. Mittels einer vergleichender Studie der optischen Rekombinationseigenschaften basierend auf realistischen Bandstruktursimulationen, Photolumineszenz- und Elektrolumineszenzspektroskopie, folgern wir, dass die Silizium-Germanium Legierungszusammensetzung der Nanostrukturen und deren räumlichen Abmessungen die strahlende Rekombinationseffizienz dominieren. Beide Parameter sind jedoch durch kinetische und thermodynamische Betrachtung von einander abhängig und haben einen konkurrierenden Einfluß auf die strahlende Rekombinationsrate. Die starke Korrelation zwischen dem Legierungsgehalt und den Nanostrukturabmessungen resultiert in der Tatsache, dass man entweder die räumlichen Eigenschaften durch einen größeren Elektron-Loch Wellenfunktionsüberlapp optimieren kann, oder die Eigenschaften im reziproken Raum durch eine starke Verschmierung der Lochwellenfunktion optimiert.

Contents

1. Si based light sources

The present thesis evaluates the potential of germanium (Ge) based 3D quantum confining structures as active emitters in the silicon (Si) system. Here a combination of goal-oriented epitaxy with subsequent realistic band structure simulations allows for a detailed understanding of the occurring recombination properties. Both the applicability as well as the validity of obtained predictions is experimentally verified by optical spectroscopy. In addition we will use the obtained results to optimize the emitters towards device applications in combination with photonic crystals and light emitting diode structures.

Why is a silicon based light source interesting?

A silicon (Si) based light source is very interesting not only from a physical but also from a commercial point of view. The reason for this is a vast amount of possible applications. The most prominent being a light source in integrated optoelectronic circuits [Pav08]. In such circuits the idea is to increase the data processing speed of computer chips by exploiting the superior transmission speed and bandwidth of photons compared to electrons. Here to interconvert between electrical and optical signals light sources are needed which fulfill the requirements of a high efficiency and room-temperature applicability. Furthermore, such a light source should be complementary metal oxide semiconductor (CMOS) compatible as this allows to use already existing fabrication technologies.
Another possible application with strongly increasing potential is gas- or biosensing [Dor09a]. Here one uses either the absorption bands of molecules, which is possible for some materials like H_2O [Geb10] or the refractive index dependent change of photonic crystal cavity modes [Zab08, Dor09b] as measurement principle.
Both applications require light sources which are efficient and which can be fabricated on-chip. Moreover they should be comparable inexpensive. Up to now, besides the efficiency, group IV materials fulfill these requirements.

What is the problem of silicon?

The recombination of electrons and holes in a semiconductor is described by two competing processes: The radiative recombination rate, which is governed by Fermi's golden rule [Fox06] and the non-radiative recombination rate. Silicon suffers from the fundamental problem of being an indirect band gap material. The indirect band gap results in the fact that the radiative recombination of electrons and holes is not possible without the emission or absorption of a phonon for momentum conservation. This results in a long radiative recombination lifetime of several milliseconds [Ham80]. The long radiative lifetime has to compete with non-radiative processes like Auger-recombination or

the recombination at crystalline defects. Even in high purity silicon the non-radiative lifetime is usually of the order of nanoseconds [Pav08]. This results in a low optical internal quantum efficiency of the order of 10^{-6}. Thus, one million electron hole pairs are required to generate one photon. Especially in regard of lasing fast non-radiative recombination processes like Auger-recombination [Nil73] prevent the population inversion which is necessary for optical amplification.

What is the state of the art?

Since more than 20 years many people tried different approaches to circumvent the indirect band gap problem to achieve an efficient silicon based light source. One approach was the use of anodized porous silicon [Can95] which shows room temperature luminescence both in the visible [Tsy94] as well as in the near-infrared [Fau93, Can90] energy region. Another interesting and promising idea is the use of the intra-atomic transition of rare-earth atoms. Here especially the erbium intra-4f shell transition is interesting as the resonant wavelength of this transition is 1.54μm [Sti97]. Still some groups are working on erbium doping [And12] in silicon due to its strong and narrow luminescence which is even present at room temperature and in electroluminescence [Yer10]. Additional approaches use for example crystal defects [Shk09, Bao07]. Another idea has been the band structure folding in the Brillouin zone using SiGe superlattices to achieve a direct band gap [Gnu74, Kas75, Men93, Zel86]. But, so far the only monolithic all silicon laser presented is based on stimulated Raman scattering [Ron05].
However, all of these approaches so far did commercially not prevail either due to the fact that optical gain could not be achieved or in latter case they are technologically not applicable due to a necessary optical pumping.
Besides those monolithic approaches some groups now aim for a hybrid integration of group III-V light sources on silicon [Fan06, Tan11, Tan12]. Those approaches are very promising as III-V light sources are already widely used.
A further approach, based on a monolithic integration on silicon (Si), is the integration of germanium (Ge) nanostructures on Si. This heterostructure approach relies on a confinement induced spreading of the hole wave function in k-space to allow for a quasi-direct recombination. Such structures already attracted huge interest in the past 20 years where many groups investigated SiGe quantum wells [Stu91, Fuk92, Shi94, Bru92] and also islands [Das01, Sch95, Sun95]. Despite of the quasi-direct recombination detailed photoluminescence spectroscopy studies have shown that the luminescence intensity is still rather weak. However, a detailed study about the limiting processes and concerning possible solutions is still missing.
The scope of this thesis was, therefore, to demonstrate the realization of building blocks for a potential Si-based light source. Here in a first part we aim for a deep understanding of the optical properties of epitaxial fabricated (Si)Ge based three dimensional confinement structures by a combination of realistic band structure simulations and optical spectroscopy. In a second part we evaluate additional building blocks by embedding such (Si)Ge nanostructures into two-dimensional photonic crystals and P-I-N diode structures. This allows to investigate the coupling of the emitters with photonic crystal

cavities and to demonstrate electrical current injection. In the following we address this object in nine chapters.

In **chapter 2** we will shortly explain the concepts, which are necessary to understand the theoretical and experimental results of this thesis. Given the long interest in the epitaxial fabrication and the optical characterization of SiGe heterostructures chapter 2 will also give a detailed overview about selected results of the last 20 years.

Chapter 3 utilizes a comparative study of band structure simulations and optical photoluminescence spectroscopy of nominally pure Ge hut clusters to link the structural parameters height, length and germanium content of the hut clusters with the optical transition energy and the intensity. We find that the type II band alignment inherently limits the radiative efficiency of the quasi-direct no-phonon transition in Ge hut clusters. Further calculations of the electron-hole wave function overlap with an extended structural parameter range identify the lattice mismatch mediated interconnection between the Ge content and the hut cluster size as the major problem preventing the invention of more efficient Ge based emitters. We deduce that a low Ge content and a small size is required for a large spatial electron-hole wave function overlap and a large spreading of the hole wave function in k-space.

In **chapter 4** we aim for an increasing spatial electron-hole wave function overlap by enhancing the intermixing of Ge islands with silicon by increasing the growth temperature. With a higher growth temperature we thermodynamically reduce the Ge content due to an enhancement of Si diffusion. However this results in a larger island size and in a change of the island morphology towards pyramids and domes. These island morphologies offer lower radiative recombination rates and intensities than Ge hut clusters. We find two major reasons for this: The larger size which overcomes the effect of a lower Ge content on the spatial overlap integral. And the larger size resulting in a smaller spreading of the hole wave function in k-space.

The conclusions of the previous chapters we address in **chapter 5** where we introduce the co-deposition of silicon and germanium. In contrast to an increasing growth temperature which was utilized in chapter 4 co-deposition allows to reduce the Ge content more independently of the island size. For the SiGe hut clusters we find that the effect of the reduced Ge content on the electron-hole wave function is exactly compensated by the small increase of the island size. However, we also find that the quasi-directness of the transition is maintained. Moreover the co-deposition lowers the transition energy which in combination with the comparable high luminescence intensity makes SiGe hut clusters a very interesting and versatile emitter morphology.

Our investigations have shown that the radiative recombination rate is limited by the spatial separation of the electrons and holes. This can be optimized by further lowering the Ge content. In **chapter 6** we continue the co-deposition approach in molecular beam epitaxy by the fabrication of SiGe quantum well segments which we call SiGe islands. Band structure simulations solely based on experimental determined structural parameters reveal that these islands obtain a three dimensional type I confinement. This results in an eight times higher luminescence intensity compared to Ge and SiGe hut clusters as a result of a higher electron-hole wave function overlap and a reduced non-radiative recombination channel. However, the large size of these islands results in a degradation

of the k-space recombination properties. Therefore, phonon assisted recombination processes can compete with the no-phonon assisted recombination.
This nicely shows that it is not possible to optimize both the k-space and the real space electron-hole wave function overlap of (Si)Ge based light emitters using standard fabrication schemes.
Furthermore, the SiGe islands offer an additional luminescence mechanism which has previously been found in molecular beam epitaxial quantum wells. We show extensive studies on the origin of this luminescence studies and obtain evidence that this luminescence might stem from recombination within germanium rich regions in the SiGe alloy. In addition we find that these SiGe islands nucleate in a laterally self-ordered face centered cubic structure with a high degree of ordering.
A further enhancement of the radiative efficiency seems to be not possible in the (Si)Ge system due to the interconnection of the structural properties size and Ge content. Without employing more exotic epitaxial methods we need external methods to enhance the radiative recombination efficiency. Therefore, we employ two dimensional photonic crystals where **chapter 7** introduces the theoretical aspects about photonic crystals. A short summary of the mathematical basics and the resulting formation of a photonic band structure is given. Also photonic crystal cavities are introduced.
In **chapter 8** we embed laterally ordered type I SiGe islands in two dimensional silicon on insulator photonic crystal micro-cavities. We find an enhancement of the luminescence intensity by a factor of 6-12 when exciting the SiGe islands in a photonic environment. In addition we succeed in detecting a luminescence signal from one layer of SiGe islands even up to room temperature.
Two final device applications are presented in **chapter 9 and chapter 10**. Here we present germanium island light emitting diodes without and with two dimensional photonic crystal. We will investigate the temperature stability of the P-I-N diode design and we will elucidate that electrical current injection is more efficient than optical excitation. Finally, we will show indication for mode enhancement in electrical contacted SiGe based photonic crystal cavities.
In a complementary thesis [Hau12], based on material and technology developed in the present work, two and three dimensional photonic crystal micro-cavities are used to invest and exploit cavity quantum electrodynamics phenomena like the Purcell effect for an enhanced radiative recombination.

2. Scientific background of (Si)Ge based light emitters

2.1. Nucleation of germanium heterostructures

Silicon and germanium are indirect band gap materials [Car66, Phi62] with a low optical internal quantum efficiency [Pav08]. To enhance the radiative recombination rate it is possible to combine both materials. The formation of heterostructures where germanium is sandwiched between silicon then allows the trapping of charge carriers. This trapping can result in a spreading of the charge carrier wave function in k-space implicating a quasi-direct transition.
The fabrication of heterostructures is possible using epitaxial methods like molecular beam epitaxy [1] or chemical vapor deposition. Both methods allow the deposition of germanium on silicon substrates with atomic precision.
In 1975 Kasper *et al* [Kas75] have shown for the first time the successful heteroepitaxy of Si/SiGe heterostructures. This initiated a vast increasing research interest in this topic leading to a well understanding of the epitaxial process. It turned out that the deposited germanium adopts the crystal symmetry of the underlying silicon substrate including the lattice constant. The 4.2% lattice mismatch [Abs89] between silicon and germanium results in a biaxial compression of germanium in-plane and an uniaxial tensile strain component in growth direction. In thermodynamic equilibrium this leads to an increasing strain energy which scales with the layer thickness according to $E_{strain} \propto \epsilon^2 d$ [Hua98]. With increasing germanium layer thickness the system tries to minimize the strain energy either by the formation of misfit dislocations [Mat74] or by the nucleation of three dimensional heterostructures with distinct facets [Bru02, Eag90, Mo90].
For growth conditions, which we employ in the context of this thesis, the strain relaxation via the formation of three dimensional islands is favored. The formation of Ge based heterostructures follows the so called Stranski-Krastanow mechanism [Bru02]. Here a three dimensional island structure occurs at a certain critical thickness. It is determined by the thickness at which it is more favorable for the system to increase the surface energy while decreasing the strain energy [Sta04]. The resulting structure then consists of a pseudomorphically strained wetting layer with a thickness of approximately three to four monolayers. Above are the three dimensional strain relaxed islands [Fuk97].
However, additional material deposition can remove the wetting layer in favor of bigger islands [Bre09a]. This process is called Ostwald ripening [Ros98].

[1] A detailed introduction about the used molecular beam epitaxy system is given in [Ebe90, Mie01]

2.2. Germanium heterostructure morphologies

The critical thickness for island formation can be extended by replacing pure germanium with silicon-germanium which results in a reduced strain energy [Kas04] due to a reduced lattice mismatch. The resulting two dimensional layer is called quantum well [Bea84]. Upon the deposition of more than three to four monolayers of pure germanium first unstable nucleation centers called pre-pyramids or mounds [Vai00] form. These unstable structures evolve into quantum dots or islands with continued deposition of germanium . These three dimensional heterostructures are categorized in three different morphologies called hut clusters [Kam99], pyramids [Ros99, Ter02] and domes [Ros99]. In figure 2.1

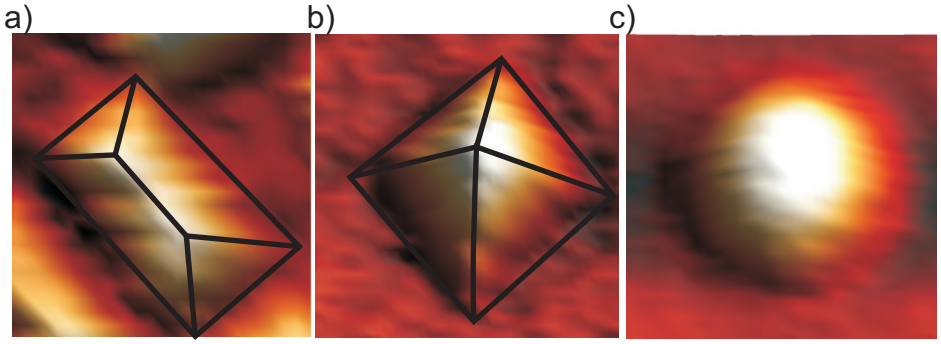

Figure 2.1.: Atomic force microscopy image of a single germanium (a) hut cluster, (b) pyramid and (c) dome. The black lines highlight the edges of the quantum dot or island morphologies with their different facets.

atomic force microscopy images of single (a) Ge hut clusters, (b) pyramids and (c) domes illustrate the shape of each morphology. Figure (a) shows a Ge hut cluster which is a metastable [MR98b] island morphology. The image shows the rectangular shape, whereas the black lines indicate the {105} facets [Mo90]. In (b) we show one exemplary pyramid. This morphology is energetically stable and differs from Ge hut clusters in the quadratic base and a larger size. Pyramids are {105} faceted [Ros99, Ter02]. Domes are even larger and have a circular base [Ros99]. Moreover domes are multifaceted where the {113},{105} and {15 3 23} are the most prominent facets [Rob09].
It has been shown by different groups that during the epitaxy pyramids and domes can coexist [Ros99, Wan07] and that pyramids can convert to domes and vice versa [Kam98, Vos00, MR98a]. Hereby, the change of the morphology is abrupt [MR98a].
In contrast to Ge hut clusters [Bou05], domes and pyramids have a lateral size larger than or comparable to the De Broglie wave length of heavy holes (hh) in Ge. Thus, the lateral confinement is very weak and it is, hence, not correct to assume a 0D confinement. Therefore, when referring to pyramids or domes we will speak of Ge islands. Throughout this thesis the terms hut cluster and quantum dots will be used equivalently [Bou05]. The occurrence of different morphologies can be explained by following equation which describes the necessary energy for the nucleation of an island with volume V and facet

angle Θ.

$$\Delta E = 4\Gamma V^{2/3} tan^{1/3}(\Theta) - 6E_{strain} V tan(\Theta) \tag{2.1}$$

Here Γ is the free energy change resulting from the formation of an island [Ros98, Dar99, Dar02]. Using this formula Tersoff *et al* [Ter94] calculated the necessary energy for islands with different facet angles as a function of the volume. In conclusion, they found that larger islands favor dome shape whereas smaller islands favor the {105} facet and, therefore, pyramidal shape. However, the energetic consideration of the morphologies does not explain the presence of the hut cluster morphology as they share the same facet angles as the pyramids. Here additional surface kinetic considerations have to be taken into account.

2.3. Surface diffusion of adatoms

Surface diffusion of germanium material is very important in germanium epitaxy as it determines the length germanium adsorbed atoms (adatoms) can diffuse on the surface before losing their kinetic energy and binding to the crystal. The surface diffusion length is strongly dependent on the growth temperature and J. Nützel described it with [Nüt95]:

$$\Delta_{kin} = \Delta_0 \sqrt{\frac{R_0}{R}} exp\left(-\frac{E_s}{k_B T}\right) \tag{2.2}$$

Here R/R_0 is the normalized growth rate. Δ_0 and E_s are experimental fitting parameters. With increasing growth temperature the diffusion length of the germanium adatoms increases resulting in less nucleation spots and larger islands [Nüt95, Spe93]. For low growth temperatures the limited diffusion of adatoms favors specific crystallographic directions. In the case of germanium on silicon the diffusion along the elastically soft [100]-direction [Käs99, Jes98, Mon04]. The non-symmetric diffusion results in the elongated shape of hut clusters [MR98b]. Hut clusters are thermodynamicaly metastable [MR98b] and will convert into pyramids and domes with increasing temperature.

2.4. Intermixing of germanium heterostructures with silicon

Until now we only spoke about pure germanium islands but extensive and systematical Raman spectroscopy [Tan03, Tsa94] or X-ray diffractometry [MaP02] work revealed that germanium heterostructures where pure germanium is deposited suffer from interdiffusion with silicon. This interdiffusion or intermixing with silicon is a strain driven process [Wan01c]. Especially during capping with silicon the system tries to minimize the strain energy by reducing the lattice constant. This can happen either by the diffusion of germanium into the surrounding silicon matrix, or due to diffusion of silicon into the germanium islands. Both processes occur but the diffusion constant of silicon in germanium is much higher [Sch91]. Therefore, we can neglect the diffusion of germanium

into the silicon in the whole discussion of this thesis. In first order the intermixing with silicon can be described by the second Fick's law [Gav08, Sch97b]:

$$\frac{\partial x(z,t)}{\partial t} = D(T_c) \cdot \frac{\partial^2 x(z,t))}{\partial z^2} \tag{2.3}$$

with

$$D(T_c) = D_0 \cdot exp\left(-\frac{E_a}{k_b T_c}\right) \tag{2.4}$$

where D is the diffusion constant of silicon into germanium and T_c is the growth temperature. This approach however neglects strain. To take strain into account more sophisticated models need to be employed. Sonnet and Kelires for example used an atomistic quasi-equilibrium approach based on Monte Carlo simulations to link the composition profile with the strain field [Son02].
More detailed explanation of the epitaxy are given in the literature [Bou05, Den03, Kam97, Abs96b, Mie01]. But the qualitative considerations of section 2.1 section 2.2 section 2.3 and section 2.4 are sufficient to understand the epitaxial formation of Ge based heterostructures as conducted in this thesis.
Moreover, there are already many detailed experimental investigations concerning the structural properties of Ge based heterostructures which we will introduce in the next sections.

2.5. Topographic properties of germanium quantum dots and islands

The structural parameters of Ge islands depend on two epitaxial parameters: the growth rate and the substrate temperature. In chemical vapor deposition the substrate temperature is the temperature of the evaporation chamber and, therefore, also defines the growth rate. Molecular beam epitaxy is more versatile as the growth rate and substrate temperature (also called growth temperature T_c) are independent of each other.
It has been shown that the morphological shape of Ge heterostructures is directly influenced by the growth temperature. Hereby Ge hut clusters form at growth temperatures below $\approx 550°C$ [Den04]. For higher temperatures the epitaxy kinetics are not limited and pyramids and domes evolve [Jin03]. This shape transition is a result of equation 2.2 showing that a higher growth temperature results in a larger surface diffusion length of adatoms. This increases the amount of atoms which form the islands resulting in larger islands [Abs96b]. If the amount of incoming atoms is fixed this also yields a reduced amount of free nucleation spots on the surface and, thus, the island density is reduced [Abs96b].
Quantitative investigations using atomic force microscopy or scanning tunneling microscopy show that hut clusters are the smallest quantum dot morphology with typical lengths of approximately 15-35 nm and typical heights of 1-3 nm, respectively [Tan04]. Densities of the order of 10^{11} cm^{-2} are reported [Tan04]. Pyramids are significantly larger with lateral lengths of 50 nm [Bru02] and lower densities of the order of 10^8 cm^{-2}

to 10^{10} cm^{-2}. Domes are the largest morphology with diameters of up to several 100 nm reported in literature [Kam98]. With the fixed facet angles this results in typical heights of $\approx$ 7 nm. The larger size leads to a lower density of the order of 10^8 cm^{-2} to 10^9 cm^{-2} [Bru02].
During capping the structural properties change. Cross-sectional transmission electron microscopy or selective etching techniques combined with atomic force microscopy have shown that especially at elevated temperatures the islands flatten and increase their lateral dimensions. This is accompanied by the formation of additional facets [Sut98].
The capping of islands is very important for optical experiments. The silicon matrix reduces the amount defect states at the island surface which degrade the luminescence properties by providing non-radiative recombination centers [Fuk95].

2.6. Composition of germanium heterostructures

Capping not only influences the size but also the alloy conformation of the islands. Using Raman spectroscopy many groups determine the average Ge content from the shift of the phonon frequency [2].
Systematic investigations of quantum wells [Tsa94] and of different quantum dot and island morphologies [Tan03, Gro97] have shown that the average Ge content strongly decreases with increasing growth temperature. According to equation 2.4 a higher temperature favors the diffusion of silicon into germanium and, thus, the average Ge content of the islands is reduced. This process is called intermixing.
In recent years some groups combined selective etching methods and subsequent atomic force microscopy [Zha10] to map the Ge content profile of Ge islands. The results nicely show that intermixing is not an isotropic process. Rather than that it is is a strain driven process. Therefore, interdiffusion is most prominent where the strain energy is highest [Rai02]. This is the case at the base of islands, where the strain is not relaxed.
Experimentally, the selective etching method nicely shows that the germanium profile can be described by a germanium rich core and top and a silicon rich shell and base [Den03, Zha10].

2.7. Band structure of Ge heterostructures

In figure 2.2 we exemplary present the simulated band structure in growth direction of one Ge island. For simplicity the Ge island is modeled with an obelisk shape. The base diameter is 20 nm and the height is 3 nm, respectively. The germanium content is set to 50%. A wetting layer with a thickness of 0.5 nm is included in the simulation. Details about the simulation method can be found in the appendix A.
From top to bottom we find the Γ conduction band, the eight degenerated L-bands and the six Δ conduction bands. Below the band gap we find the heavy hole, the light hole and the split-off valence band. The black horizontal lines indicate the ground state

[2] The experimental method and the subsequent analysis is described in the appendix B.3.

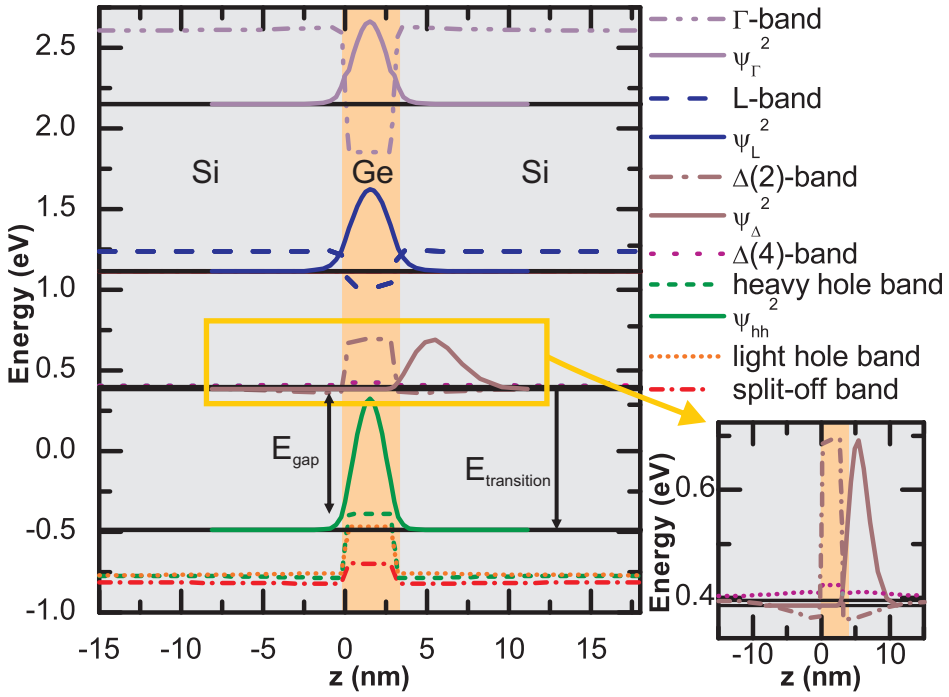

Figure 2.2.: Calculated band structure of an obelisk shaped Ge island with a Ge content of 50% a height of 3 nm and a length of 20 nm. The black horizontal lines indicate the ground state energy of the respective bands. The electron (hole) probability densities are plotted with the same color as the corresponding bands using solid lines. The inset shows a zoom on the Δ conduction band.

energies of the individual bands. The difference between those energies is the transition energy, which is the energy of a photon emitted by the radiative recombination of electron and hole. Furthermore, we plot the electron and hole probability density of those ground states using solid lines. The simulations show that Ge islands still have an indirect transition in k-space as the lowest conduction bands are located in the Δ direction. This also shows that the band structure is silicon-like as the lowest conduction band in pure Ge is located at the L-point. Both the Δ-band and the valence bands have a higher energy in the Ge region and, thus, we conclude a spatially indirect transition between electrons in the silicon matrix and holes confined in the germanium. This can also be seen in the electron and hole probability densities which are spatially separated. This verifies the experimental [Das01, Wan01a, Hua01] observed and theoretical calculated [EK06] type II band alignment.

Influence of strain on the band structure

Strain affects the spatial position of atoms in the crystal lattice and, therefore, the periodic potential in the Schrödinger equation. Such deviations are expected to have an

effect on the band structure. Finite element calculations have shown that the strain in silicon is dominated by the uniaxial strain component. The hydrostatic part only plays a minor role [Sch00]. The silicon matrix above and below the island is tensile strained in-plane whereas the silicon matrix is compressively strained next to the island. In the Ge region the in-plane lattice constant is compressively strained, whereas the lattice constant in growth direction is tensile strained.
In figure 2.2 we observe the influence of strain in the simulations as strain results in a shift of the band energies. The sixfold degeneracy of the Δ-bands [EK06] is lifted both in the silicon matrix as well as in the germanium island. Due to the symmetric island shape the four in-plane Δ-bands (purple dotted lines) remain degenerated. As the resulting bands are fourfold degenerate we will call these bands $\Delta(4)$ bands [Sch97a, Abs96a]. The two Δ-bands (gray dash dotted line) in growth direction have a different energy shift. As the two directions are equivalent we will call these bands $\Delta(2)$-bands.
Above and below the island the silicon is tensile strained. This leads to a lowering of the band edges in this crystallographic direction [Vog93]. The compressive strain next to the island leads to a rising band energy in the in-plane direction [EK06].
For the Ge islands the in-plane lattice constant is compressively strained resulting in a rise of the band energy. In growth direction the island is tensile strained resulting in a lowering of the band gap. Thus, the sixfold degeneracy of the Δ-bands is lifted similar to the silicon matrix.
In the same manner the strain lifts the degeneracy of the heavy and light hole bands.
The strain induced lowering of the $\Delta(2)$ band above and below the island can be directly seen in the inset of figure 2.2. It leads to the formation of weakly confined energetic states for electrons.
In summary, the hole is strongly confined within the island. The Δ-valley electrons are located in the vicinity of the island. Hereby the confinement is only provided by the tensile strain. This leads to a spatially indirect recombination of type II. Moreover we have seen that the Δ valleys are the conduction band minima resulting in a k-space indirect band alignment.

Influence of Ge content on the band alignment

The spatial separation of the charge carriers due to the type II band alignment is a major drawback for optical properties. Theoretical work conducted by Van de Walle *et al* [VdW86] and other groups [Peo86] has shown that two dimensional SiGe quantum wells with reduced Ge content might offer a spatial type I confinement. Such a type I confinement, where both the electrons and holes are located within the heterostructure is strongly desired for superior optical properties.
Due to the expected strong impact of a type I band alignment on optical properties extensive studies concerning the band alignment in SiGe quantum wells have been conducted by many different groups. Fukatsu *et al* [Fuk93] and Houghton *et al* [Hou95] proposed a type I band alignment for compressively strained SiGe quantum wells based on photoluminescence experiments. On the contrary, Wachter *et al* [Wac92], Baier *et al* [Bai94] and Thewalt *et al* [The97] claim that the type I band alignment is only due to

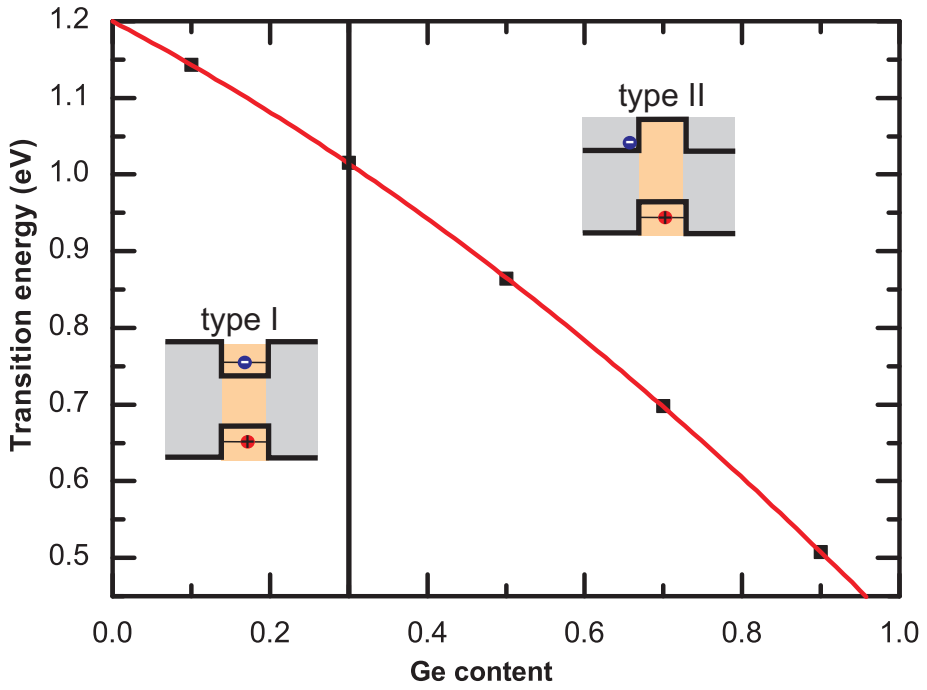

Figure 2.3.: Calculated transition energy as a function of the Ge content of an obelisk shaped Ge island with a height of 3 nm and a length of 30 nm.

band bending caused by strong optical excitation which results in charge carrier accumulation. Some controversy regarding the type I band alignment rises from theoretical calculations as pseudopotential calculations conducted by Rieger *et al* [Rie93] as well as 30 band k*p calculations conducted by El Kurdi *et al*[EK06] affirm the presence of a type II band alignment for all Ge fractions.
Similar systematic investigations for three dimensional heterostructures are comparably rare but unambiguous. El Kurdi *et al*[EK06] performed 30 band k*p band structure calculations and they found a type II confinement for lens shaped islands for all Ge contents. In addition photoluminescence experiments [Das01, Wan01a, Hua01] lead to the conclusion of a type II band alignment for Ge islands whatever morphology is present. Therefore, there is no controversy regarding the band alignment of Ge three dimensional heterostructures.
The Ge content of the heterostructures is not only responsible for the band alignment but also for the transition energy [EK06, Nov03]. In figure 2.3 we exemplarily present our own calculations of the transition energies of an obelisk shaped island with a base length of 30 nm and a height of 3 nm as a function of the Ge content. The Ge content is varied between 10% and 90%. The island is modeled with a constant Ge profile. The transition energy decreases with increasing Ge content. In good approximation the band gap of an

unstrained SiGe alloy can be approximated using a polynomial approach [Web89]:

$$E_{gap-SiGe}(x) = 1.155 - 0.43x + 0.206x^2 \tag{2.5}$$

We use the same formula to fit the data points and we receive:

$$E_{gap-SiGe-island}(x) = 1.200 - 0.543x - 0.251x^2 \tag{2.6}$$

with a very high degree of confidence of 99.997%. Variations in the parameters between equations 2.5 and 2.6 are caused by different strain fields and the three dimensional shape. Interestingly the simulated band offset has a transition from a type II to a type I band alignment when reducing the Ge content below 30%. This is in contrast to simulation results from El Kurdi *et al* [EK06]. Thus, we conclude that the theoretical calculated band alignment is strongly dependent on the Ge content but also on shape and size of the island [Bas06, Ali96].

Influence of topographic parameters on the band structure

Finally we consider the island size influencing the band structure. In first approximation one usually describes the electronic structure of islands by a cubic quantum box with infinite barrier heights [Qua]. In this approximation the carrier energy follows a hyperbolic behavior:

$$E(x) = \frac{\hbar^2\pi^2}{2}\left(\frac{n_x^2}{m_{xx}L_x^2} + \frac{n_y^2}{m_{yy}L_y^2} + \frac{n_z^2}{m_{zz}L_z^2}\right) \tag{2.7}$$

Here n is a positive integer, m_{xx}, m_{yy}, m_{zz} are elements of the effective mass tensor and L is the width of the quantum well in a certain direction.
This assumption, however, neglects the influence of strain and a non-cubic shape, which both depend on the size of the island. Therefore, we perform k*p calculations using the same model as in the previous section. Now we fix the Ge content to 50% while changing the length of the island from 10 to 60 nm. We want to emphasize that the island is modeled with a symmetric base. The resulting transition energies we plot in figure 2.4(a) as a function of the island length. A decreasing transition energy with an increasing length is observed. Our simulations show that the transition energy decreases double-exponentially with an increasing size. For completeness we also present the dependence of the transition energy as a function of the island height in figure 2.4(b). Here we calculate the band structure of islands with a Ge content of 50% and a length of 40 nm. With an increasing height we find that the transition energy exponentially decreases [EK06].
The deviation of the double-exponential or exponential trend from the hyperbolic trend in equation 2.7 already shows that the model of a quantum box with infinite barrier heights is not sufficient to describe Ge island structures as strain effects, a non-cubic shape and composition gradients are not included in such a simplified model. Thus, more sophisticated band structure calculations based on realistic structural input parameters are necessary to understand the electronic structure of Ge islands.

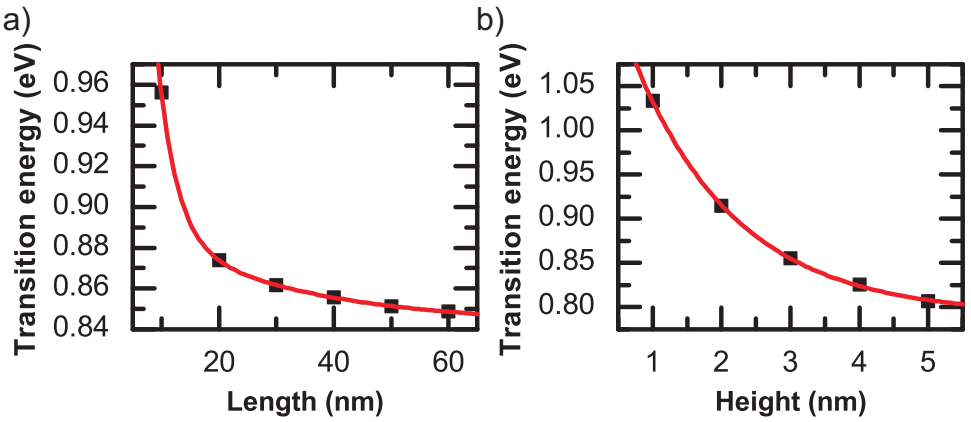

Figure 2.4.: (a)Calculated transition energy as a function of the length of an obelisk shaped Ge island with a height of 3 nm and a Ge content of 50%. (b) Calculated transition energy as a function of the height of an obelisk shaped Ge island with a length of 40 nm and a Ge content of 50%.

2.8. Optical properties of Ge islands

The radiative recombination rate of electrons from the conduction band with holes from the valence band can be described by Fermi's golden rule [Fox06].

$$\Gamma_{i\to f} = \frac{2\pi}{\hbar} |M_{if}|^2 \rho(\hbar\omega) \tag{2.8}$$

where $\rho(\hbar\omega)$ is the density of photon states. M_{if} is the optical matrix element which is defined as:

$$M_{if} = \langle f | H | i \rangle = \int \psi_f^*(\mathbf{r}) H(\mathbf{r}) \psi_i(\mathbf{r}) d^3\mathbf{r} \tag{2.9}$$

with ψ being the wave functions of the initial or final states. In equation 2.9, H=-$\mathbf{p} \cdot \mathbf{E}$ is the light induced perturbation caused by the interaction of the photon electric field amplitude $\mathbf{E}$ and the exciton electric dipole $\mathbf{p}$. However equation 2.8 is only valid for direct semiconductor materials. For indirect transitions the momentum conservation rule has to be taken into account and phonon assistance is necessary. When including the electron-phonon interaction matrix element W_{12} [Pok04] equation 2.8 transforms into:

$$\Gamma_{i\to f} = \frac{2\pi}{\hbar} |M_{if}|^2 |W_{12}|^2 \rho(\hbar\omega) \rho(\hbar\omega_{phonon}) \tag{2.10}$$

The necessity for a three particle process strongly reduces the radiative recombination rate and, thus, the radiative recombination time. Therefore, fast non-radiative recombination processes like Auger recombination cannot be neglected. As a matter of fact in Si the non-radiative recombination rate is larger than the radiative recombination rate [Pav08] and we define the internal quantum efficiency η as:

$$\eta = \frac{\Gamma_{rad}}{\Gamma_{rad} + \Gamma_{non-rad}(T)} \tag{2.11}$$

In pure silicon the internal quantum efficiency is approximately 10^{-6} [Pav08].
Up to now we assumed that the transition is phonon assisted. But according to Heisenberg's uncertainty relation $\Delta x \Delta k \geq \hbar/2$ [Rob29] a spatial confinement like in SiGe heterostructures results in a spreading of the wave function in k-space. The strain induced confinement of the electrons in the silicon matrix results in a spreading of the electron wave function towards the Γ-point. In addition the strong confinement of the holes inside the SiGe heterostructure spreads the hole wave function from the Γ-point towards the Δ-point. In fact the second process is much more likely because according to the simulations in figure 2.2 the confinement energy of the ground state electron is only of the order of 10 meV whereas the confinement energy of the ground state hole is of the order of 270 meV. Thus, the hole is spatially much more confined and the spreading of the hole wave function is much larger.
This can allow for phononless transitions, which indeed have been shown in SiGe quantum wells [Fuk92, Bru92, Stu91]. For Ge islands many groups claim a phononless transition [Das01, Fuk97, Lar03] as well as phonon assisted recombination [Wan01a], both without any unambiguous proof.
Hence, it is theoretically necessary to include phonons in the theoretical consideration. Unfortunately up to now there are no methods to calculate the electron-phonon interaction matrix element W_{12} in nanostructures. Within this thesis, we will assume the phonon matrix element to be constant for all investigated samples as we expect an equal crystal quality. Furthermore, we will see that the island size does only vary by a small amount.
Equation 2.10 suggests that radiative recombination does not only require an overlap of the wave function in k-space but also in real space. Using the dipole approximation the optical matrix element is governed by the optical oscillator strength between the final and initial state [Ror93]:

$$f_{if} = \frac{2m\omega_{if}}{3\hbar} \left|\langle \psi_f(\mathbf{r}) \left|\mathbf{r}\right| \psi_i(\mathbf{r})\rangle\right|^2 = \frac{2m\omega_{if}}{3\hbar} \left|\langle \phi_f(\mathbf{r}) u_f(\mathbf{r}) \left|\mathbf{r}\right| \phi_i(\mathbf{r}) u_i(\mathbf{r})\rangle\right|^2 \tag{2.12}$$

Here ϕ is the envelope function of the initial or final state and u is the Bloch function describing the crystal periodicity [Blo29]. The envelope function varies slowly compared to the Bloch function and, therefore, the oscillator strength can be approximated as [Coo84, Har05]:

$$\langle \phi_f u_f \left|\mathbf{r}\right| \phi_i u_i\rangle \approx \langle u_f \left|r\right| u_i\rangle \langle \phi_f | \phi_i\rangle + \langle u_f | u_i\rangle \langle \phi_f \left|r\right| \phi_i\rangle \tag{2.13}$$

For interband transitions, which we will study throughout this thesis, the second term is zero as the Bloch functions of different bands are orthogonal at the same position [Har05, Coo84]. Thus, the optical matrix element M_{if} is proportional to the squared electron-hole wave function overlap.

$$O = \langle \phi_f | \phi_i \rangle = \int \left|\phi_f \phi_i\right| d^3r \tag{2.14}$$

Inserting equation 2.14 into 2.11 and with the assumption that the radiative recombination rate is smaller than the non-radiative recombination rate we can calculate the

luminescence intensity [Hau10]:

$$I_{PL} = PR\eta \propto |\langle \phi_f | \phi_i \rangle|^2 \tag{2.15}$$

Here P is the external photon detection probability of the experimental setup and R is the charge carrier excitation rate. There are only few calculations regarding the overlap integral and none concerning the whole transition strength in the SiGe system. In 2006 El Kurdi *et al* calculated the spatial electron hole wave function overlap for Ge islands as a function of the germanium content [EK06]. They found that the overlap integral increases for a decreasing germanium content. The reason for this is that an increasing silicon content inside the island delocalizes the hole wave function. The stronger delocalization results in a penetration of the hole wave function into the silicon barrier [EK06, Ror93]. In addition the electron has a higher probability for residing in the Ge island. A general study concerning the overlap integral in type II confinement structures has been conducted by Madureira *et al* in 2007. Solving the single-particle Schrödinger equation in the Hartree-Fock approximation for InP/GaAs type II quantum dots, they conclude that the electron-hole wave function overlap and, hence, the carrier lifetime is very sensitive on the exact shape of the quantum dots [Mad07]. Experimentally, Yakimov *et al* [Yak00] tried to deduce the oscillator strength of Ge islands using absorption spectroscopy. They found an oscillator strength of 0.5 which is about 10 times higher than the calculated results from El Kurdi *et al* [EK06].
Although there are already detailed investigations concerning the topographic parameters (see section 2.5) of the band alignment and band structure (see section 2.7) as well as of the optical properties (see section 2.8) there is no systematic study on the combination of experiment and theory. Also there is no experimental study regarding the overlap of electron and hole wave functions via luminescence intensity comparisons. Therefore, within the next chapters we will present optical investigations on different SiGe three dimensional confinement structures. Moreover we will compare the experimental results with the predictions from k*p band structure calculations.

3. Properties of Ge hut clusters

The key requirements for a high radiative efficiency are a strong electron-hole wave function overlap both in k-space and in real space.
Because of Heisenberg's uncertainty relation [Rob29] the smallest Ge quantum dot morphology is expected to offer the optimum recombination properties in k-space.
Therefore, we begin with an investigation of Ge hut clusters [Kam99] whereby we quantitatively investigate the spatial overlap by a growth study with a varying growth temperature. To asses the potential for an enhanced luminescence intensity realistic simulations, based on a structural analysis [Tan03, Nüt95, Spe93], in comparison with photoluminescence experiments elucidate the influence of different structural properties on the spatial electron-hole wave function overlap.

3.1. Structural properties of germanium hut clusters

The Ge hut clusters investigated in this chapter are fabricated at the WSI using a Riber32 ultra high vacuum solid-source molecular beam epitaxy system. Detailed information on the epitaxy system are given in reference [Ebe90, Fri92]. The substrate wafer is a standard intrinsic Si wafer with an orientation of (001). We epitaxially fabricate Ge quantum dots using material deposition rates of 0.4 Å/s and 0.1 Å/s for Si and Ge, respectively. These rates are deduced from previous studies [Bou05] in our group. The growth temperature T_c varies between $\approx$ 300°C and $\approx$ 425°C. At higher growth temperatures, the morphology transforms into pyramids and domes (see chapter 4). Lower temperatures are expected to degrade the crystal quality. If not stated otherwise all samples consist of eight layers of quantum dots each containing a two dimensional equivalent of eight monolayers of nominally pure Ge. To prevent strain induced stacking of the quantum dot layers [Cha03a, Sch99] the individual quantum dot layers are separated by a 20 nm Si spacer layer. For optical investigations, the samples are capped by an approximately 100 nm thick Si capping layer to eliminate an influence of surface states (see section 2.5). Additionally, one layer of surface quantum dots prepared with the same epitaxy conditions as the capped ones is deposited on top of the heterostructure for structural investigations using atomic force microscopy.

3.1.1. Topographic properties of germanium hut clusters

In figure 3.1, we show three dimensional atomic force microscopy images of three different samples where we use growth temperatures of (a) 298°C, (b) 346°C and (c) 424°C. All three images illustrate hut clusters with a rectangular base and an inclination angle

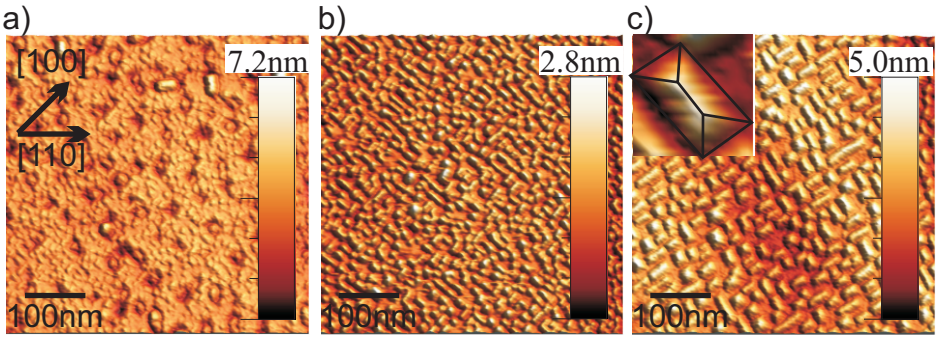

Figure 3.1.: Atomic force microscopy images of Ge hut clusters grown at (a) 298°C, (b) 346°C and (c) 424°C upon the deposition of nominally 8 monolayers of pure Ge. The area of the image is 500 nm x 500 nm. The inset in (c) shows a zoom on one hut cluster. The individual facets are highlighted with black lines.

relative to the surface of 11° corresponding to a {105} facet [Mo90]. The individual sidewalls are highlighted in the inset of 3.1(c) using black lines. The atomic force microscopy images show that hut clusters are always elongated in [100] direction. For all growth temperatures the surface is covered by a homogeneous distribution of high density quantum dots. A quantitative analysis of the length and height as a function of the growth temperature is given in figure 3.2. The analysis is conducted according to the scheme described in the appendix B.1. The sketch in the upper left corner of figure 3.2 illustrates how the length is defined. The longer side of the hut clusters is the length and the smaller side is the width which is not shown here but used as input parameter for the band structure simulations in section 3.2. The width follows the same trend as the length. Both the length and the height of the hut clusters linearly increase with increasing growth temperature due to an enhanced surface diffusion length[Nüt95, Spe93]. The height increases from 0.8±0.1 nm at T_C=298°C to 1.8±0.1 nm at T_C=424°C whereas the length increases from 17.8±1.0 nm to 35.6±1.6 nm. This trend agrees well with previous studies from other groups as described in chapter 2.5.

To further strengthen the argument of a diffusion dependent kinetic growth mechanism figure 3.3 presents the hut cluster density as a function of the length (a) and growth temperature (b). In (a), we see that the quantum dot density decreases as a function of the hut cluster length. The red line is a guide for the eye and connects the first and last value. All data points lie on this red line indicating a linear dependence. The strong correlation is caused by the fact that an increasing growth temperature results in an enhanced kinetic energy of the germanium adatoms. Thus, an enhanced growth temperature, which causes the larger length, results in an enhanced diffusion length according to equation 2.2. Hence, incoming adatoms can reach an already existing nucleation spot, which is further apart rather than creating a new nucleation spot [Bru02].

In a different representation figure 3.3 (b) shows that the hut cluster density reduces

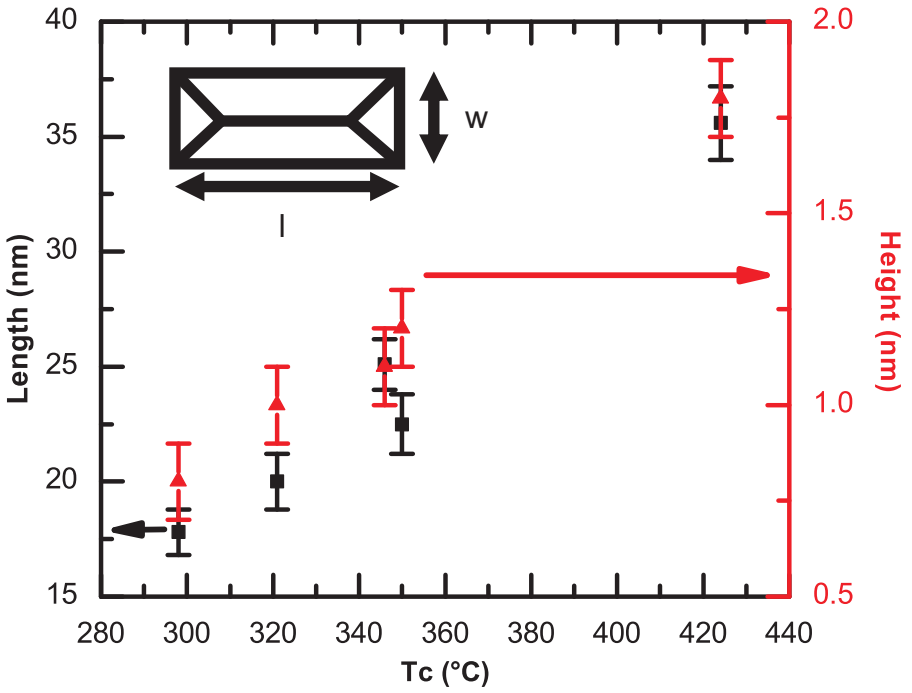

Figure 3.2.: Hut cluster length (black squares left axis) and hut cluster height (red triangles red axis) as a function of the growth temperature. The sketch in the left upper corner illustrates the hut cluster shape and defines the parameters length and width

with increasing growth temperature. This is a result of a reduced amount of nucleation spots. The average density which is of the order of 10^{11}cm^{-2} is comparable to literature values [Ara11, Koh04]

3.1.2. Germanium content of hut clusters

We determined the Ge content using Raman spectroscopy measurements. The setup as well as the analysis principle is described in the appendix B.3. In summary, Raman spectroscopy allows to measure the frequency shift of the silicon and germanium lattice vibrations which changes due to the Ge hut clusters. Using equation B.1 the frequency shift of the Ge-Ge lattice vibration determines the average Ge content. In figure 3.4, we present the resulting Ge content for various growth temperatures. It is clearly visible that the average Ge content exponentially decreases with increasing growth temperature from roughly 86% at $\approx 300°\text{C}$ to 57% at $\approx 424°\text{C}$ [Nüt95]. This we attribute to an increased intermixing of the quantum dots with silicon (see chapter 2.4). However, it is important to mention that the Ge content determined by Raman spectroscopy is averaged over many quantum dots. Moreover, it does not give any information about inhomogeneous

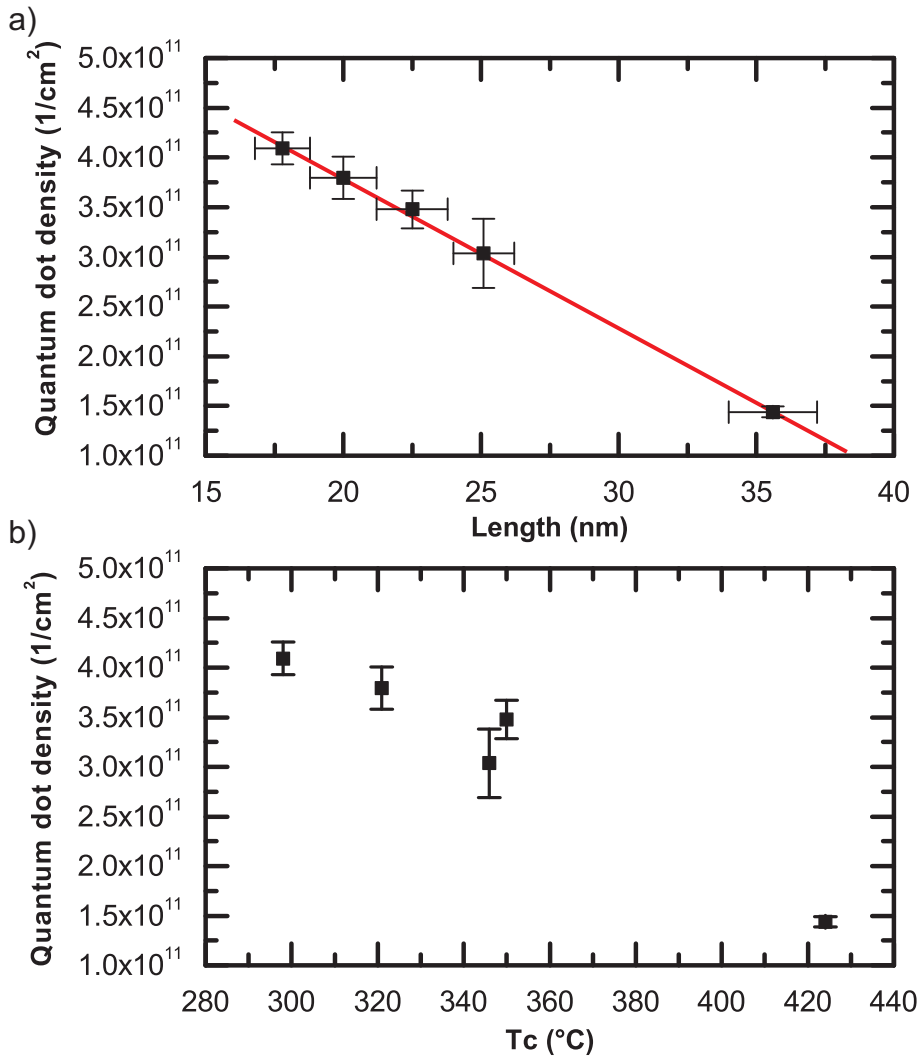

Figure 3.3.: (a) Hut cluster density as a function of the hut cluster length. The red line is a guide for the eye to indicate a linear trend. (b)Hut cluster density as a function of the growth temperature.

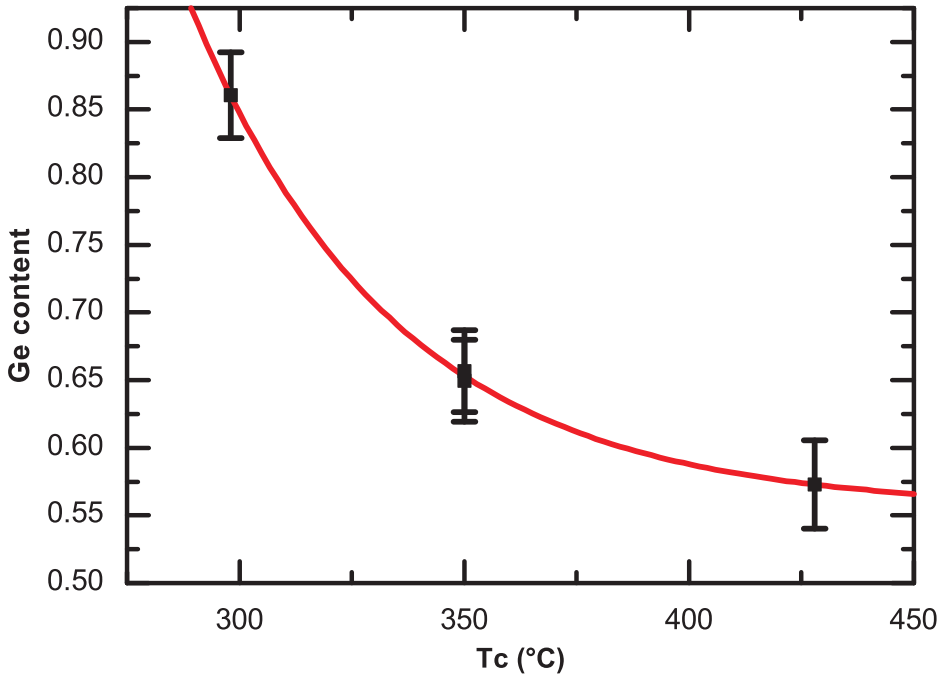

Figure 3.4.: Average Ge content function of the growth temperature. The data points are calculated from the Raman shift of the Ge-Ge lattice vibration according to equation B.1.

Ge contents which we expect from recent studies mentioned in section 2.4.
In summary, we conclude that the fabrication of Ge hut clusters is limited to a certain parameter space. In table 3.1 there is a summary of the structural parameters length, width, height, density and average Ge content. All parameters are linked by the growth temperature, which is the only parameter that is changed during epitaxy. Using higher growth temperatures no hut clusters form anymore. Instead pyramids and domes occur as we will introduce in chapter 4.

T_c (°)	length (nm)	width (nm)	height (nm)	density (10^{11}cm^{-2})	Ge content
298	17.8±1.0	12.9±0.6	0.8±0.1	4.1±0.2	0.86±0.03
321	20.0±1.2	14.2±0.5	1.0±0.1	3.8±0.2	
346	25.1±1.1	13.3±0.4	1.1±0.1	3.0±0.3	
350	22.5±1.3	13.6±0.5	1.2±0.1	3.5±0.2	0.65±0.03
424	35.6±1.6	21.7±0.5	1.8±0.1	1.4±0.5	0.57±0.03

Table 3.1.: Summary of the structural parameters length, width, height, density and Ge content, which describe the parameter space which is possible to fabricate by varying the growth temperature and depositing nominally eight monolayers of pure germanium.

3.2. Band structure calculations of germanium hut clusters

We will now utilize the previously determined values from table 3.1 as input parameters for realistic band structure calculations using nextnano++ [Bir07]. Although several groups did extensive studies on the Ge profile of Ge islands [Zha10, Den03, DS08] and of the wetting layer[Bre08] there are no studies on Ge hut cluster shaped quantum dots. Given the comparable small size of hut clusters, compared to the other Ge island morphologies, we assume the Ge content to be constant within the size of the simulation grid. The modeled Ge wetting layer consists of three monolayers with the same Ge content as the hut clusters. This design is then used as simulation model for solving the single band Schrödinger equation.

3.2.1. Calculated germanium hut cluster transition energies

In figure 3.5 (a), we present the band structure of a Ge hut cluster with a length of 22.5 nm, a width of 13.6 nm and a height of 1.3 nm. The inset illustrates the shape of a Ge hut cluster. The lines next to the hut cluster illustration depict the [100], [-100], [0-10] and [010] directions. The color coding is in analogy to the four $\Delta(4)$-bands. The x axis in (a) resembles the height (z(nm)) of the quantum dot in growth direction. Here, z=0 equals the base of the wetting layer. Four different bands are calculated. In orange we show the heavy hole valence band which ranges from approximately -0.8 eV to -0.3 eV. In contrast to the simple cuboid model in figure 2.2 the sixfold degeneracy of the Δ-band is completely lifted. The reason for this is the non-symmetric shape of the Ge hut clusters resulting in a non-symmetric in-plane strain. This changes the effective mass of the Δ-valleys in-plane relative to each other.
Figure 3.5 (b) summarizes the transition energy defined in 3.5 (a) as a function of the growth temperature. Here table 3.1 links the growth temperature with the input parameters. Starting from 320°C up to 350°C the transition energy increases approximately linear. For a higher growth temperature of 424°C the transition energy strongly decreases again. The increasing behavior between 320°C and 350°C is a result of the increasing silicon content inside the hut clusters, which increases from $\approx 20\%$ to $\approx 35\%$. A further increase of the growth temperature only results in an enhancement of the silicon content to 43%, whereas both, the lateral size as well as the height of the hut cluster increase by a factor of approximately 1.33. In conclusion, we find that for growth temperatures up to 350°C the Ge content is the dominant parameter which determines the transition energy of Ge hut clusters as it is influenced most by a change of the growth temperature.

3.2.2. Calculated optical properties of germanium hut clusters

The semi-logarithmic plot in figure 3.6 presents the electron-hole wave function overlap (see section 2.8) of a Ge hut cluster with a length of 22.5 nm, a width of 13.6 nm and a height of 1.3 nm. We calculated the recombination of different excited electron states in the four L-bands and the three Δ-bands with the heavy hole ground state. The electron-hole wave function overlap decreases for the first five electron states of the L-bands. For

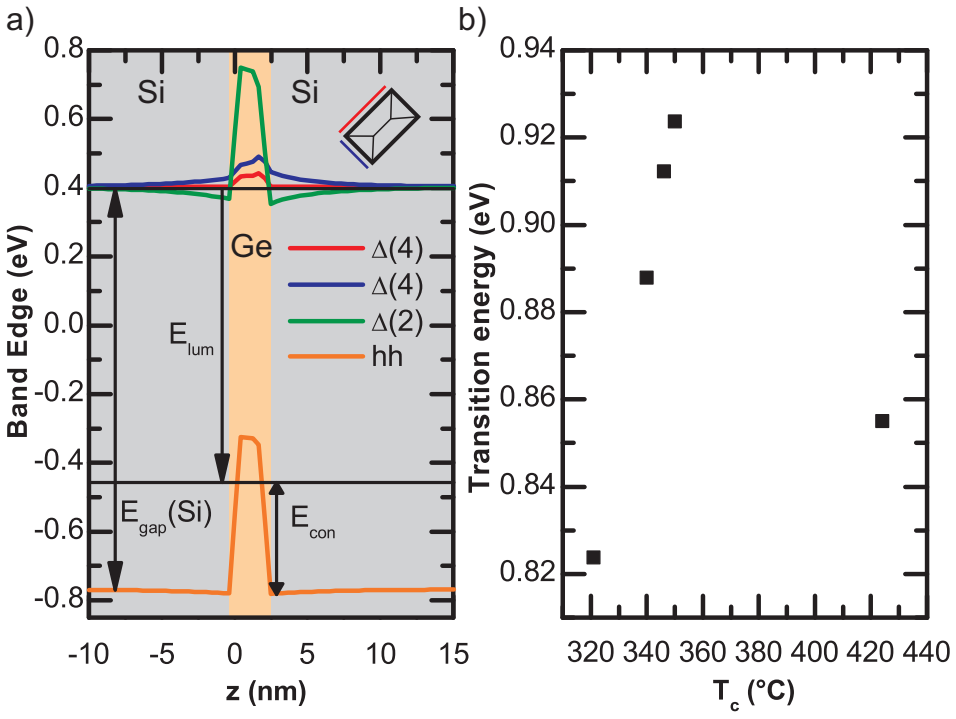

Figure 3.5.: (a) Band structure of a Ge hut cluster. The black vertical lines indicate the ground state electron and hole energy. The red and blue lines indicate the in-plane Δ-band. The green line represents the Δ(2)-band in growth direction. In orange we sketch the heavy hole valence band. In addition we define the Si band gap E_{gap}, the confinement energy E_{con} and the transition energy E_{lum}. The color coding of the inset illustrates the direction of the two Δ(4)-directions. (b) Transition energy of Ge hut clusters as a function of the growth temperature.

higher states an oscillating behavior is observed. The overlap is the same for all L-bands due to the energetic degeneracy and has a maximum of 70%. The spatial overlap of the different Δ-hh transition is between 10^{-12}% and 3%. It varies between the different crystallographic directions. In general, there is no distinct trend whether the overlap is stronger for a certain Δ-direction.
The electron-hole wave function overlap is highest for the fourfold degenerated L-bands. These bands offer a type I confinement with a spatially direct transition. Unfortunately, the L-band states have a much higher energy than the Δ-band states and are populated with a very low probability. Electrons in the L-band thermalize into the Δ-band before recombining with a hole. The overlap of the Δ-band states with the heavy hole is much weaker of the order of 10^{-12}% (forbidden transition) to 3%. This is a direct result of the spatial type II band alignment which separates the electrons and holes. Because of

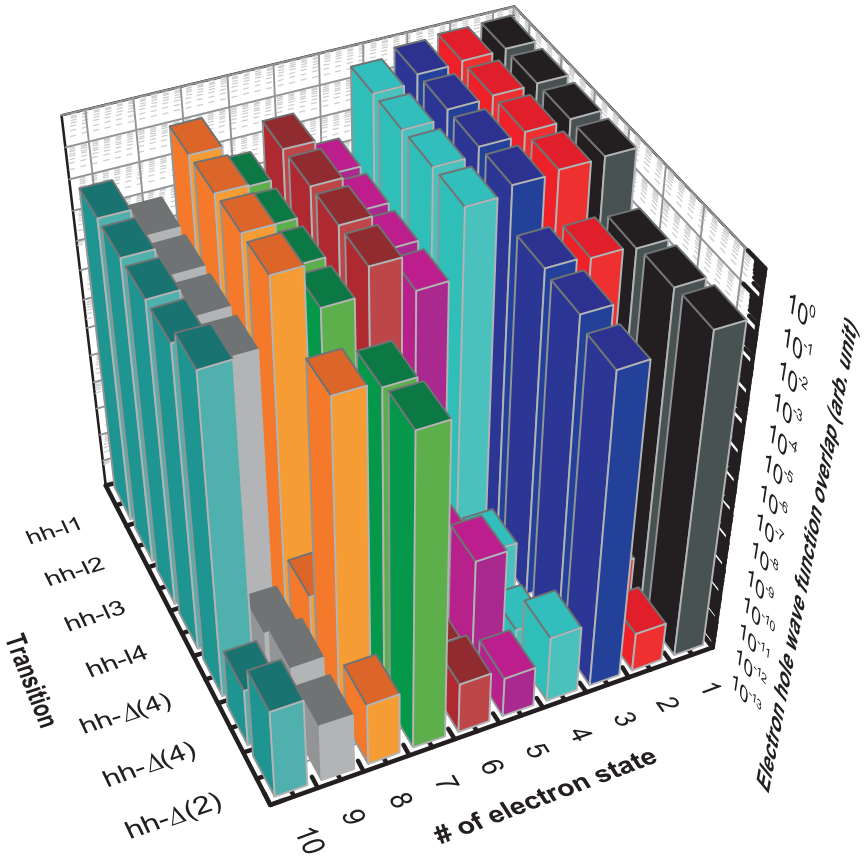

Figure 3.6.: Electron-hole wave function overlap of ground state and excited electrons in the L- and Δ-bands with the ground state heavy hole. The quantum dot is modeled as a Ge hut cluster with a length of 22.5 nm, a width of 13.6 nm and a height of 1.3 nm.

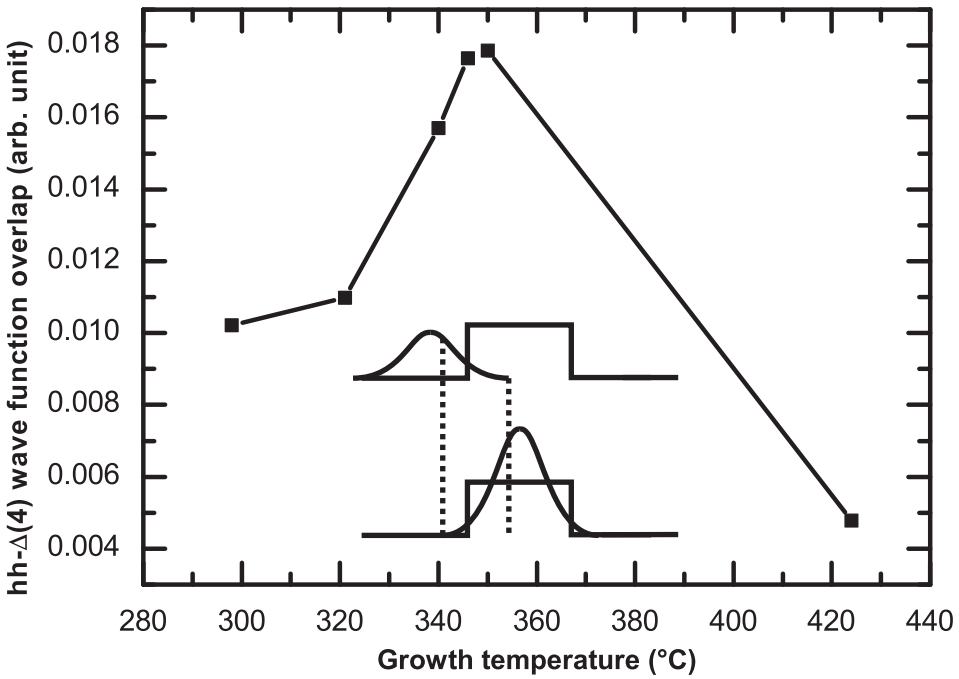

Figure 3.7.: Electron-hole wave function overlap of the $\Delta(4)$- heavy hole transition as a function of the growth temperature. The inset indicates the overlap in one dimension.

that we expect a very low radiative recombination rate.
For optical recombination we, therefore, expect that the luminescence intensity is strongly dependent on the spatial position of both the electron and hole. Growth parameters are desired where the electron wave function penetrates far into the hut cluster because of the strong hole confinement within the hut cluster. We perform the same study for the whole epitaxy parameter space defined in table 3.1 to identify these growth parameters. Figure 3.7 depicts the resulting overlap integral between the $\Delta(4)$-band electron ground state and the heavy hole ground state as a function of the growth temperature. In addition, the inset shows a sketch of the electron-hole wave function overlap in one dimension. The electron-hole wave function overlap first rises with an increasing growth temperature until it reaches a maximum of approximately 1.8% at a growth temperature of 350°C. For an even higher growth temperature the overlap is strongly reduced again to $\approx 0.4\%$.

The structural investigations in section 3.1.1 yield that with an increasing growth temperature the Ge content varies exponentially until it slowly saturates at growth temperatures higher than 350°C. A reduced Ge content results in a delocalization of the hole inside the hut cluster. Moreover, the energy barrier between quantum dot and Si matrix is reduced resulting in a higher penetration probability of the electron inside the island. Both effects provide an increasing overlap. At higher temperatures the Ge

content saturates whereas the size continues to increase linearly. A larger size is leading to a further separation of the electrons and holes reducing the overlap.
In conclusion, we find two growth temperature dependent regimes which result in a non-monotonic electron-hole wave function behavior. Up to at least 350°C the decreasing Ge content dominates the radiative recombination rate whereas for higher growth temperatures the electron hole separation due to a larger size is more prominent.
According to these considerations, we expect a maximum in the intensity at ≈ 350°C.

3.3. Photoluminescence spectroscopy on germanium hut clusters

To verify the theoretical predictions resulting from the band structure simulations and to experimentally identify the epitaxy parameters, which are most suitable for optical devices we perform photoluminescence spectroscopy measurements. The experimental setup for all measurements in this section is described in the appendix B.4.1.

3.3.1. Optical properties as a function of growth temperature

In figure 3.8(a) we present a photoluminescence waterfall plot of Ge hut clusters grown at different growth temperatures. The excitation power is 3 mW at a wavelength of 473 nm. The measurement temperature is approximately 10 K. The graph shows the normalized intensity as a function of the luminescence energy and wavelength, respectively.

At approximately 1.16 eV to 1.0 eV the silicon substrate emits photons. The Ge hut cluster luminescence is located around 0.77 eV.
As silicon is an indirect band gap material, the recombination from the Δ-valley to the valence band requires the assistance of a phonon. In this case, three different phonon assisted recombinations can be identified: A Si-TA assisted process at 1.13 eV, a Si-TO assisted process at 1.09 eV and the Si-TO+O^{Γ} recombination at 1.03 eV [Dav89, Cor93]. We normalize the luminescence intensities to the Si-TO line, which is the strongest silicon related recombination [Cor93], to account for the same amount of silicon in all samples. Moreover, the crystal quality is expected to be of the same order for the used growth temperatures. From both effects we expect the same phonon density of states and the electron-phonon coupling matrix element to be of the same order. The Ge hut cluster luminescence is broadened due to the topographic size variation [Loc10]. Furthermore, higher states are expected to be occupied [Bou01] due to the necessarily high excitation power.
The sample grown at 346°C shows additional peaks at 0.82 and 0.85 eV, which are not present for the other samples. The triple-peak structure is still not yet understood. The atomic force microscopy images yield no distinct size variation. Furthermore, the growth temperature variation between the eight individual hut cluster layers is only ± 2°C, thus, there should be no structural differences between those hut clusters. The temperature is determined using a thermocouple element assembled at the back of the wafer. The ex-

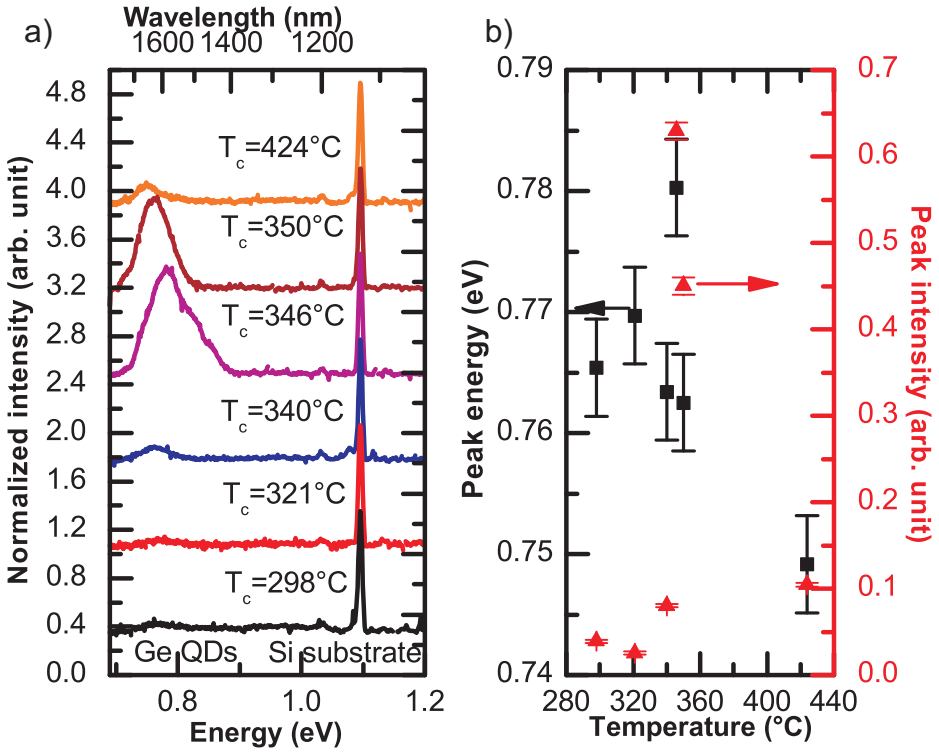

Figure 3.8.: (a) Photoluminescence intensity as a function of the luminescence energy for Ge hut clusters grown at (from top to bottom) 424°C, 350°C, 346°C, 340°C, 321°C and 298°C. The intensities are normalized to the Si-TO line. The excitation wavelength is 473 nm, the excitation power 3 mW and the temperature 10 K. (b) Peak energy (black squares) and peak intensity (red triangles) of the Ge hut cluster luminescence as a function of the growth temperature.

citation power density is the same as for all investigated structures, hence, there should be no further blueshift due to state filling.
For better comparison figure 3.8 (b) summarizes the peak energies and peak intensities determined by Gaussian fits as a function of the growth temperature. The peak energy uses the left y-axis and is shown with black squares. For the intensity we use the right y-axis and red triangles, respectively. The peak energy increases from 0.76 eV to 0.78 eV until a growth temperature of 346°C is reached. At higher growth temperatures the peak energy shows a redshift to 0.75 eV. The peak intensity is rather weak for the samples grown at 298°C and 321°C. Up to 346°C, the intensity rises by a factor of 20. When the growth temperature is further enhanced the intensity decreases again.
The energy trend plotted in figure 3.5 (b) is qualitatively the same as predicted in the calculation of the transition energies in figure 3.5. The small variation of $\approx$ 10 meV

arises mainly from the neglected Coulombic influence of neighboring hut clusters which reduces the ground state energy of the $\Delta(4)$-bands by ≈ 4 meV for distances lower than 10 nm [Bre09b]. Also the simulation model is simplified by the usage of a constant average Ge content.
In addition, the photoluminescence intensity follows the theoretical calculated trend of the $\Delta(4)$ electron-heavy hole wave function overlap in section 3.2.2. The good agreement between the simulations and the experiments strongly supports the validity of the used simulation model. Hence, we assume that the assumptions of a constant or not present phonon influence and a constant non-radiative recombination rate which are used to simplify equation 2.10 into equation 2.14 is correct for hut clusters. For the $\Delta(2)$-electron-heavy hole overlap no agreement with the experimental intensity is found. Thus, we can state several conclusions, which are based on our theoretical considerations. The comparison of the electron-hole wave function overlap of the $\Delta(4)$ bands with the photoluminescence intensity yields that the electron ground state of Ge hut clusters is located in the $\Delta(4)$-bands and not in the $\Delta(2)$-bands. This supports calculations of the ground state energy as a function of the distance between Ge quantum dots performed by Brehm *et al* [Bre09b].
A larger size of the quantum dots quenches the intensity as indicated by the strong decrease of the intensity for growth temperatures higher than 350°C. This is caused by a larger separation of the electrons and holes. Furthermore, a lower Ge content, which is a result of a higher growth temperature, results in a stronger penetration of the electrons into the Ge barrier, whereas the hole gets more delocalized into the Si matrix (see section 2.8). However, with the deposition of pure germanium there is a limit for the silicon content according to strain minimization and concentration gradients (see equation 2.4). Thus, for the available molecular beam epitaxy system and for nominally pure Ge hut clusters we find an optimal growth temperature at ≈ 350°C.

3.3.2. Optical properties as a function of temperature

For light source application it is also important to investigate the temperature dependent luminescence as room temperature luminescence and a high stability of the transition energy is desired. Exemplarily figure 3.9 shows the temperature dependent photoluminescence of a sample where the growth temperature was 424°C. In (a) we show the evolution of the luminescence intensity as a function of the energy and temperature. The intensity monotonically decreases and vanishes between 100 and 110 K. Also the luminescence energy shows a clear redshift with increasing temperature. To quantify the evolution averaged over all hut clusters we fit the spectra using two Gaussians as highlighted using the gray dashed lines for the spectrum at T=20 K. We use a Gaussian lineshape to account for the statistical size variation which causes the broadening. Figure 3.9(b) summarizes the integrated intensity in a semi-logarithmic plot as a function of the reciprocal temperature. Figure 3.9 (c) shows the peak energies.
By plotting the integrated intensity in an Arrhenius plot as a function of 1000/T, we

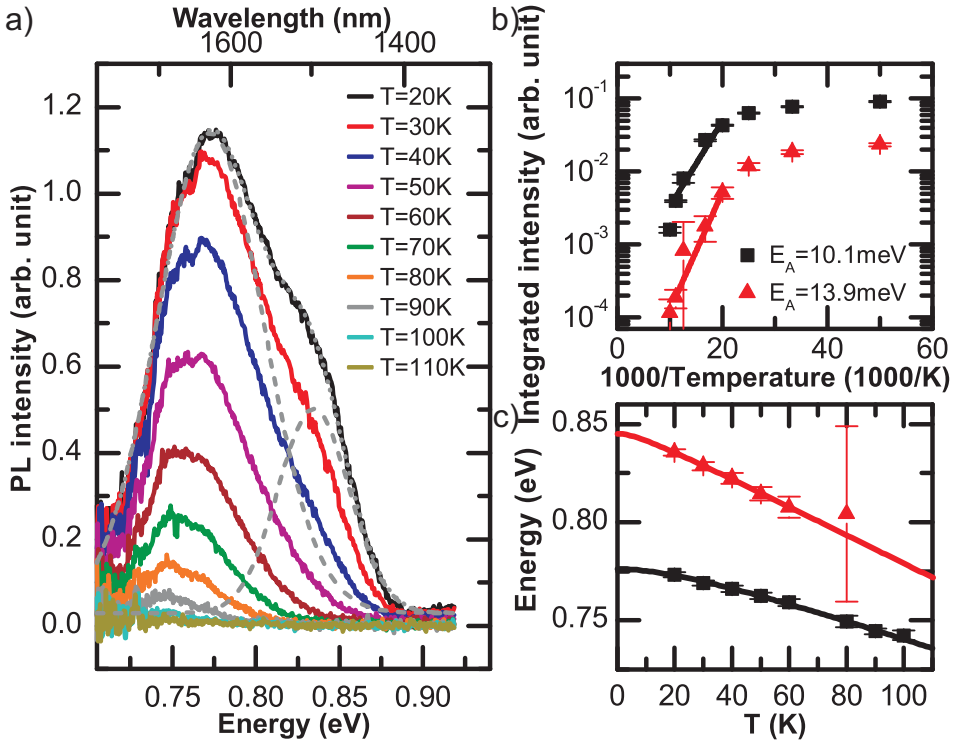

Figure 3.9.: (a) Photoluminescence intensity as a function of the luminescence energy and the temperature. The temperature is varied from 20 to 110 K (top to bottom). The gray dashed lines illustrate the two Gaussian fits of the spectra with 20 K. The gray dotted line illustrates the sum of both fitting curves. (b) Arrhenius plot of the integrated intensity. The higher energetic peak is shown in red triangles, the lower energetic one with black squares. (c) Peak energy as a function of the temperature. The solid lines are a theoretical fit according to equations 3.3

can extract the activation energy E_A of the recombination with following equation:

$$I(T) = I_0 \cdot e^{-\frac{E_A}{k_b T}} \tag{3.1}$$

I_0 is the intensity at 0 K and k_b is the Stefan-Boltzmann constant. The slope of the Arrhenius plot corresponds to E_A/k_b. In table 3.2 we summarize the resulting activation energies for all investigated samples.

We think that the activation energy is the thermal energy which is necessary to separate the electrons from the holes which are bound in an exciton [Tak92]. As the electron is only weakly confined by strain effects the exciton binding energy prevents the electron diffusion.

Table 3.2 lists the exciton binding energy for the $\Delta(4)$-hh transition, which is calculated

T_c (°C)	E_{A1} (meV)	E_{A2} (meV)	$E_{exciton}$ (meV)
298	3.0± 0.1		4.7
346	3.4 ±0.4		4.1
424	10.1 ±1.4	13.9 ±0.3	2.0

Table 3.2.: Activation energies and exciton binding energies of Ge hut clusters at different growth temperatures.

according to:

$$E_{exciton} = \frac{e}{4\pi \mathbf{r} \cdot \epsilon_0 \cdot 11.9 \cdot (1 + 0.55 \cdot x_{Ge})}[eV] \tag{3.2}$$

Here, ϵ is the dielectric constant, and $\mathbf{r}$ the distance between electron and hole. The distance is determined by 50% of the electron and hole probability density. Dvurechenskii *et al* have calculated the exciton binding energy for pyramidal shaped Ge quantum dots by calculating the energy needed to move an electron to infinity [Dvu02]. Depending on the charging state of the quantum dot they deduced binding energies between 9 meV and 37 meV which support our results in table 3.2.
The experimental activation energies and the theoretically calculated exciton binding energies are in good agreement. We think the variation for the sample fabricated at 424°C is reasonable as the simulations do not include gradients of the Ge content which are expected to have a larger effect on bigger hut clusters due to a larger separation of the electrons and holes.
Figure 3.2(c) summarizes the Ge hut cluster luminescence energy redshift. The high energetic peak has a larger redshift from approximately 0.83 eV to 0.80 eV from 20 to 60 K. The lower energetic peak shifts from 0.77 to 0.74 eV in a temperature range from 20 to 100 K. We attribute the redshift to the temperature dependent change of the band gap. This band gap variation can be quantified using an empirical formula proposed by Varshni[Var67]:

$$E_{gap} = E_0 - \frac{\alpha T^2}{T + \beta} \tag{3.3}$$

Here E_0 is the band gap energy at 0 K. α and β are empirical constants depending on the material.
The individual parameters are listed in table 3.3. The slope describing the energy shift of the lower and higher energy peak is different and there are several possible explanations. Larsson *et al* [Lar03] proposed that the higher energetic peak might stem from electron-hole recombination in the $\Delta(4)$-bands whereas the lower energetic peak stems from the $\Delta(2)$-valley. They conclude that at higher temperatures and sufficient high excitation power the thermal energy can lift an electron into the higher bands. They propose that those bands have a higher electron probability density in the Ge hut cluster and, hence, they are influenced by a higher Ge content. This would result in a change of the Varshni parameters. However, our band structure simulations yield that the experimental determined offset of $\approx$ 60 meV between the two recombination energies is much larger than the energy difference of the Δ-valleys. In addition, excitation power dependent photo-

luminescence measurements reveal that both peaks have the same power dependence, thus, excited states in higher energetic bands can be excluded as reason.
A second explanation for the different temperature dependent slopes of the two peaks is the recombination including the emission of a phonon which is common in the SiGe system [Fuk95]. Several groups [Tsu82, Men84] measured the phonon spectra as a function of temperature. In first approximation, they found a modification of the phonon frequency of approximately $\Delta E/E = -5.4 \cdot 10^{-5}/°C$ from 20°C to approximately 800°C. However the observed temperature dependent shift is too large to be explained by a simple one Si-Si phonon transition. It is still possible that different phonons from different energy states are involved. This would indicate that a fit using two Gaussians is too simple.
A further simple explanation, which is also supported by atomic force microscopy studies in section 3.1.1, is a bimodal distribution of Ge hut clusters. The atomic force microscopy images in figure 3.1 show for the sample grown at 424°C that a few hut clusters evolve into stable pyramids. This could explain the second peak. The size difference between pyramids and hut clusters results in different strain profiles and, thus, Ge contents. The different size and Ge content yields a change of the band structure and luminescence energy. This explanation is further supported by the increasing value of α for higher silicon contents which is expected from literature [Var67] and observed in our experiments.
In summarize, for most light source applications the excitonic recombination rate of Ge

T_c (°)	E_0 (eV)	α (eV/K)	β (K)
298	0.739±0.002	$1.32 \cdot 10^{-4} \pm 1.15 \cdot 10^{-4}$	15.00 ± 74.09
346	0.744±0.001	$3.72 \cdot 10^{-4} \pm 1.56 \cdot 10^{-4}$	53.41 ± 42.48
424	0.844±0.003	$7.48 \cdot 10^{-4} \pm 9.4 \cdot 10^{-5}$	13.01 ± 13.17
	0.776±0.001	$4.86 \cdot 10^{-4} \pm 7.2 \cdot 10^{-5}$	37.59 ± 23.54

Table 3.3.: Parameters for the Varshni fit of the temperature dependent photoluminescence measurements.

hut clusters is too weak as the luminescence intensity already vanishes at ≈ 100 K.

3.4. Increasing electron-hole overlap with decreasing size

The obtained experimental and theoretical results reveal that a maximum luminescence intensity is achieved at a growth temperature of ≈ 350°C. Furthermore, the calculations show that a decreasing size results in an increasing electron-hole wave function overlap. To profit from these results, we conducted a second growth study where we reduce the amount of deposited material to seven and six nominal monolayers at the optimal growth temperature of ≈ 350°C.

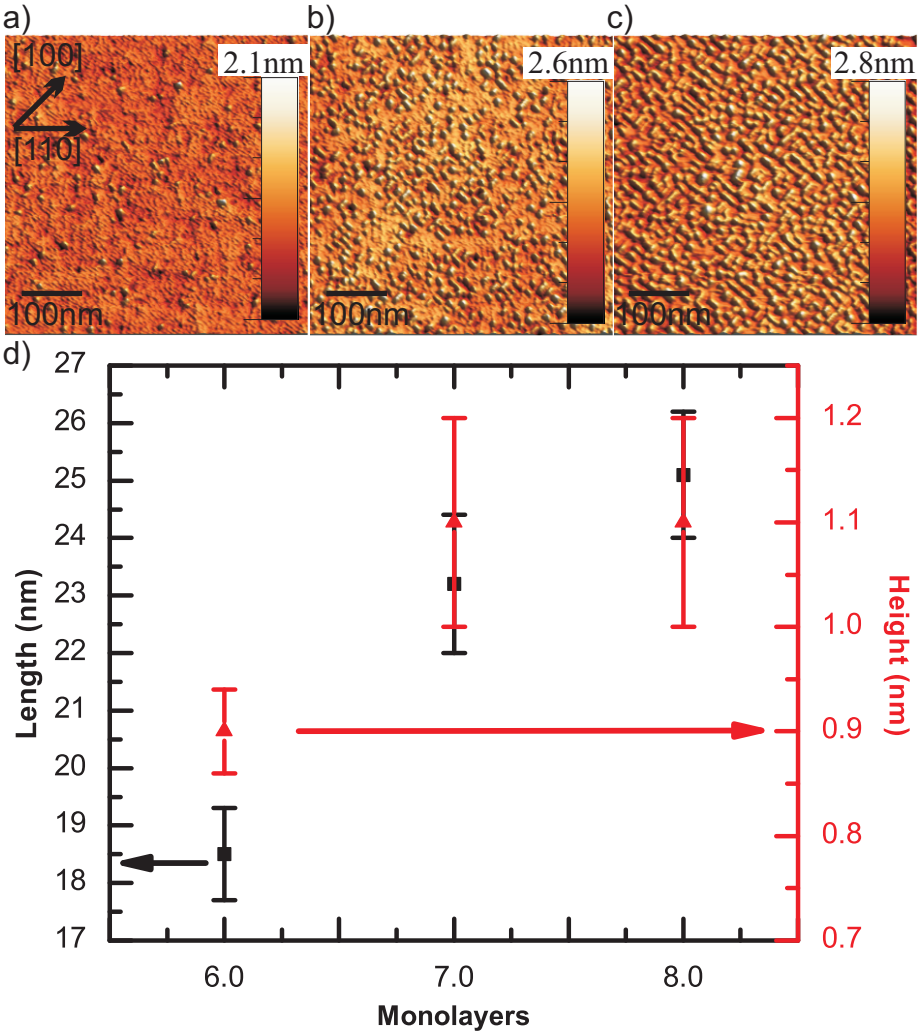

Figure 3.10.: Atomic force microscopy images of Ge hut clusters grown with (a) 6, (b) 7 and (c) 8 monolayers. (d) Hut cluster length (black squares, left axis) and hut cluster height (red triangles, right axis) as a function of the amount of deposited monolayers. The growth temperature is approximately 345°C

3.4.1. Size and Ge content as a function of the amount of deposited material

Figure 3.10 shows atomic force microscopy images of the three different samples fabricated at $\approx 350°C$. In (a) we see a sample containing six monolayers of Ge, in (b) seven monolayers and in (c) there are eight deposited monolayers. Figure 3.10 (d) shows the quantitative analysis of the extracted quantum dot lengths and heights. From the critical thickness, which is three to four monolayers (see chapter 2.2) in the Si-Ge system nucleation spots form. At six monolayers this nucleation spots lead to the formation of hut clusters, which align at the [100] direction and consist of the typical rectangular based {105} faceted shape. The quantum dot density is $\rho = 7.0 \cdot 10^{10}\text{cm}^{-2} \pm 2.7 \cdot 10^{9}\text{cm}^{-2}$. Upon further material deposition, the density linearly increases as additional nucleation spots are created. At nominally seven deposited monolayers, we obtain a hut cluster density of $\rho = 1.8 \cdot 10^{11}\text{cm}^{-2} \pm 2.8 \cdot 10^{10}\text{cm}^{-2}$ and at 8 monolayers $\rho = 3.0 \cdot 10^{11}\text{cm}^{-2} \pm 3.5 \cdot 10^{10}\text{cm}^{-2}$. This behavior is the same as in the previous work of Christian Miesner [Mie01] who conducted similar growth studies at the WSI. Figure 3.10 (d) shows the hut cluster length and height as a function of the amount of deposited material. The length almost linearly increases over the whole measurement range, whereas the quantum dot height shows some saturation behavior. This is in contrast to Christian Miesner's [Mie01] work who found a constant behavior.
Furthermore, from Raman spectroscopy, we deduce the average Ge contents which we summarize in table 3.4. Within the error the Ge content does not significantly change if we deposit six, seven or eight monolayers of Ge on the substrate at the same temperature. Thus, we conclude that the intermixing does not depend on the amount of deposited material. Using this structural parameters we can perform the same analysis of the optical spectroscopy of Ge hut clusters as before.

Thickness (ML)	Ge content
6	0.66±0.03
7	0.71±0.03
8	0.66±0.03

Table 3.4.: Ge content of Ge hut clusters with different amount of deposited monolayers determined by Raman spectroscopy.

3.4.2. Photoluminescence and electron-hole wave function overlap as a function of the amount of deposited material

Figure 3.11 (a) shows a waterfall plot of the normalized photoluminescence intensity as a function of the energy and the amount of nominal deposited material. The intensity is normalized to the Si-TO phonon line. The excitation power is ≈ 8 mW at a wavelength of 514.5 nm. The temperature is 10 K. In figure 3.11 (b), we present the peak energies as a function of the nominal deposited material. A clear blueshift for a reduced amount of material is observed.

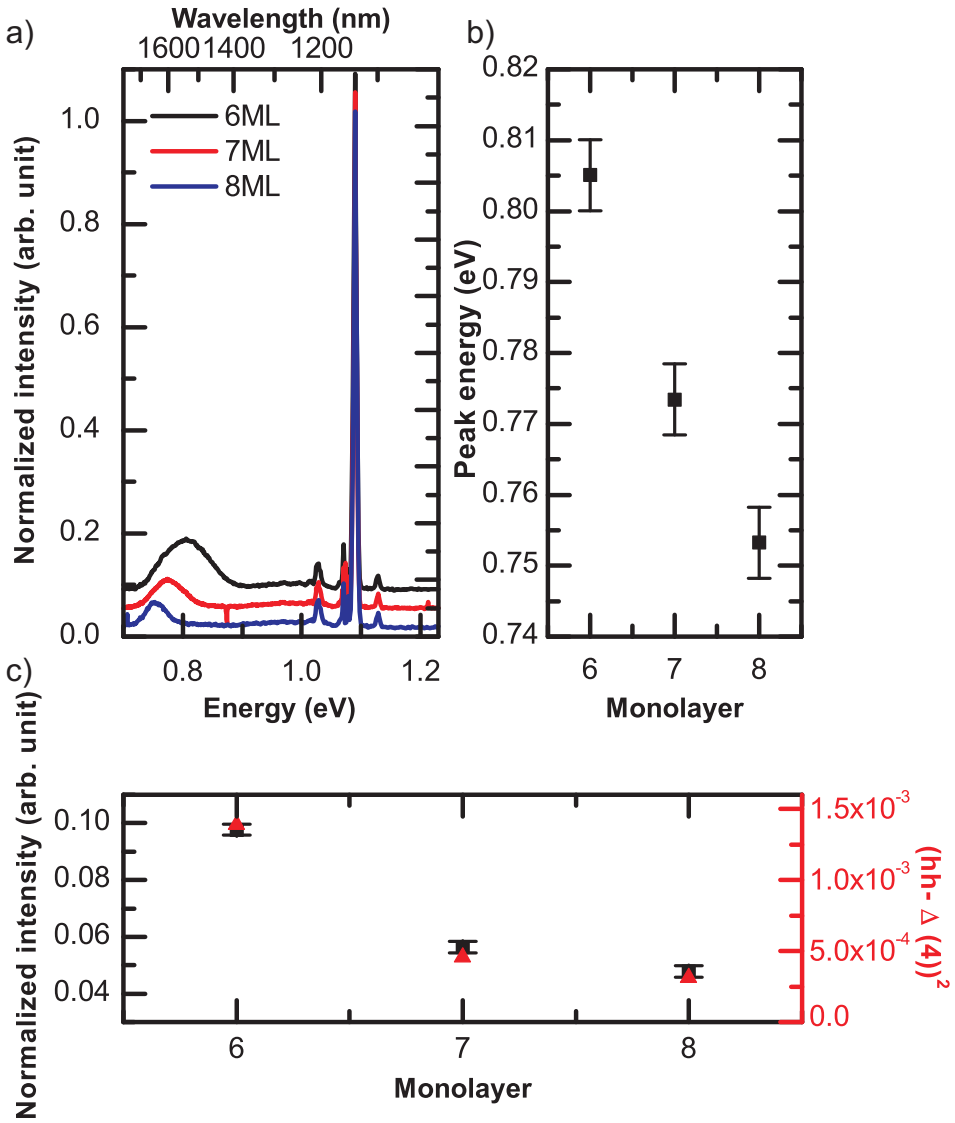

Figure 3.11.: (a) Waterfall plot of the normalized photoluminescence intensity as a function of the amount of deposited material. The measurements are performed at 10 K. The excitation wavelength is 514.5 nm and the power is approximately 8 mW. (b) Peak energy as a function of the amount of nominally deposited monolayers. (c) Peak intensity (squares) and theoretical calculated squared electron-hole wave function overlap (triangles) as a function of the amount of nominal deposited material.

Figure 3.11(c) summarizes the peak intensity (squares) and the calculated squared electron-hole wave function overlap (triangles) as a function of the deposited amount of material. We find that smaller quantum dots exhibit a higher luminescence intensity as well as a higher overlap integral. Furthermore, we find a good agreement between experiment and simulation.

The blueshift of the energy with decreasing amount of material is a direct result of a reduced hut cluster size (see figure 3.10). Due to the fact that the Ge content is the same for all quantum dots the reduced size shifts the hole energy states closer the silicon band edge resulting in a higher transition energy. We attribute the decreasing peak intensity for larger quantum dots to a further separation of the electrons and holes. This is confirmed by the calculations of the electron-hole wave function overlap. We deduce the maximum overlap from the calculations to $\approx 3.7\%$. This is very low compared to III-V semiconductor quantum dots, where the overlap is higher than 60%. Such a high overlap results in a 400 times higher radiative recombination rate and, thus, in a 400 times lower spontaneous recombination lifetime.
For the SiGe system, typical radiative lifetimes are in the μs to ms regime [Tsy09, Kam05]. This is approximately 1000 times longer than for III-V semiconductor heterostructures where 0.1 ns to μs have been reported [Nis12, Kre05]. We find that our calculation of the electron-hole wave function overlap agrees well with experimental result of the radiative lifetimes in different material systems.
When the radiative transition in the Ge hut clusters would require the assistance of a phonon due to an indirect transition in k-space even larger radiative lifetimes were expected. Therefore, we conclude that the emission of Ge hut clusters is a quasi-direct no-phonon transition. This is possible due to the spreading of the hole wave function in k-space [Rob29].

3.5. Summary and conclusion

The theoretical and experimental investigations of this chapter show that the radiative recombination in Ge hut clusters is a quasi-direct no-phonon assisted recombination. This results in a much higher recombination efficiency and temperature stability compared to pure silicon where recombination is only possible with the assistance of phonons. We, furthermore, show that the band alignment of hut clusters is always of type II. This results in a spatial separation of electrons and holes to a large degree. The maximum overlap we could achieve has been 3.7% for the ground state transition from the $\Delta(4)$-valley to the heavy hole state. Literature values show a difference of approximately 1000 for the radiative recombination time which agrees well with the squared difference of the electron-hole wave function overlap between Ge and III-V based light emitters. This indicates that it is indeed the type II band which inherently limits the radiative efficiency. Thus, the indirect nature in k-space is found to be of negligible influence on the intensity.

3.6. Electron-hole wave function overlap as a function of different structural parameters

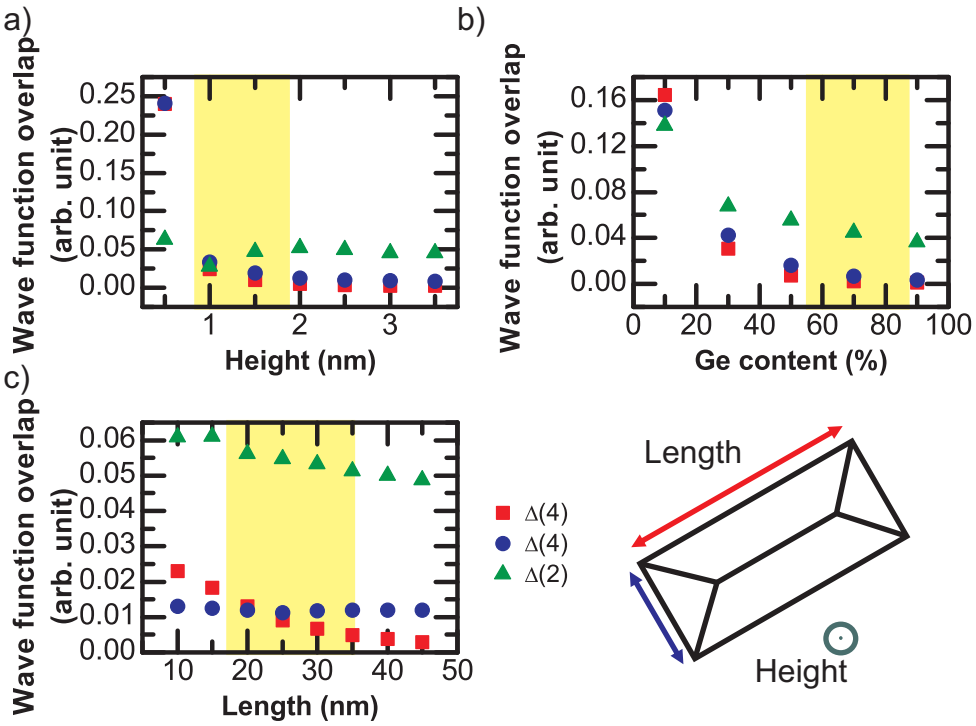

Figure 3.12.: Electron-hole wave function overlap of the Δ band - heavy hole transition for a varying Ge content, length and height. For each simulation only one parameter is changed. The starting parameters are l=35.6 nm, h= 2.1 nm and x_{Ge}=0.57. The yellow highlighted region illustrates the experimental determined parameter range. The lower right sketch illustrates the color scheme of the different Δ-directions.

The structural parameters strongly influence the electron-hole wave function overlap despite of the limiting influence of the type II band alignment on the radiative efficiency. A further optimization of the luminescence intensity requires to quantitatively investigate the influence of the structural parameters length, height and Ge content. We now show in figure 3.12 calculations of the overlap integral while independently varying length, height and Ge content. The quantum dot is modeled as a hut cluster deposited at 424°C (see table 3.1). The yellow shaded region highlights the experimentally determined parameter range. We would like to note that for all parameter combinations presented here the simulations exhibit localized hole states inside the Ge region.
Figure 3.12 (a) shows the overlap integral as a function of the hut cluster height. With decreasing height we find that the overlap integral rises for all Δ-directions. Within the experimental parameter range the overlap integral varies by ≈ 2%. For a height larger

than 2-3 nm, a saturation of the overlap integrals occurs. Below a height of 1 nm the overlap integral of the hh-$\Delta(4)$ transition strongly rises by a factor of approximately five to a maximum value of 25% at a height of 5Å. The saturation for larger heights is mainly caused by a further spatial spreading of the hole wave function which almost homogeneously occupies the quantum dot. This is only the case for simulations based on a constant Ge content. The strong increase of the overlap integral below a height of 1 nm is a result of a strong leaking of the hole wave function into the silicon matrix.
In (b) the overlap as a function of the Ge content is depicted. As predicted by El Kurdi *et al* [EK06] the overlap integral increases for a decreasing Ge content. The influence on the overlap is 2% within the experimental observed Ge contents. But a further decrease of the Ge content lower than 30% results in a strong increase up to values of 16%
Here, a lower Ge content results in a larger delocalization of the hole wave function. Additionally the penetration barrier for electrons induced by the Ge quantum dot reduces. In combination both effects result in a larger overlap.
The hut cluster length has only a minor impact on the electron hole wave function overlap. Figure 3.12 (c) shows that within the experimental parameter range the overlap varies by only 1%. Also for an extended parameter space the overlap varies only by 2%. It is interesting to note that a varying length does change the overlap in growth direction due to a changing aspect ratio. The spatial overlap of the width does not alter as this size is not varied.
Of all investigated parameters the height and the Ge content have the strongest influence on the electron-hole wave function overlap, thus, having the biggest influence on the optical properties. An optimal Ge based emitter consists of a very small height and a low Ge content. Unfortunately, from epitaxy point of view there is a certain trade-off as a small size requires a large lattice mismatch. On the other side a low Ge content results in a reduced lattices mismatch.
The simplest method to lower the Ge content is to employ further intermixing by increasing the growth temperature. This results in a change of the island morphology and will always result in a larger size. However, the dominating effect can only be ascribed by structural analysis as size and Ge content have different temperature and strain dependent trends.

4. Germanium pyramids and domes

The easiest approach for reducing the average Ge content, which is necessary for a higher electron-hole wave function overlap, is a further increase of the growth temperature. However, an increasing growth temperature results in a change of the morphology from hut clusters to a bimodal distribution of pyramids and domes [Ros99].
We will begin with a structural characterization of the islands which is necessary to identify the possible sizes accessible with our molecular beam system. This is followed by photoluminescence experiments where the emission properties are compared with our previous study of Ge hut clusters.

4.1. Structural investigation of germanium pyramids and domes

Figure 4.1 shows atomic force microscopy images of Ge pyramids and domes grown at (a) 430°C (b) 441°C and (c) 659°C. All samples consist of only one layer of buried islands deposited on thinned SOI substrate (see appendix C) to allow a subsequent fabrication of photonic crystal slabs.

At this growth temperatures the formation of hut clusters is suppressed. Instead a bimodal distribution of quadratic based {105} faceted pyramids [Ros99] and circular shaped multifaceted domes[Ros99] forms. The lateral size of the AFM images is 1x1μm^2. Figure 4.1 (a) shows pyramids and domes with a low size variation. In figure 4.1 (b) the domes maintain their circular round shape but the structural quality of the pyramids reduces. At this temperature pyramids start to merge and cluster. Besides the bimodal

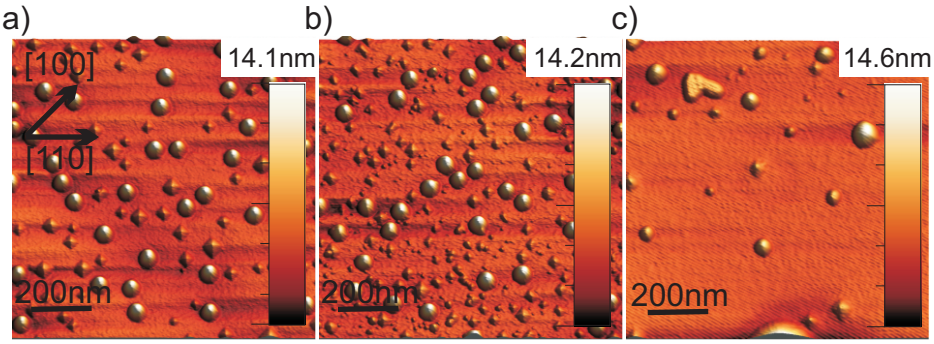

Figure 4.1.: Atomic force microscopy images of a bimodal distribution of pyramids and domes grown at (a) 430°C (b) 441°C and (c)659°C.

T_c (°C)	d_{pyr} (nm)	$h_{pyr.}$ (nm)	$\rho_{pyr.}$ (10^9cm^{-2})	r_{dome} (nm)	h_{dome} (nm)	ρ_{dome} (10^8cm^{-2})
413	42.2±1.3	3.0±0.1	11.1±0.2	65.0±1.0	10.0±0.3	30.0±0.6
430	40.8±1.0	3.1±0.1	6.2±0.8	65.3±0.9	9.1±0.2	34.0±0.3
441	49.5±2.7	3.5±0.2	14.0± 0.3	67.5±10.7	8.9±1.2	39.0±0.8
659	54.6±1.8	4.3±0.2	1.6±0.03	66.9±4.9	6.8±0.7	8.0±0.2

Table 4.1.: Analysis of the structural parameters of pyramids and domes grown at different temperatures. The errors resemble the statistical size variation.

distribution figure 4.1(c) indicates big Ge conglomerates which have a random size and shape. The high growth temperature results in a very high diffusion length of adatoms resulting in these very large Ge clusters.

According to the analysis procedure in the appendix B.1, we determine the lateral size and the height of the islands. They are summarized in table 4.1. As for Ge hut clusters an increasing growth temperature leads to an increasing lateral size of the Ge domes and pyramids [Abs96b, Ton03]. It is interesting to note that the height of the pyramids increases in the same manner as the height of the domes decreases. Pyramids gain roughly 33% in height by raising the growth temperature from 413° to 659°, whereas the domes loose approximately 30% in height. This is possible as the aspect ratio (h/d) of pyramids is fixed to 0.7 due to the {105} facets, while domes are not fixed in their aspect ratio as they consist of several stable facets.

4.2. Photoluminescence spectroscopy of Ge pyramids and domes

Photoluminescence measurements are performed at 10 K and with an excitation wavelength and power of 488 nm for the sample grown at 430°C and 659°C or 532 nm for the sample grown at 413°C and 441°C[1]. The excitation powers are approximately 2 mW (488 nm) or 6 mW (532 nm), respectively. In figure 4.2 we present a semi-logarithmic photoluminescence waterfall plot of pyramids and domes. The y-axis shows the photoluminescence intensity normalized to the Si-TO phonon replica. The growth temperature is increasing from bottom to top. The luminescence at ≈ 1.12 eV, 1.08 eV and 1.05 eV stems from the silicon substrate [Cor93, Dav89]. The high excitation power and low temperature leads to the condensation of a so called electron hole droplet [Kel86] which can be observed at ≈ 15 meV lower energies compared to each phonon replica [Kit89]. This is an electron hole plasma forming due to an excessive amount of charge carriers and a low temperature. The Coulomb interaction between the electrons and holes leads to a reduction of the energy compared to the band gap [Ham76]. Still, the recombination of this plasma is indirect in k-space and, hence, it requires the assistance of a

[1]The change of the laser wavelength influences the penetration depth and, thus, the net excitation power in the island region. The change of the laser has been necessary as the previously used Argon ion laser lost its power stability.

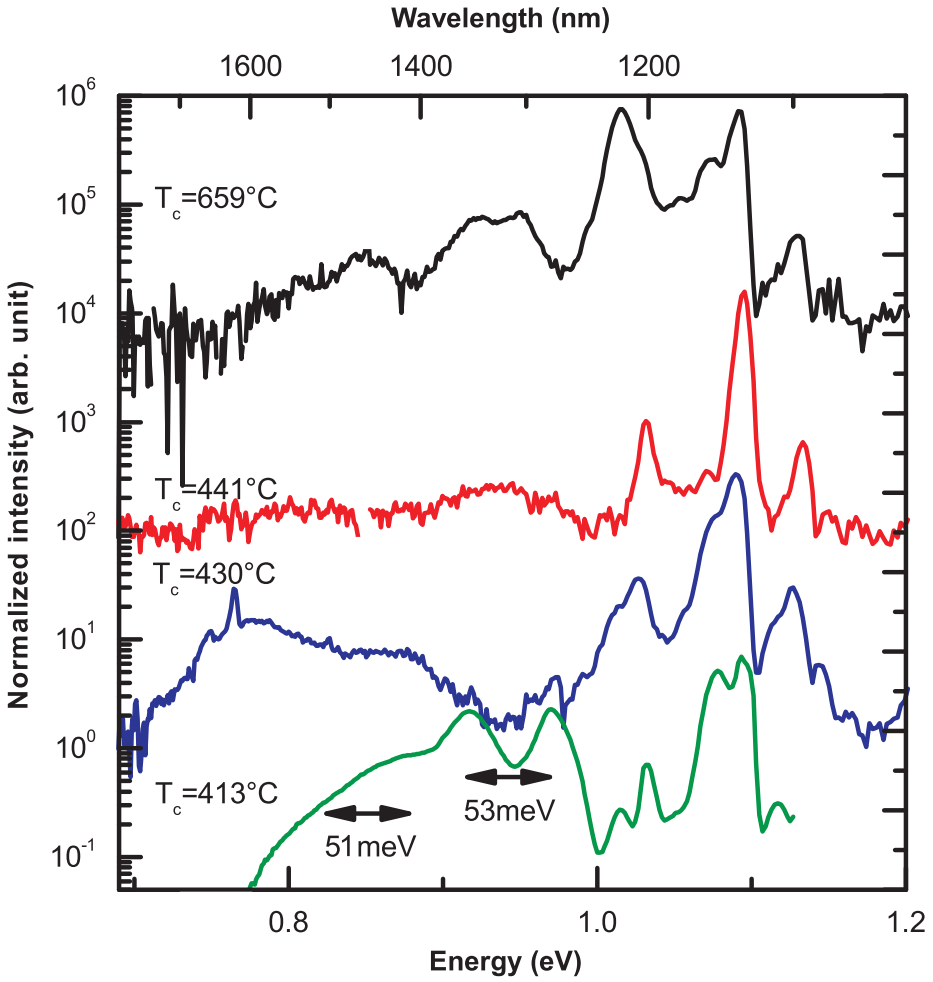

Figure 4.2.: Low temperature photoluminescence waterfall semilogarithmic plot of the Ge pyramids and domes grown at (bottom to top) 413°C, 430°C, 441°C and 659°C.

phonon to conserve the momentum. Furthermore, the Ge islands provide an enhanced luminescence in the near infrared energy region.
The islands grown at 413°C yield a four peak structure. The luminescence peaks are centered at 0.970 eV, 0.917 eV, 0.876 eV and 0.825 eV. The two lower energetic peaks are hardly visible but can be separated by a two Gaussian fit.
We attribute the two higher energetic peaks to the Ge domes as they usually exhibit a lower Ge content [MaP02]. We attribute the remaining peaks to the Ge pyramids.
The higher(lower) energetic peaks are separated by 53(51) meV which is the energy of a SiGe TO phonon in a SiGe lattice. For samples fabricated at 413°C and with nominally eight monolayers of Ge we do not expect such pronounced wetting layer luminescence [Mie01]. Thus, we conclude that the peak at 0.917 and 0.825 eV are phonon

T_c (°C)	Normalized intensity (arb. units)
413	0.33
430	0.34
441	0.08
659	0.88
hut cluster	0.89

Table 4.2.: Maximum photoluminescence intensity of pyramids and domes fabricated with different growth temperatures and of the most intense hut clusters extrapolated to eight island layers. The intensity is always normalized to the Si-TO phonon replica.

assisted recombinations and the luminescence at 0.970 and 0.876 eV are no-phonon recombination.
At higher growth temperatures the double peak structure of pyramids and domes vanishes. Nevertheless, we can identify the bimodal distribution of pyramids and domes. At 659°C the structure emits light at 0.951 eV, 0.924 eV and 0.853 eV. An assignment of these emission energies is difficult. One possibility is to attribute the emission line at 0.951 eV to the emission of the domes. The peaks at 0.924 eV and 0.853 eV might stem from larger Ge clusters and pyramids which we observe in figure 4.1(c). However we are not confident enough to ascribe the peaks unambiguously in this way.
The higher luminescence energy of the pyramid and dome ensembles compared to Ge hut clusters indicates a lower Ge content.
The normalization of the intensity to the Si-TO phonon replica allows to qualitatively compare the intensities of pyramids/domes and hut clusters. In table 4.2 we summarize the maximum intensities of the Ge islands and of the most intense hut cluster samples. The intensity values are taken at the maximum peak height and can be a sum of different island morphologies or recombination channels. To account for the eight quantum dot layers in our hut cluster sample we multiply the Ge island luminescence by eight. Here we assume that the intensity of each island layer is approximately the same. The hut cluster sample has been fabricated at 346°C
When comparing the normalized intensities we also have to consider that our Ge hut clusters have been deposited on standard Si wafers whereas the Ge islands have been deposited on SOI substrate. SOI wafers consist of less Si than standard Si wafers. Therefore, the intensity of the Si-TO phonon assisted recombination is expected to be lower. Thus, the normalization conducted for the Ge islands exaggerates the intensity of the Ge islands compared to our Ge hut clusters samples. The luminescence intensity of pyramids and domes is much lower than that of Ge hut clusters. Only for very high growth temperatures, we obtain comparable values but the origin of the bright luminescence is not yet understood.
The reason for the lower intensity is that at sufficient high growth temperatures the effect of an enhanced electron-hole wave function overlap resulting from a reduction of the Ge content is exceeded by the influence of a larger size. Therefore, methods are

necessary to reduce the Ge content while maintaining a small island size.

4.3. Summary and conclusion

In this chapter, we presented the structural and optical characterization of island ensembles obtained when raising the growth temperature compared to Ge hut clusters. We deduce from the spectral position of the luminescence that the Ge content of the islands is indeed reduced compared to hut clusters. However, a bimodal distributions of pyramids and domes appears.
Because of the strain dependent intermixing, the trade-off between Ge content and size limits the radiative efficiency of these island morphology. The increasing size of the island ensemble completely overbears an increasing spatial electron-hole wave function overlap caused by the reduced Ge content.
In addition, the occurrence of a phonon assisted recombination channel shows that the spreading of the wave function in k-space is smaller compared to Ge hut clusters. Therefore, pyramids and domes are no promising Ge based light emitters. We require growth schemes which allow to vary the size independently of the Ge content to increase the potential of Ge as a potential light emitter. One possibility might be the co-deposition of Si and Ge which so far has not been investigated in detail.
Despite of the weak emitter properties, pyramids and domes can still be used for fundamental studies. Because of the luminescence energy at 0.8 eV (1550 nm) and 0.95 eV (1300 nm) which allows for detection using InGaAs CCDs the presented samples grown at 413°C and 430°C were used by Norman Hauke to investigating the coupling to two dimensional photonic crystal cavities[Hau11, Hau12].

5. Growth of SiGe hut clusters using SiGe co-deposition

The previous experiments and simulations have shown that, for a high radiative recombination rate, Ge based emitters require a small size and a low Ge content. But those two requirements exclude each other as a high growth temperature which is required for a low Ge content also results in a large island size.
In this chapter, we will for the first time try to use co-deposition to realize SiGe hut clusters with a small size and a low Ge content. With co-deposition we aim for circumventing the requirement for diffusion mediated Ge content reduction. Therefore, co-deposition is expected to allow for an to some extent independent tuning of size and Ge content.

5.1. Silicon germanium co-deposition

As we have seen in section 3.1.2 silicon intermixing is not sufficient to achieve Ge contents of less than 57%. for nominally pure Ge hut clusters. A further reduction of the hut cluster Ge content requires some changes in the growth procedure. One method to achieve a reduced Ge content is to directly enforce the incorporation of silicon. This requires a continuing growth of silicon whereas the germanium deposition starts. Thus, silicon and germanium are co-deposited at the same time as sketched in figure 5.1. Here silicon atoms are indicated as red circles and Ge atoms are indicated as green circles. The left sketch illustrates the standard case of an intermixing during the deposition of nominally pure germanium. During the capping process silicon atoms diffuse into the quantum dot from the silicon matrix. The right sketch shows the co-deposition process. During the co-deposition silicon and germanium atoms hit the surface and, hence, they can be directly incorporated.

As SiGe has a lower lattice constant than pure Ge, the strain energy between the two layers is lower [Kas04]. This results in a higher critical thickness for the formation of three dimensional structures. Reflection high energy electron diffraction allows to deduce a minimum layer thickness of $\approx$ 19.6 Å corresponding to a 2D equivalent of approximately 16 monolayers for three dimensional growth. The total growth rate is approximately 0.2 Å/s. We used two different growth temperatures at 310°C and 390°C and alloy concentrations of $Si_{0.35}Ge_{0.65}$, $Si_{0.42}Ge_{0.58}$ and $Si_{0.50}Ge_{0.50}$.

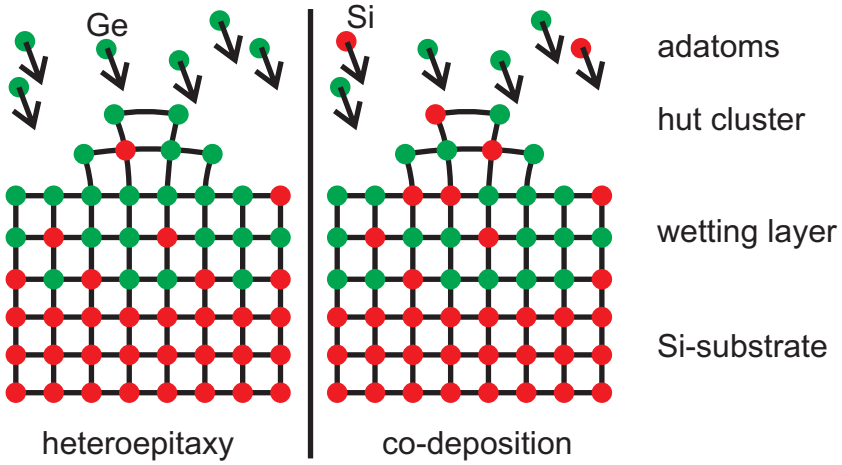

Figure 5.1.: Sketch of the co-deposition epitaxy method. The left part shows the standard heteroepitaxy where germanium atoms are deposited on the surface and silicon interdiffuses. The right panel illustrates the co-deposition where silicon and germanium atoms are evaporated at the same time yielding the nucleation of an alloy.

5.2. Structural properties of SiGe hut clusters

We conduct both atomic force microscopy as well as Raman spectroscopy measurements to investigate the impact of the SiGe co-deposition. Theses experiments allow us to determine the size of the SiGe hut clusters and the Ge content.

5.2.1. Topographic properties of SiGe hut clusters

Figure 5.2 shows atomic force microscopy images of SiGe hut clusters grown at 310°C with a nominal Ge content of (a) 0.65, (b) 0.58 and (c) 0.5. For a growth temperature of 310°C with a nominal Ge content of 0.65 (a), small hut cluster shaped quantum dots with a base length of approximately 19.5 nm and a width of 12.6 nm form. The height is 0.8 nm. Besides the hut clusters the surface is not atomically flat. With a lower Ge content of 0.58 (b) and 0.50 (c) the formation of hut clusters is suppressed and only a rough surface with several flat plateaus forms during the deposition.
The lower images show SiGe hut clusters deposited at a growth temperature of 390°C and with a nominal Ge content of (d) 0.65, (e) 0.58 and (f) 0.5. The increased growth temperature allows for the formation of SiGe islands down to a Ge content of 0.50 (f). But the quantum dot density strongly decreases. Hut clusters do not form at 310°C but at 390°C due to a limited surface diffusion length at reduced temperatures (see section 2.3). For comparison, we summarize the density and size of the investigated hut clusters in table 5.1. Compared to pure Ge hut clusters (see table 3.1) the density is reduced by approximately one order of magnitude. We want to highlight that we

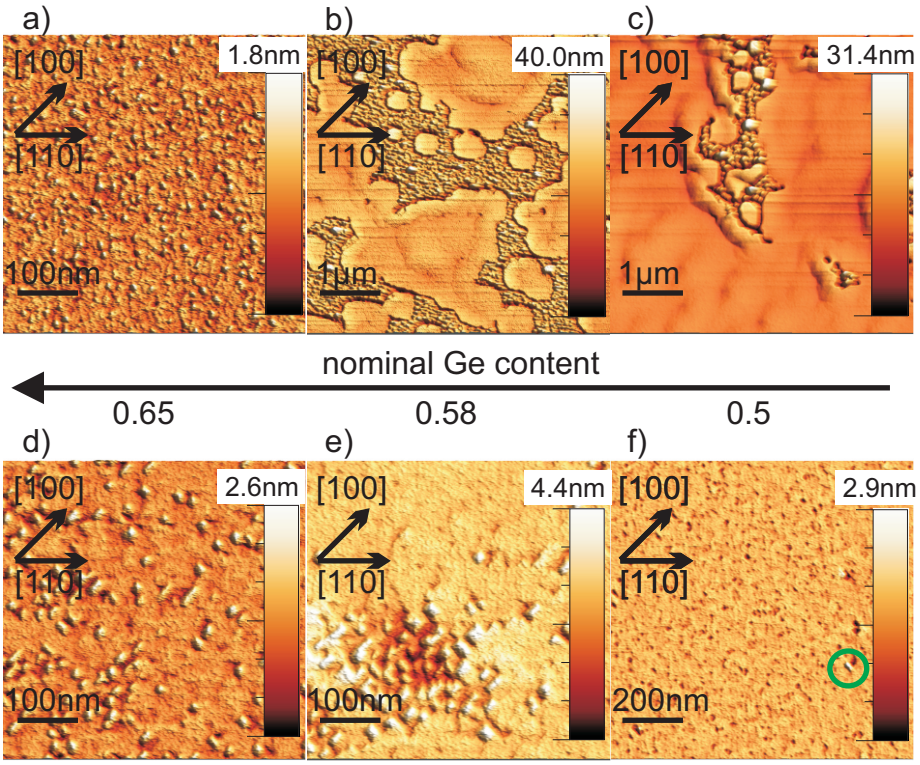

Figure 5.2.: Atomic force microscopy images of SiGe hut clusters, for a growth temperature of T_C=310°C and a nominal Ge content of (a) 0.65, (b) 0.58 and (c) 0.5 and a growth temperature of 390°C with a nominal Ge content of (d) 0.65, (e) 0.58 and (f) 0.5. The green circle in (f) highlights one single SiGe hut cluster.

T_c (°C)	x_{Ge}(%)	d (nm)	w (nm)	h (nm)	$\rho(10^9/cm^2)$
310	65	19.5±0.6	12.6±0.4	0.77±0.03	35.4±2.1
390	65	28.4±1.2	20.3±0.6	1.36±0.06	47.8±1.0
390	58	28.1±1.2	20.7±0.7	1.74±0.08	7.6±0.2
390	50	33.5	19.6	1.06	>0.1

Table 5.1.: Analysis of the structural parameters of SiGe hut clusters fabricated with different Ge content and at different growth temperatures.

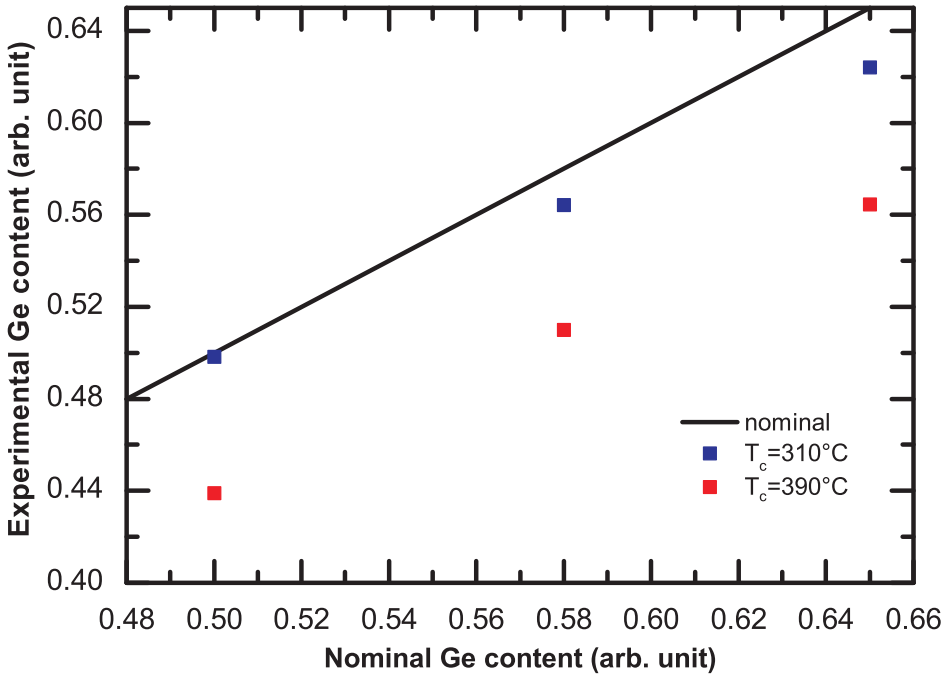

Figure 5.3.: Experimental determined Ge content as a function of the nominal Ge content for different growth temperatures 310°C (blue squares) and 390°C (red triangles). The black line indicates the nominal deposited Ge content.

achieved the fabrication of hut clusters with a density of less than one quantum dot per square micrometer. The hut cluster is highlighted with a green circle in figure 5.2 (f). The presence of {105} facets is confirmed by facet analysis. This is a remarkable result as Ge quantum dots with such a low density have not been published before. Although such a low density of quantum dots is unfavorable for possible light sources it may pave the way for single quantum dot experiments. Such experiments are necessary to get a more detailed knowledge about the electronic structure of Ge quantum dots.

5.2.2. Ge content of SiGe hut clusters

For a complete structural description of the SiGe hut cluster morphology, we now perform Raman spectroscopy measurements to determine the average Ge content. In figure 5.3, we present the experimental determined Ge content as a function of the nominal deposited Ge content for growth temperatures of 310°C and 390°C. The black line depicts the nominal deposited Ge content. The experimental determined Ge content linearly decreases with decreasing nominal Ge content. Furthermore, a higher growth temperature yields a lower Ge content.

The Raman spectroscopy results allow for several interesting conclusions. In pure Ge hut clusters, the average Ge content reduces by 8% at 310°C and by 40% at 390°C, whereas co-deposition sustains a reduction by less than 5% and 13%, respectively. This reveals that the effect of silicon diffusion into the germanium region (see section 2.4) is strongly suppressed with the co-deposition approach.
Furthermore, the slope of the experimental Ge content differs from the nominal Ge content. The structures fabricated at 310°C and 390°C reveal the same slope. Thus, we find that the intermixing of the SiGe hut clusters with Si is a concentration dependent process as proposed by simple Fick's law (see equation 2.4).
Therefore, the experimental and the nominal Ge content equal at x_{Ge}=50% and for a growth temperature of 310°C. Unfortunately the atomic force microscopy image in figure 5.2(c) proves that this epitaxy parameters do not allow the formation of quantum dots.
We conclude that SiGe co-deposition allows the fabrication of SiGe alloys with a Ge content as desired especially at reduced temperatures. This is very interesting as previously published theoretical calculations by d'Avezac *et al* have shown that a $SiGe_2Si_2Ge_2SiGe_n$ superlattice on $Si_{0.4}Ge_{0.6}$ might offer a direct band gap silicon based material [d'A12].

5.3. Photoluminescence spectroscopy of SiGe hut clusters

In the following photoluminescence spectroscopy measurements and corresponding band structure simulations give an insight about the impact of a reduced Ge content on the electron and hole probability densities and the corresponding recombination energies.

Figure 5.4 presents a waterfall plot of the photoluminescence spectroscopy measurements from SiGe hut clusters grown at T_C=310°C and 390°C and with a nominal Ge content of 0.50, 0.58 and 0.65. The measurement temperature is 8 K and the excitation power is ≈ 3 mW at an excitation wavelength of 488 nm.
Above an energy of 1 eV the luminescence stems from the silicon substrate with the Si-TA assisted process at 1.13 eV, a Si-TO assisted process at 1.09 eV and the Si-TO+O^{Γ} recombination at 1.03 eV. The additional broad luminescence at an energy range from approximately 0.9 to 0.7 eV stems from the SiGe hut clusters. A clear blueshift is observed for a decreasing Ge content.
In general, the intensity is higher for hut clusters deposited at 390°C compared to those deposited at 310°C. From the atomic force microscopy images in figure 5.2 we extract the information that the samples deposited at 310°C do not show a three dimensional hut cluster structure. Thus, we expect not a three dimensional confinement. Electrons and holes can diffuse in-plane, where they can reach non-radiative recombination centers. This results in a lowering of the internal quantum efficiency.
The samples with a growth temperature of 390°C show a maximum luminescence intensity comparable to that of pure Ge hut clusters at a growth temperature of 350°C. On a scale normalized to the Si-TO phonon replica both signals are comparable to the Si-TO transition intensity. So far this is the highest luminescence intensity we have observed.
Figure 5.4(b) depicts the peak energy of the SiGe hut cluster luminescence as a function

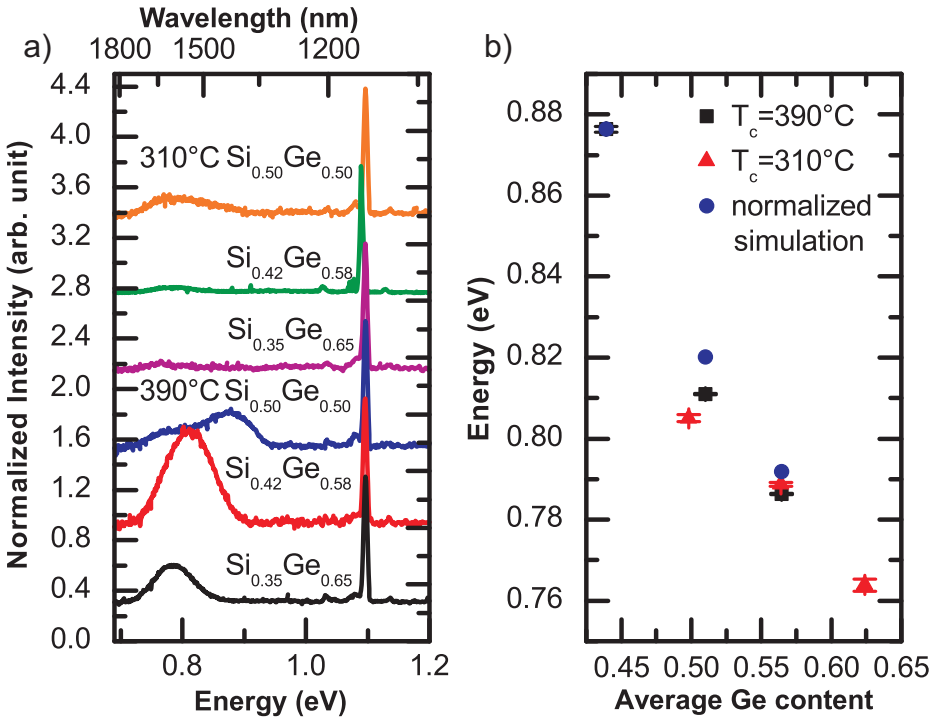

Figure 5.4.: (a) Photoluminescence waterfall plot of SiGe hut clusters grown at (from top to bottom) T_C=310°C and with a nominal Ge content of 0.50, 0.58 and 0.65 and at 390°C and with a nominal Ge content of 0.50, 0.58 and 0.65. (b) Peak energies of the SiGe hut clusters from (a) as a function of the average Ge content determined using Raman spectroscopy. (see figure 5.3). The blue circle indicate the normalized theoretical determined transition energies.

of the experimental determined average Ge content. In addition, we present the calculated transition energies for the hut clusters at a deposition temperature of 390°C. The transition energy has been normalized to the highest experimental determined value. In general, the luminescence energy decreases with increasing Ge content. This is the same behavior as in chapter 3.3. We receive a good agreement between our experimental and theoretical trends. Thus, we conclude that indeed the changing Ge content, which changes the band offset between quantum dot and Si matrix, is responsible for the changing transition energy.

5.4. Summary and conclusion

We find that at a low growth temperature of 310°C the reduced lattice mismatch between the co-deposited alloy and the substrate suppresses the formation of quantum

dots. With a higher growth temperature the rising surface diffusion length allows for the formation of SiGe hut clusters.
Similar to pyramids and domes the reduced Ge content results in a lower strain energy leading to larger quantum dots. But SiGe quantum dots have a size two times smaller than pyramids or domes. This results in a superior intensity compared to pyramids and domes due to a smaller separation of electrons and holes.
In comparison with nominally pure Ge hut clusters, we find similar intensities. This denotes that the larger size of SiGe quantum dots compensates the positive effect of the decreased Ge content. This is also verified by calculations of the electron-hole wave function overlap where we find $\approx 2\%$ for nominally pure Ge hut clusters deposited at 350°C and 1.2% for $Si_{0.42}Ge_{0.58}$ hut clusters.
Because of the mutual dependency of the quantum dot size and Ge content, the intensity is inherently limited by the spatial type II confinement separating the electrons and holes. Therefore, further improvements need to directly change the confinement properties towards a type I band alignment.
SiGe hut clusters offer further advantages. The reduced concentration gradient between Si matrix and SiGe hut cluster reduces the SiGe intermixing allowing a better adjustment of the desired Ge content. Moreover, the new growth scheme allows the fabrication of hut clusters with a very low density of one quantum dot per square micrometer being three orders of magnitude lower than for nominally pure Ge hut clusters.
In summary, when comparing all so far presented Ge based emitters, SiGe hut clusters have the highest potential as their luminescence intensity is comparably high and their emission energy can be almost independently tuned towards the very important telecommunication wavelength of 0.8 eV.

6. Laterally self-ordered SiGe islands with type I band alignment

Our investigations have shown that the type II band alignment inherently limits the radiative efficiency of the (Si)Ge system. But, as mentioned in chapter 2.7 there has been some theoretical work [VdW86, Phi62] on SiGe-Si quantum wells suggesting that a reduced Ge content in quantum wells might result in a type I band alignment.
Unfortunately quantum wells only provide a one dimensional confinement in growth direction. There is no in-plane confinement and, hence, electrons and holes can diffuse inside the quantum well, where they can reach non-radiative recombination centers. To overcome such charge carrier diffusion local epitaxial growth was employed using shadow masks [Bru95] or post-growth reactive ion etching [Kös96]. These fabrication methods produced promising results but require post- and/or preprocessing steps, which can damage the structure or induce additional non-radiative recombination centers. Thus, a direct epitaxy of type I quantum well segments with a three dimensional confinement is desired.
In this chapter, we will introduce the direct epitaxy of SiGe quantum well segments (SiGe islands). These SiGe islands form in a self-organized face centered cubic structure. We deduce from band structure simulations, which are solely based on experimentally determined structural parameters, a spatially direct type I transition, which is a major result of this thesis. Furthermore, a possible explanation for the phenomena of a broad luminescence peak observed both in our SiGe islands and in molecular beam epitaxy grown quantum wells is given.

6.1. Structural properties of SiGe islands

Using co-deposition of silicon and germanium, we prepared SiGe islands with a Ge content of nominally 30%. Due to the reduced lattice mismatch more material is required to form islands. Thus, nominally 15 to 80 monolayers (ML) of SiGe alloy have been deposited at a growth temperature of 630°C. The silicon growth rate is 0.4 Å/s and the Ge growth rate is 0.18 Å/s. Figure 6.1 shows atomic force microscopy images of $Si_{0.7}Ge_{0.3}$ islands with a deposition of nominally (a) 15, (b) 25, (c) 40, (d) 55 and (e) 80 monolayers of SiGe alloy. Figure 6.1 (f) presents a zoom on one $Si_{0.7}Ge_{0.3}$ island with nominally 40 monolayers of material. The insets depict the two dimensional fast Fourier transform (FFT) of the corresponding samples.
With the deposition of nominally 15 monolayers a flat layer of $Si_{0.7}Ge_{0.3}$ forms. The surface is rough with a root mean square of approximately 5.1 Å corresponding to four monolayers of $Si_{0.7}Ge_{0.3}$. The FFT image shows no distinct features. Figure (b) depicts

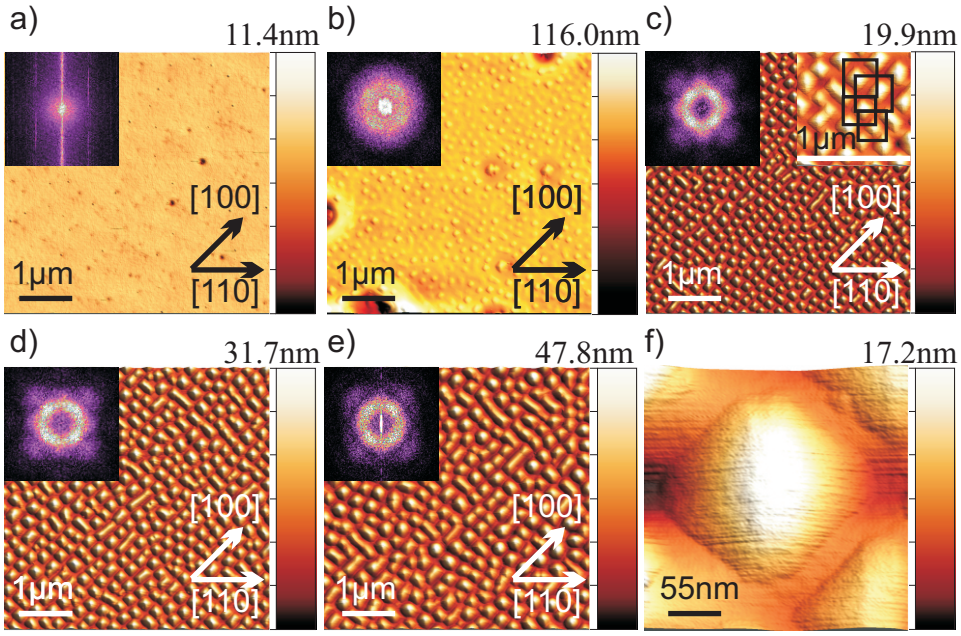

Figure 6.1.: Atomic force microscopy images of $Si_{0.7}Ge_{0.3}$ islands where a layer thickness of (a) 15, (b) 25, (c) 40, (d) 55 and (e) 80 monolayers of SiGe alloy is deposited. (f) shows the zoom on one island with an amount of deposited material which equals 40 monolayers. The insets show the two dimensional fast Fourier transform of the corresponding atomic force microscopy image The right inset in (c) shows a zoom in on several islands and depicts the face centered cubic ordering.

the formation of three dimensional $Si_{0.7}Ge_{0.3}$ islands. The creation of the islands is an unorganized self-assembled process as indicated in the FFT image where no symmetry is observable.
For nominally 40 monolayers (c) the whole surface is covered by a homogeneous distribution of rectangular based $Si_{0.7}Ge_{0.3}$ islands. At 55 monolayers (d) the atomic force microscopy image shows islands which merge together and additional smaller islands on interstitial nucleation sites. After the deposition of even more material (e) the pyramidal shape of the islands vanishes in favor of a more round dome-like shape. In the zoom-in in figure 6.1 (f) a single island is depicted. The islands are quadratic based along the [100]-direction and have a pyramidal shape.
Interestingly upon the deposition of 30 to 55 monolayers the pure self-assembly process is replaced by a self-assembled lateral self-organized formation of $Si_{0.7}Ge_{0.3}$ islands. The islands do not form at random nucleation spots anymore. In fact, the FFT and the real-space image denote a fourfold face centered cubic symmetry. The right inset of figure 6.1(c) highlights the ordering by black rectangles. Each island is surrounded by

four islands. We can rule out stacking [Bru01] induced ordering because the ordering is also observed for one layer of uncapped islands. For deposition thicknesses above 55 ML the ordering is lost as more islands occupy interstitial nucleation spots.
Governed by the atomic force microscopy images, we deduce that the critical thickness of a $Si_{0.7}Ge_{0.3}$ alloy for the formation of islands is between 20 and 25 monolayers. Using the lattice constant of $Si_{0.7}Ge_{0.3}$, which can be calculated by the formula [Dis64],

$$a_{Si_{1-x}Ge_x} = 0.5431 + 0.01992x + 0.0002733x^2(nm) \tag{6.1}$$

we obtain the two dimensional equivalent layer thickness which is approximately 2.75 nm or 3.43 nm, respectively. Even up to 80 monolayers, which resemble a layer thickness of approximately 11 nm the layer thickness is thinner then the critical thickness for the nucleation of dislocations [Mat74, Mat75]. Thus, we expect a pseudomorphic strained dislocation free $Si_{0.7}Ge_{0.3}$ alloy.
To quantify the influence of the material deposition figure 6.2 summarizes the size of the $Si_{0.7}Ge_{0.3}$ islands. The island length is plotted using black squares. Two values in blue circles at 40 and 80 monolayers illustrate the length determined using cross-sectional transmission electron microscopy. The same accounts for the island height (red triangles) where the pink diamonds indicate the transmission electron microscopy data. The error bars resemble the statistical size variation of the islands. With increasing amount of deposited material both the island height and island length rise. The solid lines indicate fits of the respective data points. Due to the island pyramidal shape we expect the islands volume to fulfill following requirement:

$$V = 1/3 \cdot l^2 \cdot h \tag{6.2}$$

Here l is the island length and h the island height. Indeed we can fit the atomic force microscopy data using a linear model with a slope of 0.11 nm/ML for the island height. This supports the model as it allows to deduce that the island height increases by roughly one monolayer after the deposition of one monolayer of $Si_{0.7}Ge_{0.3}$. The y-axis intercept is 0.12 nm which is close to the height of one monolayer of $Si_{0.7}Ge_{0.3}$ which has a height of 0.14 nm. We fit The island length using the formula:

$$l = a \cdot x^b \tag{6.3}$$

with a = 25.1 nm and b = 0.45. Thus, we see that the island length increases with the square root of the amount of material governed by the fact that adatoms can diffuse in x and y direction.
The aspect ratio which we define as island height over island length of the islands is less than 0.04. Pure Ge islands, which consist of {105} facets (pyramids) or {113} and {15 3 23} facets offer a typical aspect ratio of 0.07 or 0.15, respectively. Thus, we conclude that other or additional facets are dominating. A facet analysis reveals dominating inclination angles of the order of 8-11° and smaller angles of 2-5°. The former angles resemble either {105} (11.31°), {1 1 10} (8.05°) or {117} (11.42°) facets. The latter might resemble an {1 1 20} (4.04°) facet. As theoretical strain model calculations [Sta04] reveal

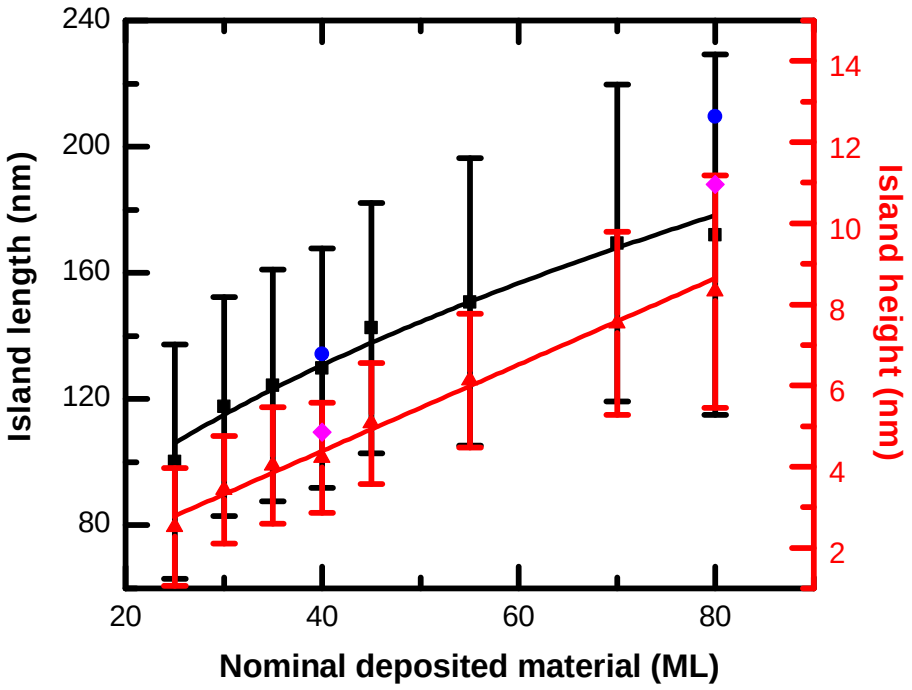

Figure 6.2.: Length (black squares) and height (red triangles) of $Si_{0.7}Ge_{0.3}$ islands taken from the atomic force microscopy images. The solid lines indicate the fit of the respective data points. The blue circles indicate the island length determined by transmission electron microscopy and the pink diamonds indicate the island height determined by transmission electron microscopy.

that the {105} facet is one of the most stable in the SiGe system we conclude that the two dominating facets are the {105} and the {1 1 20} facets. This further strengthens the conclusion of a pyramidal shape.

We investigate the shape and size of buried islands using transmission electron microscopy. This is important as we expect a significant flattening during the capping process due to the high growth temperature. Figure 6.3 presents high angle annular dark field (HAADF) cross-sectional scanning transmission electron microscopy (STEM) images of islands consisting of 40 nominal monolayers of material. Part (a) shows an overview over several uncapped and capped island. The upper bright undulated pyramids are the surface islands investigated by atomic force microscopy. The capped islands are visible 100 nm below the surface layer. The red line highlights the curvature of one capped island. The brighter regions within the Si matrix indicate the presence of thickness variations induced during the sample preparation. The inset shows the 2D fast Fourier transform of the crystal structure of one island. Part (b) illustrates a HAADF high resolution cross-sectional scanning transmission electron microscopy image of one

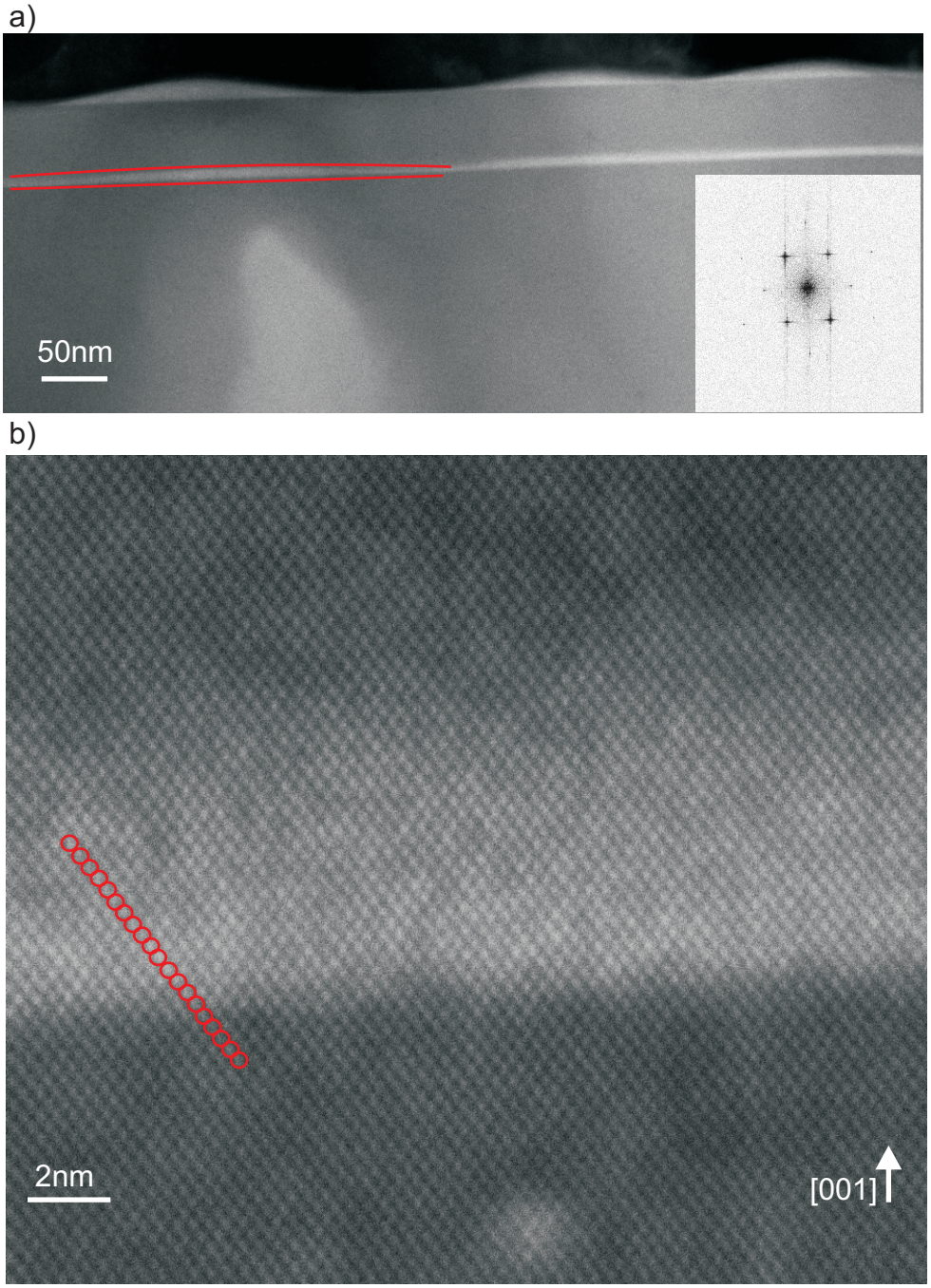

Figure 6.3.: (a) Cross-sectional scanning transmission electron microscopy image in HAADF mode of $Si_{0.7}Ge_{0.3}$ islands with nominal 40 monolayers of deposited material. The inset shows the fast Fourier transform of the crystal structure of one island.(b) Zoom in on the same sample.

island. The red circles highlight the position of the atom columns.
The transmission electron microscopy images, especially the highlighted red lines in figure 6.3 (a) prove that the capped layer still consists of three dimensional islands and not of a two dimensional quantum well. Furthermore, figure (a) shows that the surface islands are connected by a thinner wetting layer than the buried islands. Thus, we conclude that upon the formation of islands the material from the wetting layer is transferred into the islands. This indicates material redistribution according to the Ostwald ripening process [Ros98]. During capping of the islands material diffuses back and forms a stable wetting layer. This is consistent with our expectation of a slight flattening and broadening of the islands which also occurs for pure Ge islands [Kir04].
The spatial position of the atom columns in figure 6.3(b) denotes that the islands are pseudomorphically strained. The in-plane $Si_{0.7}Ge_{0.3}$ lattice constant completely adopts the lattice constant of the underlying silicon substrate. This is a very interesting result as it imposes the usage of a pseudomorphic strain model in the following k*p band structure simulations.
Finally, the scanning tunneling electron microscopy images prove a high crystal quality. The reciprocal space scattering image, which is depicted in the inset reveals no electron scattering apart from the regular lattice planes, which indicates an undisturbed lattice. Also the real space STEM images show, that the $Si_{0.7}Ge_{0.3}$ islands and the silicon matrix are dislocation free.
Energy dispersive X-ray spectroscopy line scans along the island in vertical and horizontal direction allow a mapping of the Ge content and the Ge profile. The Ge content is lowest at the base of the island and in the wetting layer. In vertical direction the Ge content almost linearly increases until a maximum content of $\approx 30\%$. At the top the Ge content slightly decreases again. In horizontal direction the Ge content is higher in the middle of the island and lower to the side. Thus, we conclude that these islands consist of a Ge rich core surrounded by a Si rich shell. The reason for this is that only the shell is exposed to the silicon matrix. Therefore, Si atoms only can diffuse into the island from the matrix. The higher Si content of the shell also is a diffusion barrier for additional Si atoms. Thus, the core of the island is to some degree preserved from intermixing. Raman spectroscopy measurements in back scattering geometry (see section B.3) yield an average Ge content of approximately 25% which agrees with the maximum Ge content of 30% determined by energy dispersive X-ray spectroscopy.
In conclusion, the co-deposition of silicon and germanium allows the fabrication of laterally self-ordered dislocation free pseudomorphically strained $Si_{0.7}Ge_{0.3}$ islands, which preserve their three dimensional shape during the capping process. Both the lateral ordering and the low nominal Ge content make the $Si_{0.7}Ge_{0.3}$ islands an interesting nanostructure for optical applications. The lateral size of the $Si_{0.7}Ge_{0.3}$ islands is far above the De Broglie wavelength resulting in a quantum well like behavior of the islands. Hence, these islands might also offer a type I band alignment because of the low Ge content [VdW86, Peo86].

6.2. Optical characterization and modeling of SiGe islands

In the following, we present photoluminescence spectroscopy measurements to investigate the optical properties of $Si_{0.7}Ge_{0.3}$ islands. The excitation wavelength is 488 nm at an excitation power of 2.3 mW. The experimental temperature was 18 K. The waterfall plot in figure 6.4 shows the resulting luminescence as a function of the emission energy for samples with a nominal amount of (from top to bottom) 15, 20, 25, 30, 35, 40, 45, 55 and 70 monolayers of material. All spectra are normalized to the Si-TO phonon peak at $\approx$ 1.1eV. This normalization is valid as the same substrate wafer is used for all structures resulting in a constant amount of Si. In addition, the crystal quality is of the same order due to a constant growth temperature.
The Si substrate emits light assisted by the Si-TA (1.13 eV), Si-TO (1.10 eV) and Si-TO+O^{Γ} (1.03 eV) phonon [Dav89]. In addition, the $Si_{0.7}Ge_{0.3}$ alloy exhibits several distinct peaks showing a redshift with the deposition of more material. These luminescence peaks we find from 1 to 0.7 eV. The $Si_{0.7}Ge_{0.3}$ luminescence splits into three parts. Two sharp peaks and one broad luminescence. For the later discussion, concerning the origin of the broad luminescence we indicate the luminescence energies of the D1 (807 meV), D2 (874 meV), D3 (939 meV) and D4 (997 meV) silicon dislocation luminescence [Dav89].
We first want to highlight that the luminescence shape, showing a two peak structure, differs from that of pure Ge islands presented in chapter 3. In fact the luminescence shape is similar to that of molecular beam epitaxy grown SiGe quantum wells [Bru92, Men92, Noë90, Wac92]. Chemical vapor deposited quantum wells [Bre92, Fuk95] do not show the broad luminescence. Up to now the broad luminescence was attributed to D1-D4 dislocations or other kinds of structural defects. But the spectral position of the luminescence in comparison to the dislocations energies reveals that another explanation is required. In section 6.3 we will have a closer look on the origin of the broad luminescence.
The two sharper luminescence peaks stemming from the $Si_{0.7}Ge_{0.3}$ alloy undergo a clear redshift with the deposition of an additional amount of material. This yields the conclusion that they are confinement induced. Furthermore, both peaks are separated by $\approx$ 56 meV resembling the energy of a SiGe-TO^{Δ}_{SiSi} phonon [Dea67]. Thus, and in analogy to SiGe quantum wells, we attribute the higher energetic peak to a no-phonon (NP) transition and the lower energetic peak to a transversal optical phonon assisted transition (TO).
The presence of a no-phonon and TO phonon transition as well as the comparable intensities of both peaks indicates a rather weak spreading of the electron and hole wave function in k-space. The no-phonon transition, which is a two particle process has a higher transition strength than the TO phonon process being a three particle process. Therefore, the comparable intensity can only be explained by a weak wave function spreading in k-space which implies a low hole probability density at the Δ-points and a low electron probability density at the Γ-point.

In figure 6.5 a quantitative analysis of the luminescence peak energy as a function of the nominal deposited material is shown. Black squares depict the transition energy of

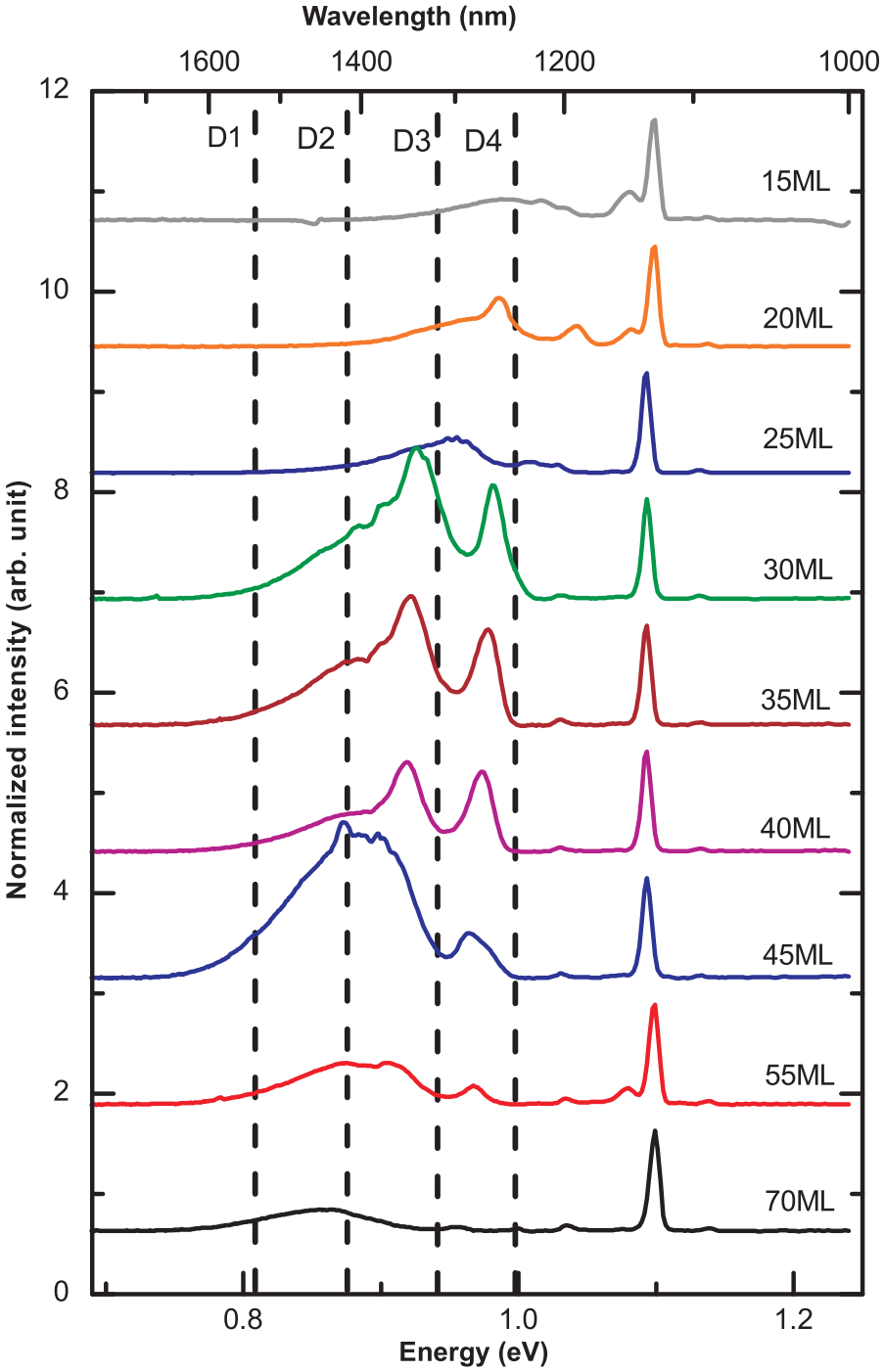

Figure 6.4.: Normalized low temperature photoluminescence waterfall plot of $Si_{0.7}Ge_{0.3}$ islands where a different amount of material is deposited. The excitation wavelength is 488 nm and the excitation power is 2.3 mW. The temperature is 18 K.

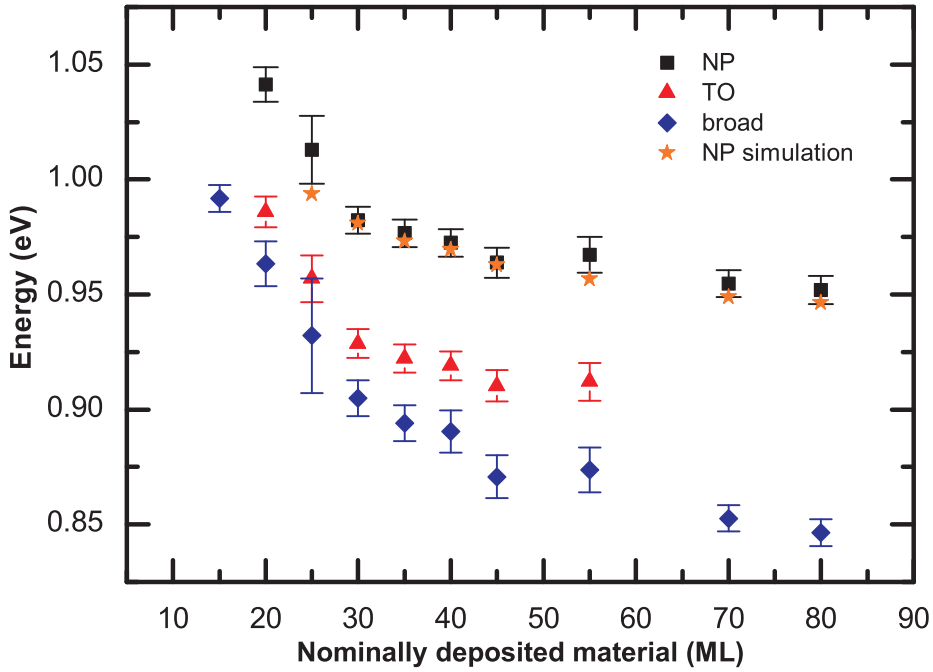

Figure 6.5.: Peak energy as a function of the nominally deposited material for the no-phonon (squares) and transversal optical phonon (triangles) assisted process as well as for the broad luminescence (diamonds) of $Si_{0.7}Ge_{0.3}$. In addition the stars indicate the no-phonon transition energy calculated using eight band k*p band structure simulations.

the no-phonon line. Red triangles show the TO phonon assisted recombination. Blue diamonds indicate the peak energy of the broad luminescence. Moreover, we calculate the transition energy using eight band k*p band structure simulations (orange stars). The simulation uses only the experimental determined structural parameters from section 6.1 as input and involve no fitting parameter. In contrast to chapter 3, the model uses a linear Ge profile for the Ge content with a low Ge content at the base and a high Ge content at the apex of the island. This linear profile is verified by energy dispersive X-ray spectroscopy. All peaks show a clear redshift with increasing material which saturates at approximately 70 monolayers. Upon the deposition of more material the potential well is broadened and the energy of the hole and electron state shifts closer to the lower energies.
In addition, we find a very good agreement between experiment and simulation. By carefully changing different simulation parameters we find a changing transition energy. For example a change of the island height from 2.6 to 3.5 nm results in a redshift of 10 meV. A removal of the three dimensional confinement in favor of a quantum well shape using the same amount of deposited material leads to a blueshift of 69 meV at a nominal material thickness of 40 ML. This proves the validity of the used model and of

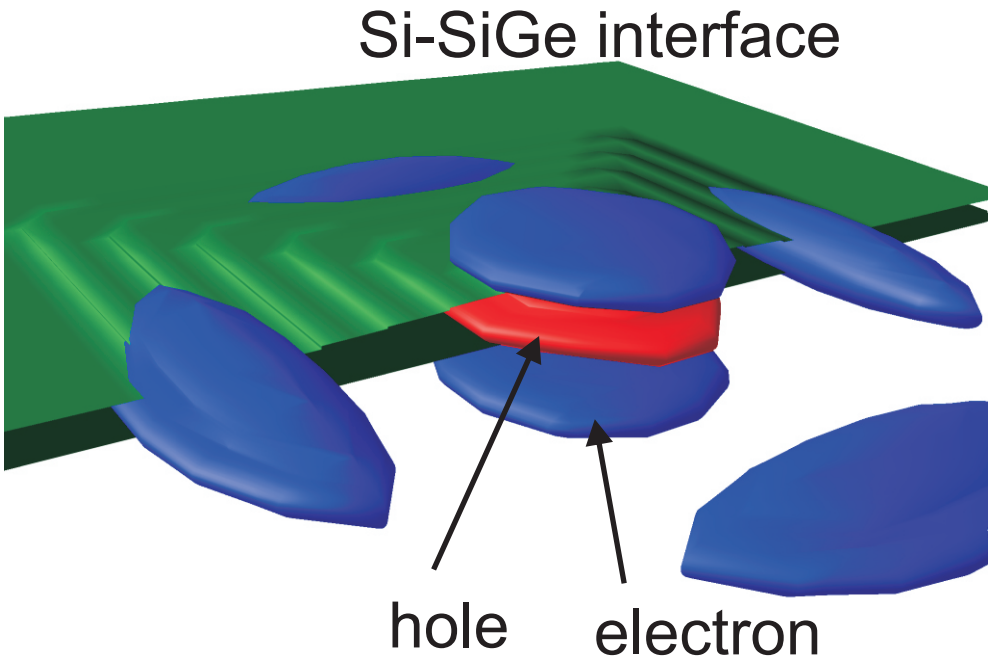

Figure 6.6.: Three dimensional plot of the electron (blue) and hole (red) probability density. The green background illustrates the Si-$Si_{0.7}Ge_{0.3}$ interface. The island is modeled according to the experimental data of an island with nominally 40 monolayers.

the following conclusions.
All samples consist of only one layer of $Si_{0.7}Ge_{0.3}$ islands. However, the normalized intensity of the no-phonon or transversal optical phonon assisted recombination process is quantitatively ≈ 0.98 arb. units. For eight layers of pure Ge hut clusters (see chapter 3) or of SiGe hut clusters (see chapter 5) we have found values of ≈ 0.89 arb. units. Thus, the radiative recombination rate of $Si_{0.7}Ge_{0.3}$ islands is approximately eight times larger as for hut clusters.

6.2.1. Band alignment of $Si_{0.7}Ge_{0.3}$ islands

To explain the comparably high intensity of the $Si_{0.7}Ge_{0.3}$ islands we performed k*p band structure simulations and investigated the electron and hole probability density distribution. Exemplarily for an island consisting of 40 ML we show the isosurfaces of the electron and hole probability densities in figure 6.6. The Si-SiGe interface of the island and the wetting layer is indicated by the green background. The heavy hole ground state (red) is centered in the island. The electron probability density is indicated in blue

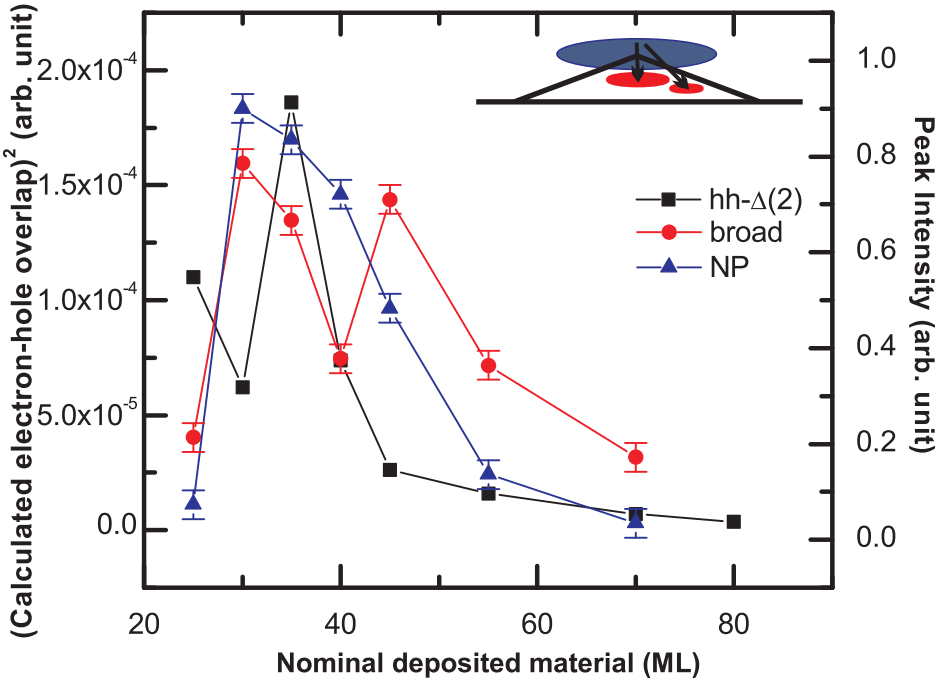

Figure 6.7.: (black squares left y-axis) Theoretical calculated squared electron-hole wave function overlap as a function of the amount of deposited material and (right axis) the experimental determined intensity of the no-phonon (blue triangles) and broad (red circles) luminescence. The inset sketches the spatial position of the ground state $\Delta(2)$ electron and a heavy hole.

and splits into six parts for the six different Δ valleys. The $\Delta(2)$ electrons are above and below the island with a non-zero probability inside the island. The four fold degenerate $\Delta(4)$ valleys are confined at the lower edges of the island inside the $Si_{0.7}Ge_{0.3}$ island. This is a clear indication for a type I confinement giving rise to the higher radiative recombination efficiency.
In addition to the type I confinement, we want to highlight that the confinement is not one dimensional as in SiGe quantum wells. Electrons and holes are confined in all three spatial directions further enhancing the intensity by preventing charge carrier diffusion. In conclusion, we find a three dimensional type I confinement for our $Si_{0.7}Ge_{0.3}$ island which explains the comparably strong luminescence intensity. Moreover, we calculated the electron-hole wave function overlap according to equation 2.14 and summarize the squared result of the $\Delta(2)$-heavy hole transition in figure 6.7 using black squares (left y-axis). The right y-axis depicts the experimental determined peak intensity of the no-phonon transition (blue triangles) and the broad luminescence (red circles). Furthermore, the inset illustrates the spatial electron and hole position in growth direction. The hole is located inside the island and the electron is located above the island with a decent

overlap into the SiGe barrier.
For the squared electron-hole overlap, we find an increase from approximately 25 to 35 nominal deposited monolayers. For further deposition of material the squared overlap integral decreases approximately exponentially. The same trend is reproduced in the peak intensity of the no-phonon and of the broad transition.
The decreasing behavior can be explained with the increasing height and length of the islands resulting in a further separation of the electron and hole ground state. We want to highlight that the intensity of the broad luminescence, whose identity we want to further investigate in section 6.3, follows the calculated electron-hole overlap. This indicates that the broad luminescence depends on the island's electron and/or hole states. One possible transition is sketched in the inset where the electron recombines with a locally trapped hole inside the island.
The electron-hole wave function overlap for the $\Delta(4)$ bands shows qualitatively the same decreasing behavior. The only difference is a weaker overlap due to a larger spatial separation of electrons and holes. However, the attractive Coulomb interaction between the electrons and holes inside the island which is not included in our simulations should result in a quantitatively higher electron-hole wave function overlap for all calculated bands as electrons and holes can diffuse within the islands.
The nice agreement between the experiment and the simulation further strengthens the validity of our simulation model and of the conclusion of a type I band alignment.

6.2.2. Temperature dependent photoluminescence spectroscopy

A further comparison of Ge quantum dots (see section 3.3.2) and $Si_{0.7}Ge_{0.3}$ islands is given by temperature dependent photoluminescence measurements conducted with an excitation power of 4.2 mW. Figure 6.8 exemplary shows the results for a sample deposited with nominally 30 monolayers of material. Figure 6.8 (a) depicts the PL luminescence spectrum for $Si_{0.7}Ge_{0.3}$ islands. Upon increasing temperature the luminescence shifts to lower energies. Furthermore, we find a prominent global quenching of the luminescence intensity. This quenching effect is stronger for the no-phonon and transversal optical phonon transition than for the broad luminescence.
Three Gaussians fit the individual $Si_{0.7}Ge_{0.3}$ peaks and the integrated intensity is plotted as a function of 1/T for the (b) no-phonon, (c) transversal optical phonon and (d) broad luminescence. We fit the integrated intensity using the formula [Wac92]:

$$\frac{I(T)}{I(T_0)} = \left(1 + a \cdot T^n \cdot exp(-\frac{E_a}{k_b T})\right)^{-1} \tag{6.4}$$

Here $I(T_0)$ is the intensity extrapolated to zero Kelvin. The expression aT^n is a measure for the effective density of states for the initial and final states [Wac92]. The exponent n depends on the dimensionality of the confinement. A three dimensional confinement should obtain n=3/2 (blue line) whereas a quantum well should obtain n=1/2 (red line). In figure 6.8 the fit well describes the observed temperature behavior. Unfortunately, the quality of the fit is the same for both possible exponents, thus, any conclusion about the dimensionality of the confinement by the temperature dependent measurements is

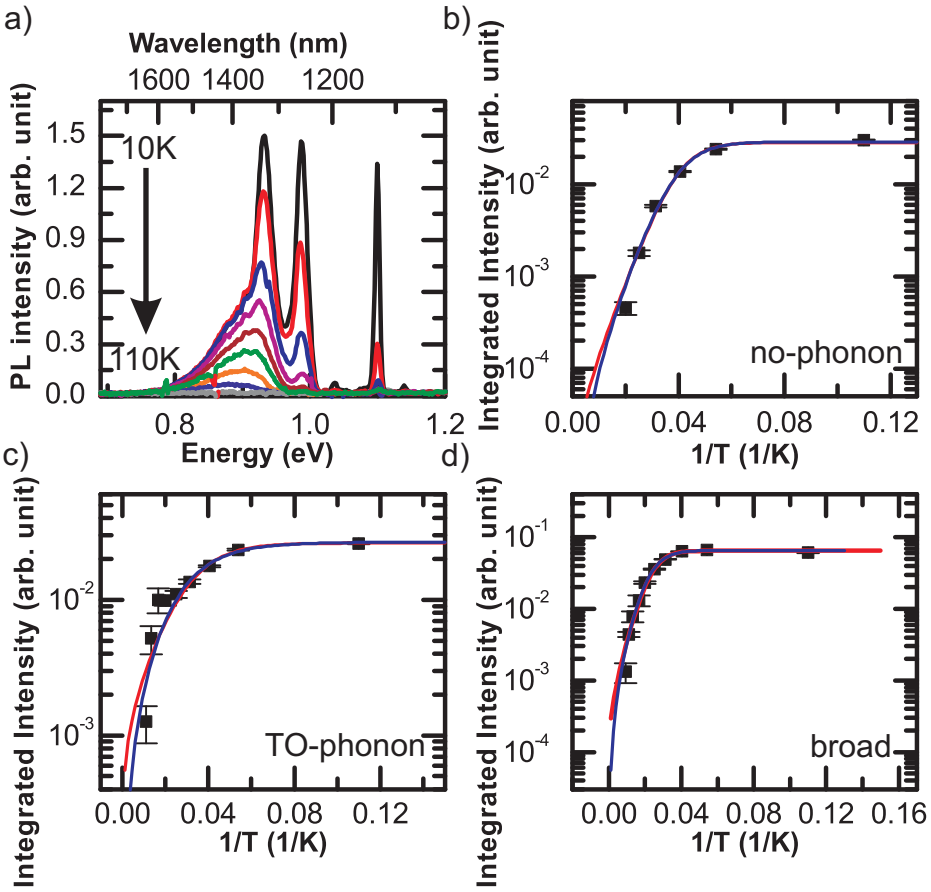

Figure 6.8.: (a) Temperature dependent photoluminescence spectra of $Si_{0.7}Ge_{0.3}$ islands where we deposit nominally 30 ML of material. From top to bottom we use 9 K, 18 K, 25 K, 32 K, 40 K, 50 K, 60 K, 75 K, 90 K and 110 K as temperatures.. Integrated intensities of the (b) no-phonon, (c) transversal optical phonon and (d) broad luminescence as a function of 1/T. All graphs are fitted using equation 6.4 with an exponent of 1/2 (red line) and 3/2 (blue line).

not possible.
Nevertheless, we can extract the activation energies and list them in table 6.1. With the

Thickness (ML)	E_{NP} (meV)	E_{TO} (meV)	E_{broad} (meV)	n
15			1.3±1.1	0.5
30	10.1±1.4	3.3±1.0	10.3±1.2	1.5
40	7.7±1.1	2.6±3.1	8.7±2.3	1.5
55	7.9±1.4		18.0±2.3	1.5
80			1.4±0.6	1.5

Table 6.1.: Activation energies of Ge hut clusters at different growth temperatures.

atomic force microscopy, transmission electron microscopy images and the simulation results showing a three dimensional structure the activation energy is calculated for an exponent of n=1.5 except for the sample with 15 monolayers of material where only a wetting layer is visible.
The activation energies of the no-phonon transitions are usually higher than those of the transversal optical phonon transition. In addition, the activation energies of the broad luminescence are the highest of all recombination mechanisms. Thus, the confinement which is responsible for the broad luminescence has to be stronger than that responsible for the no-phonon transition.
If we compare these activation energies with those of pure Ge hut clusters depicted in table 3.2, we find comparable values. Both the luminescence of the hut clusters and the luminescence of the $Si_{0.7}Ge_{0.3}$ islands vanishes completely for temperatures above 100 to 110°C. This is reasonable as the confinement for the electrons is only of the order of $\approx$ 10 meV in both structures.

6.3. Explanation of the broad luminescence

In the following we will try to explain the broad luminescence whose origin is still unclear even in literature. Several groups attribute the broad luminescence in quantum wells to dislocations [Shu97] or simply to defects [Bru92]. Other groups use so called alloy or L-bands [Web89] as explanation. One group uses the idea of interstitial platelets. These are either, Si interstitial atoms or small substitional or interstitional Ge rich regions [Row93].

6.3.1. Dislocations or structural defects

The cross-sectional HAADF high resolution scanning transmission electron microscopy images in figure 6.3 show no distinct amount of misfit dislocations in the $Si_{0.7}Ge_{0.3}$ island regions. Furthermore, the photoluminescence spectra in figure 6.4 depicted the luminescence energies of the optical dislocation transitions. Some graphs might indicate the presence of dislocations but as the luminescence shifts with the amount of material we conclude that dislocations cannot explain the broad luminescence [Ves92].

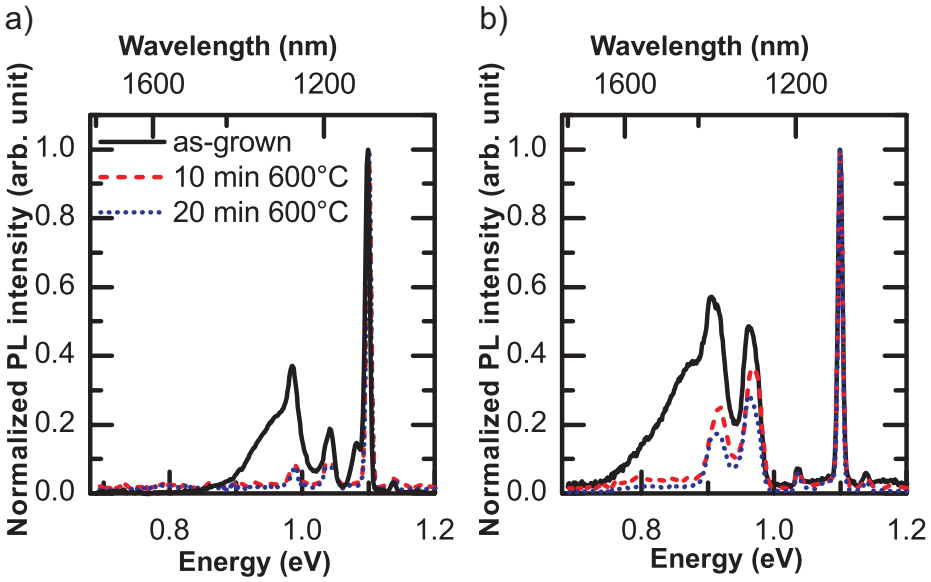

Figure 6.9.: Normalized intensity as a function of the energy and annealing time for $Si_{0.7}Ge_{0.3}$ islands grown with (a) 20 and (b) 45 monolayers of material. The excitation power is 2.4 mW. The measurement temperature is 18 K.

6.3.2. Annealing of the crystal structure

Annealing experiments allow to investigate the dependence of the broad luminescence on the crystal structure. Two samples with nominally 20 and 45 monolayers of $Si_{0.7}Ge_{0.3}$ have been placed in a rapid thermal annealer which uses radiation heat in nitrogen atmosphere to heat the sample to 600°C. The annealing time is ten minutes. Afterwards photoluminescence experiments are conducted using the 488 nm laser at an excitation power of 2.4 mW and at a temperature of 18 K. This procedure is repeated two times. Figure 6.9 illustrates the resulting photoluminescence spectroscopy data. The left image shows the sample with 20 monolayers of material, the right one shows the sample with 45 monolayers, respectively. The intensity is normalized to the Si-TO phonon line, which is expected to be unaffected by the annealing process, as no change of the Si substrate is expected. The black solid line shows the as-grown sample, the red dashed line indicates the spectrum after the first annealing step. The blue dotted line displays the spectrum after the second annealing step.

We find a universal decrease of the normalized intensity of the $Si_{0.7}Ge_{0.3}$ islands upon annealing of the sample. Furthermore, the no-phonon and transversal optical phonon line shift to higher energies. The reason is a flattening of the islands and a further intermixing of the islands with silicon [Sch98, Bou04]. The most prominent result is the complete vanishing of the broad luminescence. Thus, we conclude that the broad luminescence is caused by the crystal structure. Either crystalline defects which can act as charge carrier traps might be cured due to the temperature treatment or Ge rich

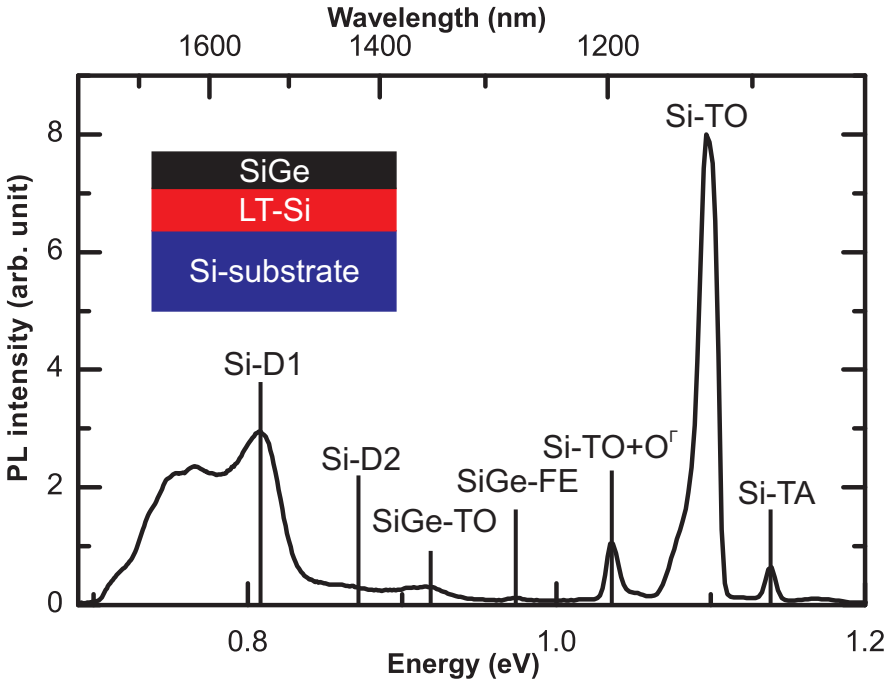

Figure 6.10.: Photoluminescence spectroscopy measurement of a 500 nm thick $Si_{0.8}Ge_{0.2}$ alloy deposited on top of a low temperature Si buffer.

clusters might dissolve due to a redistribution of the alloy.

6.3.3. SiGe alloys without confinement

A further experiment is the investigation of a 500 nm thick $Si_{0.8}Ge_{0.2}$ alloy on a low temperature Si buffer [1]. If the broad luminescence is caused by the SiGe alloy we expect a redshift due to the lower Ge content and a missing confinement. A typical photoluminescence spectrum of such an alloy is shown in figure 6.10. The inset illustrates the layer structure. The spectrum yields the presence of several prominent peaks. The high energetic peaks above 1 eV stem from the Si substrate. The low energetic features stem from the $Si_{0.8}Ge_{0.2}$ alloy and from Si dislocations. At an energy of approximately 0.973 eV the free exciton line of the $Si_{0.8}Ge_{0.2}$ is visible. At an energy of 0.917 eV the SiGe TO phonon replica is observed [Web89, Len92]. Moreover, we find two peaks, which we attribute to the Si-D1 (807 meV) and Si-D2 (874 meV) dislocations [Dav89]. Such dislocations often occur in low temperature Si buffers [Sai10]. Finally, a broad luminescence peak at approximately 0.75 eV is observed. The existence of a broad luminescence at lower energies inside a 500 nm thick alloy layer proves that it is not

[1] The growth has been conducted by Jürgen Sailer in his PhD thesis [Sai10]

caused by the confinement. It stems from the SiGe alloy itself.

6.3.4. Growth method

In literature such a broad luminescence is only observed in molecular beam epitaxial deposited quantum wells [RH98]. Usually molecular beam epitaxy is expected to result in a higher material purity and a higher crystal quality of the deposited material than chemical vapor deposition as no molecular compounds are used as incident material. Besides that a huge difference between chemical vapor deposition and molecular beam epitaxy is the growth rate, which is much lower in molecular beam epitaxy. The lower growth rate is usually expected to result in a better crystal quality as the adatoms have more time to form a perfect crystal [Ric90] (see section 2.3). Furthermore, in chemical vapor deposition the complete epitaxy chamber is filled with a homogeneous distribution of precursor gas, whereas the MBE surfactants are usually placed in effusion or electron evaporation cells at a certain angle towards the substrate wafer [Ebe90]. This results in a deposition gradient of material.
Silicon and germanium are completely soluble from x_{Ge} = 0-100% [Dis64]. Furthermore, a homogeneous mixing is the energetically most favorable state as the strain energy is reduced. Still the position of silicon and germanium atoms is given by statistics and by the position of the electron beam evaporators. Thus, it is reasonable that the inhomogeneous deposition of Ge in a molecular beam epitaxy can result in small nanometer sized SiGe clusters with a higher Ge content than desired. The presence of such inhomogeneities is supported by cross-sectional transmission electron microscopy images of Demchenko *et al* who investigated the local atomic structure of SiGe self-assembled islands [Dem07]. We believe such Ge clusters are basically Ge rich SiGe quantum dots in a $Si_{0.7}Ge_{0.3}$ alloy. The argumentation of quantum dots inside of islands has also been established in 2010 by Brehm *et al* to explain differences in the excitation power dependent photoluminescence of SiGe pyramids and domes deposited on pit-patterned and planar substrates [Bre10].

6.3.5. SiGe cluster model

In figure 6.11 we sketch the band structure of higher Ge content cluster inside a SiGe island in growth direction. The gray shaded region resembles the silicon matrix, the orange region is the $Si_{0.7}Ge_{0.3}$ island. The green region resembles the cluster with a higher Ge content. The horizontal lines indicate the energy of the individual states. Also the electron and hole probability densities are sketched. We think that the higher Ge content results in the formation of a quantum dot with an individual confinement inside the $Si_{0.7}Ge_{0.3}$ island. This results in the formation of additional states and possible transitions with lower energy. Due to the size and content variation of such quantum dots a broad luminescence is expected.
To evaluate this assumption we simulate the transition energy of a Ge cluster with an average Ge content of 40% and a size of 20 nm times 20 nm times 6 nm inserted in a

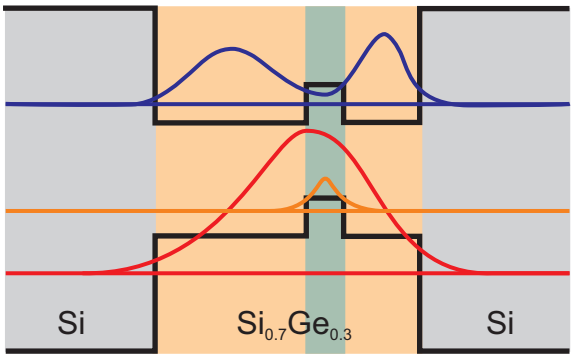

Figure 6.11.: Illustration of the band structure of a SiGe quantum dot inside a $Si_{0.7}Ge_{0.3}$ island in growth direction. The horizontal lines indicate the energy of the ground states for the electron and the heavy hole inside the island and inside the quantum dot.

$Si_{0.7}Ge_{0.3}$ island with a deposition thickness of nominally 40ML. The resulting transition energy of 0.90 eV agrees with the experimental determined value for the broad luminescence at 0.89 eV.

To further prove this assumption of Ge rich clusters we take another look on figure 6.3(b). The HAADF scanning transmission electron microscopy detection mode is highly sensitive on the atomic mass. The image now shows strong variations in the contrast on a small scale which indicates either thickness fluctuations of the sample or a variation of the Ge content. If we take all indications into account we conclude that indeed fluctuations in the Ge content are responsible for the broad luminescence.

Unfortunately a direct proof for the existence of Ge rich cluster in the $Si_{0.7}Ge_{0.3}$ islands is still missing. The resolution of energy dispersive X-ray spectroscopy is not high enough to reveal information about the Ge content fluctuations. Raman spectroscopy only gives information about the average Ge content. Furthermore, cross-sectional scanning tunneling microscopy allowing atomic resolution is not applicable in the SiGe system as the sample facets do not cleave atomically flat.

Nevertheless such Ge rich clusters inside the $Si_{0.7}Ge_{0.3}$ island would fulfill the requirement to explain all previously obtained results.

- The broad luminescence energy can be described using clusters with a Ge content of $\approx 40\%$.
- The higher Ge content results in a decrease of the luminescence energy compared to the no-phonon line.
- The broad luminescence involves either the island electron or the heavy hole ground state.
- The Ge cluster, which is expected to have a type II confinement shifts with the confinement of the $Si_{0.7}Ge_{0.3}$ island.

- The activation energy is higher than that of the $Si_{0.7}Ge_{0.3}$ island no-phonon luminescence due to a stronger hole confinement.
- The broad luminescence vanishes upon annealing as the SiGe clusters dissolve due to a redistribution of the silicon and germanium atoms.
- The broad luminescence is present in a deposited alloy without a further confinement.

Therefore, we are quite confident to attribute the broad luminescence to SiGe clusters inside the $Si_{0.7}Ge_{0.3}$ islands.

6.4. Conclusion about $Si_{0.7}Ge_{0.3}$ islands

In summary, this chapter shows the fabrication of active $Si_{0.7}Ge_{0.3}$ emitters which offer a high luminescence intensity due to a three dimensional type I confinement. The type I band alignment and the resulting strong luminescence intensity of the $Si_{0.7}Ge_{0.3}$ islands make them the most promising candidates for light source applications of all investigated confinement structures. The photoluminescence intensity is eight times higher than that of Ge based islands. In addition, these SiGe islands, which are prepared using co-deposition of silicon and germanium, organize themselves in a lateral face centered cubic structure. The lateral self-ordering is very interesting as it allows the lateral positioning of cavities or gates towards the islands.

6.5. Evaluation of (Si)Ge based emitters

Independently of the material system an emitter with a high recombination efficiency requires a high electron-hole wave function overlap both in k-space as well as in real space.
The here presented study on different quantum dot and island morphologies has shown that Ge hut clusters provide the best overlap in k-space due to their small size. Also in real space a comparable high spatial overlap of $\approx 3.7\%$ has been achieved.
In k-space with the exception of SiGe hut clusters no other investigated morphology offers comparable good properties. Here pyramids, domes and SiGe islands share the disadvantage of a weak hole spreading in k-space which leads to the occurrence of competing phonon assisted recombination channels.
In real space our simulations have shown that a further improvement requires a small size and a low Ge content. These, however, are excluding properties as a low Ge content results in a low lattice mismatch which always leads to an increasing size.
Photoluminescence experiments on ensembles of Ge pyramids and domes verify this assumption as approximately three times lower intensities are observed. For these island morphologies the intensity reducing effect of the three to four times larger size overcomes the increasing effect of a lower Ge content.

The idea to circumvent the trade-off between size and Ge content using co-deposition of Si and Ge at low temperatures does only reveal comparable spatial overlap integrals of the order of 1.2%. But the possibility for an additional epitaxial degree of freedom by tuning the Ge content makes SiGe hut clusters the most interesting quantum dot morphology.
In conclusion, SiGe and Ge hut clusters are so far the best emitter in terms of k-space optimization due to their small size. However, we find that all quantum dot morphologies share a type II band alignment which inherently limits the radiative efficiency by a low spatial electron-hole wave function overlap.
With a spatial type I band alignment in SiGe islands we obtain approximately eight times higher luminescence intensities as for the best hut cluster samples. This, however, is not reflected in the calculations of the spatial overlap integral where we get an overlap of $\approx 1.3\%$. But this calculations neglect Coulomb attraction which has a larger effect on the charge carrier distance in type I structures than in type II structures. This Coulomb interaction is expected to result in a higher quantity of the electron hole wave function overlap. Hence, we find that SiGe islands are the optimum emitters in real space because of their spatial type I confinement. On the other side SiGe islands have the drawback of a weaker electron and hole spreading in k-space which is reflected by the presence of phonon assisted recombination channels.
This consideration directly shows that it seem to be not possible to optimize both the real space and the k-space electron-hole wave function overlap. Therefore, we think that (Si)Ge emitters will always be less efficient than compound semiconductor quantum dots. Thus, additional effects need to be employed for a higher radiative efficiency and/or a higher extraction efficiency of photons which is limited by the large refractive index contrast of silicon to air. One solution is to tailor the photonic environment with photonic crystals.

7. Theory of photonic crystals

In analogy to semiconductor crystals Eli Yablonovitch [Yab87] and Sajeev John [Joh87] proposed that a periodic lattice of refractive indices leads to the formation of photonic band structures. Such a band structure can consist of frequency regions with a zero photon density of states in certain directions which are called photonic band gap. The zero density of states in such regions results in the fact that photons with a certain energy cannot propagate leading to a redistribution of emitted photons.
In two dimensions such structures have been first experimentally shown by Krauss *et al.* [Kra96] in 1996. Since then photonic crystals attracted increasing interest in both optics and photonics. In this section we will shortly explain the theoretical concepts of photonic crystals which are necessary to understand the experimental results of this thesis. You can find further information in general textbooks [JJ08].

7.1. The master equation

Mathematically a photonic crystal is described by the so called master equation [JJ08]:

$$\nabla \times \left[\frac{1}{\epsilon_r(\mathbf{r})} \nabla \times H(\mathbf{r},t) \right] = -\frac{1}{c^2} \frac{\partial^2}{\partial t^2} H(\mathbf{r},t) \tag{7.1}$$

Here H is the magnetic field and ϵ_r is the dielectric constant. This equation can be derived from the basic Maxwell equations by using the following assumptions [JJ08]:

- There are no space charges and no electric currents ($\rho(\mathbf{r},t) = 0$ and $j(\mathbf{r},t) = 0$)
- All used materials are isotropic and non-dispersive (dielectric constant ϵ is a real scalar)
- No non-linear effects occur
- Silicon is non-magnetic (magnetic susceptibility $\mu(\mathbf{r}) = 1$)

Using the operator:

$$\Theta = \nabla \times \left[\frac{1}{\epsilon(\mathbf{r})} \nabla \times \right] \tag{7.2}$$

and eliminating the time dependence by using the Ansatz $H(\mathbf{r},t) = H(\mathbf{r})e^{iwt}$ we can reformulate formula 7.1 to resemble an Eigenvalue problem:

$$\Theta \left| H(\mathbf{r}) \right\rangle = \frac{\omega^2}{c^2} \left| H(\mathbf{r}) \right\rangle \tag{7.3}$$

To describe the translation symmetry of the periodic lattice we introduce the lattice constant a, the reciprocal lattice vector $\mathbf{k}$ and the Bravais vector $\mathbf{R}$. This allows for a simplification of the Eigenvalue in formula 7.3 by applying the Bloch-Floquet theorem [SJ03] for periodic structures. This theorem enables the separation of the wave function in a lattice-periodic and a plane wave part.

$$H(\mathbf{r}) = H_k(\mathbf{r})e^{i\mathbf{kr}}, \quad \text{with} \quad H_k(\mathbf{r}) = H_k(\mathbf{r}+\mathbf{R}) \tag{7.4}$$

If we substitute equation 7.4 into equation 7.3 we get:

$$\Theta_k H_k(\mathbf{r}) = \frac{\omega_n^2(\mathbf{k})}{c^2} H_k(\mathbf{r}) \tag{7.5}$$

with

$$\Theta_k = \left[(\nabla + i\mathbf{k}) \times \frac{1}{\epsilon_r(\mathbf{r})}(\nabla + i\mathbf{k})\times\right] \tag{7.6}$$

Equation 7.5 is the final equation which defines the dispersion relation of a photonic crystal. With exception of 1D problems the solution requires numerical methods [Zab08]. The two most used methods are the plane wave expansion method [Joh01] and the finite difference time domain method [Yee66]. The plane wave expansion method solves the master equation in an iterative approach. The latter method calculates the time dependent light propagation in a photonic crystal.
During this thesis we only use the plane wave expansion method as the dispersion relation is sufficient for the results we present here. For the simulation we use the open source software mpb developed at the MIT [Joh01].
Interestingly, the master equation lacks of a fundamental length scale. Hence, the master equation and its results are scalable in the lattice constant a. Therefore, we can use a/λ as unit free length and all photonic crystals with the same dielectric conformation share the same band structure providing they only differ in a.

7.2. Two-dimensional photonic crystal slabs

Nowadays photonic crystal structures exist in 1D as distributed Bragg reflectors [Mac94] in 2D as photonic crystal slabs [Hau10] as well as in 3D [Hau12, Lin98]. Still 2D photonic crystal slabs are the most common design due to their ease in fabrication. These slabs consist of air holes in a free standing dielectric membrane. The translation symmetry of the lattice is broken in out-of-plane direction.
The broken symmetry results in several changes of the dispersion relation. First of all it restricts the formation of a photonic band structure to the in-plane direction. The out-of-plane photonic density of states remains a continuum of states. However, the large index contrast between the surrounding air ($\epsilon_{air} \approx 1.0$) and the slab material (ϵ_{Si}=3.45 [Li80]) results in a refractive index confinement due to total internal reflection.
Without translation symmetry the electric field can no longer be defined in purely transverse electric (TE) and transverse magnetic (TM) waves. To overcome this problem we now redefine the polarization by the direction of the electric-field vector (**E**-field) with

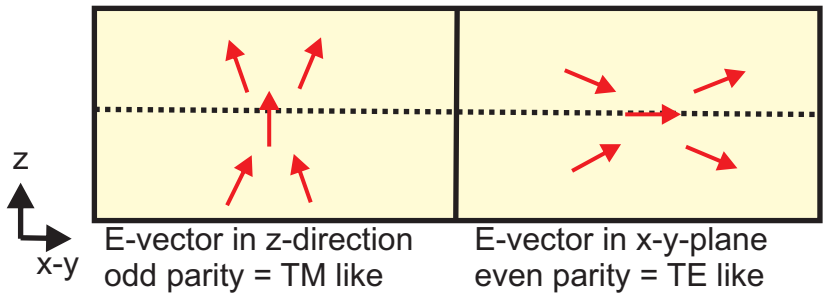

Figure 7.1.: Illustration of transverse magnetic-like and transverse electric-like **E**-field direction.

respect to the z=0 plane[JJ08] as illustrated in figure 7.1. The yellow region illustrates the cut-plane of a photonic crystal slab in z-direction. The red arrows indicate the direction of the **E**-field vector. If the **E**-field vector points perpendicular to the z=0 plane, we define the **E**-fields transverse magnetic-"like" (odd parity). If the **E**-field points parallel to the z=0 plane then we call the **E**-fields transverse electric-"like" (even parity). TE-like and TM-like modes or bands can be mathematically calculated independently. For a slab patterned with a triangular lattice of air holes, which we use during this thesis, a TE-like band gap is favored, whereas often no TM-like photonic band gap is present [JJ08]. Thus we exclude TM-like modes in the further discussion.
Finally, it has been shown that there are only incomplete band gaps [JJ08] in 2D photonic crystals. Such an incomplete band gap exists only in a restricted wave vector region which is given by the so-called light cone [JJ08]. The light cone is a direct consequence of the conservation law for ω and $\mathbf{k}$ and defined by $\omega = ck_{||}$. Out-of-plane meaning above the light cone there is a continuum of leaky waves which are not confined to the photonic crystal slab. This leads to an incomplete band gap as at certain frequencies photons can couple to this continuum of waves.
In figure 7.2, we summarize the resulting band properties of a 2D photonic crystal slab. Figure 7.2 (a) illustrates a 2D photonic crystal slab which consists of a triangular lattice of air holes in a freestanding silicon membrane. Here, we define the lattice constant a, the air hole radius r and the slab height h. Figure 7.2 (b) is a sketch of the etched air hole lattice and of the corresponding reciprocal lattice with its hexagonal shaped first Brillouin zone. The irreducible Brillouin zone is highlighted in orange and is defined as the path between the high symmetry points Γ, K and M. In figure 7.2(c), we plot the calculated photonic band structure of a photonic crystal slab as depicted in (a). Hereby, the slab height is h/a=0.71 and the r/a ratio is 0.33. The gray shaded region is the light cone. Between the first and the second band at frequencies of a/λ=0.26-0.36 the photonic band gap is observed and highlighted in orange. The simulation also includes a cavity which we will introduce in the next section. The H3 cavity shape is illustrated in the inset. The horizontal lines within the photonic band gap are so called photonic crystal cavity modes.

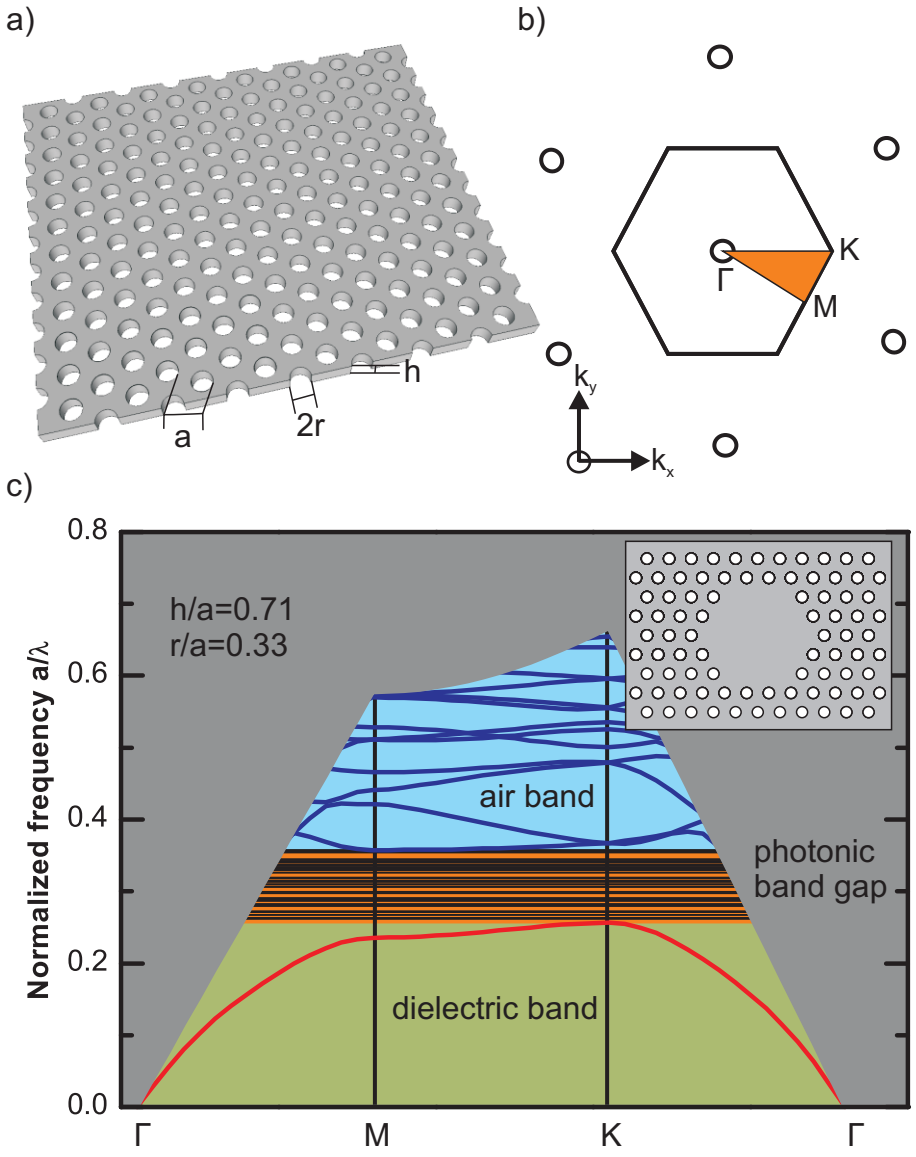

Figure 7.2.: (a) Illustration of a 2D photonic crystal slab which consists of a free standing membrane of higher refractive index material where a triangular lattice of air holes is etched. a is the lattice constant of the air holes, r the radius of one air hole and h is the height of the slab. (b) Corresponding first Brillouin zone of the reciprocal lattice of a photonic crystal. The orange region shows the irreducible Brillouin zone. (c) Calculated photonic band structure for a 2D photonic crystal slab with a h/a ratio of 0.71 and a r/a of 0.33. The gray shaded region resembles the light cone. The lowest band is the dielectric band. In orange the photonic band gap is highlighted and in turquoise we highlight the air band. A photonic crystal H3 cavity is included whose shape is illustrated in the inset. The black horizontal lines in the photonic band gap frequency range indicate the cavity modes.

7.3. Photonic crystal cavities

Since the discovery of photonic crystals, cavities are a major research area [Nom06, Aka03] as they break the translation symmetry of the periodic lattice. The broken symmetry, which is indicated by the hexagonal removal of 19 holes in the inset of figure 7.2 (c) results in the formation of resonances in the photonic density of states. According to Fermi's Golden rule in equation 2.8 the radiative recombination efficiency is enhanced by such resonances in the optical density of states ρ. The cavity design depicted in figure 7.2 (c) is a H3 cavity [Oli02].
Photons are efficiently trapped in a cavity by the surrounding photonic band gap acting like a mirror. The confinement efficiency of a cavity is determined by the time a photon stays inside the cavity before escaping or being reabsorbed. This is quantified by the cavity quality factor.

$$Q = \frac{\lambda}{\Delta\lambda} = \omega\tau \tag{7.7}$$

Hereby, λ is the cavity resonant wavelength, ω is the cavity resonant frequency, $\Delta\lambda$ is the line width and τ is the photon lifetime inside the cavity. In the band structure, which is plotted in figure 7.2 we find that an H3 defect cavity results in the formation of 49 localized states inside the photonic band gap. Hereby the spectral position of the localized states is given by the air hole radius, the slab height and the cavity design. The amount of cavity modes depends on the cavity design. Due to the large size an H3 cavity sustains many cavity modes, whereas for example an L3 cavity, which is formed by the omission of three holes in a row, sustains only six cavity modes [Aka03].

8. Coupling of SiGe islands to 2D Si photonic crystals

The combination of Ge pyramids and domes (presented in chapter 4) with photonic crystals has been previously shown by different groups [El 08, Xia06] and in the cooperative thesis of Norman Hauke [Hau11, Hau12]. Tremendous enhancement factors up to 1000 and room temperature luminescence in resonance with cavity modes have been demonstrated [Xia08]. In this chapter we now focus on investigating the prospect of further enhancing the intensity of $Si_{0.7}Ge_{0.3}$ islands (presented in chapter 6.

8.1. Photonic crystal design

The fabrication of two dimensional photonic crystals requires the use of SOI substrates. Therefore, we prepared a new sample consisting of nominally 45 monolayers of $Si_{0.7}Ge_{0.3}$. Atomic force microscopy images verify the formation of three dimensional islands. Furthermore, photoluminescence spectroscopy measurements proof the existence of a no-phonon and a transversal optical phonon transition.

In figure 8.1, we present the final photonic crystal structure. The fabrication is explained in the appendix E.1. Figure 8.1 (a) shows the scanning electron microscopy image of a photonic crystal with a so-called H3 cavity [Ren08]. The photonic crystal has a hexagonal shape with a triangular lattice of air holes. In the middle some holes are omitted to form a photonic crystal H3 micro-cavity. Next to the photonic crystal quadratic holes are etched which are helpful in the under-etching process as they allow an easy infiltration with hydrofluoric acid. Figure 8.1 (b) shows the zoom on the cavity region and defines the parameters lattice constant a and radius r. Here, the lattice constant is a$\approx$290 nm and the radius r$\approx$100 nm. The height of the slab is h=270 nm.

We want to highlight that the surface layer of $Si_{0.7}Ge_{0.3}$ island is visible in the scanning electron microscopy images. Exemplarily one island is highlighted in red. Thus, we find that approximately 28 islands are spatially coupled to the H3 cavity. Of these 28 islands 13 are partially etched by the air holes in the vicinity of the cavity. This etching we expect to result in the formation of surface defects, which may act as non-radiative recombination channel. The high amount of non-etched islands is the reason why we have chosen the H3 as cavity design although different cavity designs like L3 [Aka03] or A1 [Kur06] are known to have higher quality factors.
We obtain the design parameters for the fabrication of the photonic crystals from numerical plane wave expansion simulations (see chapter 7). The calculations yield that an H3 cavity maintains more than 49 cavity modes. The qualitative shape of the cavity modes stays the same over a wide set of parameters.

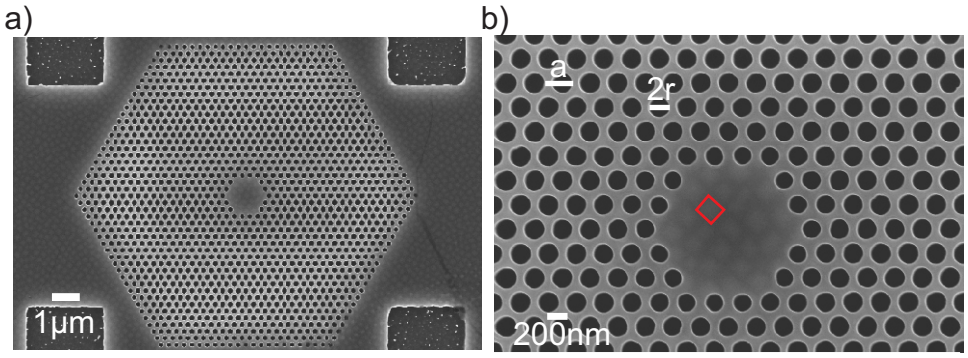

Figure 8.1.: (a) Scanning electron microscopy image of a two dimensional photonic crystal with an H3 cavity. (b) Zoom on the cavity region.

In figure 8.2, a representative selection of the electric field distribution of some cavity modes profiles is given. The cavity modes exhibit different circular and elongated shape. In addition, one can find electric field maxima on many different positions. This allows a good coupling of almost every island to the cavity. Furthermore, the mode profiles show that a large fraction of the electric field is localized in the silicon material inside the cavity. Therefore, we expect a weak influence of surface defects, which might be introduced during the reactive ion etching process.

8.2. Optical investigations of $Si_{0.7}Ge_{0.3}$ islands coupled to two-dimensional H3 photonic crystal cavities

We investigated the influence of the photonic crystal on the $Si_{0.7}Ge_{0.3}$ island luminescence intensity by means of micro-photoluminescence experiments. We expect that the emission intensity is strongly enhanced in resonance with the cavity modes [Hap02]. The setup is explained in the appendix B.4.2. If not stated otherwise all experiments in this section use a temperature of 25 K and an excitation wavelength of 532 nm with an excitation power of 5 mW. The laser is focused to a circular spot with a radius of $\approx$ 900 nm which resembles a power density of approximately 20 MW/cm^2.
The waterfall plot in figure 8.3 presents the photoluminescence intensity in counts per 200 seconds as a function of the emission energy. The different graphs resemble an increasing r over a ratio from bottom to top. All three graphs show at least eight Lorentzian line shaped peaks [JJ08] in resonance with the $Si_{0.7}Ge_{0.3}$ island emission. The peaks shift to higher energy with increasing r/a ratio. A higher r/a ratio results in a decreasing cavity size. With a smaller cavity size the electric field has a higher probability in the low refractive index material air leading to an increasing energy of the resonant mode. This shift is a clear indication for the presence of cavity modes [Li06].
In the next step, we perform temperature dependent micro-photoluminescence spectroscopy measurements on $Si_{0.7}Ge_{0.3}$ islands and on $Si_{0.7}Ge_{0.3}$ islands in resonance with

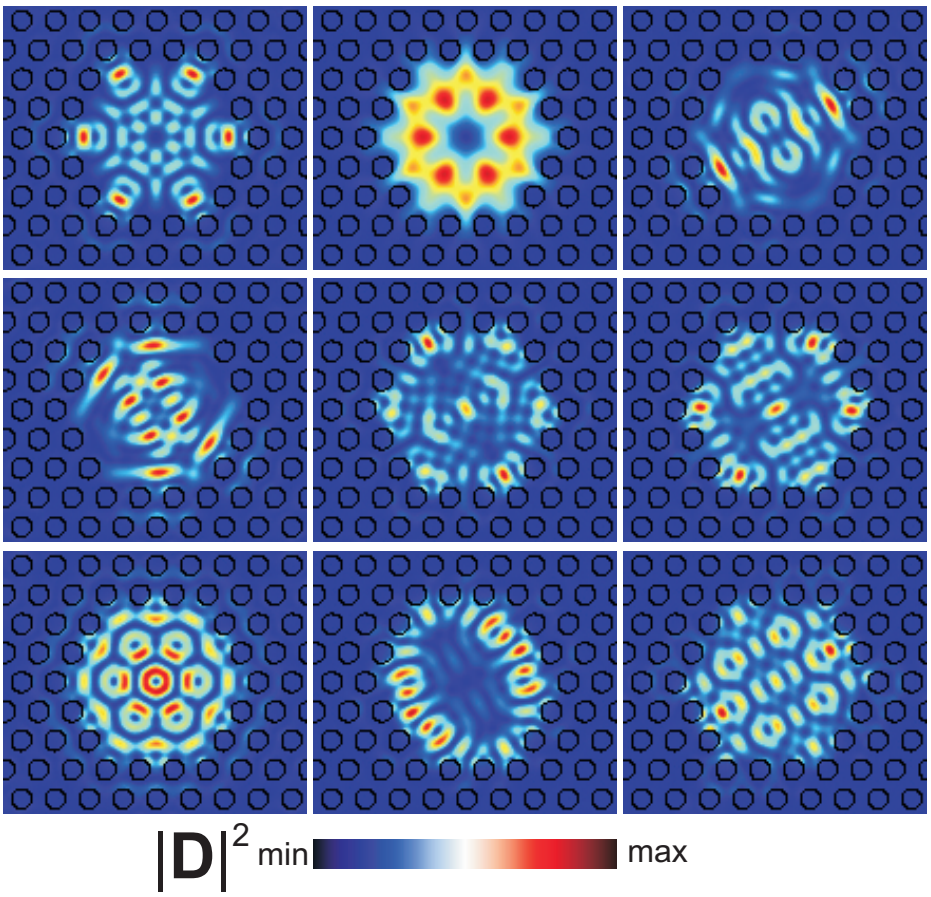

Figure 8.2.: Selection of the electric displacements of several cavity modes of an H3 cavity.

a H3 cavity. The lattice constant is a≈300 nm and r/a ratio is 0.3. The spectra are summarized in the waterfall plot in figure 8.4. In figure 8.4 (a), we present the temperature dependence of the as-grown $Si_{0.7}Ge_{0.3}$ islands. In figure 8.4 (b), we present the temperature dependence of the $Si_{0.7}Ge_{0.3}$ islands in a H3 cavity. Both spectra reveal the presence of a no-phonon and a transversal optical phonon transition as described in section 6.2. The luminescence intensity vanishes with increasing temperature like in chapter 6.2.2. Without photonic effects it vanishes at T≈ 220 K. Within the photonic band gap the luminescence is strongly enhanced and in resonance with the cavity modes several Lorentzian shaped peaks are observed the most prominent at 0.922 eV, 0.935 eV, 0.958 eV, 0.967 eV, 0.974 eV, 0.985 eV and 1.01 eV. Moreover the emission can be observed up to room temperature with a peak intensity of one photon per second.
The enhancement in resonance with the cavity modes is caused by an enhancement of the photonic density of states and maybe due to Purcell effect [Hau12] which is a shortening of the exciton lifetime [Fox06]. The maximum enhancement in resonance with a

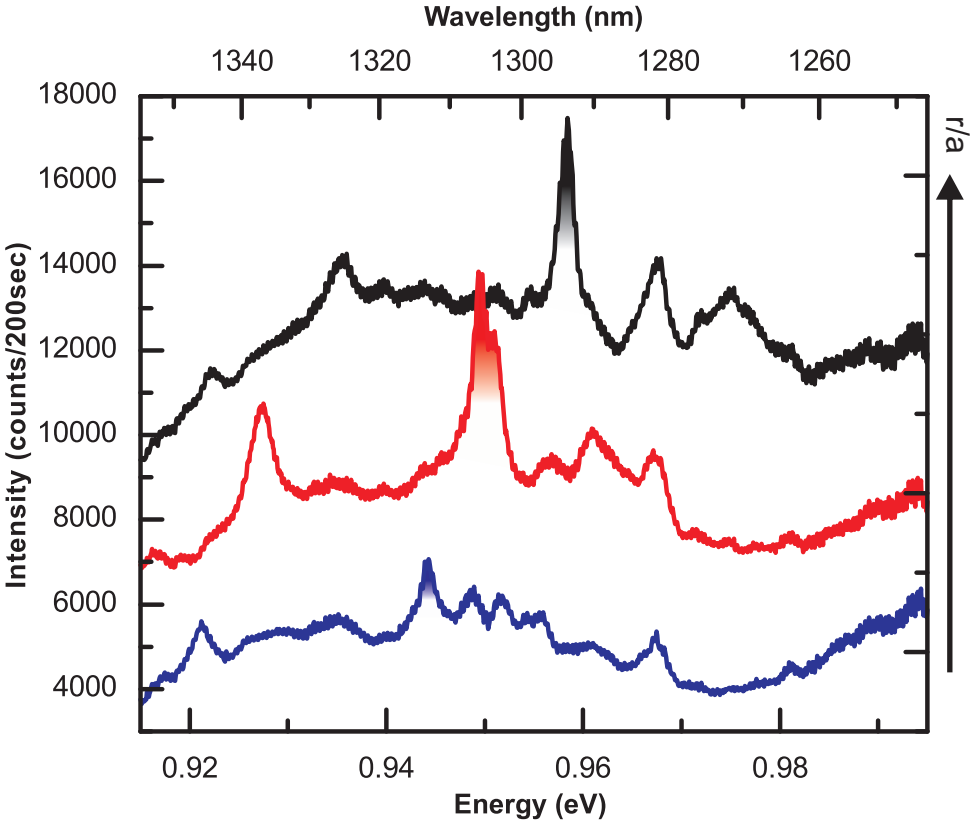

Figure 8.3.: Low temperature micro-photoluminescence spectra of $Si_{0.7}Ge_{0.3}$ islands coupled to three different H3 cavities with increasing r/a ratio from bottom to top.

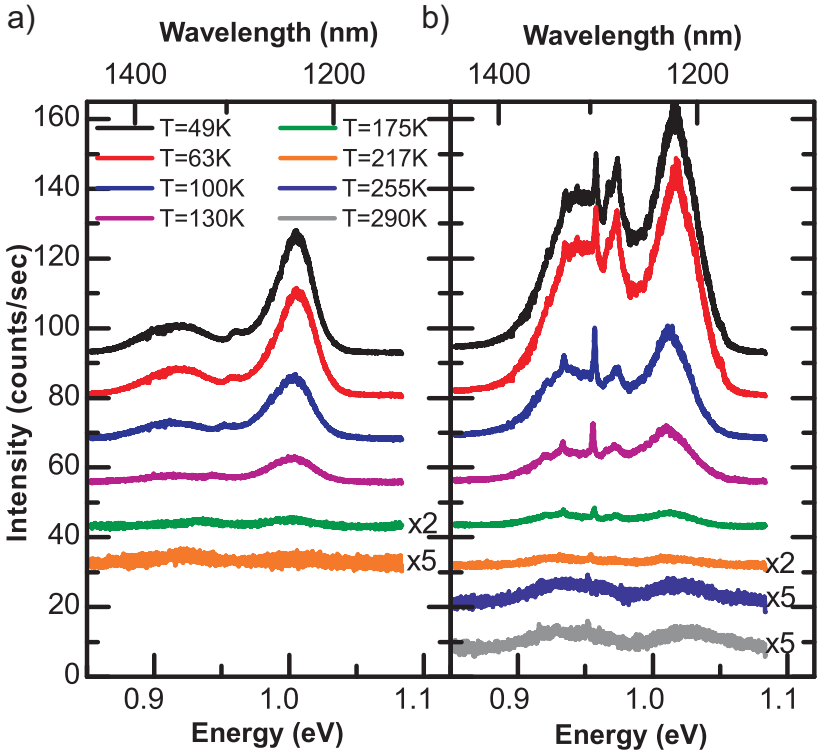

Figure 8.4.: Waterfall plot of a series of temperature dependent micro-photoluminescence experiments on (a) $Si_{0.7}Ge_{0.3}$ islands and on (b) $Si_{0.7}Ge_{0.3}$ islands embedded in a 2D photonic crystal with an H3 cavity.

cavity mode is twelve. The overall enhancement factor for the $Si_{0.7}Ge_{0.3}$ island luminescence intensity in a photonic band gap is approximately six to ten between 0.85 eV and 1.04 eV. This enhancement is a result of the redistribution of the light emission inside the photonic band gap. This is not an enhancement of the radiative recombination rate, in fact it is only a redistribution of the emitted light which enhances the collection efficiency. The possibility to detect room temperature luminescence without photonic enhancement effect is a very interesting result. It allows to deduce that the temperature independent optical recombination rate η_{rad} of the $Si_{0.7}Ge_{0.3}$ islands is large enough to compete with the temperature dependent non-radiative recombination rate $\eta_{non-rad}$(T) up to room temperature. Only the isotropic emission profile of the islands and reflection at the silicon-air interface prevent the detection of emitted photons at room temperature.

This argument is further strengthened by the quantified analysis of the activation energies according to equation 6.4. Table 8.1 summarizes the resulting activation energies for the no-phonon luminescence centered at 1.00 eV and the TO-phonon assisted recombination centered at 0.915 eV. In addition the activation energy of the cavity mode at 0.958 eV is included. Within the error there is no significant change of the activation

	$E_{A-low-energetic}$ (meV)	$E_{A-high-energetic}$ (meV)	$E_{A-cavity}$ (meV)
as-grown	25.8±7.2	38.7±12.8	
photonic crystal	21.5±6.1	21.2±6.3	67.0±13.8

Table 8.1.: Activation energy of $Si_{0.7}Ge_{0.3}$ islands in and out of a photonic band gap and of $Si_{0.7}Ge_{0.3}$ coupled to a photonic crystal H3

energy inside and outside of a photonic band gap. This is reasonable as only the collection efficiency is enhanced. The activation energy is at least three times enhanced in resonance with the cavity indicating enhanced recombination properties. Here effects like an enhanced photonic density of states and maybe a Purcell effect [Fox06] result in a higher temperature stability.

8.3. $Si_{0.7}Ge_{0.3}$ islands as room temperature light emitter

In this chapter, we have successfully shown room temperature near infrared photoluminescence using the strongly enhanced luminescence of type I $Si_{0.7}Ge_{0.3}$ islands coupled to two dimensional silicon photonic crystals. At low temperatures, we have shown an enhancement of approximately six to twelve when measuring on the patterned structure compared to unpatterned islands. Even up to room temperature this enhancement is observed which results in an intensity of approximately one photon per second over a broad energy range. The experiments allow us to conclude that the radiative recombination rate of the $Si_{0.7}Ge_{0.3}$ islands is large enough to compete with the temperature dependent non-radiative recombination rate up to room temperature.

9. Ge island light emitting diodes

The possibility for room temperature luminescence in resonance with a photonic crystal is a promising result for future device applications. However, most devices require electrical current injection and, thus, diode structures are necessary. Electroluminescence from Ge islands has previously been investigated by Apetz *et al* and other groups [Ape95, Bru00] as a function of the injected current and temperature. Moreover, room temperature electroluminescence from many stacks of islands has been observed in 2003 by Talalaev *et al* [Tal03]. For our goal of an electrically contacted photonic crystal diode with embedded Ge islands we will now first present a systematic electro-optical characterization of the emitter properties of molecular beam epitaxy Ge islands fabricated on vertical SOI P - I - N diodes. We will investigate the temperature stability and the dependence of the luminescence intensity on the injection current.

9.1. Light emitting diode design

For electric charge carrier injection a P-I-N diode profile with highly doped p and n regions is chosen to achieve good ohmic contacts and a high density of charge carriers. The doping profile is sketched in figure 9.1. We have chosen Ge islands (see chapter 4) as emitter morphology because of their lower emission energy compared to Ge hut clusters which also allows for detection using an InGaAs CCD at our micro-photoluminescence setup. The diode is fabricated according to the procedure in the appendix E.2 on top of a SOI wafer with a buried oxide thickness of 3 μm and a thinned (see appendix C) device layer of 50 nm thickness. The boron doped p-layer has a nominal acceptor density of $5{\cdot}10^{18}$ cm^{-3}. The p-layer is deposited at $\approx$ 330-340°C. The Ge islands are embedded in a 40 nm thick intrinsic layer. The growth temperature for the Ge islands is 430°C at a thickness of nominally six monolayers. For this growth temperature which is comparable to that in chapter 4, we expect a bimodal distribution of pyramids and domes. Finally the sample is capped using 115 nm of phosphorous doped silicon with a donor density of $5{\cdot}10^{18}$ cm^{-3} at a growth temperature of 400-330°C. For this growth temperatures no diffusion of dopants into the germanium islands is expected [Nüt95].
The doping results in a significant change of the band structure properties. In figure 9.2, we present one dimensional band structure calculations of the diode design from figure 9.1. The gray shaded region is the intrinsic device layer. The blue region marks the p-doped region. The orange region indicates the n-doped silicon. In white the intrinsic region with the Ge islands is depicted. The simulation reveals a big drawback of the device design as the p-doped region is sandwiched between two intrinsic regions. Thus, injected charge carriers can diffuse to the intrinsic region at the back side, where they recombine at the silicon dioxide interface. However, this cannot be circumvented as no

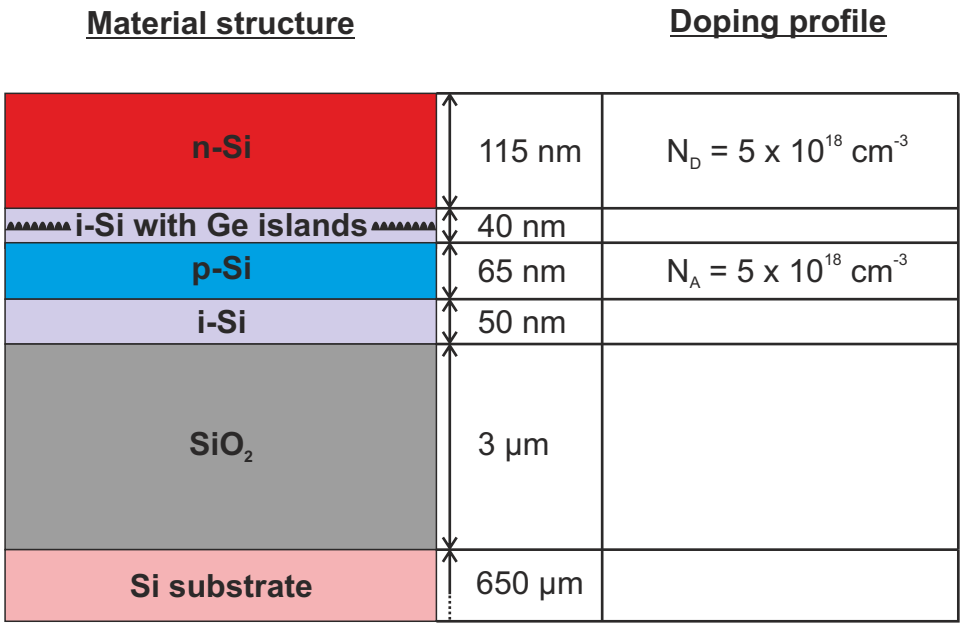

Figure 9.1.: Layer structure and doping profile of a P-I-N diode with embedded Ge islands. Taken from [Gei11].

doped SOI wafers are available from our suppliers. The band structure yields a type II confinement for holes. This is in analogy to section 2.7 and section 3.2. The Fermi energy crosses the heavy hole band at the position of the Ge islands. This agrees nicely with the calculation of the electron and hole densities in figure 9.2 (b). Holes have a six times higher density in the Ge islands ($7.8 \cdot 10^{18}\mathrm{cm}^{-3}$) than in the p-doped contact region ($1.4 \cdot 10^{18}\mathrm{cm}^{-3}$). Electrons are only located in the n-doped region with a density of $2.4 \cdot 10^{18}\mathrm{cm}^{-3}$.
To verify the diode behavior of the sample, we determine the current voltage characteristic (Figure 9.3) at room temperature and at 10 K in semi-logarithmic scale. The diode characteristic is measured in the dark to prevent the excitation of photocarriers. The data are corrected for the contact series resistance. This we determine at the limit of a high voltage where a linear slope in the current voltage characteristic is observed. As $R = R_{diode} + R_{contact}$ and as the resistance of the diode approaches zero for large voltages we can extract the contact resistance from the linear slope. The series resistance is $\approx 200\ \Omega$ at room temperature and $\approx 740\ \Omega$ at 9 K, respectively. We find a clear rectifying behavior which proves the existence of a diode. The leakage current at -1 V is j=0.53 A/cm^2. At +1 V it is j=1.56 A/cm^2. Furthermore, we find that the conductivity of the diode is reduced by one order of magnitude from 300 K to 9 K caused by a

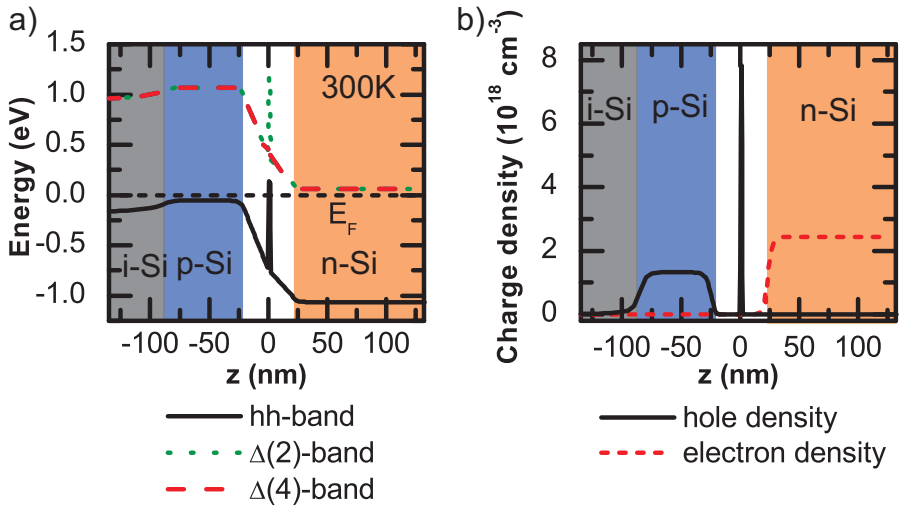

Figure 9.2.: (a) Band structure of a P-I-N diode in one dimension calculated with nextnano++ at 300 K in growth direction. The black solid line indicates the heavy hole band. The green doted line is the $\Delta(2)$ band and the red dashed line is the $\Delta(4)$ band. The Fermi energy is included as black dashed line. (b) Charge carrier density of electrons (red dashed line) and holes (black solid line).

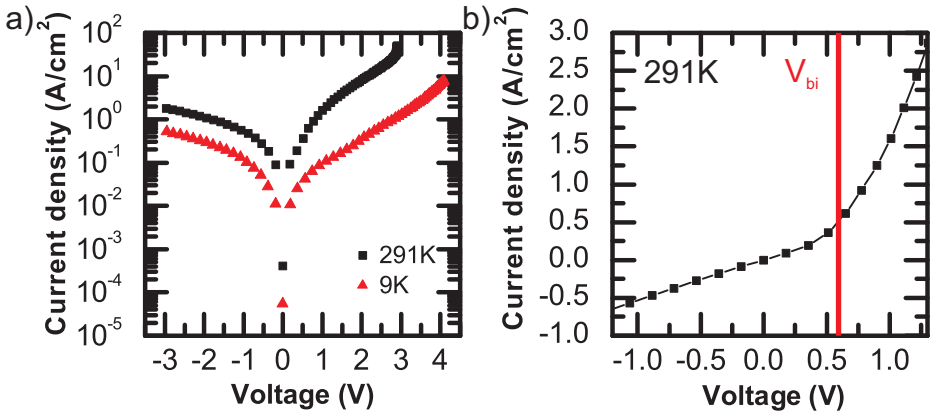

Figure 9.3.: (a) Corrected current voltage characteristic of a P-I-N diode in the dark at 9 K and 291 K. (b) Room temperature diode characteristic from -1 V to 1 V. The onset of the exponential increase is determined as built-in voltage V_{bi}.

reduction of the ionized dopants [Sze81].
Figure 9.3 (b) shows a zoom on the room temperature diode characteristic from -1 V to 1 V. At roughly V_{bi} ≈0.6 eV efficient charge transport across the P-I-N structure occurs. This is the voltage at which flat band condition is reached. From our simulations, in figure 9.2 we obtain a built-in field of V_{bi}=1.01 eV. The low experimentally determined built-in field is an indication for a lower effective doping concentration which can occur due to diffusion and/or interstitial lattice sites [Sze81].

9.2. Electro-optical properties of Ge islands in P-I-N diodes

When applying a forward bias at the diode junction the built-in voltage reduces and minority carriers are injected into the space charge region [Sze81]. Holes then occupy the energy states in the germanium islands where they are efficiently trapped. These trapped holes can spontaneously recombine with injected electrons resulting in light emission. This effect we detect using an electroluminescence setup described in the appendix B.4.1.

9.2.1. Temperature dependent electroluminescence

Electroluminescence measurements are performed as a function of the temperature for a net current density of j=0.5 Acm^{-2}. Due to the temperature dependence of the diode conductivity the applied voltage varied from 2.7 V to 3.4 V. Figure 9.4 shows a waterfall plot of the resulting spectra. From top to bottom the temperature is increased from 9 K to 105 K.
No signal from the Si substrate is detected which is reasonable as Ge islands are placed directly in the space charge region, where the radiative recombination takes places. Due to the strong hole confinement there are no holes available inside the Si matrix.
Three peaks are observed at energies of ≈ 0.86 eV, ≈ 0.92 eV and ≈ 0.98 eV. With increasing temperature all peaks exhibit a clear redshift and a reduction of the intensity. Here the two higher energetic peaks vanish faster than the lower energetic peak. At 50 K they are only visible as small shoulders in the spectrum.
The fact that the higher energetic peaks vanish faster than the lower energetic peak is an indication for a weaker confinement. In addition, the peaks are separated by roughly 50 meV. This energy resembles the energy of a SiGe-TO phonon in a SiGe lattice [Dea67]. Thus, we attribute the two higher energetic peaks to a no-phonon and a transversal optical phonon assisted recombination in the wetting layer [Wan01a, Wan01b]. This argument is further strengthened as the full width at half maximum (FWHM) of the lowest energetic peak is 65 meV, whereas the FWHM of the higher energetic peaks are ≈ 40 meV and ≈ 30 meV, respectively. Due to the island size variation, a larger FWHM than for a flat wetting layer is expected [Leo95, Sei96].
This allocation is also reasonable as the sample consists of only six monolayers of nominally pure Ge. Previously, the existence of a wetting layer at such deposition thicknesses

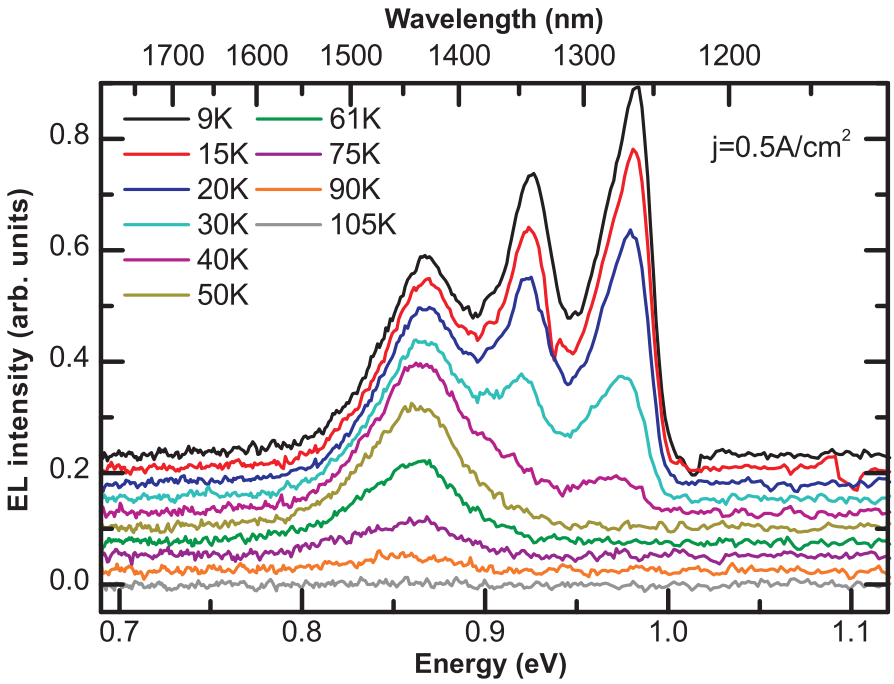

Figure 9.4.: Waterfall plot of temperature dependent electroluminescence spectroscopy with a net current density of 0.5 Acm^{-2}

Transition	E_a (meV)	α (eV/K)	β (K)
Ge islands	3	$3.48 \cdot 10^{-4}$	71.37
wetting layer TO	1	$4.00 \cdot 10^{-4}$	59.74
wetting layer NP	0.8	$1.00 \cdot 10^{-3}$	98.23

Table 9.1.: Quantitative activation energy and fitting parameters for the integrated intensity and the peak energy of figure 9.4.

has been observed [Mie01].
We quantitatively analyze the peak energy and the integrated intensity by fitting all three peaks with a Gaussian lineshape. From an Arrhenius analysis and equation 6.4 we then deduce the activation energies and list them in table 9.1. We also list the Varshni parameters, which we use to fit the peak energies according to equation 3.3. The activation energy of the islands is of the order of 3 meV. This is similar to the results in section 3.3. The wetting layer luminescence has a three times lower activation energy caused by a reduced dimensionality of the confinement. Thus, the intensity vanishes faster than that of the islands.
In addition, the Varshni parameters are comparable to those in table 3.3. Again different slopes occur for the transversal optical and the no-phonon transitions which is consistent

with our results in section 3.3.

9.2.2. Current density dependent electroluminescence

At a constant temperature of 10 K and 40 K we now vary the amount of injected current. This directly changes the applied voltage and, thus, the band bending. We vary the current density from 0.05 Acm^{-2} to 5 Acm^{-2} corresponding to a voltage across the diode between U≈1.7 V and U≈4.0 V at 10 K and from U≈1.3 V to U≈4.7 V at 40 K. In figure 9.5, we present two waterfall plots of electroluminescence spectroscopy measurements at 10 K and 40 K for varying current injection.
From top to bottom the current density is decreasing. Three peaks are observed at 0.86 eV, 0.92 eV and 0.97 eV. According to our results in the previous section we attribute the lower energetic peak to the island luminescence. The higher energetic peaks stem from a transversal optical phonon assisted recombination and a no-phonon recombination in the wetting layer. Due to the higher temperature, the luminescence signal is lower at 40 K for all investigated current densities as non-radiative recombinations have a higher probability.
Moreover, the peaks show a clear blueshift for low current injections. At 10 K the islands reveal a blueshift of 4.5 meV from 0.075-0.5 Acm^{-2}. The transversal optical phonon assisted and the no-phonon recombination yield a blueshift of 6 meV and 11 meV, respectively. This is attributed to state filling effects [Bou01] and charge carrier induced band bending [Bai94].
At a current density higher than 0.5 Acm^{-2} no further blueshift occurs. Thus, we expect all islands to be fully occupied. At high current densities above 2.5 Acm^{-2} corresponding to a voltage drop of U≈3.5 V the peaks stemming from the wetting layer merge and are no longer distinguishable.
Figure 9.6 illustrates the integrated intensity of the island and wetting layer luminescence in a double-logarithmic plot as a function of the current density for a temperature of 10 K. According to Chang *et al*, the relationship of the integrated intensity I and the current density is described by $I \propto j^m$ [Cha03b]. The exponent m then yields information about the recombination mechanism. For the island luminescence, we obtain a slope of m=1.67±0.20 and for the wetting layer emission slopes of m≈ 2 for current densities up to 0.2 Acm^{-2}. For larger current densities the slope is roughly 0.67 for all transitions. At even higher current densities above 3 Acm^{-2} the island slope reduces to m≈ 0.19±0.09. At high current densities there is a competition between Auger recombination with a rate of $\Gamma_{Auger} \propto n^3$ and the radiative recombination with a rate of $\Gamma_{rad} \propto n^2$, where n is the hole or electron density [Häc94]. In the rate equation 2.11, this results in an exponent of 0.67 which nicely agrees with the experimental obtained exponent of 0.66-0.73 occurring for current densities between 0.25 Acm^{-2} and 3 Acm^{-2} indicating the presence of Auger recombination. Above 3 Acm^{-2} the loss rate equals the radiative rate and, therefore, the integrated intensity saturates.

The superlinear slope (m ≈ 2) of the integrated intensity for low current densities has been reported for SiGe quantum wells by Apetz *et al* [Ape95]. For Ge islands a linear dependence has been observed by Chang *et al* [Cha03a]. In contrast, for GaAs quantum

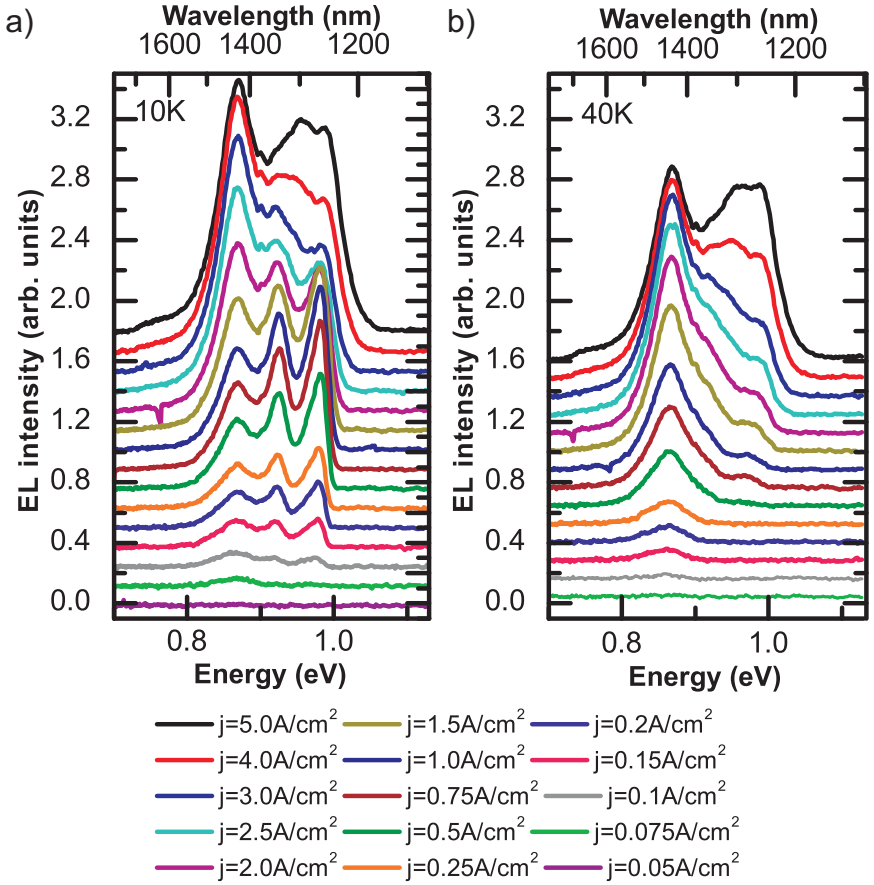

Figure 9.5.: Current dependent electroluminescence spectroscopy waterfall plot at 10 K and 40 K.

dots an exponent of one is observed for the excitonic emission and an exponent of two for the biexcitonic transition [Mat03].
A superlinear exponent of two is referred to the recombination from bound excitons which form from free electrons and holes [Coo90, Sch92]. Under the condition of optical excitation this cannot be observed in the GaAs system as the relaxation processes, which lead to the formation of excitons are in the ps timescale. Thus, in GaAs quantum dots the excitonic recombination rate is independent of the population density. In the SiGe system the type II band alignment prevents the direct formation of excitons. Holes which are injected from the contacts are efficiently trapped in the islands. This gives rise to a band bending, which depends on the amount of the confined holes. The band bending then results in the accumulation of electrons. The following formation of bound excitons then depends on the population density of electrons which are attracted by the band bending and holes which induce this band bending. In summary, this results in a quadratic increase of the recombination rate with the pumping power. A deviation

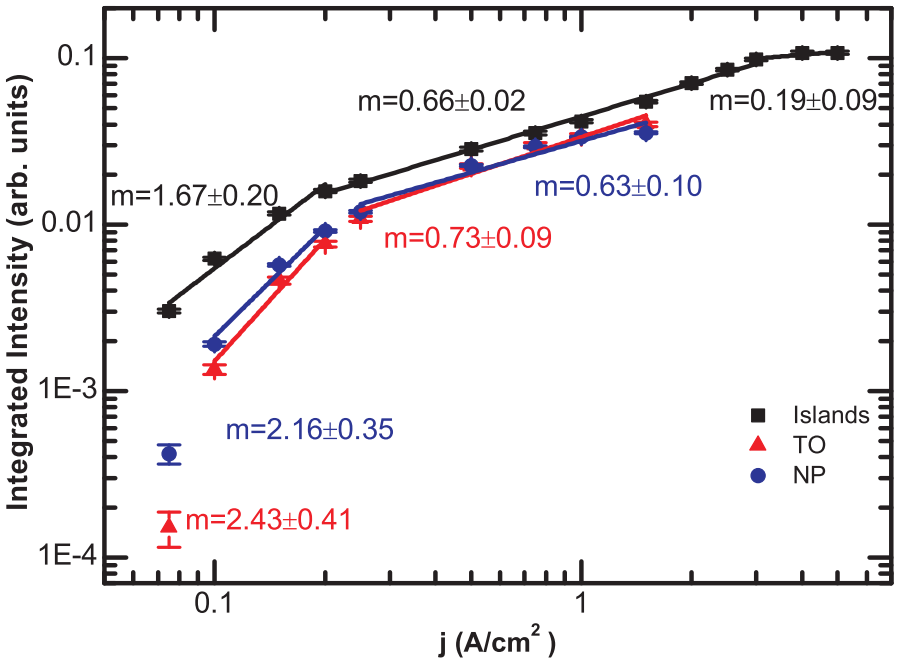

Figure 9.6.: Double-logarithmic plot of the integrated intensity over the current density at 10 K. Linear fits are included to extract the slope and to deduce the presence of Auger recombination.

towards lower values might indicate that some charge carriers recombine before forming excitons. We think that the good agreement between the experimental exponent and the theoretical expected value of two is a direct measure for the high crystal quality. A quantified analysis at 40 K reveals the same behavior as at 10 K.
In the next step we want to compare the efficiency of electroluminescence and photoluminescence. Using the Beer-Lambert law

$$I = I_0 e^{-\alpha x} \tag{9.1}$$

for absorption of light, where I is the absorbed power and I_0 the incident power, and an absorption coefficient of α=6.68·10^3 cm^{-1} [Vir11] for a wavelength of 532 nm, we can estimate the amount of charge carriers created by photoluminescence. Assuming an incident power of 3 mW, a reflectivity of 37% [Vir11] and a slab height of 270 nm $\approx$ 0.19 mW are absorbed inside the Si slab. Here back-scattering at the silicon-silicon dioxide interface is neglected. We can calculate the amount of excited charge carrier per second by assuming that each photon creates only one charge carrier. We normalize this to the area of the excitation spot ($\approx$100 μm) and receive a lower limit for the charge density of $n_{PL} = 1.18 \cdot 10^{19}$ s^{-1}cm^{-2}. This corresponds to an electrical current injection of $\approx$ 1.89 Acm^{-2}.
From figure 9.5, we deduce an intensity of $\approx$ 1 arb. unit at this current density. For a similar undoped sample (see figure 4.1 430°C) an intensity of 0.12 arb. unit was observed

using optical excitation. Although there might be some uncertainties due to excitation alignment and a different sample design with a mesa structure for electroluminescence, we qualitatively conclude that electrical injection is more efficient than optical excitation. The higher efficiency for electrical charge injection is based on five mechanism. First of all hot charge carriers are injected rather than an excitation far above the band gap. Therefore, no thermalization process occurs. Such a process can locally heat the sample and, thus, enhance the probability for non-radiative recombination.
Moreover, in photoluminescence charge carriers created in the Si matrix have to diffuse towards the islands whereas in electroluminescence the drift velocity induced by the external electric field pulls the charge carriers through the space charge layer, where the islands reside.
This also yields a reduced amount of charge carriers, which recombine in the Si-matrix rather than in the islands explaining the absence of any phonon assisted recombination stemming from the Si substrate in electroluminescence.
Furthermore, the band bending, which is shown in figure 9.2 yields the formation of a triangular potential for electrons in the vicinity of the islands. Thus, electrons might be trapped in one dimension resulting in a reduction of non-radiative recombination.
Finally, the band bending results in a shift of the hole probability density towards the vicinity of the island. This increases the electron-hole wave function overlap and results in a larger radiative recombination rate.

9.3. Summary and conclusion

In conclusion, we have successfully shown the fabrication of P-I-N diodes with embedded Ge islands. Using Ge islands samples where only 6 ML of material are deposited we find luminescence stemming from the islands and from a wetting layer. But no luminescence from the Si substrate has been observed. This shows that the Ge islands efficiently trap injected holes in the space charge region.
Furthermore,we deduce that electrical current injection is at least eight times more efficient than optical excitation. This is done via a comparison of the luminescence intensity of optical excitation and electrical current injection. At the same time we find no difference in the temperature stability of different excitation methods. However, the spectroscopy intensity is still very weak because of the low photon collection efficiency.

10. Two dimensional photonic crystal light emitting diodes with embedded Ge islands

The final device idea, which we aim for in this chapter, is a Ge island P-I-N diode patterned with a two dimensional photonic crystal resonator for collection efficiency and cavity enhancement. Up to now such devices have been shown on GaAs substrate with single InGaAs quantum dots as active emitters for an electrical tunable single photon source [Lau09]. Light emitting diodes with photonic crystals have been shown in different material systems like PbSe in silicon [Heo10] and GaN/InGaN [Kim07, Kim05]. Also the implementation of organics in SiO_2/SiN_x two dimensional light emitting photonic crystal diodes has been shown [Do03]. But up to date no such experiments have been performed on the SiGe system.

10.1. Electrical characterization of photonic crystal diodes

A new sample has been prepared at a growth temperature of $\approx 470°C$ within the island layer. From previous growth studies (see chapter 4) we can deduce that such a growth temperature results in a bimodal distribution of pyramids and domes. Using the procedure from the appendix E.3 we fabricated a diode patterned with a photonic crystal.
Figure 10.1 (a) shows the diode mesa with several photonic crystals of different r/a ratios. The r/a ratio is varied by changing the e-beam dose. The mesa size is smaller (300 μm x 400 μm) than in the previous section to increase the current density. A zoom in on one photonic crystal is shown in 10.1 (b). The photonic crystal consists of a triangular pattern of air holes in the silicon slab. In the middle three holes in a row are omitted to form an L3 cavity. Furthermore, the two neighboring holes along the cavity are shifted outwards by 0.15a to optimize the quality factor [Aka03].
In figure 10.1 (c) we present the diode characteristic before (black squares) and after (red circles) the patterning process at 300 K and after the patterning process at 10 K (blue triangles). A nice rectifying behavior is observed with a leakage current of $3{\cdot}10^{-1}$ mAcm^{-2} at 1 V for the unpatterned and 1 mAcm^{-2} for the patterned diode. In addition the forward biased current decreases by a factor of four. Here the new area due to the removal of the air holes is considered. The degradation of both the leakage current and of the forward biased current is attributed to the fabrication process where the reactive ion etching process creates surface defects within the air hole surface [Ben92]. The rectifying behavior however proves the presence of a diode which can be used for optoelectronic investigations.

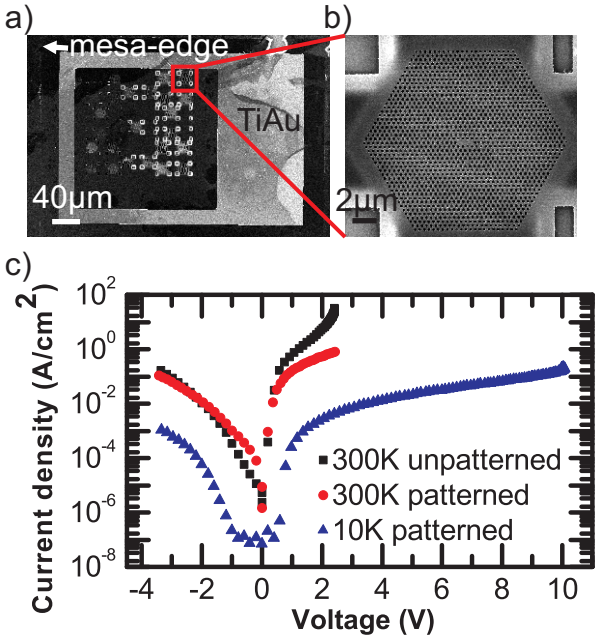

Figure 10.1.: (a) Diode mesa with TiAu front contact and several photonic crystals of different r/a ratio. (b) Zoom in on the photonic crystal investigated in figure 10.2. The r/a ratio is 0.33, the lattice constant is a=380 nm. In the middle, an L3 cavity is observed where three holes in a row are omitted. (c) Corrected diode characteristic for the here fabricated sample before and after the patterning process at 300 K and at 10 K.

10.2. Micro-electroluminescence of two dimension photonic crystals with embedded Ge islands

To investigate the influence of one photonic crystal, we perform micro-electroluminescence and micro-photoluminescence spectroscopy measurements on a photonic crystal with a lattice constant of a=380 nm and an r/a ratio of 0.33. From theoretical plane wave expansion calculation we deduce that the six cavity modes should be located at 0.856 eV, 0.901 eV, 0.937 eV, 0.944 eV, 0,952 eV and 0.982 eV. In figure 10.2, the experimental results of the electroluminescence and photoluminescence are plotted in figure 10.2. The black line shows the micro-photoluminescence spectrum measured on the cavity position at 14 K with an excitation power of 1 mW. The red line shows the micro-electroluminescence spectrum measured at the cavity position with a current injection of 2.1 Acm^{-2}. The blue line is the micro-electroluminescence spectrum measured on the unpatterned region.
Photoluminescence spectroscopy yields the presence of six cavity modes which are shifted to the blue by approximately 20 meV compared to the theoretical predictions indicated by vertical green lines. This shift can be explained by fabrication uncertainties like a

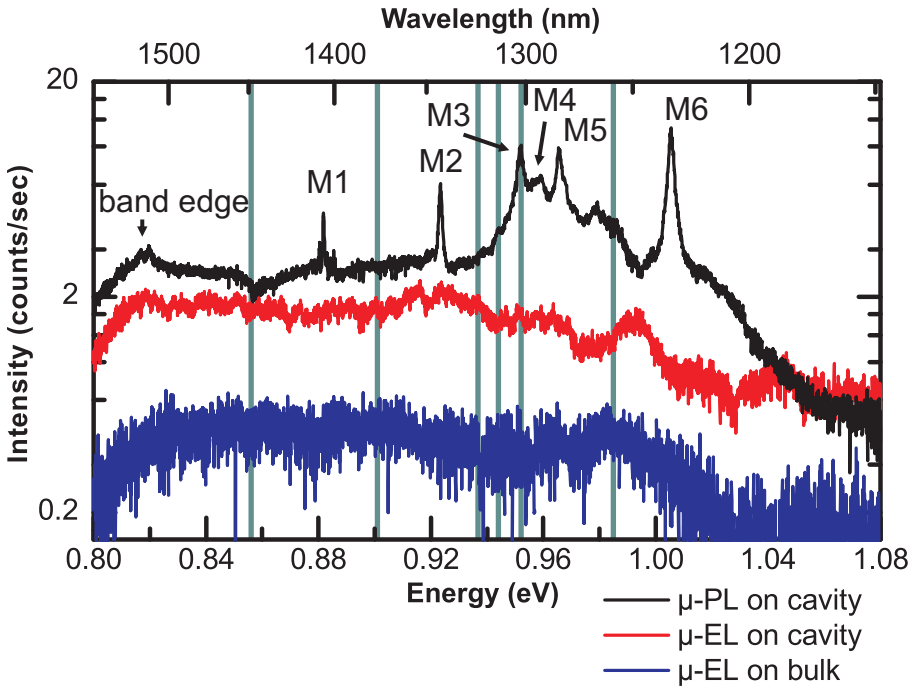

Figure 10.2.: Micro-photoluminescence and micro-electroluminescence spectra of a photonic crystal P-I-N diode with a lattice constant of 380 nm and an r/a ratio of 0.33. The embedded islands are pumped with 2.1 Acm^{-2} (EL) or 1 mW (PL). The temperature is 14 K. The photoluminescence spectra is taken on the cavity (black). The electroluminescence spectra is taken besides the patterned region (blue) and on the cavity (red). Vertical green lines mark the theoretical position of the cavity modes.

varying hole size or a non-cylindrical hole shape. The micro-electroluminescence measured besides the photonic crystal yields the presence of island luminescence from 0.8 eV to 1.05 eV with an intensity of less than 0.5 counts per second.
This signal is strongly enhanced by a factor of at least three when detecting on the photonic crystal region shown in red. Both the electroluminescence and the photoluminescence demonstrate the presence of a band edge mode at ≈ 0.82 eV which proves the existence of a photonic band gap in the measurement region [Yab91].
The strong enhancement when detecting on the photonic crystal region is due to a redistribution of the light emission resulting in an enhancement of the collection efficiency. However, in contrast to the photoluminescence experiments no cavity modes are observed which is quite astonishing as indeed photonic effects are present indicated by the band edge mode and the luminescence enhancement.
Looking at the differences in the measurement principle, it is possible to explain the absence of cavity modes in the electroluminescence. When exciting with a laser, charge

carriers are only excited in the cavity region and, therefore, recombination hardly occurs outside the cavity region as charge carrier diffusion is limited due to the surface states at the air hole surface. Thus, light is emitted very locally. In electroluminescence charge carriers are injected into the space charge region over the whole area. Therefore, light is emitted from every island in the diode at the same time. Furthermore, the detection spot size is approximately 12 μm which is much larger than the cavity size. Therefore, much more light from the photonic crystal region is detected in electroluminescence than in photoluminescence. Thus, it is possible that in electroluminescence the integrated intensity from the photonic crystal region is more intense than the locally excited intensity from the photonic crystal mode. Moreover, the etched air holes create an additional axis resistance into the electrical system. Therefore, it is likely that charge carriers injected into the diode cannot reach the cavity region. This assumption is supported by the presence of the band edge mode indicating the presence of photonic effects.
The high axis resistance favors other cavity designs like the A1 cavity [Kra96] or simple W1 waveguides [Lon00]. Such designs would allow for electrical access to the cavity along the waveguide. The missing cavity of the latter waveguide design is compensated by an emission from fabrication uncertainties [Top07].
First indication for cavity mode enhancement in micro-electroluminescence we achieved with an L3 cavity in a p^+nn^+ diode where the intrinsic and n doped layers in figure 9.1 are replaced by 20 nm of n doped ($N_A = 2 \cdot 10^{17}$ cm^{-3}), 115 nm of $N_A = 5 \cdot 10^{17}$ cm^{-3} and 20 nm of $N_A = 5 \cdot 10^{18}$ cm^{-3} doped silicon. The Ge islands are still exactly at the middle of the silicon slab. Furthermore, the diode was further scaled down to a mesa size of 200 x 150 μm^2 for even higher charge densities. In figure 10.3, we show the micro-electroluminescence and micro-photoluminescence spectra when pumping with an electrical current density of 8.3 Acm^{-2} (black curve) or an optical excitation power of 4 mW (red curve).
The photoluminescence spectra shows two modes at $\approx$ 0.93 eV and $\approx$ 1.00 eV. From simulations we deduce that these are modes M4 and M5 of the L3 cavity. The electroluminescence spectrum is very noisy due to a low signal of only 0.3 counts per second. We observe a clear peak at $\approx$ 1.00 eV which fits very nicely to the mode emission obtained in micro-photoluminescence. We fit both peaks using a Lorentzian line shape and extract a quality factor of 66 for the photoluminescence experiment and 89 for the electroluminescence experiment. These two quality factors are in very good agreement with each other.
Hence, we deduce that this result is a first strong indication for mode enhancement from Ge islands coupled to an electrically contacted two-dimensional photonic crystal cavity. This is a major step towards an efficient silicon-germanium based light source.

10.3. Conclusions about SiGe based device applications

In chapter 8 we have shown that photonic crystals strongly enhance the extraction efficiency of $Si_{0.7}Ge_{0.3}$ islands in vertical direction. With the enhanced collection efficiency we find that even without any photonic effects the radiative recombination rate can com-

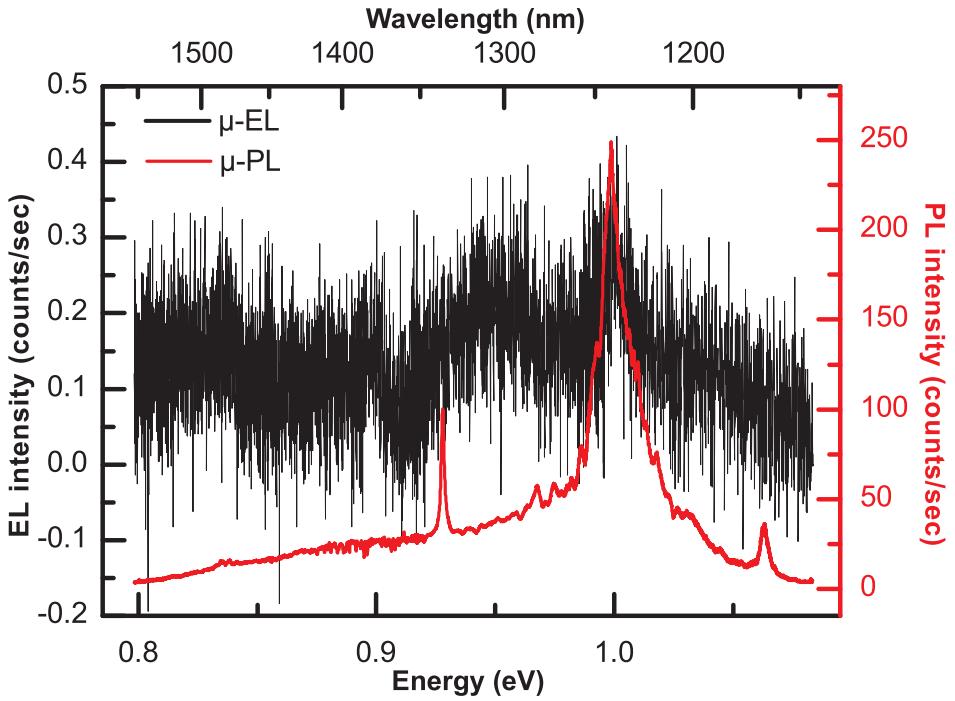

Figure 10.3.: Micro-electroluminescence (black curve) and micro-photoluminescence (red curve) measured at 14 K with an electrical current density injection of 8.3 Acm^{-2} and an optical excitation power of 4 mW.

pete with the non-radiative recombination rate up to room temperature. Without any photonic crystal the refractive index induced vertical confinement results in degradation of the collection efficiency.
Furthermore, we have shown that electrical current injection in P-I-N diodes with Ge based emitters offers the possibility for a higher current to photon conversion efficiency compared to optical excitation. But a combination of both effects, photonic crystals and electrical current injection, requires further experiments as the axis resistance of the photonic crystal air holes prevents a good electrical access to the islands.
We think that on-chip applications, where the light is guided in in-plane waveguides seem to be the most promising path for future applications. Here the low extraction efficiency is circumvented by the waveguiding effect. Moreover waveguides can allow for an efficient charge transport to the islands.

11. Summary and conclusion

Within this thesis we have investigated the radiative recombination properties of various (Si)Ge based three dimensional confinement structures as well as their coupling with two-dimensional photonic crystals. In addition, we embedded Ge islands into P-I-N diode structures to evaluate the effect of electrical current injection.
(Si)Ge islands, which form by means of a 4.2% lattice mismatch between Si and Ge, have been comprehensively studied within the last 20 years. However, until beginning of this thesis there has been no systematic investigation of the dominating parameters influencing the radiative recombination properties and of the recombination properties themselves. To fill this gap and to asses the potential of various (Si)Ge based light emitters we, in the first part of this thesis, have presented a systematic epitaxial study in different kinetic and thermodynamic regimes. In combination with a comparative study of realistic band structure simulations and photoluminescence spectroscopy we have evaluated both the real space and the k-space recombination properties of various quantum dot and island morphologies. In summary, there is a strong correlation between the island dimensions and the alloy composition via the lattice mismatch between Si substrate and SiGe alloy. Both parameters dominate the radiative recombination properties but with a competing influence.
Qualitatively we experimentally and theoretically have found that a low Ge content and a small quantum dot size is required for a large spatial electron-hole wave function overlap. Furthermore, very small sizes are required for a quasi-direct recombination in k-space.
To achieve a very small size we employed very low growth temperatures between $\approx$ 300-400°C resulting in limited surface kinetics for the adatoms with a small surface diffusion length. This leads to the formation of Ge hut clusters. This quantum dot morphology sustains a no-phonon transition from an electron in the $\Delta(4)$-valley with a heavy hole indicating that the hole wave function spreading is large enough to prevent a possible three particle process with assistance of a phonon.
However, the low growth temperature also inevitably limits the intermixing of the hut clusters with Si and, thus, nominally pure Ge hut clusters always have a high Ge content. The small size and the high Ge content now provide a spatial type II band alignment where electron and hole are spatially separated. This results in a very weak electron-hole wave function overlap which we quantitatively calculate to a value of 3.7%. This is approximately 20 times lower than for III-V quantum dots resulting in a 400 times longer radiative recombination time. This is consistent with published values of the radiative recombination time where a difference of approximately 1000 is observed.
For a higher electron-hole wave function overlap a lower Ge content is required. An easy approach to achieve this is an increasing growth temperature. Enhanced thermodynam-

ics now increase both the surface diffusion length of adatoms and the interdiffusion with Si. This results in the formation of a bimodal distribution of pyramids and domes as surface kinetics are no longer limited. Indeed pyramids and domes obtain a lower Ge content than Ge hut clusters but due to the correlation between Ge content and size which is governed by the lattice mismatch the size is strongly reduced. This results in an even further separation of the electrons and holes and, therefore, in a lower electron-hole wave function overlap compared to nominally pure Ge hut clusters.
This nicely shows that small sizes induced by limited surface kinetics are necessary for a high luminescence intensity. Therefore, growth schemes are required which allow the independent tuning of the Ge content from the island or quantum dot size. We evaluate the approach of Si and Ge co-deposition. This approach allows for low growth temperatures, which maintain the limited surface kinetics. At the same time a reduction of the supplied Ge adatoms results in a lower Ge content. This technique slightly lifts the correlation between Ge content and size and, therefore, the fabrication of SiGe hut clusters is possible which however show qualitatively the same radiative recombination rate as nominally pure Ge hut clusters. The biggest advantage of SiGe hut clusters is that the fine tuning of the Ge content allows for a larger flexibility in the adjustment of the desired recombination energy.
Based on our experimental and simulation analysis we conclude that all these island morphologies exhibit a type II band alignment inherently limiting the radiative efficiency. At the same time Ge and SiGe hut clusters show a quasi-direct recombination revealing an optimum spreading of the hole wave function in k-space.
For optimizing the spatial electron-hole wave function overlap we follow the path of further reducing the Ge content by means of co-deposition of Ge and Si at high temperatures of 630°C. The resulting $Si_{0.7}Ge_{0.3}$ islands, which are quantum well segments, offer an eight times higher luminescence intensity. This we attribute to a spatial type I band alignment. This conclusion we receive from realistic k*p band structure simulation where no fit parameters have been used as input parameter. Instead of this the simulations are based only on the experimental determined structural island properties size and Ge content. The spatial type I band alignment is expected to result in a larger electron-hole wave function overlap due to a stronger influence of the attractive Coulomb interaction between the confined charge carriers. Because of the large size of these $Si_{0.7}Ge_{0.3}$ islands the hole wave function spreading in k-space is significantly reduced. This allows for a second radiative recombination channel including the assistance of a phonon.
In summary, the competitive connection between the Ge content and the island height strongly limits the potential of Ge based light emitters. It seems not possible to optimize the k-space and the real space recombination properties at the same time because of the fact that it is so far not possible to fabricate small, type I emitters with a low Ge content. This would require growth methods which allow for a completely independent tuning of the Ge content and the size. This is something the here employed method of co-deposition does not achieve. Such growth schemes might involve the implementation of additional materials like carbon or tin for lattice constant engineering or the deposition on pre-strained strained substrates.
As a second part of this thesis we deal with embedding (Si)Ge based light emitters

into photonic crystals and P-I-N diodes. By combining $Si_{0.7}Ge_{0.3}$ islands with two dimensional photonic crystals we obtained additional information concerning the radiative recombination rate. In resonance with the photonic band gap photoluminescence spectroscopy measurements reveal an intensity of at least one photon per second up to room temperature over a broad energy range without any cavity. Without the photonic crystal the luminescence already vanishes at 217 K. The fact that the improvement of the collection efficiency without any further photonic effect is enough for such a strong enhancement indicates that the radiative recombination rate of the $Si_{0.7}Ge_{0.3}$ islands is large enough to compete with the non-radiative recombination rate. This allows to deduce that the large refractive index difference is a major issue for future applications. Thus, we assign the highest potential to a future in-plane device idea.
Furthermore, we have embedded Ge islands into vertical P-I-N diode structures to asses the potential of electrical charge carrier injection which is necessary for future device applications. By comparing photoluminescence intensities and electroluminescence intensities of Ge islands we found that electrical injection of hot charge carriers is at least eight times more efficient than optical excitation.
In combination with two dimensional photonic crystals the electroluminescence intensity is enhanced by a factor of approximately three because of the redistribution of the light emission. This is lower than for an excitation with photoluminescence. The reason for this is a high axis resistance due to the photonic crystal air holes. So far this prevents a strong cavity mode enhancement as charge carriers cannot diffuse into the cavity region. However, first indication for mode enhancement has been observed and we expect better results using a new diode design. Here we suggest the embedding of approximately 8 layers of $Si_{0.7}Ge_{0.3}$ islands rather than pure Ge islands in waveguide cavities. Eight island layers would strongly enhance the charge trapping carrier efficiency while maintaining the slab thickness. Moreover a waveguide cavity would allow the diffusion of charge carriers into the cavity region. Furthermore, we could profit from the higher radiative efficiency of $Si_{0.7}Ge_{0.3}$ islands compared to pure Ge islands.
In conclusion, we think that for a commercial impact in terms of an efficient silicon based light source new fabrication schemes have to be invented, which allow the fabrication of small and low Ge content quantum dots with a type I band alignment. Otherwise the low radiative efficiency will always be too small for a commercial application. Therefore, if no way is found to independently tune the Ge content from the island or quantum dot size Ge heterostructures can only be used as an interesting model system in research but not for an efficient silicon based light source in future silicon optical integrated circuits.

A. K*p band structure simulations

Semiconductor crystals consist of a periodic lattice of nuclei and an immediate consequence of this periodicity is the formation of an electronic band structure [Kit89]. This band structure consists of electronic bands with a non-zero density of states and a band gap which is an energy region with a zero density of states. The band structure determines most of the electronic and optical properties of semiconductors [Sin93]. Therefore, deep knowledge of at least the lowest energetic conduction and valence bands is required to understand occurring phenomena. During this thesis we performed extensive band structure calculations using the simulation software nextnano++ [Bir07] which was developed in the group of Prof. Vogl at the WSI. In the following, we will very briefly discuss the basic concept of the k*p approximation and the envelope function theory. For further reading we refer to the PhD thesis of T. Andlauer [And09] and M. Zibold [Zib07].

A.1. Multi-band k*p effective mass approach

The periodic structure of atoms is mathematically described by a many-particle Hamiltonian [Kit89] where the mean field approximation [Pre99] allows to reduce the complexity of the n-body problem to a one-body problem with the lattice periodic potential V(x+$\mathbf{R}$) = V(x). $\mathbf{R}$ is the Bravais lattice vector :

$$\hat{H}\psi_n(x) = \left[\frac{\mathbf{p}^2}{2m_0} + V(x)\right]\psi_n(x) = E_n\psi_n(x) \tag{A.1}$$

Using Bloch's theorem [Blo29] we can rewrite the eigenfunctions $\psi_n(x)$ as

$$\psi_{n,\mathbf{k}}(x) = exp(i\mathbf{k}\cdot\mathbf{r})u_{n,\mathbf{k}}(x) \tag{A.2}$$

$u_{n,\mathbf{k}}(x)$ is the Bloch factor which contains the crystal periodicity $u_{n,\mathbf{k}}(x) = u_{n,\mathbf{k}}(x+\mathbf{R})$. By inserting equation A.2 into equation A.1 we obtain following relation:

$$\hat{H}(\mathbf{k})u_{n,\mathbf{k}}(x) = \left[\frac{\mathbf{p}^2}{2m_0} + V(x)\right]u_{n,\mathbf{k}}(x) = E_n u_{n,\mathbf{k}}(x) \tag{A.3}$$

The solution of this relation results in the dispersion relation of the band eigenenergies E_n as a function of the wave vector $\mathbf{k}$ in the first Brillouin zone.
However it requires numerical methods and simplifications to solve these n equations. We will use the k*p method which simplifies the calculation by utilizing the fact that charge carriers occupy only the conduction band minima and valence band maxima.

The k*p method calculates the band structure only in a small interval surrounding the high symmetry k-points $\mathbf{k}_0$. Close to $\mathbf{k}_0$, we expand $\hat{H}$ and $\mathrm{u}_{n,\mathbf{k}}(\mathrm{x})$ around $|\mathbf{k}-\mathbf{k}_0|$. Then the Hamiltonian in equation A.3 splits in a constant extreme part and a $\mathbf{k}$ dependent part. The Bloch factors $\mathrm{u}_{n,\mathbf{k}}(\mathrm{x})$ then form a complete orthonormal basis of the infinite dimensional equation system for all n energy bands. However, only a few of those bands are occupied and, hence, physically relevant. In the following consideration, we only take the physical relevant bands into account. All other bands are treated as perturbation. Using this assumptions we end up with the following Hamiltonian:

$$\hat{H'}_{\nu\mu}(\mathbf{k}) = \hat{H}_{\nu\mu}(\mathbf{k}) + \sum_{\alpha} \frac{\hat{H}_{\nu\alpha}(\mathbf{k})\hat{H}_{\alpha\mu}(\mathbf{k})}{E_{\nu}(\mathbf{k}_0) - E_{\alpha}(\mathbf{k}_0)} \tag{A.4}$$

with

$$\hat{H}_{\nu\mu}(\mathbf{k}) = \left[E_{\mu}(\mathbf{k}_0) + \frac{\hbar^2}{2m_0}(\mathbf{k}^2 - \mathbf{k}_0^2)\right]\delta_{\nu\mu} + \frac{\hbar}{m_0}(\mathbf{k}-\mathbf{k}_0)\cdot\mathbf{p}_{\nu\mu} \tag{A.5}$$

Here $\mathbf{k}_0$ is the wave vector where the energy bands have an extreme value, and $\mathbf{p}_{\mu\nu}$ is the momentum matrix element between the different band edge states [Sin93].
To solve this Hamiltonian, two different approaches are possible; The first approach calculates the bands individually. This so called effective mass approximation (EMA) reduces the matrix equation A.4 to a scalar by treating the perturbation with an effective mass tensor m^*.

$$\begin{aligned}\hat{H}_n^{EMA}(\mathbf{k}) &= E_n(\mathbf{k}_0) + \frac{\hbar^2}{2m_0}(\mathbf{k}^2-\mathbf{k}_0^2) + \frac{\hbar^2}{m_0^2}\sum_{\alpha\neq n}\frac{|(\mathbf{k}-\mathbf{k}_0)\cdot\mathbf{p}_{n\alpha}|^2}{E_n(\mathbf{k}_0)-E_{\alpha}(\mathbf{k}_0)} \\ &= E_n(\mathbf{k}_0) + \frac{\hbar^2}{2m_0}(\mathbf{k}-\mathbf{k}_0)^T\frac{1}{m^*}(\mathbf{k}-\mathbf{k}_0)\end{aligned} \tag{A.6}$$

This approach is from computational point of view very fast compared to calculations where several bands are involved. However, it only gives sufficient accurate results when the energy difference between the individual bands is large [And09].
We only use this approach for calculations where we want to calculate the wave function and not the exact energy of the individual energy states. Especially for the p-type degenerate valence bands we require a multi-band model, as the individual bands are energetically coupled and suffer from spin-orbit coupling. Therefore, when not stated otherwise, we use an eight band k*p approach when calculating the transition energies or the electron and hole probabilities. In this approach equation A.4 becomes an eight×eight matrix where a relativistic correction term considers the spin-orbit interaction [And09]. This is solved in an iterative process.
Thus, we get a good insight on the heavy and light hole as well as the split-off band and the Γ conduction band. As nextnano++ is not capable of an 14 band algorithm, we always calculate the X- and the L-band using the single band approach. We think this is sufficient enough for qualitative conclusions as those conduction bands are energetically well separated.

A.2. Envelope function theory for non-periodic nanostructures

As stated above the electronic band structure is a direct result of the lattice periodic potential. However, nanostructure like islands, break the translation symmetry and, thus, the lattice is not completely periodic anymore. Bloch's theorem is no longer valid and the previously stated method can no longer be used. The envelope function approximation (EFA), however, makes it possible to adopt this theory to quantum dots or other nanostructures.
In this approach the charge carrier wave functions is a superposition of Bloch functions:

$$\psi(x) = \sum_n F_n(x)\psi_{n,\mathbf{k}_0}(x) \tag{A.7}$$

$F_n(x)$ hereby is called the envelope functions which is assumed to vary slowly compared to the lattice constant.
Using this Ansatz one can reformulate the Schrödinger equations. The exact math is given in the PhD thesis of Till Andlauer [And09] and Tobias Zibold [Zib07]. Exemplarily, for the conduction band in single band approximation one has to solve

$$H^{EMA,EFA} = -\frac{\hbar^2}{2}\nabla \cdot \left(\frac{1}{m^*}\right)\nabla + E_c(x) + V_{ext}(x). \tag{A.8}$$

Here E_c is the conduction band energy and V_{ext} is a possible external potential.

A.3. Modeling of Ge nanostructures in Nextnano++

To calculate the band structure a simulation model of the nanostructure has to be defined. This model is based on following procedure:

1. defining global parameters
2. defining simulation grid
3. defining structure
4. defining simulation properties

The temperature, the substrate and the crystal directions are global parameters which influence the material properties of silicon and germanium. In our case the temperature varies between 10 and 20 Kelvin. The crystal geometry is x = {100}, y={010} and z={001}. z is the growth direction throughout this thesis.
The simulation grid is very important as it determines the resolution of the calculation. A smaller simulation grid results in a higher resolution but also leads to a much larger computation time.
Next we define the structure were we use different geometrical objects like cuboids or

obelisks of different sizes to model the desired structure. Each object has a size and an alloy content. Furthermore, the alloy content can be modeled with a gradient to take the intermixing of silicon into the germanium into account [Zha10]. Also the doping of the structure is defined here. The doping library consists of different materials where the exact binding energies and degeneracies are defined. In addition, for computational reason a quantum region is defined. Only inside of this region the Schrödinger equation is solved self-consistently saving computation time.
We always include strain into our calculations which can be modeled using two different approximations: a minimizing model and a pseudomorphic model. The calculations are based on the linear continuum elasticity theory [Pry98] were the minimizing model minimizes the global strain of the system. The pseudomorphic model strains the nanostructure according to the substrate.
For all calculations which involve small Ge quantum dots, we use the minimizing model. For larger SiGe islands, which we present in chapter 6 we use the pseudomorphic strain model as transmission electron microscopy images prove a pseudomorphic epitaxy.
The band edges and eventually the charge carrier densities are calculated in a classical Poisson equation approach. For calculations concerning P-I-N diodes which we conduct in chapter 9 the band structure is altered by the charge carrier transport and occurring recombinations. Thus, we iteratively calculate the current transport using the Shockley-Read-Hall model followed by the Poisson equation.
At last we calculate the Schrödinger equation for several bands, where we individually decide, whether to use a multi-band k*p approach or the single band approach. k*p calculations use a complex wave function as basis. Single band calculations imply a real wave function. Thus, for calculating the overlap integral the single band approach is necessary for the hole states to allow subsequent integration with the electron state of the Δ-valley which is always calculated in single band approach given the lack of a 14-band k*p algorithm. Calculations of the transition energies in chapter 3, 4 and 5 use the single band approach for calculation speed reasons. A comparison with k*p calculations reveals that the single band approach is sufficient to qualitatively describe the observed experiment trends. In chapter 6, the k*p approach determines the transition energy as high accuracy is needed to prove the validity of the simulation model.
The material library listed in tables A.1 and A.2 can be altered but we use the predefined values which have been taken from literature.

Parameter	Value	Reference
lattice constant	5.4304 Å	[Spr12]
lattice constant expansion	1.8138· 10^{-5} Å/K	[Spr12]
dielectric constant	11.7	Silvaco
elastic constants		
C_{11}	165.77 GPa	[Spr12]
C_{12}	63.93 GPa	[Spr12]
C_{44}	79.62 GPa	[Spr12]
Γ-band		
effective mass	0.156	
deformation potential	-10.39	[Wei99]
L-band		
longitudinal effective mass	1.420	
transversal effective mass	0.130	
deformation potential	-2.02	[Wei99]
uniaxial deformation potential	16.14	[VdW86]
Δ-band		
longitudinal effective mass	0.916	[Boe90]
transversal effective mass	0.190	[Boe90]
deformation potential	3.40	[Wei99]
uniaxial deformation potential	9.16	[VdW86]
valence-bands		
heavy hole effective mass	0.537	[Boe90]
light hole effective mass	0.153	[Boe90]
split-off hole effective mass	0.234	[Boe90]
deformation potential	2.05	[Wei99]
uniaxial deformation potential$_b$	-2.10	[Lau71]
uniaxial deformation potential$_d$	-4.85	[Lau71]

Table A.1.: Complete list of all simulation parameters used for the band structures of silicon.

Parameter	Value	Reference
lattice constant	5.6579 Å	298.15 K [Spr12]
lattice constant expansion	5.8· 10^{-5} Å/K	[Sze81]
dielectric constant	16.2	[Spr12]
elastic constants		
C_{11}	128.53 GPa	[Spr12]
C_{12}	48.26 GPa	[Spr12]
C_{44}	66.80 GPa	[Spr12]
Γ-band		
effective mass	0.038	
deformation potential	-10.41	[Wei99]
L-band		
longitudinal effective mass	1.57	
transversal effective mass	0.0807	[Sch97a]
deformation potential	-4.35	[Wei99]
uniaxial deformation potential	15.13	[VdW86]
Δ-band		
longitudinal effective mass	1.350	
transversal effective mass	0.290	
deformation potential	0.14	[Wei99]
uniaxial deformation potential	9.42	[VdW86]
valence-bands		
heavy hole effective mass	0.316	
light hole effective mass	0.0424	
split-off hole effective mass	0.095	
deformation potential	-0.35	[Wei99]
uniaxial deformation potential$_b$	-2.86	[Cha77]
uniaxial deformation potential$_d$	-5.28	[Cha77]

Table A.2.: Complete list of all simulation parameters used for the band structures of germanium.

B. Experimental techniques

B.1. Atomic force microscopy

We use atomic force microscopy to determine the topological size distribution of surface islands. An Asylum Research MFP 3D atomic force microscopy is used in tapping mode. According to the specifications the tip radius is smaller than 10 nm.
The analysis of the images uses the open source software WSxM [Hor07]. With WSxM sizes and densities are determined manually. All data points are determined by an average of 30 islands on three different positions.
For the analysis in chapter 6 we use Gwyddion [Nec12]. Gwyddion is capable of an automatic mechanism for quantitative analysis but only for a non-varying island shape as it can not distinguish between different morphologies. The automatic algorithm averages over several hundred islands. The error analysis includes the statistical size variation and the systematical error of the non-zero tip size and of the measurement step size. However, the systematic error is 2 orders of magnitude lower than the statistic error.

B.2. Transmission electron microscopy and energy dispersive X-ray spectroscopy

All presented transmission electron microscopy and energy dispersive X-ray spectroscopy measurements are performed in collaborations with Prof. Zweck from the Universität Regensburg and with Dr. Döblinger from the Ludwig Maximilians Universität München. The sample preparation and first experiments have been conducted at the Universität Regensburg whereas the presented measurements have been conducted at the Ludwig Maximilians Universität using a FEI Titan 80-300 with a operating voltage of 300 kV. All presented measurements are taken in the HAADF-STEM mode which offers a high-Z contrast.

B.3. Raman spectroscopy

Raman spectroscopy measurements are conducted in back-scattering geometry. The 514.5 nm line of an Argon Ion laser was used for the excitation. The excitation power is 3-4 mW with a focus diameter of approximately 1 μm. All measurements are performed at room-temperature and under ambient conditions. The scattered intensity is spectrally dispersed using a Dilor X-Y-triple spectrometer. The spectral resolution is between 1 and 3.8 cm^{-1}. The detection is conducted using a nitrogen cooled CCD.
Raman spectroscopy does not directly reveal the Ge content. In fact it reveals the

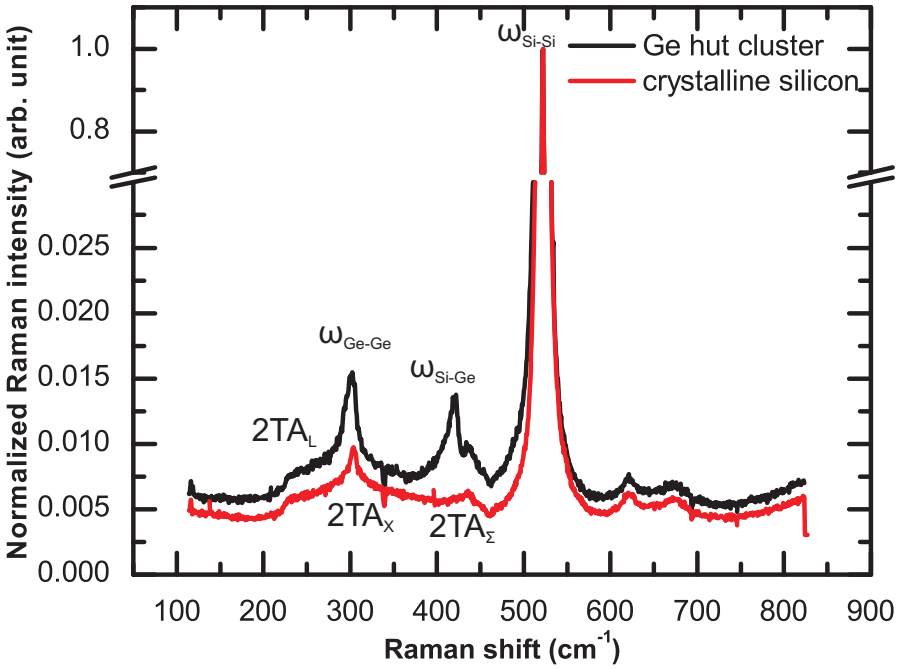

Figure B.1.: Raman spectrum of a hut cluster sample and a crystalline Si reference. The Si wafer has the same specifications as the substrate for the hut cluster sample. The Intensities of both spectra are normalized to the intensity of the Si-Si-LO phonon intensity.

frequency shift of the laser scattered at phonons. In a two atomic base the phonon frequency is a function of the mass of both atoms [Kit89]. The phonon frequency in an alloy depends on the neighboring atoms and, therefore, on the composition ratio of the alloy species. In our system there are several possibilities: A Si atom can vibrate in a Si matrix, a Ge atom can vibrate in a Ge matrix and a Si can vibrate in a Ge lattice or the other way around. In the quantized phonon picture this results in SiSi, GeGe and SiGe phonons.

Figure B.1 exemplarily shows the Raman intensities of Ge hut clusters deposited at 424°C and of an unprocessed Si substrate wafer. The intensities of both graphs are normalized to the maximum intensity of the Si-Si-LO phonon mode at ≈ 520 cm^{-1} stemming from the Si substrate or capping layer [Gro97, Tan03]. Three modes at 225 cm^{-1}, 301 cm^{-1} and 435 cm^{-1} are attributed to vibrations in the silicon substrate or the silicon capping layer. According to the literature we label them as Si-TA-vibrations of second order in L, X or Σ direction [Tan03]. The hut cluster sample yields two additional features at 302.2 cm^{-1} and 421.9 cm^{-1}. The first is a Ge-Ge lattice vibration [Gro97, Tan03, Alo89]. The latter is a Si-Ge phonon. An additional peak for localized Si-Si phonons is expected at ≈ 500 cm^{-1} [Gro97, Alo89]. However, this phonons we do not observe in our samples.

For calculating the average Ge content we follow the method introduced by Dominique Bougeard [Bou05, Tan03]. First we subtract the Si reference from the Ge hut cluster sample to remove the influence of the Si substrate. It has been shown that the average Ge content can be estimated by the frequency shift of the ω_{Ge-Ge}-LO mode relative to the bulk material. Next we assume a fully strained island with an average strain of approximately -3.5% [Bou05]. This strain results in a frequency shift of 13.5 cm^{-1} compared to the bulk germanium phonon mode at 300.8 cm^{-1}. If one compares this value with the experimental value of the Ge-Ge-LO mode the resulting frequency shift is inserted in the empirical formula [Ren71]

$$\omega_{Ge-Ge}(LO) = 263.8 + 37x_{Ge}(cm^{-1}) \tag{B.1}$$

to deduce the average Ge content x_{Ge}.

B.4. Photoluminescence and electroluminescence spectroscopy

For optical investigations we use two different setups which differ in their excitation spot size. We use a macro-photoluminescence and a micro-photoluminescence setup. Both setups can be applied for electroluminescence measurements.

B.4.1. Macroscopic-photoluminescence and electroluminescence

To conduct luminescence measurements on unpatterned structures, we use a so called macro-photoluminescence setup. Here the excitation laser is either an Argon ion laser with a wavelength of 514.5 nm or 488 nm and a maximum power of approximately 30 mW or a Diode pumped solid state laser with a wavelength of 532 nm and a maximum power of 200 mW. Furthermore, a second diode pumped solid state laser with an excitation wavelength of 473 nm and a maximum power of 100 mW is available. For all lasers the excitation energy is far above the band gap.
For later noise filtering the excitation signal is chopped at frequencies between 20 and 68 Hz. The laser light is directed on the sample using a cold mirror, which is transmissive in the near infrared region and reflective in the visible. We focus the light on the sample using an achromatic lens with a focus length of 7.5 cm. The diameter of the excitation spot is ≈ 100 μm. The sample is placed in a liquid Helium flow cryostat from Cryo Industries. The luminescence of the sample is collected and then focused on the entrance slit of a Triax 550 grating monochromator using achromatic lenses. After the spectral filtering, we detect the luminescence signal using a North Coast Ge Detector. The detector output voltage is finally detected in Lock-In technique.
For electroluminescence measurements, we replace the optical excitation of the laser with an electrical current injection using a Keithley 2400 DC bias source. In addition the detection signal is directly chopped in front of the spectrometer entrance.

B.4.2. Microscopic-photoluminescence and electroluminescence

As photonic crystal cavities are of micrometer size the detection and excitation spot need to be of the same size. Therefore, an 100x near-infrared coated microscope objective with a focus spot diameter of approximately 1 μm replaces the optical lens system. The excitation uses a diode pumped solid state laser with a wavelength of 532 nm and a maximum power of 200 mW. The luminescence signal is guided to the entrance slit of a Triax 320 grating monochromator where it is spectrally dispersed. The detection is performed using a nitrogen cooled InGaAs imaging CCD line array.
Here again, electroluminescence experiments require to replace the optical excitation with an electrical current injection using a Keithley 2400 DC bias source.

C. Silicon on insulator and germanium on insulator thinning procedure

This appendix shortly summarizes the wafer-thinning procedure for the preparation of the silicon on insulator substrates. Such wafer-thinning is required as there are no commercial available silicon on insulator wafers with a micrometer thick buried oxide and a device layer of less than 50 nm. Also there are no such commercial silicon and insulator wafers with a highly doped device layer needed for the P-I-N-diode structures of this thesis. There are several possible methods for silicon wafer-thinning:

- Reactive ion etching
- Thermal oxidation with subsequent hydrofluoric acid treatment
- Isotropic wet etching

The thinned substrate has to fulfill a high standard of purity to allow subsequent introduction into the molecular beam epitaxy chamber. Especially contaminations including metal have to be avoided. Therefore, we exclude the first method because of possibly unwanted surface contamination.

C.1. Wafer-thinning by thermal oxidation

Silicon in combination with oxygen leads to the formation of silicon-dioxide. Silicon-dioxide is highly unstable against hydrofluoric acid treatment whereas silicon is stable against hydrofluoric acid [Wil03]. The combination of both chemical processes can be used to thin the device layer of a silicon on insulator wafer. Natural oxidation is a very slow process but elevated temperatures can strongly fasten the oxidation process.
Basically there are two possible oxidation mechanism: Dry oxidation, which takes place in pure oxygen atmosphere and wet oxidation, which takes place in humid oxygen atmosphere.
Dry oxidation is a gentle process which results in an interface with few defects and a silicon-dioxide of high quality. Unfortunately this process is very slow with oxidation rates of 0.2-0.3 nm/min at 900°C [1].
Wet oxidation on the other side is fast. But it results in many defects within the silicon-dioxide and at the interface [wik12]. As we anyway will remove the silicon-dioxide the

[1] Experimental result of S. Koynov

quality of the oxide is unimportant and, hence, we use the latter process. Wet oxidation follows the stoichiometric equation:

$$Si + 2H_2O \rightarrow SiO_2 + 2H_2(g) \tag{C.1}$$

In the WSI a self made oxidation oven is available which reaches temperatures up to 1000°C under dry or humid oxygen atmosphere. High temperatures are desired as they result in an enhanced process speed. The thermal oxidation process follows the Deal-Grove model [Dea65]:

$$t + \tau = \frac{x^2}{B} + \frac{A \cdot x}{B} \tag{C.2}$$

Here x is the oxide thickness, t the reaction time and τ is a corrective term which accounts for an already existing oxide barrier. B/A is the linear rate constant and B the parabolic rate constant both depending on the oxidation mode, on the crystallographic orientation and on the ambient partial pressure and temperature.
For our experiments, we use an oxidation temperature of 900°C and an oxygen flow of six arbitrary units [2]. Preceding we remove the natural oxide with 5% hydrofluoric acid to allow for a homogeneous oxidation. We confirm the resulting slab thickness with ellipsometry and reactive ion etching including subsequent atomic force microscopy measurements. We find a silicon removal rate which is unstable although we carefully treated the oxidation parameters. Also it is only of the order of approximately 0.4 nm/min, which is much lower than the theoretical predicted 1.0 nm/min.
In addition microscope images yield that the subsequent hydrofluoric acid treatment induces so called HF defects [Nau06] into the slab. These defects arise when hydrofluoric acid diffuses through the surface layer into the buried oxide. The removal of the buried oxide results in a breaking of the silicon slab. This degrades the surface quality for subsequent epitaxy.

C.2. Wafer thinning by isotropic wet chemical etching

Another approach for the wafer-thinning process is isotropic wet chemical etching. This requires the combination of an oxidizing chemical which in our experiments is 60% nitric acid (HNO_3) and an oxide removing acid which is 0.03% hydrofluoric acid (HF) diluted in water. We mix nominally 348 ml of 69% HNO_3 and 52 ml of 0.26% HF to obtain such concentrations.
According to the stoichiometric formulas C.3, C.4, C.5 and C.6 the nitric acid first dissociates to NO_2 which oxidizes the silicon. Afterwards the hydrofluoric acid removes the silicon-dioxide [Mic12].

$$HNO_2 + HNO_3 \rightarrow 2NO_2 + H_2O \tag{C.3}$$

$$2NO_2 + Si \rightarrow Si^{2+} + 2NO_2^- \tag{C.4}$$

$$Si^{2+} + 2(OH)^- \rightarrow SiO_2 + H_2 \tag{C.5}$$

[2] The flow meter does not give a more exact unit.

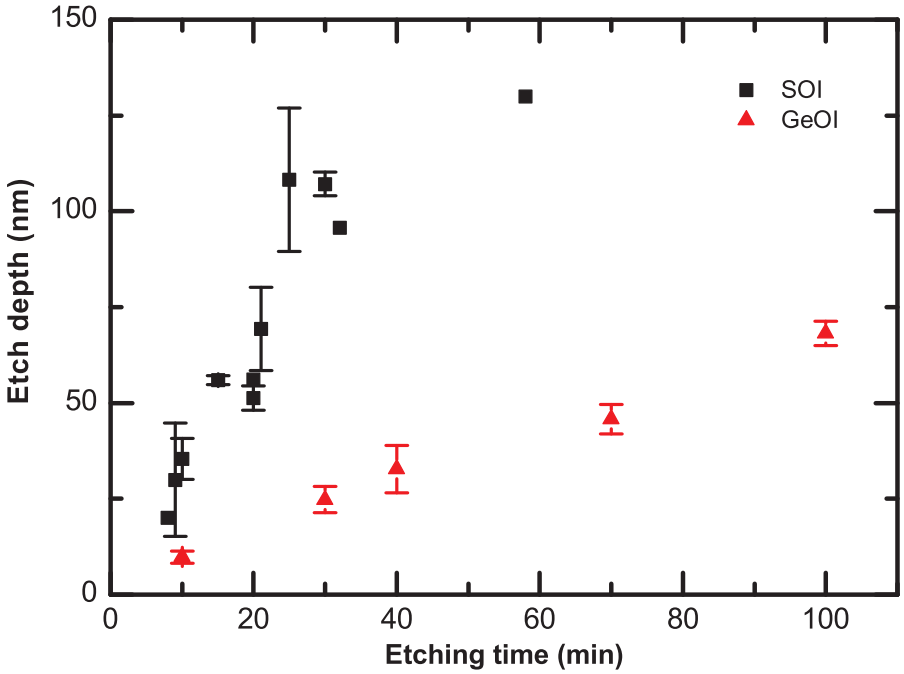

Figure C.1.: Etching rate for SOI (black squares) and GeOI (blue triangles) wafers with a mixture of HF/HNO_3. The concentration for the SOI wafer is 0.03% HF : 60% HNO_3 and for the GeOI wafer 0.1% HF : 42% HNO_3, respectively.

$$SiO_2 + 6HF \rightarrow H_2SiF_6 + 2H_2O \tag{C.6}$$

The surface quality is reasonable high for subsequent overgrowth with a roughness mean square of approximately 5 nm. The etching rate is $\approx$ 3 nm/min and strongly depends on the hydrofluoric acid concentration. This we deduce from figure C.1 where the etching depths for several SOI etching runs are plotted. Experimentally it is rather difficult to always mix the same concentrations. Thus, the etching rates are never the same.
Furthermore, we want to highlight that the etchant degrades over time with or without the etching process. This is indicated by the saturation of the etching depth in figure C.1. The degradation during the etching process is a result of the formation of H_2SiF_6 which reduces the available fluorine atoms. The degradation without the etching process is a result of a dissociation process in sunlight. The latter process is slow enough to not to influence the etching rates throughout the process. Another big advantage of the wet chemical etching process is that it is also suitable for the removal of germanium. However, it is interesting to note that the etching rate for a standard intrinsic germanium wafer is much higher than for a germanium on insulator wafer. For the first case we find an etching rate of 1.7 nm/sec, whereas we find an etching rate of 0.6 nm/min for the germanium on insulator wafer. The latter was etched with a higher HF concentration of 1% and a nitric acid concentration of 42%. Exemplarily in figure C.1 we show the etching depth for a GeOI. Furthermore, we want to highlight that the wet etching of

germanium strongly degrades the surface quality up to a complete loss of crystalinity. We always use the wet etching process because of a faster etching rate.

C.3. Germanium hut clusters deposited on silicon and silicon-on-insulator substrates

With exception of the chapter 3 and chapter 5 all samples have been fabricated using SOI substrate for a possible integration in SOI photonic crystal slabs. This not only requires changes in the technological preparation of the epitaxy. In fact a change of the substrates is expected to change the epitaxy itself as SOI wafers have an intrinsic non-zero strain [Poz05] component. To verify this we have performed X-ray diffraction experiments using the asymmetric (224)-reflex. The resulting diffraction vector **h** in reciprocal lattice units allows to calculate the in-plane and out-of-plane lattice constant:

$$A_{||} = \frac{1}{\mathbf{h}_{||}} \cdot \frac{\lambda}{2} \cdot \sqrt{h^2 + k^2} \tag{C.7}$$

$$A_{\perp} = \frac{1}{\mathbf{h}_{\perp}} \cdot \frac{\lambda}{2} \cdot \sqrt{l^2} \tag{C.8}$$

Here h, k and l are the Miller indices of the corresponding reciprocal lattice point and λ is the X-ray wavelength.
This analysis yields an in-plane lattice constant of $a_{\perp}$=5.4351 Å and a lattice constant parallel to the growth direction $a_{||}$=5.4537 Å. This differs from the literature value 5.4307 Å [Hab90] and corresponds to a strain of 0.4% in growth direction and 0.8% perpendicular to the growth direction. However sample cleaning and wafer-thinning (see appendix C) results in a slight increase of the strain to $e_{\perp}$=0.9% and $e_{||}$=0.5%.
Furthermore, the oxide layer with its different thermal conductivity [Vir11] results in a change of the growth temperature at the wafer surface.
This pre-strained and the different deviation in growth temperature at the substrate surface result in a change of the quantum dot growth. Thus, in figure C.2 we compare atomic force microscopy images of two hut cluster samples one deposited on silicon and one on SOI. The growth temperatures are approximately 345°C for both samples and we deposited 8 times 8 monolayers of nominally pure Ge. We see that the pre-strained SOI substrate leads to a slightly decreasing quantum dot density and an increasing size. However, the changes are of minor significance and are not further regarded within this thesis.

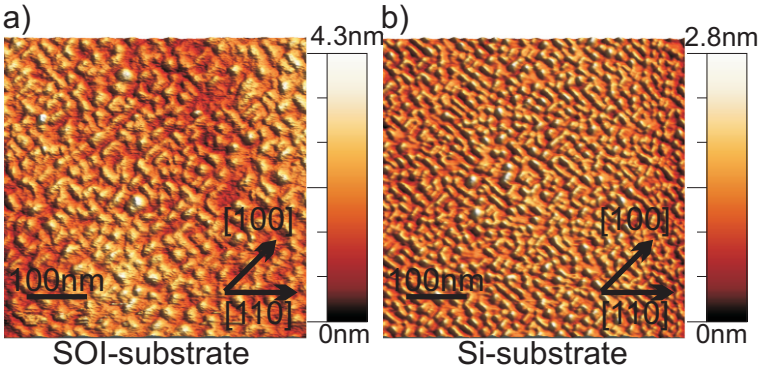

Figure C.2.: Atomic force microscopy images of Ge hut clusters grown on SOI or silicon substrate.

D. Monomodal epitaxy of germanium domes or pyramids

Pyramids and domes usually form in a bimodal distribution (see section 2.2 and chapter 4). However, it is possible to fabricate monomodal distributions of pyramids or domes by choosing proper growth conditions.
At a growth temperature of approximately 510°C and a deposition of eight nominal monolayers of germanium a homogeneous distribution of Ge domes forms. A reduced growth temperature of 410°C with a deposition of six monolayers results in the formation of pyramids. Figure D.1 shows atomic force microscope images of the surface islands for both samples. Figure D.1 (a) depicts a monomodal distribution of domes, which cover the whole surface. Figure D.1 (b) denotes the formation of a monomodal distribution of pyramids. Due to the reduced amount of material which we use for the growth the density is comparable low and few pyramids have a slight elongated shape.

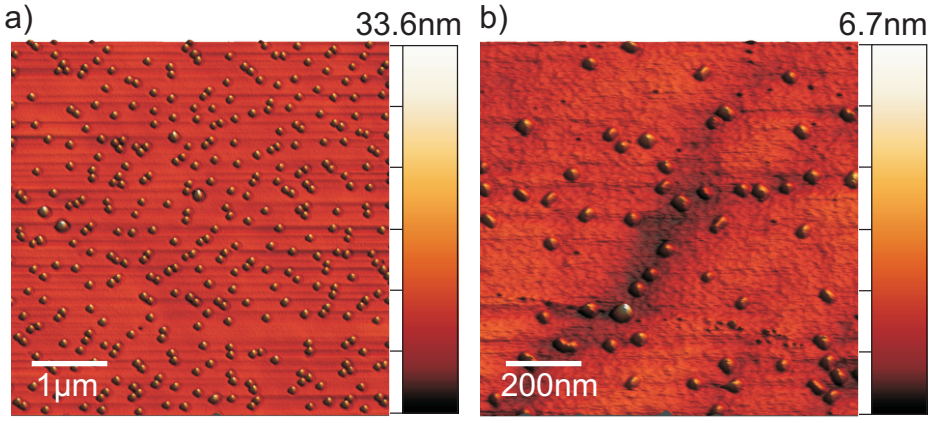

Figure D.1.: Atomic force microscopy image of a monomodal distribution of (a) domes and (b) pyramids.

E. Device fabrication

E.1. Fabrication of two-dimensional photonic crystals

The fabrication of two dimensional photonic crystals is sketched in figure E.1 which shows an illustrated cross-section of a SOI wafer with embedded islands:
(a) The wafer consists of a 605 μm thick Si handle wafer. On top, there is a 3 μm thick silicon dioxide layer. The device layer consists of 270 nm silicon with one layer of islands in the middle. The device layer is epitaxially grown after a thinning procedure, which is described in the appendix C.
(b) The fabrication of photonic crystals requires electron beam lithography as the structural size of the air holes is usually of the order of several hundred nanometers. After a cleaning step using acetone and isopropanol a droplet of poly (methyl methacrylate) (PMMA) [Mic01] 950K dissolved in anisol with a solid content of 3.75% is deposited onto the sample. The spin coating takes 40 seconds at a rotation speed of 3500 rotations per minute. This results in a resist thickness of approximately 180 nm. The spin coating is succeeded by a three minute softbake on a hotplate at 180°C.
(c) The desired structure is transferred into the PMMA using a RAITH eLine system. We use an acceleration voltage of 10 kV with an aperture of 10 μm size. This results in typical beam currents of approximately 22 pA. The exposure dose is set to 50-120 $\mu As/cm^2$. Norman Hauke determined the circular exposure method as the best to form circular shaped holes [Hau12] and, thus, we continue using this method. After the illumination, we develop the PMMA using the developer AR600-56 [All09] for 90 seconds. The developing is stopped by placing the sample in isopropanol for 30 seconds.
(d) We transfer the photonic crystal pattern into the silicon device layer with an inductively coupled plasma reactive ion etching process. In the WSI, an Oxford PlasmaLab 80Plus [Oxf] is available. The parameters for the etching process are summarized in table E.1. Here Si is etched according to the stoichiometric formula:

Parameter	Value	unit
SF_6 flow	20	sccm
C_4F_8 flow	30	sccm
Etchant pressure	15	mTorr
RF power	15	Watt
ICP power	220	Watt
Temperature	25	°C

Table E.1.: Parameters for a highly anisotropic silicon reactive ion etching process.

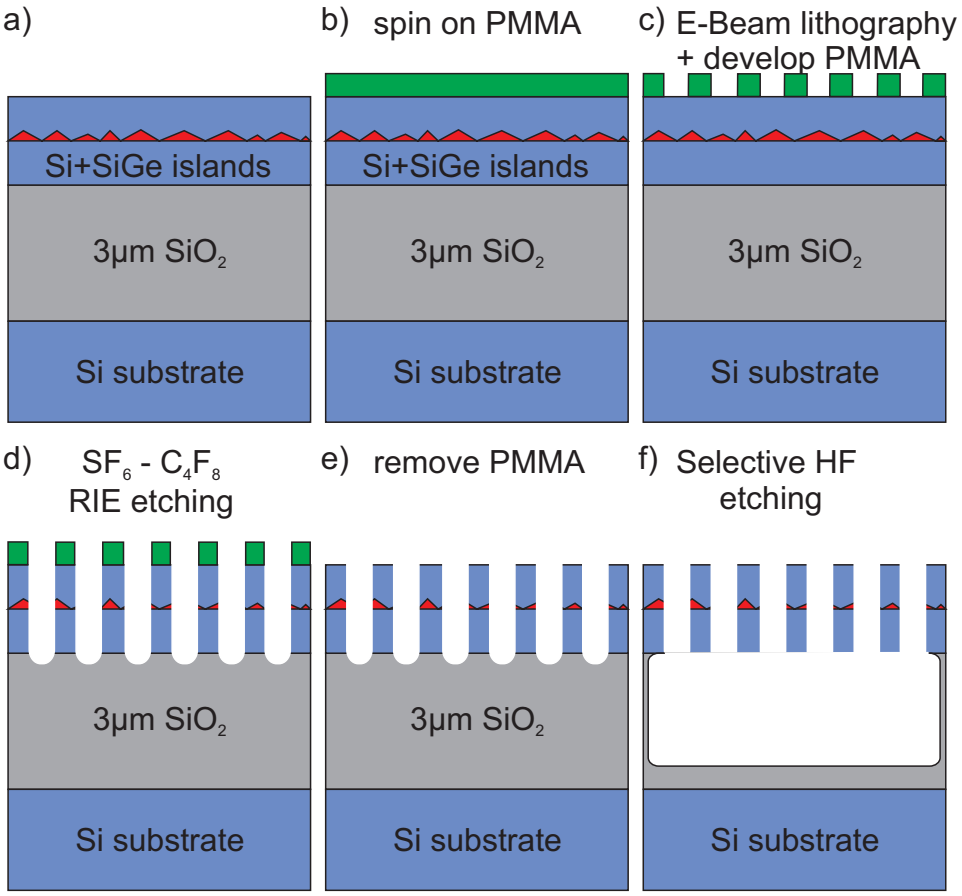

Figure E.1.: Fabrication of a two dimensional photonic crystal with embedded SiGe islands. (a) Fabrication starts with a standard silicon on insulator wafer with one embedded layer of islands. (b) PMMA is spinned on the sample and subsequent (c) electron beam lithography is performed to define a triangular lattice of air holes. (d) Reactive ion etching transfers the PMMA pattern into the silicon device layer. (e) PMMA is removed and finally (f) the photonic crystal is under-etched using hydrofluoric acid.

$$Si(s) + 4F(g) \rightarrow SiF_4(g) \tag{E.1}$$

The introduction of C_4F_8 into the etching chamber improves the anisotropy of the etching process. The carbon atoms form a passivation barrier which results in a reduction of the horizontal etching rate. The combination of both methods with the used parameters results in a silicon etch rate of approximately 4 nm/s.
(e) After the reactive ion etching the remaining resist is removed using acetone.
(f) To form a freestanding silicon membrane the underlying silicon dioxide is removed using hydrofluoric acid (HF). Therefore, the sample is placed in 5-10% HF for 30 minutes. Silicon is highly stable against HF and, thus, not removed.

E.2. P-I-N-diode processing on SOI substrate

The fabrication of a diode requires several processing steps which are sketched in figure E.2. Due to the layer structure with a 3 μm thick oxide the samples cannot be contacted with a global back contact. Rather than this both contacts have to be assembled from the top. After a cleaning step in acetone and isopropanol the surface is spin coated with photoresist S1818 at a rotation speed of 4000 rotations per minute for 40 s (Figure E.2(a)). The resist is soft baked for 15 minutes at 90°C. As indicated in figure E.2 (b) the resist is then illuminated for 10 seconds and developed using the developer AZ3518 for 20 seconds. Afterwards a hardbake is introduced at 120°C for subsequent reactive ion etching (figure E.2 (c)) were several mesa structures are defined using the etching parameters from table E.1. With the reactive ion etching the p-doped silicon layer is exposed. Thorough cleaning of the sample is required to remove the remaining resist which hardens during the reactive ion etching step. Here we use an ultrasonic bath in acetone followed by an isopropanol immersion. Remaining resist is ashed using an oxygen plasma at 200 W for 60 seconds. Finally, the sample is placed in hot acetone for up to 30 minutes and again immersed in isopropanol. Using this cleaning procedure the diode quality was strongly enhanced.
A second lithography step is performed (figure E.2 (d) and (e)) to define the evaporation mask for the contacts. The evaporation is preceded by a plasma asher step to remove resist residua which can degrade the contact quality. Directly before the evaporation the sample is placed in 10% diluted hydrofluoric acid for 30 seconds to remove the natural oxide layer. Finally the contacts are evaporated. The contact consist of 5 nm titanium as adhesion layer and 150 nm gold. The final lift-off is performed in acetone with ultrasonic (figure E.2) (f). This design offers the major drawback of using reactive ion etching for the mesa etching. Wet chemical etching using HF/HNO_3 is expected to result in less surface defects, which degrade the diode quality. But we found that the wet chemical etching often results in short circuits as the side walls are not vertical. Furthermore, the unstable etching rates in combination with the thin (65 nm) thick p-doped layer make it difficult to always etch into the doped layer. Thus, all here presented samples are fabricated using reactive ion etching.
In figure E.3(a) we show an array of P-I-N diodes fabricated on one sample. An individ-

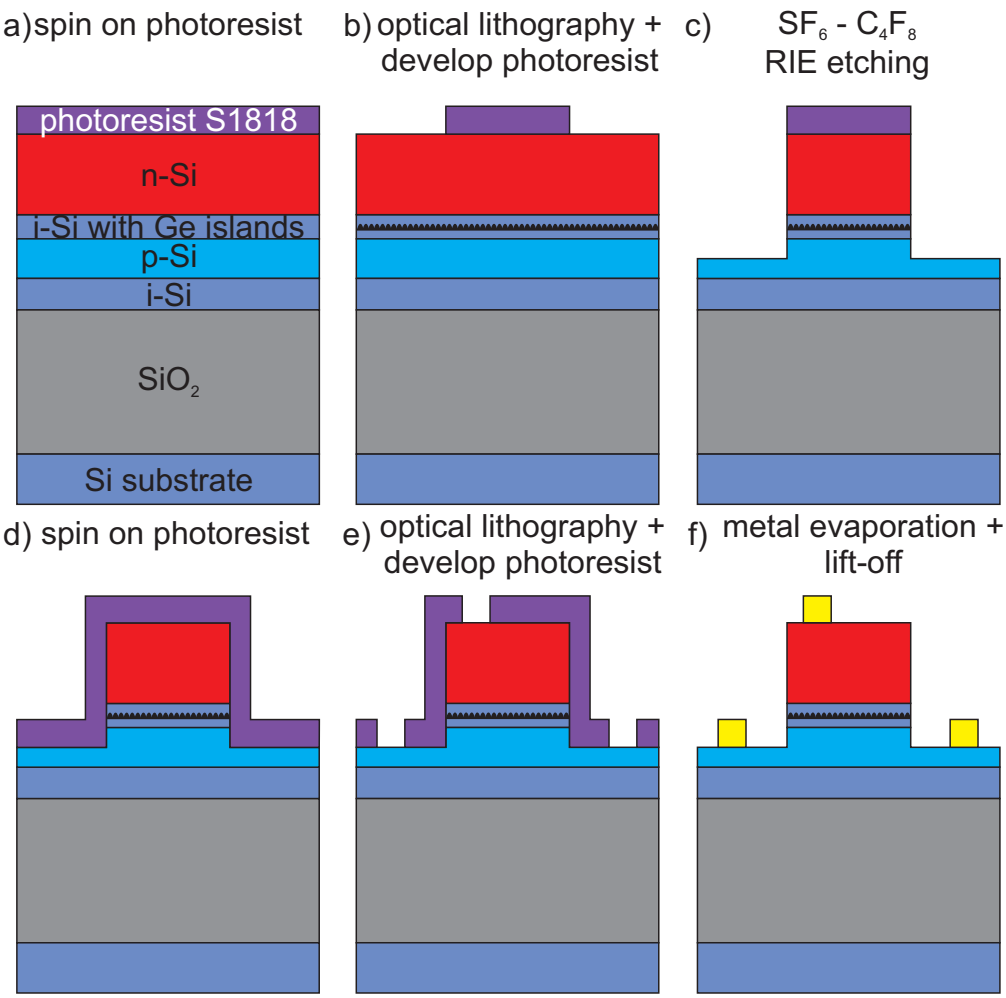

Figure E.2.: Schematic of the P-I-N diode fabrication. (a) Spin on of S1818 photoresist with (b) optical lithography and (c) subsequent reactive ion etching. After cleaning (d) an additional spin on of photoresist takes place. The following (e) lithography defines the mask for the (h) evaporation of Ti/Au contacts. Taken from [Gei11].

ual diode (b) consists of a mesa which is indicated by the grayish part. The mesa size is 800μm times 700μm. The p-doped silicon has a more purple to green color caused by interference effects with the underlying layers. The top contact opens a window of 350μm times 550μm size for optical access. The large size allows for optical investigations using macro-photoluminescence rather.

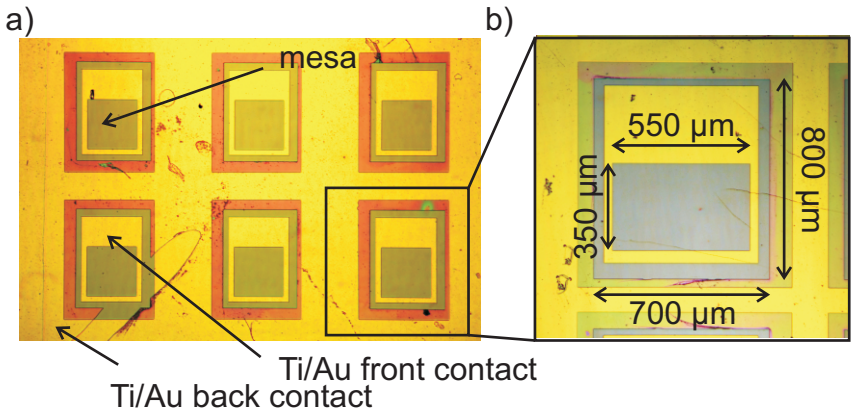

Figure E.3.: Optical microscopy image of (a) an array of P-I-N diodes. The golden color shows the TiAu contacts. The purple region is the p-doped silicon layer and the grayish region is the n doped silicon layer. (b) shows the zoom on one diode and illustrates the spatial dimensions.

E.3. Fabrication of two-dimensional photonic crystal P-I-N light emitting diodes

Using additional fabrication steps illustrated in figure E.4 the diode structure is patterned with a photonic crystal.

After the evaporation of the Ti/Au contacts the e-beam resist PMMA is spinned onto the already fabricated diode (Figure E.4 (b). Subsequent e-beam lithography and development (analog to section E.1) patterns the structure with the desired triangular hole pattern. In figure E.4 (c), we show that in the vicinity of the mesa S1818 photoresist is manually deposited. This is necessary to protect the mesa structure from the reactive ion processing step. First experiments without the photoresist have shown that the PMMA does not cover the sidewalls of the mesa and, thus, the reactive ion etching process isolates the individual diodes from the p-layer.

Afterwards the triangular air hole pattern is transferred into the diode (figure E.4 (d)). Figure E.4 (e) shows the under-etching of the silicon membrane using hydrofluoric acid. Finally, figure E.4 (f) illustrates the removal of the remaining resist.

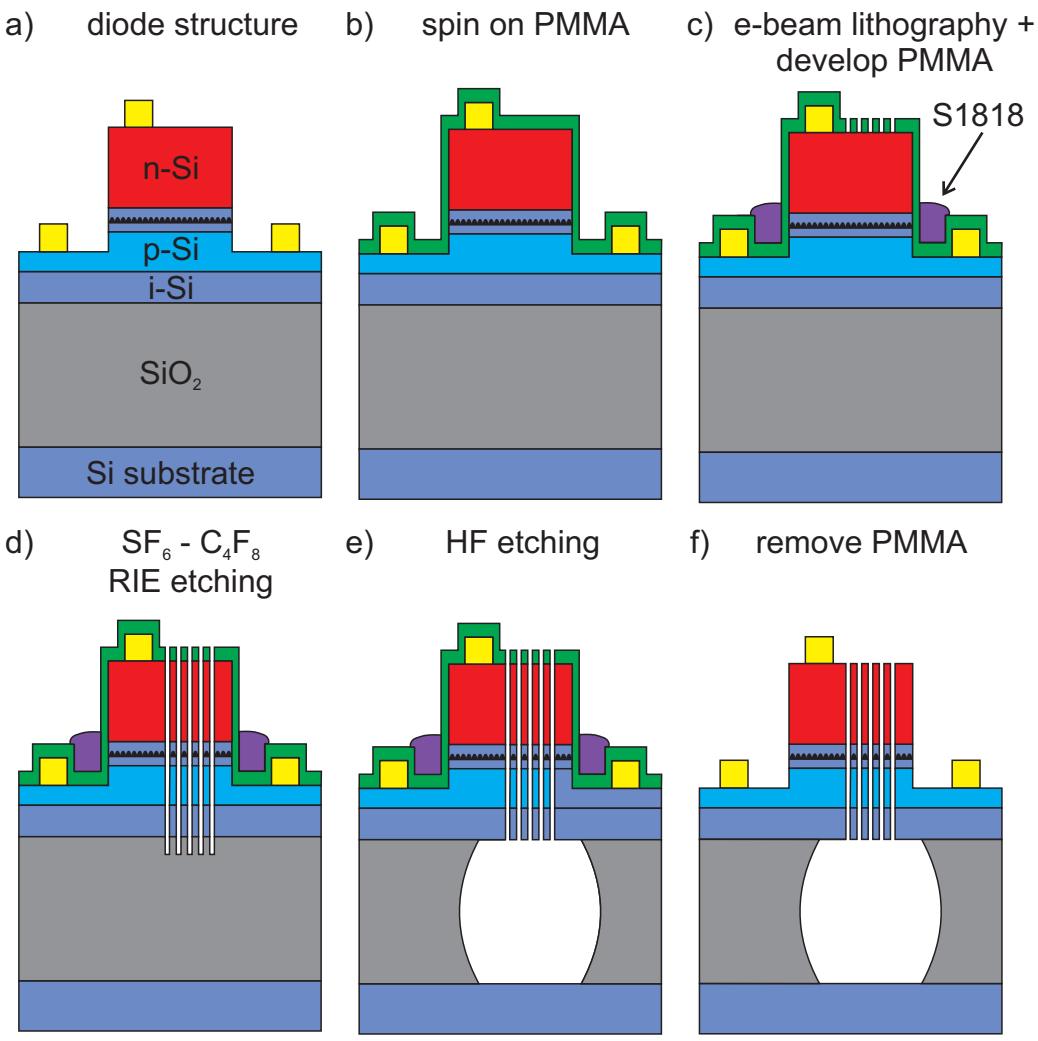

Figure E.4.: Photonic crystal processing steps for a silicon P-I-N diode structure. (a) Fabricated diode according to section 9.1. (b) Spin on off PMMA for (c) subsequent e-beam lithography. The sidewalls of the mesa are capped with S1818 photoresist for (d) reactive ion etching and (e) under-etching of the buried oxide using hydrofluoric acid. (f) Removal of resist. Taken from [Gei11]

Bibliography

[Abs89] G. Abstreiter, K. Eberl, E. Friess, W. Wegscheider, R. Zachai, *Silicon/germanium strained layer superlattices*, Journal of Crystal Growth **95**, 431 – 438 (1989)

[Abs96a] G. Abstreiter, *Electronic properties of Si/SiGe/Ge heterostructures*, Physica Scripta **1996**, 68 (1996)

[Abs96b] G. Abstreiter, P. Schittenhelm, C. Engel, E. Silveira, A. Zrenner, D. Meertens, W. Jäger, *Growth and characterization of self-assembled Ge-rich islands on Si*, Semiconductor Science and Technology **11**, 1521 (1996)

[Aka03] Y. Akahane, T. Asano, B. Song, S. Noda, *High-Q photonic nanocavity in a two-dimensional photonic crystal.*, Nature **425**, 944–947 (2003)

[Ali96] A. P. Alivisatos, *Semiconductor Clusters, Nanocrystals, and Quantum Dots*, Science **271**, 933–937 (1996)

[All09] Allresist Gesellschaft Für Chemische Produkte zur Mikrostrukturierung mBH, *AR600-56 datasheet* (2009), http://www.allresist.de/wMedia/pdf/wEnglish/produkte_ebeamresist/AR600_50.pdf

[Alo89] M. I. Alonso, K. Winer, *Raman spectra of c -$Si_{1-x}Ge_x$ alloys*, Phys. Rev. B **39**, 10 056–10 062 (1989)

[And09] T. Andlauer, *Optoelectronic and spin-related properties of semiconductor nanostructures in magnetic fields* (Verein zur Förderung des Walter Schottky Instituts der Technischen Universität München, 2009), ISBN 978-3-941650-05-3, dissertation

[And12] B. Andreev, Z. Krasilnik, D. Kryzhkov, D. Shengurov, A. Yablonskiy, V. Kuznetsov, *Luminescent properties of MBE-grown Si:Er/SOI structures*, Journal of Luminescence (2012)

[Ape95] R. Apetz, L. Vescan, A. Hartmann, C. Dieker, H. Lüth, *Photoluminescence and electroluminescence of SiGe dots fabricated by island growth*, Applied Physics Letters **66**, 445–447 (1995)

[Ara11] L. Arapkina, V. Yuryev, *CMOS-compatible dense arrays of Ge quantum dots on the Si(001) surface: hut cluster nucleation, atomic structure and array life cycle during UHV MBE growth*, Nanoscale Research Letters **6**, 345 (2011)

[Bai94] T. Baier, U. Mantz, K. Thonke, R. Sauer, F. Schäffler, H.-J. Herzog, *Type-II band alignment in Si-$Si_{1-x}Ge_x$ quantum wells from photoluminescence line shifts due to optically induced band-bending effects: Experiment and theory*, Phys. Rev. B **50**, 15 191–15 196 (1994)

[Bao07] J. Bao, M. Tabbal, T. Kim, S. Charnvanichborikarn, J. Williams, M. Aziz, F. Capasso, *Point defect engineered Si sub-bandgap light-emitting diode*, Opt. Express **15**, 6727–6733 (2007)

[Bas06] S. Baskoutas, A. F. Terzis, *Size-dependent band gap of colloidal quantum dots*, Journal of Applied Physics **99**, 013708 (2006)

[Bea84] J. C. Bean, L. C. Feldman, A. T. Fiory, S. Nakahara, I. K. Robinson, *Ge_xSi_{1-x}/Si strained-layer superlattice grown by molecular beam epitaxy*, Journal of Vacuum Science and Technology A: Vacuum, Surfaces, and Films **2**, 436–440 (1984)

[Ben92] J. L. Benton, B. E. Weir, D. J. Eaglesham, R. A. Gottscho, J. Michel, L. C. Kimerling, *Measurement of defect profiles in reactive ion etched silicon*, Journal of Vacuum Science Technology B **10**, 540–543 (1992)

[Bir07] S. Birner, T. Zibold, T. Andlauer, T. Kubis, M. Sabathil, A. Trellakis, P. Vogl, *nextnano: General Purpose 3-D Simulations*, IEEE Transactions on Electron Devices **54**, 2137 –2142 (2007)

[Blo29] F. Bloch, *Über die Quantenmechanik der Elektronen in Kristallgittern*, Zeitschrift für Physik A Hadrons and Nuclei **52**, 555–600 (1929)

[Boe90] K. W. Boer, *Survey of Semiconductor Physics* (Springer, 1990), 2 edition

[Bou01] P. Boucaud, S. Sauvage, M. El Kurdi, E. Mercier, T. Brunhes, V. Thanh, D. Bouchier, O. Kermarrec, Y. Campidelli, D. Bensahel, *Optical recombination from excited states in Ge/Si self-assembled quantum dots*, Phys. Rev. B **64**, 155 310 (2001)

[Bou04] D. Bougeard, P. Tan, M. Sabathil, P. Vogl, G. Abstreiter, K. Brunner, *Resonant Raman scattering of discrete hole states in self-assembled Si/Ge quantum dots*, Physica E: Low-dimensional Systems and Nanostructures **21**, 312 – 316 (2004)

[Bou05] D. Bougeard, *Spektroskopische charakterisierung von Germanium-Quantenpunkten in Silizium* (Verein zur Förderung des Walter Schottky Instituts der Technischen Universität München, 2005), ISBN 3-932749-74-X, dissertation

[Bre92] G. Bremond, A. Souifi, T. Benyattou, D. Dutartre, *Photoluminescence and electrical characterization of SiGe/Si heterostructures grown by rapid thermal chemical vapour deposition*, Thin Solid Films **222**, 60 – 68 (1992)

[Bre08] M. Brehm, M. Grydlik, H. Lichtenberger, T. Fromherz, N. Hrauda, W. Jantsch, F. Schäffler, G. Bauer, *Quantitative determination of Ge profiles across SiGe wetting layers on Si (001)*, Applied Physics Letters **93**, 121901 (2008)

[Bre09a] M. Brehm, F. Montalenti, M. Grydlik, G. Vastola, H. Lichtenberger, N. Hrauda, M. J. Beck, T. Fromherz, F. Schäffler, L. Miglio, G. Bauer, *Key role of the wetting layer in revealing the hidden path of Ge/Si(001) Stranski-Krastanow growth onset*, Phys. Rev. B **80**, 205 321 (2009)

[Bre09b] M. Brehm, T. Suzuki, T. Fromherz, Z. Zhong, N. Hrauda, F. Hackl, J. Stangl, F. Schäffler, G. Bauer, *Combined structural and photoluminescence study of SiGe islands on Si substrates: comparison with realistic energy level calculations*, New Journal of Physics **11**, 063 021 (2009)

[Bre10] M. Brehm, M. Grydlik, F. Hackl, E. Lausecker, T. Fromherz, G. Bauer, *Excitation Intensity Driven PL Shifts of SiGe Islands on Patterned and Planar Si(001) Substrates: Evidence for Ge-rich Dots in Islands*, Nanoscale Research Letters **5**, 1868–1872 (2010)

[Bru92] J. Brunner, U. Menczigar, M. Gail, E. Friess, G. Abstreiter, *Band gap luminescence in pseudomorphic $Si_{1-x}Ge_x$ quantum wells grown by molecular beam epitaxy*, Thin Solid Films **222**, 27 – 29 (1992)

[Bru95] J. Brunner, P. Schittenhelm, J. Gondermann, B. Spangenberg, B. Hadam, T. Köster, H. G. Roskos, H. Kurz, H. Gossner, I. Eisele, G. Abstreiter, *SiGe wires and dots grown by local epitaxy*, Journal of Crystal Growth **150, Part 2**, 1060 – 1064 (1995)

[Bru00] T. Brunhes, P. Boucaud, S. Sauvage, F. Aniel, J.-M. Lourtioz, C. Hernandez, Y. Campidelli, O. Kermarrec, D. Bensahel, G. Faini, I. Sagnes, *Electroluminescence of Ge/Si self-assembled quantum dots grown by chemical vapor deposition*, Applied Physics Letters **77**, 1822–1824 (2000)

[Bru01] K. Brunner, G. Abstreiter, *Ordering and Electronic Properties of Self-Assembled Si/Ge Quantum Dots*, Japanese Journal of Applied Physics **40**, 1860–1865 (2001)

[Bru02] K. Brunner, *Si/Ge nanostructures*, Reports on Progress in Physics **65**, 27 (2002)

[Can90] L. Canham, *Silicon quantum wire array fabrication by electrochemical and chemical dissolution of wafers*, Applied Physics Letters **57**, 1046–1048 (1990)

[Can95] L. Canham, *Luminescence Bands and their Proposed Origins In Highly Porous Silicon*, physica status solidi (b) **190**, 9–14 (1995)

[Car66] M. Cardona, F. H. Pollak, *Energy-Band Structure of Germanium and Silicon: The k·p Method*, Phys. Rev. **142**, 530–543 (1966)

[Cha77] M. Chandrasekhar, F. H. Pollak, *Effects of uniaxial stress on the electroreflectance spectrum of Ge and GaAs*, Phys. Rev. B **15**, 2127–2144 (1977)

[Cha03a] W.-H. Chang, W.-Y. Chen, A.-T. Chou, T.-M. Hsu, P.-S. Chen, Z. Pei, L.-S. Lai, *Effects of spacer thickness on optical properties of stacked Ge/Si quantum dots grown by chemical vapor deposition*, Journal of Applied Physics **93**, 4999–5002 (2003)

[Cha03b] W.-H. Chang, A. T. Chou, W. Y. Chen, H. S. Chang, T. M. Hsu, Z. Pei, P. S. Chen, S. W. Lee, L. S. Lai, S. C. Lu, M.-J. Tsai, *Room-temperature electroluminescence at 1.3 and 1.5 μm from Ge/Si self-assembled quantum dots*, Applied Physics Letters **83**, 2958–2960 (2003)

[Coo84] D. Coon, R. Karunasiri, *New mode of IR detection using quantum wells*, Applied Physics Letters **45**, 649–651 (1984)

[Coo90] D. E. Cooper, J. Bajaj, P. R. Newman, *Photoluminescence spectroscopy of excitons for evaluation of high-quality CdTe crystals*, Journal of Crystal Growth **86**, 544 – 551 (1990)

[Cor93] R. Corkish, M. A. Green, *Band edge optical absorption in intrinsic silicon: Assessment of the indirect transition and disorder models*, Journal of Applied Physics **73**, 3988–3996 (1993)

[d'A12] M. d'Avezac, J.-W. Luo, T. Chanier, A. Zunger, *Genetic-Algorithm Discovery of a Direct-Gap and Optically Allowed Superstructure from Indirect-Gap Si and Ge Semiconductors*, Phys. Rev. Lett. **108**, 027 401 (2012)

[Dar99] I. Daruka, J. Tersoff, A.-L. Barabási, *Shape Transition in Growth of Strained Islands*, Phys. Rev. Lett. **82**, 2753–2756 (1999)

[Dar02] I. Daruka, J. Tersoff, *Existence of shallow facets at the base of strained epitaxial islands*, Phys. Rev. B **66**, 132 104 (2002)

[Das01] M. W. Dashiell, U. Denker, O. G. Schmidt, *Photoluminescence investigation of phononless radiative recombination and thermal-stability of germanium hut clusters on silicon(001)*, Applied Physics Letters **79**, 2261–2263 (2001)

[Dav89] G. Davies, *The optical properties of luminescence centres in silicon*, Physics Reports **176**, 83 – 188 (1989)

[Dea65] B. E. Deal, A. S. Grove, *General Relationship for the Thermal Oxidation of Silicon*, Journal of Applied Physics **36**, 3770–3778 (1965)

[Dea67] P. J. Dean, J. R. Haynes, W. F. Flood, *New Radiative Recombination Processes Involving Neutral Donors and Acceptors in Silicon and Germanium*, Phys. Rev. **161**, 711–729 (1967)

[Dem07] I. N. Demchenko, K. Lawniczak-Jablonska, S. Kret, A. V. Novikov, J.-Y. Laval, M. Zak, A. Szczepanska, A. N. Yablonskiy, Z. F. Krasilnik, *The effect of local atomic structure on the optical properties of GeSi self-assembled islands buried in silicon matrix*, Nanotechnology **18**, 115 711 (2007)

[Den03] U. Denker, M. Stoffel, O. G. Schmidt, *Probing the Lateral Composition Profile of Self-Assembled Islands*, Phys. Rev. Lett. **90**, 196 102 (2003)

[Den04] U. Denker, H. Sigg, O. Schmidt, *Intermixing in Ge hut cluster islands*, Applied Surface Science **224**, 127 – 133 (2004)

[Dis64] J. P. Dismukes, L. Ekstrom, R. J. Paff, *Lattice Parameter and Density in Germanium-Silicon Alloys*, The Journal of Physical Chemistry **68**, 3021–3027 (1964)

[Do03] Y. R. Do, Y. C. Kim, Y.-W. Song, C.-O. Cho, H. Jeon, Y.-J. Lee, S.-H. Kim, Y.-H. Lee, *Enhanced Light Extraction from Organic Light-Emitting Diodes with 2D SiO2/SiN$_x$ Photonic Crystals*, Advanced Materials **15**, 1214–1218 (2003)

[Dor09a] D. Dorfner, *Novel photonic biosensing based on Silicon nanostructures* (Verein zur Förderung des Walter Schottky Instituts der Technischen Universität München, 2009), ISBN 978-3-941650-04-6, dissertation

[Dor09b] D. Dorfner, T. Zabel, T. Hürlimann, N. Hauke, L. Frandsen, U. Rant, G. Abstreiter, J. Finley, *Photonic crystal nanostructures for optical biosensing applications*, Biosensors and Bioelectronics **24**, 3688 – 3692 (2009)

[DS08] M. De Seta, G. Capellini, F. Evangelisti, *Alloying in* Ge(Si)Si(001) *self-assembled islands during their growth and capping: XPS and AFM study*, Phys. Rev. B **77**, 045 431 (2008)

[Dvu02] A. V. Dvurechenskii, A. V. Nenashev, A. I. Yakimov, *Electronic structure of Ge/Si quantum dots*, Nanotechnology **13**, 75 (2002)

[Eag90] D. Eaglesham, M. Cerullo, *Dislocation-free Stranski-Krastanow growth of Ge on Si(100)*, Phys. Rev. Lett. **64**, 1943–1946 (1990)

[Ebe90] K. Eberl, *Herstellung und Charakterisierung von Silizium/Germanium Heterostrukturen und kurzperiodigen Übergittern*, Doctoral thesis, TU München (1990)

[EK06] M. El Kurdi, S. Sauvage, G. Fishman, P. Boucaud, *Band-edge alignment of* SiGe/Si *quantum wells and* SiGe/Si *self-assembled islands*, Phys. Rev. B **73**, 195 327 (2006)

[El 08] M. El Kurdi, X. Checoury, S. David, T. P. Ngo, N. Zerounian, P. Boucaud, O. Kermarrec, Y. Campidelli, D. Bensahel, *Quality factor of Si-based photonic crystal L3 nanocavities probed with aninternal source*, Opt. Express **16**, 8780–8791 (2008)

[Fan06] A. Fang, H. Park, O. Cohen, R. Jones, M. Paniccia, J. Bowers, *Electrically pumped hybrid AlGaInAs-silicon evanescent laser*, Opt. Express **14**, 9203–9210 (2006)

[Fau93] P. Fauchet, E. Ettedgui, A. Raisanen, L. Brillson, F. Seiferth, S. Kurinec, Y. Gao, C. Peng, L. Tsybeskov, *Can Oxidation and Other Treatments Help Us Understand the Nature of Light-Emitting Porous Silicon?*, MRS Proceedings **298** (1993)

[Fox06] M. Fox, *Quantum Optics: An introduction* (Oxford University Press, 2006)

[Fri92] E. Friess, *Molekularstrahl-Epitaxie von dotierten Si/SiGe-Schichtsystemen: Grundlagen für neue Heterostrukturbauelemente*, Doctoral thesis, TU München (1992)

[Fuk92] S. Fukatsu, H. Yoshida, N. Usami, A. Fujiwara, Y. Takahashi, Y. Shiraki, R. Ito, *Quantum Size Effect of Excitonic Band-Edge Luminescence in Strained $Si_{1-x}Ge_x$/Si Single Quantum Well Structures Grown by Gas-Source Si Molecular Beam Epitaxy*, Japanese Journal of Applied Physics **31**, L1319–L1321 (1992)

[Fuk93] S. Fukatsu, Y. Shiraki, *Optical investigation of interwell coupling in strained $Si_{1-x}Ge_x$/Si quantum wells*, Applied Physics Letters **63**, 2378–2380 (1993)

[Fuk95] S. Fukatsu, H. Akiyama, Y. Shiraki, H. Sakaki, *Quantitative analysis of light emission from SiGe quantum wells*, Journal of Crystal Growth **157**, 1 – 10 (1995)

[Fuk97] S. Fukatsu, H. Sunamura, Y. Shiraki, S. Komiyama, *Phononless radiative recombination of indirect excitons in a Si/Ge type-II quantum dot*, Applied Physics Letters **71**, 258–260 (1997)

[Gav08] M. Gavelle, E. M. Bazizi, E. Scheid, P. F. Fazzini, F. Cristiano, C. Armand, W. Lerch, S. Paul, Y. Campidelli, A. Halimaoui, *Detailed investigation of Ge-Si interdiffusion in the full range of $Si_{1-x}Ge_x (0 \leq x \leq 1)$ composition*, Journal of Applied Physics **104**, 113524 (2008)

[Geb10] T. Geballe, *Gemini Observatory* (2010), http://www.gemini.edu/sciops/telescopes-and-sites/observing-condition-constraints?q=node/10789#Near-IR

[Gei11] R. Geiger, *Towards and efficient silicon-based LED with germanium islands as active emitters*, Diploma thesis, TU München (2011)

[Gnu74] U. Gnutzmann, K. Clausecker, *Theory of direct optical transitions in an optical indirect semiconductor with a superlattice structure*, Applied Physics A: Materials Science & Processing **3**, 9–14 (1974), 10.1007/BF00892328

[Gro97] J. Groenen, R. Carles, S. Christiansen, M. Albrecht, W. Dorsch, H. P. Strunk, H. Wawra, G. Wagner, *Phonons as probes in self-organized SiGe islands*, Applied Physics Letters **71**, 3856–3858 (1997)

[Hab90] R. Haber, W. O'Mara, L. Hunt, *Handbook of Semiconductor Silicon Technology* (William Andrew Inc., 1990), ISBN 978-0815512370

[Häc94] R. Häcker, A. Hangleiter, *Intrinsic upper limits of the carrier lifetime in silicon*, Journal of Applied Physics **75**, 7570–7572 (1994)

[Ham76] R. B. Hammond, T. C. McGill, J. W. Mayer, *Temperature dependence of the electron-hole-liquid luminescence in Si*, Phys. Rev. B **13**, 3566–3575 (1976)

[Ham80] R. Hammond, R. Silver, *Temperature dependence of the exciton lifetime in high-purity silicon*, Applied Physics Letters **36**, 68–71 (1980)

[Hap02] T. D. Happ, I. I. Tartakovskii, V. D. Kulakovskii, J.-P. Reithmaier, M. Kamp, A. Forchel, *Enhanced light emission of $In_xGa_{1-x}As$ quantum dots in a two-dimensional photonic-crystal defect microcavity*, Phys. Rev. B **66**, 041 303 (2002)

[Har05] P. Harrison, *Quantum Wells, Wires and Dots* (Wiley-Interscience, 2005), 2 edition

[Hau10] N. Hauke, T. Zabel, K. Müller, M. Kaniber, A. Laucht, D. Bougeard, G. Abstreiter, J. J. Finley, Y. Arakawa, *Enhanced photoluminescence emission from two-dimensional silicon photonic crystal nanocavities*, New Journal of Physics **12**, 053 005 (2010)

[Hau11] N. Hauke, S. Lichtmannecker, T. Zabel, F. P. Laussy, A. Laucht, M. Kaniber, D. Bougeard, G. Abstreiter, J. J. Finley, Y. Arakawa, *Correlation between emission intensity of self-assembled germanium islands and quality factor of silicon photonic crystal nanocavities*, Phys. Rev. B **84**, 085 320 (2011)

[Hau12] N. Hauke, *Enhanced spontaneous emission from silicon-based photonic crystal nanostructures* (Verein zur Förderung des Walter Schottky Instituts der Technischen Universität München, 2012), ISBN 978-3941650398, dissertation

[Heo10] J. Heo, T. Zhu, C. Zhang, J. Xu, P. Bhattacharya, *Electroluminescence from silicon-based photonic crystal microcavities with PbSe quantum dots*, Opt. Lett. **35**, 547–549 (2010)

[Hor07] I. Horcas, R. Fernández, J. M. Gómez-Rodríguez, J. Colchero, J. Gómez-Herrero, A. M. Baro, *WSXM: A software for scanning probe microscopy and a tool for nanotechnology*, Review of Scientific Instruments **78**, 013705 (2007)

[Hou95] D. C. Houghton, G. C. Aers, S.-R. E. Yang, E. Wang, N. L. Rowell, *Type I Band Alignment in $Si_{1-x}Ge_x$/Si(001) Quantum Wells: Photoluminescence under Applied [110] and [100] Uniaxial Stress*, Phys. Rev. Lett. **75**, 866–869 (1995)

[Hua98] J. Huang, Z. Ye, H. Lu, D. Que, *Calculation of critical layer thickness considering thermal strain in $Si_{1-x}Ge_x$/Si strained-layer heterostructures*, Journal of Applied Physics **83**, 171–173 (1998)

[Hua01] C. J. Huang, Y. Tang, D. Z. Li, B. W. Cheng, L. P. Luo, J. Z. Yu, Q. M. Wang, *Different transfer paths for thermally activated electrons and holes in self-organized Ge/Si(001) islands in a multilayer structure*, Applied Physics Letters **78**, 2006–2008 (2001)

[Jes98] D. E. Jesson, G. Chen, K. M. Chen, S. J. Pennycook, *Self-Limiting Growth of Strained Faceted Islands*, Phys. Rev. Lett. **80**, 5156–5159 (1998)

[Jin03] G. Jin, J. L. Liu, K. L. Wang, *Temperature effect on the formation of uniform self-assembled Ge dots*, Applied Physics Letters **83**, 2847–2849 (2003)

[JJ08] J. W. J. Joannopoulos, S. Johnson, R. Meade, *Molding the Flow of Light*, volume 2 (Princeton Universtiy Press, 2008), ISBN 978-0-691-12456-8

[Joh87] S. John, *Strong localization of photons in certain disordered dielectric superlattices*, Phys. Rev. Lett. **58**, 2486–2489 (1987)

[Joh01] S. G. Johnson, J. D. Joannopoulos, *Block-iterative frequency-domain methods for Maxwell's equations in a planewave basis*, Opt. Express **8**, 173–190 (2001)

[Kam97] T. I. Kamins, E. C. Carr, R. S. Williams, S. J. Rosner, *Deposition of three-dimensional Ge islands on Si(001) by chemical vapor deposition at atmospheric and reduced pressures*, Journal of Applied Physics **81**, 211–219 (1997)

[Kam98] T. I. Kamins, G. Medeiros-Ribeiro, D. A. A. Ohlberg, R. S. Williams, *Dome-to-pyramid transition induced by alloying of Ge islands on Si(001)*, Applied Physics A: Materials Science and Processing **67**, 727–730 (1998)

[Kam99] T. I. Kamins, G. Medeiros-Ribeiro, D. A. A. Ohlberg, R. S. Williams, *Evolution of Ge islands on Si(001) during annealing*, Journal of Applied Physics **85**, 1159–1171 (1999)

[Kam05] B. V. Kamenev, L. Tsybeskov, J.-M. Baribeau, D. J. Lockwood, *Coexistence of fast and slow luminescence in three-dimensional Si/$Si_{1-x}Ge_x$ nanostructures*, Phys. Rev. B **72**, 193 306 (2005)

[Kas75] E. Kasper, H. Herzog, H. Kibbel, *A one-dimensional SiGe superlattice grown by UHV epitaxy*, Applied Physics A: Materials Science & Processing **8**, 199–205 (1975)

[Käs99] M. Kästner, B. Voigtländer, *Kinetically Self-Limiting Growth of Ge Islands on Si(001)*, Phys. Rev. Lett. **82**, 2745–2748 (1999)

[Kas04] E. Kasper, S. Heim, *Challenges of high Ge content silicon germanium structures*, Applied Surface Science **224**, 3 – 8 (2004)

[Kel86] L. V. Keldysh, *The electron-hole liquid in semiconductors*, Contemporary Physics **27**, 395–428 (1986)

[Kim05] D.-H. Kim, C.-O. Cho, Y.-G. Roh, H. Jeon, Y. S. Park, J. Cho, J. S. Im, C. Sone, Y. Park, W. J. Choi, Q.-H. Park, *Enhanced light extraction from GaN-based light-emitting diodes with holographically generated two-dimensional photonic crystal patterns*, Applied Physics Letters **87**, 203508 (2005)

[Kim07] K. Kim, J. Choi, J. B. Park, S. C. Jeon, J. S. Kim, H. M. Lee, *Electroluminescence from lattice defects of photonic crystal slabs in blue-light-emitting diodes*, Journal of Applied Physics **102**, 046105 (2007)

[Kir04] O. Kirfel, E. Müller, D. Grützmacher, K. Kern, A. Hesse, J. Stangl, V. Holý, G. Bauer, *Shape and composition change of Ge dots due to Si capping*, Applied Surface Science **224**, 139 – 142 (2004)

[Kit89] C. Kittel, *Einführung in die Festkörperphysik* (Oldenbourg Wissenschaftsverlag, 1989), 8 edition, ISBN 3-486-21416-3

[Koh04] S. Koh, K. Konishi, Y. Shiraki, *Small and high-density GeSiC dots stacked on buried Ge hut-clusters in Si*, Physica E: Low-dimensional Systems and Nanostructures **21**, 440 – 444 (2004)

[Kös96] T. Köster, B. Hadam, J. Gondermann, B. Spangenberg, H. G. Roskos, H. Kurz, J. Brunner, G. Abstreiter, *Investigation of Si/SiGe heterostructures patterned by reactive ion etching*, Microelectron. Eng. **30**, 341–344 (1996)

[Kra96] T. Krauss, R. De La Rue, S. Brand, *Two-dimensional photonic-bandgap structures operating at near-infrared wavelengths*, Nature **383**, 699–702 (1996)

[Kre05] A. Kress, F. Hofbauer, N. Reinelt, H. Krenner, M. Bichler, D. Schuh, R. Meyer, G. Abstreiter, J. Finley, *Investigation of cavity modes and direct observation of Purcell enhancement in 2D photonic crystal defect microcavities*, Physica E: Low-dimensional Systems and Nanostructures **26**, 351 – 355 (2005)

[Kur06] E. Kuramochi, M. Notomi, S. Mitsugi, A. Shinya, T. Tanabe, T. Watanabe, *Ultrahigh-Q photonic crystal nanocavities realized by the local width modulation of a line defect*, Applied Physics Letters **88**, 041112 (2006)

[Lar03] M. Larsson, A. Elfving, P. Holtz, G. Hansson, W.-X. Ni, *Photoluminescence study of Si/Ge quantum dots*, Surface Science **532-535**, 832 – 836 (2003)

[Lau71] L. D. Laude, F. H. Pollak, M. Cardona, *Effects of Uniaxial Stress on the Indirect Exciton Spectrum of Silicon*, Phys. Rev. B **3**, 2623–2636 (1971)

[Lau09] A. Laucht, F. Hofbauer, N. Hauke, J. Angele, S. Stobbe, M. Kaniber, G. Böhm, P. Lodahl, M.-C. Amann, J. J. Finley, *Electrical control of spontaneous emission and strong coupling for a single quantum dot*, New Journal of Physics **11**, 023 034 (2009)

[Len92] L. C. Lenchyshyn, M. L. W. Thewalt, J. C. Sturm, P. V. Schwartz, E. J. Prinz, N. L. Rowell, J.-P. Noël, D. C. Houghton, *High quantum efficiency photoluminescence from localized excitons in* $Si_{1-x}Ge_x$, Applied Physics Letters **60**, 3174–3176 (1992)

[Leo95] R. Leon, S. Fafard, D. Leonard, J. L. Merz, P. M. Petroff, *Visible luminescence from semiconductor quantum dots in large ensembles*, Applied Physics Letters **67**, 521–523 (1995)

[Li80] H. H. Li, *Refractive index of silicon and germanium and its wavelength and temperature derivatives*, Journal of Physical and Chemical Reference Data **9**, 561–658 (1980)

[Li06] X. Li, P. Boucaud, X. Checoury, O. Kermarrec, Y. Campidelli, D. Bensahel, *Probing photonic crystals on silicon-on-insulator with Ge/Si self-assembled islands as an internal source*, Journal of Applied Physics **99**, 023103 (2006)

[Lin98] S. Y. Lin, J. G. Fleming, D. L. Hetherington, B. K. Smith, W. Zubrzycki, S. R. Kurtz, J. Bur, *A three-dimensional photonic crystal operating at infrared wavelengths*, Nature **394**, 1997–1999 (1998)

[Loc10] D. J. Lockwood, N. L. Rowell, I. Berbezier, G. Amiard, A. Ronda, M. Faustini, D. Grosso, *Predicting Size Distributions of Ge Nanodots from Their Photoluminescence*, Journal of The Electrochemical Society **157**, H1160–H1164 (2010)

[Lon00] M. Loncar, T. Doll, J. Vuckovic, A. Scherer, *Design and fabrication of silicon photonic crystal optical waveguides*, Lightwave Technology, Journal of **18**, 1402 – 1411 (2000)

[Mac94] M. H. MacDougal, H. Zhao, P. D. Dapkus, M. Ziari, W. H. Steier, *Wide-bandwidth distributed Bragg reflectors using oxide/GaAs multilayers*, Electronics Letters **30**, 1147 –1149 (1994)

[Mad07] J. R. Madureira, M. P. F. de Godoy, M. J. S. P. Brasil, F. Iikawa, *Spatially indirect excitons in type-II quantum dots*, Applied Physics Letters **90**, 212105 (2007)

[MaP02] R. Magalhães Paniago, G. Medeiros-Ribeiro, A. Malachias, S. Kycia, T. I. Kamins, R. S. Williams, *Direct evaluation of composition profile, strain relaxation, and elastic energy of Ge:Si(001) self-assembled islands by anomalous x-ray scattering*, Phys. Rev. B **66**, 245 312 (2002)

[Mat74] J. Matthews, A. Blakeslee, *Defects in epitaxial multilayers: I. Misfit dislocations*, Journal of Crystal Growth **27**, 118 – 125 (1974)

[Mat75] J. Matthews, A. Blakeslee, *Defects in epitaxial multilayers: II. Dislocation pile-ups, threading dislocations, slip lines and cracks*, Journal of Crystal Growth **29**, 273 – 280 (1975)

[Mat03] K. Matsuda, T. Saiki, S. Nomura, M. Mihara, Y. Aoyagi, S. Nair, T. Takagahara, *Near-Field Optical Mapping of Exciton Wave Functions in a GaAs Quantum Dot*, Phys. Rev. Lett. **91**, 177 401 (2003)

[Men84] J. Menéndez, M. Cardona, *Temperature dependence of the first-order Raman scattering by phonons in Si, Ge, and αSn: Anharmonic effects*, Phys. Rev. B **29**, 2051–2059 (1984)

[Men92] U. Menczigar, J. Brunner, E. Friess, M. Gail, G. Abstreiter, H. Kibbel, H. Presting, E. Kasper, *Photoluminescence studies of $Si/Si_{1-x}Ge_x$ quantum wells and Si_mGe_n superlattices*, Thin Solid Films **222**, 227 – 233 (1992)

[Men93] U. Menczigar, G. Abstreiter, J. Olajos, H. Grimmeiss, H. Kibbel, H. Presting, E. Kasper, *Enhanced band-gap luminescence in strain-symmetrized $(Si)_m/(Ge)_n$ superlattices*, Phys. Rev. B **47**, 4099–4102 (1993)

[Mic01] MicroChem Corp., *PMMA datasheet* (2001), http://www.microchem.com/pdf/PMMA_Data_Sheet.pdf

[Mic12] Microchemicals GmbH, *Wet chemical etching of silicon* (2012), http://www.microchemicals.eu/technical_information/silicon_etching.pdf

[Mie01] C. A. Miesner, *Intra-Valenzbandspektroskopie an SiGe-Nanostrukturen in Si* (Verein zur Förderung des Walter Schottky Instituts der Technischen Universität München, 2001), ISBN 978-3932749384, dissertation

[Mo90] Y.-W. Mo, D. E. Savage, B. S. Swartzentruber, M. G. Lagally, *Kinetic pathway in Stranski-Krastanov growth of Ge on Si(001)*, Phys. Rev. Lett. **65**, 1020–1023 (1990)

[Mon04] F. Montalenti, P. Raiteri, D. B. Migas, H. von Känel, A. Rastelli, C. Manzano, G. Costantini, U. Denker, O. G. Schmidt, K. Kern, L. Miglio, *Atomic-Scale Pathway of the Pyramid-to-Dome Transition during Ge Growth on Si(001)*, Phys. Rev. Lett. **93**, 216 102 (2004)

[MR98a] G. Medeiros-Ribeiro, A. M. Bratkovski, T. I. Kamins, D. A. A. Ohlberg, R. S. Williams, *Shape Transition of Germanium Nanocrystals on a Silicon (001) Surface from Pyramids to Domes*, Science **279**, 353–355 (1998)

[MR98b] G. Medeiros-Ribeiro, T. I. Kamins, D. A. A. Ohlberg, R. S. Williams, *Annealing of Ge nanocrystals on Si(001) at* 550°C*: Metastability of huts and the stability of pyramids and domes*, Phys. Rev. B **58**, 3533–3536 (1998)

[Nau06] O. Naumova, E. Vohmina, T. Gavrilova, N. Dudchenko, D. Nikolaev, E. Spesivtsev, V. Popov, *Properties of silicon nanolayers on insulator*, Materials Science and Engineering: B **135**, 238 – 241 (2006)

[Nec12] D. Necas, P. Klapetek, *Gwyddion: an open-source software for SPM data analysis*, Central European Journal of Physics **10**, 181–188 (2012)

[Nil73] N. Nilsson, *Band-to-band Auger Recombination in Silicon and Germanium*, Physica Scripta **8**, 165 (1973)

[Nis12] K. Nishikawa, Y. Takeda, K. Yamanaka, T. Motohiro, D. Sato, J. Ota, N. Miyashita, Y. Okada, *Over 100 ns intrinsic radiative recombination lifetime in type II InAs/GaAs$_{1-x}$Sb$_x$ quantum dots*, Journal of Applied Physics **111**, 044325 (2012)

[Noë90] J.-P. Noël, N. L. Rowell, D. C. Houghton, D. D. Perovic, *Intense photoluminescence between 1.3 and 1.8 mu m from strained Si$_{1-x}$Ge$_x$ alloys*, Applied Physics Letters **57**, 1037–1039 (1990)

[Nom06] M. Nomura., S. Iwamoto, K. Watanabe, N. Kumagai, Y. Nakata, S. Ishida, Y. Arakawa, *Room temperature continuous-wave lasing in photonic crystal nanocavity*, Opt. Express **14**, 6308–6315 (2006)

[Nov03] A. Novikov, D. Lobanov, A. Yablonsky, Y. Drozdov, N. Vostokov, Z. Krasilnik, *Photoluminescence of Ge(Si)/Si(001) self-assembled islands in the near infra-red wavelength range*, Physica E: Low-dimensional Systems and Nanostructures **16**, 467 – 472 (2003)

[Nüt95] J. Nützel, *Modulationsdotierte Silizium-Germanium-Heterostrukturen*, Doctoral thesis, TU München (1995)

[Oli02] S. N. Olivier, C. J. M. Smith, H. Benisty, C. Weisbuch, T. F. Krauss, R. Houdre, U. Oesterle, *Cascaded photonic crystal guides and cavities: spectral studies and their impact on integrated optics design*, IEEE Journal of Quantum Electronics **38**, 816 –824 (2002)

[Oxf] Oxford Instruments, *PlasmaLab80Plus*, http://www.oxfordplasma.de/systems/80plus.htm

[Pav08] L. Pavesi, *Silicon-Based Light Sources for Silicon Integrated Circuits*, Advances in Optical Technologies **2008**, 1–13 (2008)

[Peo86] R. People, J. C. Bean, *Band alignments of coherently strained Ge_xSi_{1-x}/Si heterostructures on $\langle 001 \rangle$ Ge_ySi_{1-y} substrates*, Applied Physics Letters **48**, 538–540 (1986)

[Phi62] J. C. Phillips, *Band Structure of Silicon, Germanium, and Related Semiconductors*, Phys. Rev. **125**, 1931–1936 (1962)

[Pok04] E. Pokatilov, D. Nika, A. Balandin, *Confined electron-confined phonon scattering rates in wurtzite AlN/GaN/AlN heterostructures*, Journal of Applied Physics **95**, 5626–5632 (2004)

[Poz05] S. Pozder, M. Canonico, S. Zollner, R. Liu, K. Yu, J.-Q. Lu, *Raman and XRD Strain Analysis of 3D Bonded And Thinned SOI Wafers*, AIP Conference Proceedings **772**, 1495–1496 (2005)

[Pre99] O. V. Prezhdo, *Mean field approximation for the stochastic Schrödinger equation*, The Journal of Chemical Physics **111**, 8366–8377 (1999)

[Pry98] C. Pryor, J. Kim, L. W. Wang, A. J. Williamson, A. Zunger, *Comparison of two methods for describing the strain profiles in quantum dots*, Journal of Applied Physics **83**, 2548–2554 (1998)

[Qua] Quantum dot & photonic nanostructures group homepage, *Simple view of the electronic structure*, http://pages.ief.u-psud.fr/QDgroup/modeling.html#Three-dimensional_8_band_k.p_resolution

[Rai02] P. Raiteri, L. Miglio, F. Valentinotti, M. Celino, *Strain maps at the atomic scale below Ge pyramids and domes on a Si substrate*, Applied Physics Letters **80**, 3736–3738 (2002)

[Ren71] M. Renucci, J. Renucci, M. Cardona, M. Balkanski, *Light Scattering in Solids* (Flammarion, Paris, 1971)

[Ren08] G. Ren, W.-H. Zheng, Y.-J. Zhang, M.-X. Xing, K. Wang, X.-Y. Du, L.-H. Chen, *Room-Temperature Photonic Crystal Laser in H3 Cavity on InGaAsP/InP Slab*, Chinese Physics Letters **25**, 981 (2008)

[RH98] J. C. B. R. Hull, *Germanium silicon: physics and materials* (Academic Press Inc., 1998), ISBN 978-0127521640

[Ric90] E. Richmond, J. Pellegrino, M. Twiff, S. Qadri, M. Duffy, *Unique properties of molecular beam epitaxy silicon on sapphire using in situ high-temperature substrate annealing compared with chemically vapor deposited silicon on sapphire*, Thin Solid Films **192**, 287 – 294 (1990)

[Rie93] M. M. Rieger, P. Vogl, *Electronic-band parameters in strained $Si_{1-x}Ge_x$ alloys on $Si_{1-y}Ge_y$ substrates*, Phys. Rev. B **48**, 14 276–14 287 (1993)

[Rob29] H. P. Robertson, *The Uncertainty Principle*, Phys. Rev. **34**, 163–164 (1929)

[Rob09] J. T. Robinson, A. Rastelli, O. Schmidt, O. D. Dubon, *Global faceting behavior of strained Ge-islands on Si*, Nanotechnology **20**, 085 708 (2009)

[Ron05] H. Rong, R. Jones, A. Liu, O. Cohen, D. Hak, A. Fang, M. Paniccia, *A continuous-wave Raman silicon laser*, Nature **433**, 725–728 (2005)

[Ror93] J. M. Rorison, *Excitons in type-II quantum-dot systems: A comparison of the GaAs/AlAs and InAs/GaSb systems*, Phys. Rev. B **48**, 4643–4649 (1993)

[Ros98] F. M. Ross, J. Tersoff, R. M. Tromp, *Coarsening of Self-Assembled Ge Quantum Dots on Si(001)*, Phys. Rev. Lett. **80**, 984–987 (1998)

[Ros99] F. M. Ross, R. M. Tromp, M. C. Reuter, *Transition States Between Pyramids and Domes During Ge/Si Island Growth*, Science **286**, 1931–1934 (1999)

[Row93] N. L. Rowell, J.-P. Noël, D. C. Houghton, A. Wang, L. C. Lenchyshyn, M. L. W. Thewalt, D. D. Perovic, *Exciton luminescence in $Si_{1-x}Ge_x$/Si heterostructures grown by molecular beam epitaxy*, Journal of Applied Physics **74**, 2790 –2805 (1993)

[Sai10] J. Sailer, *Materials and devices for quantum information processing in Si/SiGe* (Verein zur Förderung des Walter Schottky Instituts der Technischen Universität München, 2010), ISBN 978-3941650213, dissertation

[Sch91] R. Schorer, E. Friess, K. Eberl, G. Abstreiter, *Structural stability of short-period Si/Ge superlattices studied with Raman spectroscopy*, Phys. Rev. B **44**, 1772–1781 (1991)

[Sch92] T. Schmidt, K. Lischka, W. Zulehner, *Excitation-power dependence of the near-band-edge photoluminescence of semiconductors*, Phys. Rev. B **45**, 8989–8994 (1992)

[Sch95] P. Schittenhelm, M. Gail, J. Brunner, J. F. Nützel, G. Abstreiter, *Photoluminescence study of the crossover from two-dimensional to three-dimensional growth for Ge on Si(100)*, Applied Physics Letters **67**, 1292–1294 (1995)

[Sch97a] F. Schäffler, *High-mobility Si and Ge structures*, Semiconductor Science and Technology **12**, 1515 (1997)

[Sch97b] P. Schittenhelm, *Selbst-organisation und Selbst-Ordnung in Si/SiGe heterostrukturen* (Verein zur Förderung des Walter Schottky Instituts der Technischen Universität München, 1997), ISBN 978-3932749025, dissertation

[Sch98] S. Schieker, O. G. Schmidt, K. Eberl, N. Jin-Phillipp, F. Phillipp, *Annealing effects on carbon-induced germanium dots in silicon*, Applied Physics Letters **72**, 3344–3346 (1998)

[Sch99] O. G. Schmidt, O. Kienzle, Y. Hao, K. Eberl, F. Ernst, *Modified Stranski–Krastanov growth in stacked layers of self-assembled islands*, Applied Physics Letters **74**, 1272–1274 (1999)

[Sch00] O. G. Schmidt, K. Eberl, Y. Rau, *Strain and band-edge alignment in single and multiple layers of self-assembled Ge/Si and GeSi/Si islands*, Phys. Rev. B **62**, 16 715–16 720 (2000)

[Sei96] W. Seifert, N. Carlsson, M. Miller, M.-E. Pistol, L. Samuelson, R. Wallenberg, *In-situ growth of quantum dot structures by the Stranski-Krastanow growth mode*, Progress in Crystal Growth and Characterization of Materials **33**, 423–471 (1996)

[Shi94] Y. Shiraki, S. Fukatsu, *Investigation of luminescence in strained SiGe/Si modulated quantum well and wire structures*, Semiconductor Science and Technology **9**, 2017 (1994)

[Shk09] A. Shklyaev, Y. Nakamura, F. Dultsev, M. Ichikawa, *Defect-related light emission in the 1.4–1.7 μm range from Si layers at room temperature*, Journal of Applied Physics **105**, 063513 (2009)

[Shu97] K. Shum, P. M. Mooney, J. O. Chu, *Dislocation-related photoluminescence peak shift due to atomic interdiffusion in SiGe/Si*, Applied Physics Letters **71**, 1074–1076 (1997)

[Sin93] J. Singh, *Physics of Semiconductor and their heterostructures* (Mcgraw-Hill College, 1993), ISBN 0-07-057607-6

[SJ03] J. J. S. Johnson, *Introduction to photonic crystals: Bloch's theorem, band diagrams, and gaps (but no defects)* (2003), http://ab-initio.mit.edu/photons/tutorial/photonic-intro.pdf

[Son02] P. Sonnet, P. C. Kelires, *Monte Carlo studies of stress fields and intermixing in Ge/Si(100) quantum dots*, Phys. Rev. B **66**, 205 307 (2002)

[Spe93] B. Spencer, P. Voorhees, S. Davis, *Morphological instability in epitaxially strained dislocation-free solid films: Linear stability theory*, Journal of Applied Physics **73**, 4955–4970 (1993)

[Spr12] Springer Materials, *Landolt-Börnstein Database* (2012), http://www.springer.com/librarians/e-content/springermaterials?SGWID=1-171102-0-0-0

[Sta04] J. Stangl, V. Holý, G. Bauer, *Structural properties of self-organized semiconductor nanostructures*, Rev. Mod. Phys. **76**, 725–783 (2004)

[Sti97] J. Stimmer, A. Reittinger, E. Neufeld, G. Abstreiter, H. Holzbrecher, U. Breuer, C. Buchal, *Erbium-silicon light-emitting diodes grown by molecular beam epitaxy: Optical properties*, Thin Solid Films **294**, 220 – 222 (1997)

[Stu91] J. C. Sturm, H. Manoharan, L. C. Lenchyshyn, M. L. W. Thewalt, N. L. Rowell, J.-P. Noël, D. C. Houghton, *Well-resolved band-edge photoluminescence of excitons confined in strained $Si_{1-x}Ge_x$ quantum wells*, Phys. Rev. Lett. **66**, 1362–1365 (1991)

[Sun95] H. Sunamura, Y. Shiraki, S. Fukatsu, *Growth mode transition and photoluminescence properties of $Si_{1-x}Ge_x/Si$ quantum well structures with high Ge composition*, Applied Physics Letters **66**, 953–955 (1995)

[Sut98] P. Sutter, M. G. Lagally, *Embedding of Nanoscale 3D SiGe Islands in a Si Matrix*, Phys. Rev. Lett. **81**, 3471–3474 (1998)

[Sze81] S. M. Sze, *Physics of Semiconductor Devices* (Johne Wiley and Sons Inc, 1981)

[Tak92] T. Takagahara, K. Takeda, *Theory of the quantum confinement effect on excitons in quantum dots of indirect-gap materials*, Phys. Rev. B **46**, 15 578–15 581 (1992)

[Tal03] V. G. Talalaev, G. E. Cirlin, A. A. Tonkikh, N. D. Zakharov, P. Werner, *Room temperature electroluminescence from Ge/Si quantum dots superlattice close to 1.6 μm*, physica status solidi (a) **198**, R4–R6 (2003)

[Tan03] P. H. Tan, K. Brunner, D. Bougeard, G. Abstreiter, *Raman characterization of strain and composition in small-sized self-assembled Si/Ge dots*, Phys. Rev. B **68**, 125 302 (2003)

[Tan04] P. H. Tan, D. Bougeard, G. Abstreiter, K. Brunner, *Raman scattering of folded acoustic phonons in self-assembled Si/Ge dot superlattices*, Applied Physics Letters **84**, 2632–2634 (2004)

[Tan11] K. Tanabe, S. Iwamoto, Y. Arakawa, *Novel III-V/Si hybrid laser structures with current injection across conductive wafer-bonded heterointerfaces: A proposal and analysis*, IEICE Electronics Express **8**, 596–603 (2011)

[Tan12] K. Tanabe, K. Watanabe, Y. Arakawa, *III-V/Si hybrid photonic devices by direct fusion bonding.*, Scientific Reports **2**, 349 (2012)

[Ter94] J. Tersoff, F. K. LeGoues, *Competing relaxation mechanisms in strained layers*, Phys. Rev. Lett. **72**, 3570–3573 (1994)

[Ter02] J. Tersoff, B. J. Spencer, A. Rastelli, H. von Känel, *Barrierless Formation and Faceting of SiGe Islands on Si(001)*, Phys. Rev. Lett. **89**, 196 104 (2002)

[The97] M. L. W. Thewalt, D. A. Harrison, C. F. Reinhart, J. A. Wolk, H. Lafontaine, *Type II Band Alignment in $Si_{1-x}Ge_x/Si(001)$ Quantum Wells: The Ubiquitous Type I Luminescence Results from Band Bending*, Phys. Rev. Lett. **79**, 269–272 (1997)

[Ton03] A. A. Tonkikh, V. G. Dubrovskii, G. E. Cirlin, V. A. Egorov, V. M. Ustinov, P. Werner, *Temperature dependence of the quantum dot lateral size in the Ge/Si(100) system*, physica status solidi (b) **236**, R1–R3 (2003)

[Top07] J. Topolancik, B. Ilic, F. Vollmer, *Experimental Observation of Strong Photon Localization in Disordered Photonic Crystal Waveguides*, Phys. Rev. Lett. **99**, 253 901 (2007)

[Tsa94] J. C. Tsang, P. M. Mooney, F. Dacol, J. O. Chu, *Measurements of alloy composition and strain in thin Ge_xSi_{1-x} layers*, Journal of Applied Physics **75**, 8098–8108 (1994)

[Tsu82] R. Tsu, J. G. Hernandez, *Temperature dependence of silicon Raman lines*, Applied Physics Letters **41**, 1016–1018 (1982)

[Tsy94] L. Tsybeskov, J. Vandyshev, P. Fauchet, *Blue emission in porous silicon: Oxygen-related photoluminescence*, Phys. Rev. B **49**, 7821–7824 (1994)

[Tsy09] L. Tsybeskov, E.-K. Lee, H.-Y. Chang, D. Lockwood, J.-M. Baribeau, X. Wu, T. Kamins, *Silicon-germanium nanostructures for on-chip optical interconnects*, Applied Physics A: Materials Science & Processing **95**, 1015–1027 (2009), 10.1007/s00339-009-5111-8

[Vai00] A. Vailionis, B. Cho, G. Glass, P. Desjardins, D. G. Cahill, J. E. Greene, *Pathway for the Strain-Driven Two-Dimensional to Three-Dimensional Transition during Growth of Ge on Si(001)*, Phys. Rev. Lett. **85**, 3672–3675 (2000)

[Var67] Y. Varshni, *Temperature dependence of the energy gap in semiconductors*, Physica **34**, 149 – 154 (1967)

[VdW86] C. G. Van de Walle, R. M. Martin, *Theoretical calculations of heterojunction discontinuities in the Si/Ge system*, Phys. Rev. B **34**, 5621–5634 (1986)

[Ves92] L. Vescan, K. Schmidt, C. Dieker, H. Tang, T. Vescan, H. Lüth, *Photoluminescence of SiGe/Si quantum wells prepared by LPCVD*, Thin Solid Films **222**, 5 – 9 (1992)

[Vir11] Virginia Semiconductor Inc., *Virginia Semiconductor, Optical Properties of Silicon* (2011), http://www.virginiasemi.com/pdf/Optical

[Vog93] P. Vogl, M. M. Rieger, J. A. Majewski, G. Abstreiter, *How to convert group-IV semiconductors into light emitters*, Physica Scripta **1993**, 476 (1993)

[Vos00] N. Vostokov, I. Dolgov, Y. Drozdov, Z. Krasil'nik, D. Lobanov, L. Moldavskaya, A. Novikov, V. Postnikov, D. Filatov, *Transition from "dome" to "pyramid" shape of self-assembled GeSi islands*, Journal of Crystal Growth **209**, 302 – 305 (2000)

[Wac92] M. Wachter, K. Thonke, R. Sauer, F. Schäffler, H.-J. Herzog, E. Kasper, *Photoluminescence of confined excitons in MBE-grown $Si_{1-x}Ge_x$/Si(100) single quantum wells*, Thin Solid Films **222**, 10 – 14 (1992)

[Wan01a] J. Wan, G. L. Jin, Z. M. Jiang, Y. H. Luo, J. L. Liu, K. L. Wang, *Band alignments and photon-induced carrier transfer from wetting layers to Ge islands grown on Si(001)*, Applied Physics Letters **78**, 1763–1765 (2001)

[Wan01b] J. Wan, Y. H. Luo, Z. M. Jiang, G. Jin, J. L. Liu, K. L. Wang, X. Z. Liao, J. Zou, *Effects of interdiffusion on the band alignment of GeSi dots*, Applied Physics Letters **79**, 1980–1982 (2001)

[Wan01c] J. Wan, Y. H. Luo, Z. M. Jiang, G. Jin, J. L. Liu, K. L. Wang, X. Z. Liao, J. Zou, *Ge/Si interdiffusion in the GeSi dots and wetting layers*, Journal of Applied Physics **90**, 4290–4292 (2001)

[Wan07] K. Wang, D. C., J. L., C. Chen, *Ge/Si Self-Assembled Quantum Dots and Their Optoelectronic Device Applications*, Proceedings of the IEEE **95**, 1866 –1883 (2007)

[Web89] J. Weber, M. I. Alonso, *Near-band-gap photoluminescence of Si-Ge alloys*, Phys. Rev. B **40**, 5683–5693 (1989)

[Wei99] S.-H. Wei, A. Zunger, *Predicted band-gap pressure coefficients of all diamond and zinc-blende semiconductors: Chemical trends*, Phys. Rev. B **60**, 5404–5411 (1999)

[wik12] wikipedia, *Thermal oxidation* (2012), http://en.wikipedia.org/wiki/Thermal_oxidation

[Wil03] K. Williams, K. Gupta, M. Wasilik, *Etch rates for micromachining processing-Part II*, Microelectromechanical Systems, Journal of **12**, 761 – 778 (2003)

[Xia06] J. S. Xia, Y. Ikegami, Y. Shiraki, N. Usami, Y. Nakata, *Strong resonant luminescence from Ge quantum dots in photonic crystal microcavity at room temperature*, Applied Physics Letters **89**, 201102 (2006)

[Xia08] J. Xia, K. Nemoto, Y. Ikegami, N. Usami, Y. Nakata, Y. Shiraki, *Room-temperature light-emission from Ge quantum dots in photonic crystals*, Thin Solid Films **517**, 125 – 127 (2008)

[Yab87] E. Yablonovitch, *Inhibited Spontaneous Emission in Solid-State Physics and Electronics*, Phys. Rev. Lett. **58**, 2059–2062 (1987)

[Yab91] E. Yablonovitch, T. Gmitter, R. Meade, A. Rappe, K. Brommer, J. Joannopoulos, *Donor and acceptor modes in photonic band structure*, Phys. Rev. Lett. **67**, 3380–3383 (1991)

[Yak00] A. I. Yakimov, N. P. Stepina, A. V. Dvurechenskii, A. I. Nikiforov, A. V. Nenashev, *Excitons in charged Ge/Si type-II quantum dots*, Semiconductor Science and Technology **15**, 1125 (2000)

[Yee66] K. Yee, *Numerical solution of initial boundary value problems involving Maxwell's equations in isotropic media*, IEEE Transactions on Antennas and Propagation **14**, 302 –307 (1966)

[Yer10] S. Yerci, R. Li, L. D. Negro, *Electroluminescence from Er-doped Si-rich silicon nitride light emitting diodes*, Applied Physics Letters **97**, 081109 (2010)

[Zab08] T. Zabel, *Optical Biosensing using SOI Photonic Crystal Nanostructures*, Diploma thesis, TU München (2008)

[Zel86] C. Zeller, G. Abstreiter, *Electric subbands in Si/SiGe strained layer superlattices*, Zeitschrift fr Physik B Condensed Matter **64**, 137–143 (1986), 10.1007/BF01303694

[Zha10] J. J. Zhang, F. Montalenti, A. Rastelli, N. Hrauda, D. Scopece, H. Groiss, J. Stangl, F. Pezzoli, F. Schäffler, O. G. Schmidt, L. Miglio, G. Bauer, *Collective Shape Oscillations of SiGe Islands on Pit-Patterned Si(001) Substrates: A Coherent-Growth Strategy Enabled by Self-Regulated Intermixing*, Phys. Rev. Lett. **105**, 166 102 (2010)

[Zib07] T. Zibold, *Semiconductor based quantum information devices: Theory and simulations* (Verein zur Förderung des Walter Schottky Instituts der Technischen Universität München, 2007), ISBN 978-3-932749-87-2, dissertation

List of publications

[Dor08] D. F. Dorfner, T. Hürlimann, T. Zabel, L. H. Frandsen, G. Abstreiter, J. J. Finley, *Silicon photonic crystal nanostructures for refractive index sensing*, Applied Physics Letters **93**, 181103 (2008)

[Dor09] D. Dorfner, T. Zabel, T. Hürlimann, N. Hauke, L. Frandsen, U. Rant, G. Abstreiter, J. Finley, *Photonic crystal nanostructures for optical biosensing applications*, Biosensors and Bioelectronics **24**, 3688 – 3692 (2009)

[Hau10] N. Hauke, T. Zabel, K. Müller, M. Kaniber, A. Laucht, D. Bougeard, G. Abstreiter, J. J. Finley, Y. Arakawa, *Enhanced photoluminescence emission from two-dimensional silicon photonic crystal nanocavities*, New Journal of Physics **12**, 053 005 (2010)

[Hau11] N. Hauke, S. Lichtmannecker, T. Zabel, F. P. Laussy, A. Laucht, M. Kaniber, D. Bougeard, G. Abstreiter, J. J. Finley, Y. Arakawa, *Correlation between emission intensity of self-assembled germanium islands and quality factor of silicon photonic crystal nanocavities*, Phys. Rev. B **84**, 085 320 (2011)

[Hau12] N. Hauke, A. Tandaechanurat, T. Zabel, H. Takagi, T. Reichert, M. Kaniber, S. Iwamoto, D. Bougeard, J. Finley, G. Abstreiter, Y. Arakawa, *Enhanced spontaneous emission from a silicon-based three-dimensional photonic crystal nanocavity*, New Journal of Physics (submitted)

[Zaba] T. Zabel, N. Sircar, N. Hauke, J. Zweck, M. Döblinger, J. Finley, G. Abstreiter, Y. Arakawa, D. Bougeard, *Laterally self-ordered SiGe islands with optimized confinement properties*, (to be submitted)

[Zabb] T. Zabel, N. Hauke, J. Finley, Y. Arakawa, G. Abstreiter, D. Bougeard, *Radiative recombination properties of Ge hut clusters*, (in preparation)

F. Acknowledgment

Diese Arbeit wäre natürlich niemals möglich gewesen ohne die technische, logistische und psychologischer Hilfe von vielen verschiedenen Leuten, welchen ich hier im folgenden endlich einmal danken möchte.

Zuallererst möchte ich mich bei Gerhard Abstreiter bedanken. Ohne dich hätte es weder dieses Projekt noch meine Stelle geben. Außerdem möchte ich dir für viele Diskussionen und für deine Unterstützung danken, welche es mir auch erlaubt hat auf einigen Konferenzen viele interessante Menschen und Themengebiete kennenzulernen. Außerdem möchte ich dir für die Art danken, mit der du E24 am WSI leitest, da hier eine wundervolle Arbeitsatmosphäre geschaffen wurde mit großartigen Möglichkeiten.

Für seine immer motivierende Art und die nie endende Unterstützung möchte ich Dominique Bougeard danken. Ich habe die letzten 3 Jahre gemeinsamer Arbeit sehr genossen. Du warst für uns immer erreichbar, auch nach deinem Umzug nach Regensburg. Des weiteren möchte ich mich bedanken, dass du meine Arbeitsweise immer akzeptiert hast, aber auch an den richtigen Stellen Kritik geäußert hast. Beides zusammen denke ich hat maßgeblich zu den Ergebnissen dieser Arbeit beigetragen.
Außerdem muss ich dir an dieser Stelle noch einmal für deine groß Unterstützung während Normans und meinem Aufenthalt in Japan bedanken. Nach dem Erdbeben und der Fukushima Geschichte hast du es in vielen Skypetelefonaten verstanden unsere Anspannung, den Stress und auch Gewissensbisse zu reduzieren. Sehr hilfreich war dabei vor allem, dass du unsere Entscheidungen mitgetragen hast und mit uns objektiv über die Situation diskutiert hast.

I also want to thank Jonathan J. Finley. Although I never had a lecture with you I think that it was a good idea to do my Diploma thesis in your group. I had a lot of fun and in the end the biosensing results have been really nice. Also during my PhD thesis I always enjoyed working with you as you are a very motivating and enthusiastic person. When I had some problems, for instance when our Argon ion laser died you did not hesitate to come over into our lab for showing me how to align the etalon and how to clean the different laser components. For all those help and for the numerous helpful discussions I want to thank you.

For the strong support during my stay in Tokyo and during the whole project I want to thank Prof. Yasuhiko Arakawa. Due to your efforts I had the possibility to visit one of the most interesting and impressive locations on earth. Actually although I'm not a fan of big cities I somehow still miss Tokyo. Also the earthquake and the successive situation has been an "all-life" experience. I think that in the end I learned a lot during this time.

Meinem Projekt-, Büro-, Bier- und Wohnungspartner Norman möchte ich für unsere Freundschaft während der letzten Jahre danken. Insbesondere während unseres Aufen-

thalts in Japan hat sich gezeigt, dass wir doch sehr gut miteinander auskommen. Ganz speziell in der beengten Wohnung, bei Ausflügen nach Kobe, Kyoto, Atami,... und auch im Labor hat sich dies, denke ich, mehrmals gezeigt.
Auch werde ich wohl nie vergessen, wie wir uns gegenseitig nach Fukushima unterstützt haben und darauf geachtet haben, dass keiner von uns in Panik verfällt.

Des weiteren möchte ich mich bei meinem ersten und einzigen Diplomanden Richard bedanken. Ich hab schnell gemerkt, dass ich mir den richtigen Studenten ausgesucht habe: Einen guten Fußballer, einen sehr guten Gulasch- und Langoschkoch, einen mitdenkenden und selbstständigen Physiker und einen guten Freund. Ich wünsche dir in der Schweiz eine gute Zeit und viele gute Resultate mit verspanntem Germanium. Ich denke auch, dass ich dich schon nochmal besuche, nicht nur wegen des Käsefondues. Ach ja ich werde dich auch weiterhin "meinen Diplomanden" nennen.

Für die Einarbeitung in unseren optischen Aufbau, in Dotierung, in den Themenbereich SiGe und natürlich in unsere schicke MBE Anlage möchte ich mich bei Narayan Sircar, Jürgen Sailer and Stefan Ahlers bedanken. Ihr wart immer hilfsbereit, wenn ich, vor allem zu Beginn meiner Arbeit, mit verschiedensten Fragen ankam und habt diese immer so gut es ging beantwortet. Dadurch habe ich viel von euch gelernt.

Bei Hannes möchte ich mich für die Korrektur meiner Arbeit und für viele nette Gespräche im Büro bedanken. Es war immer lustig mit dir, vor allem wenn du wieder einmal, von "irgendetwas" genervt ins Büro kamst. Ich werde wohl nie dein Gesicht nach unserer "Rührfisch aus dem HF-Abfallkanister" Aktion vergessen. Im Nachhinein - ein Bild für Götter.

Meinem anderen Büronachbarn Hubert Riedl möchte ich meinen größten Respekt und großen Dank aussprechen. Es war eine schöne Zeit mit dir zu Arbeiten. Danke für das Wachstum einiger Proben, für die Hilfe bei den Reparaturen an der RIE, welche im letzten Jahr durch die vielen Nutzer doch recht zahlreich wurden sowie für deinen großen technischen Sachverstand, welchen du mit jedem teilst. Der ganze Lehrstuhl hat Glück einen Techniker wie dich hier zu haben. Aber nicht nur die Arbeit war mit dir immer lustig auch das drumherum, sei es nun ratschen, philosophieren oder Weißwürste essen.

Bei Andreas Wild bedanke ich mich für seine vielfache Hilfe bei Problemen mit nextnano++. und/oder Matlab. Dein großes Wissen hat mir dabei viel geholfen. Auch hatten wir viele nette Diskussionen über unterschiedlichste Probleme in der Fabrikation, welche mir viel Spaß gemacht haben. Des weiteren möchte ich mich noch für das Korrekturlesen dieser Arbeit bei dir bedanken.

Für ihre Unterstützung mit nextnano++ und für viele Diskussionen über Oszillatorstärken und Matrixelemente möchte ich mich bei Stefan Birner, Andreas Wild und Thomas Eisfeller bedanken. Der theoretischere Teil dieser Arbeit wäre ohne euch in dieser Form nicht möglich gewesen.

Mein spezieller Dank gilt Hubert Riedl, Max Bichler, Ade Ziegeltrum, Neuner Irmgard, Sonja Krauss, Claudia Paulus, Sonja Mattich, Sedlmeier Fritz, Mora Linda und Peter Weiser da ihr die technischen und chemischen Gerätschaften hier am WSI am Laufen haltet. Ich hatte im Laufe der Jahre davon viele verwendet und war immer froh wenn alles funktionierte.

Kai Müller, Stefan Lichtmannecker, Vase Jovanov, Alex Bechtold, Gregor Bracher,

Michael Kaniber, Hannes Kierig, Andreas Wild, Günther Reithmeier, Dominik Heiss, Konrad Schraml, Dance Spirkosca Jovanov, Ardelt Per-Lennart, Ilaria Zardo, Florian Klotz, Thorsten Reichert, Silvia Spiga, Markus Stallhofer, Simon Hertenberger, Daniel Rudolph, Verena Hintermayer, Stefan Funk, Steffi Mohrkötter, Senf Jörg, Schweickert Lucas, Koch Sebastian, Kammerlocher Mathias, Kaldewey Timo, Büse Alexander und der restlichen QD und SiGe group danke ich für die angenehme Zeit hier am WSI.

Die letzten drei Jahre haben wir ja nicht nur viel im Labor gearbeitet sondern auch viele Stunden auf dem Fußballfeld verbracht. Bei Gregor Bracher, Felix Höhne, Markus Stallhofer, Konrad Schraml, Simon Pütz, Richard Geiger, Hannes Kierig, Michael Kaniber, Arne Laucht, Pel(l)e, Karneck'l, Simon Pfaehler, Felix Buth, Narayan Sircar, Metzger Michael, Michael Algasinger, Andre Stegner, Simon Pfähler, Treu Julian und Christoph Kastl möchte ich mich daher für viele schöne Stunden und Tore, sowie für die ein oder andere Prellung und Schürfwunde bedanken. Hat Spaß gemacht.

Bei Sabrina möchte ich mich natürlich ganz besonders bedanken. Immerhin haben wir es hier seit dem ersten Semester gemeinsam an der TU durchgehalten und in dieser Zeit haben wir ja einiges miteinander erlebt.

Zu Felix Buth muss ich sagen, dass ich es echt schade finde, dass wir uns jetzt nicht mehr auf dem Klo über den Weg laufen werden.

Bei Julie Paye möchte ich mich für vielen netten Gespräche und U-Bahnfahrten im letzten Jahr bedanken. Ich wünsche dir, dass auch deine Diplomarbeit noch erfolgreich verläuft. Ach ja danke nochmal für die Unterstützung beim HF ätzen...

Bei Julian Treu bedanken ich mich für die Übernahme der ehrenhaften Pflicht der Fußballorganisation.

Bei den Metzgereien Karl, Funk und keine Ahnung wie sie heist, die in Eching halt wo Arne und Gregor immer eingekauft haben, bedanke ich mich für die vielen leckeren Weißwürste, Wiener, Debreciner und Leberkasbrat'l. In den letzten drei Jahren haben wir in der SiGe und QD-Group viele davon gemeinsam verdrückt. Ich favorisiere ja immer noch die Weiwürste von der Metzgerei in Eching.

Ich bedanke mich auch bei IGSSE und dem TUM - Institute for Advanced Study für die finanzielle und organisatorische Unterstützung dieser Arbeit.

Schlußendlich möchte ich mich noch bei ein paar Menschen bedanken, die nichts mit dem WSI zu tun haben, aber die mich immer unterstützt haben. Allen voran bei Tobi, Johannes und meinem Schwesterchen mit denen ich schon sehr, sehr viel erlebt habe und bestimmt auch noch sehr, sehr viel erleben werde.

Dann natürlich bei meinen Eltern, meinem Bruder und dem Rest meiner Familie, die mich immer bei all meinen Entscheidungen unterstützt haben und immer für mich da waren. Ganz besonders Dank gilt noch meinem Neffen Moritz für die vielen Lego-Burgen die wir gemeinsam aufgebaut haben und noch aufbauen werden.

Selbstständigkeitserklärung

Mit der Abgabe dieser Doktorarbeit versichere ich, dass ich die Arbeit selbstständig verfasst habe und keine anderen, als die angegebenen, Quellen verwendet habe.

München, 25.07.2012 Thomas Zabel

In der Schriftenreihe des Walter Schottky Instituts der Technischen Universität München sind bisher folgende Bände erschienen:

Vol. 1
Cornelia Engel
Si/SiGe basierende Phototransistoren
131 Seiten
ISBN 3-932749-01-4

Vol. 2
Peter Schittenhelm
Selbst-Organisation und Selbst-Ordnung in Si/SiGe-Heterostrukturen
151 Seiten
ISBN 3-932749-02-2

Vol. 3
Andreas Nutsch
Selektive Epitaxie von (GaIn)(AsP) Schichtstrukturen
129 Seiten
ISBN 3-932749-03-0

Vol. 4
Peter Baumgartner
Optische und elektronische Eigenschaften lasergeschriebener GaAs-Nanostrukturen
180 Seiten
ISBN 3-932749-04-9

Vol. 5
Walter Franz Rieger
Untersuchung der elektronischen und strukturellen Eigenschaften von GaNAlN und deren Legierungen
158 Seiten
ISBN 3-932749-05-7

Vol. 6
Markus Hauser
Oberflächenemittierende Laserdioden mit Mehrfachepitaxie
148 Seiten
ISBN 3-932749-06-5

Vol. 7
Markus Sexl
Verspannte und gitterrelaxierte In(GaAl)As Heterostrukturen
144 Seiten
ISBN 3-932749-07-3

Vol. 8
Christian Obermüller
Photolumineszenszspektroskopie mit optischen Nahfeldmethoden an GaAs-Nanostrukturen
140 Seiten
ISBN 3-932749-08-1

Vol. 9
Edilson Silveira
Inelastische Lichtstreuung an niedrig-dimensionalen Halbleiterstrukturen
104 Seiten
ISBN 3-932749-09-X

Vol. 10
Eberhard Christian Rohrer
Photoleitungs-Spektroskopie von Diamant
153 Seiten
ISBN 3-932749-10-03

Vol. 11
Thomas Wimbauer
Magnetische Resonanz-Untersuchungen an modernen Halbleitermaterialien
125 Seiten
ISBN 3-932749-11-1

Vol. 12
Herbert Verhoeven
Thermische Eigenschaften von CVD-Diamantschichten
154 Seiten
ISBN 3-932749-12-X

Vol. 13
Hans-Christoph Ostendorf
Trennung von Volumen- und Oberflächenrekombination in Silizium
128 Seiten
ISBN 3-932749-13-8

Vol. 14
Martin Städele
Dichtefunktionaltheorie mit exaktem Austausch für Halbleiter
202 Seiten
ISBN 3-932749-14-6

Vol. 15
Helmut Angerer
Herstellung von Gruppe III-Nitriden mit Molekularstrahlepitaxie
144 Seiten
ISBN 3-932749-15-4

Vol. 16
Wolfgang Heller
Spektroskopie einzelner Quantenpunkte in magnetischen und elektrischen Feldern
128 Seiten
ISBN 3-932749-16-2

Vol. 17
Molela Moukara
Pseudopotentiale mit exaktem Austausch
117 Seiten
ISBN 3-932749-17-0

Vol. 18
Ralph Oberhuber
Elektronische Struktur und Transport in verspannten Halbleiterschichtsystemen
110 Seiten
ISBN 3-932749-18-9

Vol. 19
Reiner Pech
High-Energy Boron-Implantation into Different Silicon Substrates
158 Seiten
ISBN 3-932749-19-7

Vol. 20
Christoph Martin Engelhardt
Zyklotronresonanz zweidimensionaler Ladungsträgersysteme in Halbleitern, Effekte der Elektron-Elektron-Wechselwirkung und Lokalisierung
317 Seiten
ISBN 3-932749-20-0

Vol. 21
Eduard Neufeld
Erbium-dotierte Si/SiGe-Lichtemitter und -Wellenleiter
136 Seiten
ISBN 3-932749-21-9

Vol. 22
Gert Schedelbeck
Optische Eigenschaften von Halbleiternanostrukturen hergestellt durch Überwachsen von Spaltflächen
154 Seiten
ISBN 3-932749-22-7

Vol. 23
Jürgen Zimmer
Optoelektronisches Verhalten von Dünnschichtbauelementen aus amorphem und mikrokristallinem Silizium
171 Seiten
ISBN 3-932749-23-5

Vol. 24
Berthold Schmidt
Leistungsoptimierung abstimmbarer InGaAsP/InP Halbleiterlaser
85 Seiten
ISBN 3-932749-24-3

Vol. 25
Jianhong Zhu
Ordering of self-assembled Ge and SiGe nanostructures on vicinal Si surfaces
120 Seiten
ISBN 3-932749-25-1

Vol. 26
Gerhard Groos
Herstellung und Charakterisierung von Silizium-Nanostrukturen
168 Seiten
ISBN 3-932749-26-X

Vol. 27
Uwe Hansen
Theorie der Reaktionskinetik an Festkörperoberflächen
119 Seiten
ISBN 3-932749-27-8

Vol. 28
Roman Dimitrov
Herstellung und Charakterisierung von AlGaN/GaN-Transistoren
196 Seiten
ISBN 3-932749-28-6

Vol. 29
Martin Eickhoff
Piezowiderstandsmechanismen in Halbleitern mit großer Bandlücke
151 Seiten
ISBN 3-932749-29-4

Vol. 30
Nikolai Wieser
Ramanspektroskopie an Gruppe III-Nitriden
161 Seiten
ISBN 3-932749-30-8

Vol. 31
Rainer Janssen
Strukturelle und elektronische Eigenschaften amorpher Silizium-Suboxide
275 Seiten
ISBN 3-932749-31-6

Vol. 32
Martin W. Bayerl
Magnetic resonance investigations of group III-nitrides
155 Seiten
ISBN 3-932749-32-4

Vol. 33
Martin Rother
Elektronische Eigenschaften von Halbleiternanostrukturen hergestellt durch Überwachsen von Spaltflächen
196 Seiten
ISBN 3-932749-33-2

Vol. 34
Frank Findeis
Optical spectroscopy on single self-assembled quantum dots
156 Seiten
ISBN 3-932749-34-0

Vol. 35
Markus Ortsiefer
Langwellige Vertikalresonator-Laser-dioden im Materialsystem InGaAlAs/InP
152 Seiten
ISBN 3-932749-35-9

Vol. 36
Roland Zeisel
Optoelectronic properties of defects in diamond and AlGaN alloys
140 Seiten
ISBN 3-932749-36-7

Vol. 37
Liwen Chu
Inter- und Intraband Spektroskopie an selbstorganisierten In(Ga)As/GaAs Quantenpunkten
124 Seiten
ISBN 3-932749-37-5

Vol. 38
Christian Alexander Miesner
Intra-Valenzbandspektroskopie an SiGe-Nanostrukturen in Si
100 Seiten
ISBN 3-932749-38-3

Vol. 39
Szabolcs Kátai
Investigation of the nucleation process of chemical vapour deposited diamond films
178 Seiten
ISBN 3-932749-39-1

Vol. 40
Markus Arzberger
Wachstum, Eigenschaften und Anwendungen selbstorganisierter InAs-Quantenpunkte
236 Seiten
ISBN 3-932749-40-5

Vol. 41
Markus Oliver Markmann
Optische Eigenschaften von Erbium in $Si/Si_{1-x}C_x$, $Si/Si_{1-x}Ge_x$ und Si/SiO_x Heterostrukturen
182 Seiten
ISBN 3-932749-41-3

Vol. 42
Rainer Alexander Deutschmann
Two dimensional electron systems in atomically precise periodic potential
210 Seiten
ISBN 3-932749-42-1

Vol. 43
Uwe Karrer
Schottky-Dioden auf Galliumnitrid: Eigenschaften und Anwendungen in der Sensorik
182 Seiten
ISBN 3-932749-43-X

Vol. 44
Günther Anton Johann Vogg
Epitaxial thin films of Si and Ge based Zintl phases and sheet polymers
169 Seiten
ISBN 3-932749-44-8

Vol. 45
Christian Strahberger
Vertikaler Transport und extreme Magnetfelder in Halbleitern
167 Seiten
ISBN 3-932749-45-6

Vol. 46
Jan Schalwig
Feldeffekt-Gassensoren und ihre Anwendung in Abgasnachbehandlungssystemen
125 Seiten
ISBN 3-932749-46-4

Vol. 47
Christopher Eisele
Novel absorber structures for Si-based thin film solar cells
126 Seiten
ISBN 3-932749-47-2

Vol. 48
Stefan Hackenbuchner
Elektronische Struktur von Halbleiter-Nanobauelementen im thermodynamischen Nichtgleichgewicht
213 Seiten
ISBN 3-932749-48-0

Vol. 49
Andreas Sticht
Herstellung und Charakterisierung von dünnen Silizium/Siliziumoxid-Schichtsystemen
166 Seiten
ISBN 3-932749-49-9

Vol. 50
Giuseppe Scarpa
Design and fabrication of Quantum Cascade Lasers
193 Seiten
ISBN 3-932749-50-2

Vol. 51
Jörg Frankenberger
Optische Untersuchungen an zweidimensionalen Ladungsträgersystemen
158 Seiten
ISBN 3-932749-51-0

Vol. 52
Doris Heinrich
Wavelength selective optically induced charge storage in self-assembled semiconductor quantum dots
144 Seiten
ISBN 3-932749-52-9

Vol. 53
Nicolaus Ulbrich
Entwurf und Charakterisierung von Quanten-Kaskadenlasern und Quantenpunktkaskaden
133 Seiten
ISBN 3-932749-53-7

Vol. 54
Lutz Carsten Görgens
Analyse stickstoffhaltiger III-V Halbleiter-Heterosysteme mit hochenergetischen schweren Ionen
116 Seiten
ISBN 3-932749-54-5

Vol. 55
Andreas Janotta
Doping, light-induced modification and biocompatibility of amorphous silicon suboxides
180 Seiten
ISBN 3-932749-55-3

Vol. 56
Sebastian Tobias Benedikt Gönnenwein
Two-dimensional electron gases and ferromagnetic semiconductors: materials for spintronics
198 Seiten
ISBN 3-932749-56-1

Vol. 57
Evelin Beham
Photostromspektroskopie an einzelnen Quantenpunkten
186 Seiten
ISBN 3-932749-57-X

Vol. 58
Po-Wen Chiu
Towards carbon nanotube-based molecular electronics
116 Seiten
ISBN 3-932749-58-8

Vol. 59
Tobias Graf
Spin-spin interactions of localized electronic states in semiconductors
194 Seiten
ISBN 3-932749-59-6

Vol. 60
Stefan Klein
Microcrystalline silicon prepared by hot wire CVD: preparation and characterisation of material and solar cells
157 Seiten
ISBN 3-932749-60-X

Vol. 61
Markus Krach
Frequenzverdreifacher mit Anti-Seriellem Schottky-Varaktor für den Terahertzbereich
156 Seiten
ISBN 3-932749-61-8

Vol. 62
Ralph Thomas Neuberger
AlGaN/GaN-Heterostrukturen als chemische Sensoren in korrosiven Medien
153 Seiten
ISBN 3-932749-62-6

Vol. 63
Sonia Perna
Wasserstoff-Passivierung von trikristallinem Silizium durch hydrogenisiertes Siliziumnitrid
136 Seiten
ISBN 3-932749-63-4

Vol. 64
Oliver Schumann
Einfluss von Stickstoff auf das Wachstum und die Eigenschaften von InAs-Quantenpunkten
148 Seiten
ISBN 3-932749-64-2

Vol. 65
Gerhard Rösel
Entwicklung und Charakterisierung von Typ-II-Heterostrukturen für die Abstimmregion in abstimmbaren Laserdioden
101 Seiten
ISBN 3-932749-65-0

Vol. 66
Angela Link
Zweidimensionale Elektronen- und Löcher-Gase in GaN/AlGaN Heterostrukturen
156 Seiten
ISBN 3-932749-66-9

Vol. 67
Matthias Sabathil
Opto-electronic and quantum transport properties of semiconductor nanostructures
156 Seiten
ISBN 3-932749-67-7

Vol. 68
Frank Fischer
Growth and electronic properties of two-dimensional systems on (110) oriented GaAs
139 Seiten
ISBN 3-932749-68-5

Vol. 69
Robert Shau
Langwellige oberflächenemittierende Laserdioden mit hoher Ausgangsleistung und Modulationsbandbreite
198 Seiten
ISBN 3-932749-69-3

Vol. 70
Andrea Baumer
Structural and electronic properties of hydrosilylated silicon surfaces
163 Seiten
ISBN 3-932749-70-7

Vol. 71
Andreas Florian Kreß
Manipulation of the Light-Matter-Interaction in Photonic Crystal Nanocavities
185 Seiten
ISBN 3-932749-71-5

Vol. 72
Markus Grau
Molekularstrahlepitaktische Herstellung von antimonidischen Laserdioden für die Gassensorik
138 Seiten
ISBN 3-932749-72-3

Vol. 73
Karin Buchholz
Microprocessing of silicon on insulator substrates and biofunctionalisation of silicon dioxide surfaces for sensing applications in fluids
170 Seiten
ISBN 3-932749-73-1

Vol. 74
Dominique Bougeard
Spektroskopische Charakterisierung von Germanium-Quantenpunkten in Silizium
154 Seiten
ISBN 3-932749-74-X

Vol. 75
Jochen Bauer
Untersuchungen zum kontrollierten Wachstum von InAs-Nanostrukturen auf Spaltflächen
140 Seiten
ISBN 3-932749-75-8

Vol. 76
Ingo Bormann
Intersubband Spektroskopie an Silizium-Germanium Quantenkaskadenstrukturen
124 Seiten
ISBN 3-932749-76-6

Vol. 77
Hubert Johannes Krenner
Coherent quantum coupling of excitons in single quantum dots and quantum dot molecules
160 Seiten
ISBN 3-932749-77-4

Vol. 78
Ulrich Rant
Electrical manipulation of DNA-layers on gold surfaces
249 Seiten
ISBN 3-932749-78-2

Vol. 79
René Todt
Widely tunable laser diodes with distributed feedback
152 Seiten
ISBN 3-932749-79-0

Vol. 80
Miroslav Kroutvar
Charge and spin storage in quantum dots
150 Seiten
ISBN 3-932749-80-4

Vol. 81
Markus Maute
Mikromechanisch abstimmbare Laser-Dioden mit Vertikalresonator
170 Seiten
ISBN 3-932749-81-2

Vol. 82
Frank Ertl
Anisotrope Quanten-Hall-Systeme, Vertikale Ultrakurzkanal- und Tunneltransistoren
170 Seiten
ISBN 3-932749-82-0

Vol. 83
Sebastian M. Luber
III-V semiconductor structures for biosensor and molecular electronics applications
212 Seiten
ISBN 978-3-932749-83-4

Vol. 84
Claudio Ronald Miskys
New substrates for epitaxy of group III nitride semiconductors: challenges and potential
207 Seiten
ISBN 978-3-932749-84-1

Vol. 85
Sebastian Friedrich Roth
n- and p-type transport in (110) GaAs substrates, single- and double-cleave structures
138 Seiten
ISBN 978-3-932749-85-8

Vol. 86
Mario Gjukic
Metal-induced crystallization of silicon-germanium alloys
309 Seiten
ISBN 978-3-932749-86-5

Vol. 87
Tobias Zibold
Semiconductor based quantum information devices: Theory and simulations
151 Seiten
ISBN 978-3-932749-87-2

Vol. 88
Thomas Jacke
Weit abstimmbare Laserdiode mit vertikal integriertem Mach-Zehnder-Interferometer
165 Seiten
ISBN 978-3-932749-88-9

Vol. 89
Nenad Ocelić
Quantitative near-field phonon-polariton spectroscopy
174 Seiten
ISBN 978-3-932749-89-6

Vol. 90
Kenji Arinaga
Control and manipulation of DNA on gold and its application for biosensing
111 Seiten
ISBN 978-3-932749-90-2

Vol. 91
Hans-Gregor Hübl
Coherent manipulation and electrical detection of phosphorus donor spins in silicon
162 Seiten
ISBN 978-3-932749-91-9

Vol. 92
Andrea Friedrich
Quanten-Kaskaden-Laser ohne Injektorbereiche
140 Seiten
ISBN 978-3-932749-92-6

Vol. 93
Oliver Dier
Das Materialsystem (AlGaIn) (AsSb): Eigenschaften und Eignung für GaSb-basierte Vertikalresonator-Laserdioden
174 Seiten
ISBN 978-3-932749-93-3

Vol. 94
Georg Steinhoff
Group III-nitrides for bio- and electrochemical sensors
197 Seiten
ISBN 978-3-932749-94-0

Vol. 95
Stefan Harrer
Next-generation nanoimprint lithography: Innovative approaches towards improving flexibility and resolution of nanofabrication in the sub-15-nm region
161 Seiten
ISBN 978-3-932749-95-7

Vol. 96
Stefan Ahlers
Magnetic and electrical properties of epitaxial GeMn
184 Seiten
ISBN 978-3-932749-96-0

Vol. 97
Emanuele Uccelli
Guided self-assembly of InAs quantum dots arrays on (110) surfaces
172 Seiten
ISBN 978-3-932749-97-1

Vol. 98
Shavaji Dasgupta
Growth optimization and characterization of high mobility two-dimensional electron systems in AlAs quantum wells
152 Seiten
ISBN 978-3-932749-98-8

Vol. 99
Werner Hofmann
InP-based long-wavelength VCSELs and VCSEL arrays for high-speed optical communication
142 Seiten
ISBN 978-3-932749-99-5

Vol. 100
Robert Lechner
Silicon nanocrystal films for electronic applications
227 Seiten
ISBN 978-3-941650-00-8

Vol. 101
Nebile Işık
Investigation of Landau level spin reversal in (110) oriented p-type GaAs quantum wells
114 Seiten
ISBN 978-3-941650-01-5

Vol. 102
Andreas Florian Härtl
Novel concepts for biosensors using diamond-based field effect transistors
255 Seiten
ISBN 978-3-941650-02-2

Vol. 103
Felix Florian Georg Hofbauer
Realization of electrically tunable single quantum dot nanocavities
160 Seiten
ISBN 978-3-941650-03-9

Vol. 104
Dominic F. Dorfner
Novel photonic biosensing based on silicon nanostructures
169 Seiten
ISBN 978-3-941650-04-6

Vol. 105
Till Andlauer
Optoelectronic and spin-related properties of semiconductor nanostructures in magnetic fields
157 Seiten
ISBN 978-3-941650-05-3

Vol. 106
Christoph Bihler
Magnetic semiconductors
190 Seiten
ISBN 978-3-941650-06-0

Vol. 107
Michael Huber
Tunnel-Spektroskopie im Quanten-Hall-Regime
164 Seiten
ISBN 978-3-941650-07-7

Vol. 108
Philipp Achatz
Metal-insulator transition and super-Conductivity in heavily boron-doped diamond and related materials
151 Seiten
ISBN 978-3-941650-08-4

Vol. 109
Sebastian Strobel
Nanoscale contacts to organic molecules based on layered semiconductor substrates
140 Seiten
ISBN 978-3-941650-09-1

Vol. 110
Ying Xiang
Semiconductor nanowires and templates for electronic applications
152 Seiten
ISBN 978-3-941650-10-7

Vol. 111
Michael Kaniber
Non-classical light generation in photonic crystal nanostructures
177 Seiten
ISBN 978-3-941650-11-4

Vol. 112
Martin Hermann
Epitaktische AlN-Schichten auf Saphir und Diamant
216 Seiten
ISBN 978-3-941650-12-1

Vol. 113
Dominik Heiss
Spin storage in quantum dot ensembles and single quantum dots
196 Seiten
ISBN 978-3-941650-13-8

Vol. 114
Tillmann Christoph Kubis
Quantum transport in semiconductor nanostructures
253 Seiten
ISBN 978-3-941650-14-5

Vol. 115
Lucia Steinke
Magnetotransport of coupled quantum Hall edges in a bent quantum well
194 Seiten
ISBN 978-3-941650-15-2

Vol. 116
Christian Lauer
Antimonid-basierte Vertikalresonator-Laserdioden für Wellenlängen oberhalb 2 μm
180 Seiten
ISBN 978-3-941650-16-9

Vol. 117
Simone Maria Kaniber
Optoelektronische Phänomene in hybriden Schaltkreisen aus Kohlenstoffnanoröhren und dem Photosystem I
136 Seiten
ISBN 978-3-941650-17-6

Vol. 118
Martin Heiß
Growth and properties of low-dimensional III-V semiconductor nanowire heterostructures
172 Seiten
ISBN 978-3-941650-18-3

Vol. 119
Sandro Francesco Tedde
Design, fabrication and characterization of organic photodiodes for industrial and medical applications
277 Seiten
ISBN 978-3-941650-19-0

Vol. 120
Danche Spirkoska Jovanov
Fundamental properties of self-catalyzed GaAs nanowires and related heterostructures
200 Seiten
ISBN 978-3-941650-20-6

Vol. 121
Jürgen Sailer
Materials and devices for quantum Information processing in Si/SiGe
158 Seiten
ISBN 978-3-941650-21-3

Vol. 122
Ilaria Zardo
Growth and raman spectroscopy studies of gold-free catalyzed semiconductor nanowires
184 Seiten
ISBN 978-3-941650-22-0

Vol. 123
Andre Rainer Stegner
Shallow dopants in nanostructured and in isotopically engineered silicon
185 Seiten
ISBN 978-3-941650-23-7

Vol. 124
Andreas J. Huber
Nanoscale surface-polariton spectroscopy by mid- and far-infrared near-field microscopy
144 Seiten
ISBN 978-3-941650-24-4

Vol. 125
Marco Andreas Höb
Funktionalisierung von Gruppe IV-Halbleitern
186 Seiten
ISBN 978-3-941650-25-1

Vol. 126
Daniel Claudio Pedone
Nanopore analytics – electro-optical studies on single molecules
114 Seiten
ISBN 978-3-941650-26-8

Vol. 127
Casimir Richard Simeon Katz
Multi-alloy structures for injectorless Quantum Cascade Lasers
131 Seiten
ISBN 978-3-941650-27-5

Vol. 128
Barbara Annemarie Kathrin Baur
Functionalization of group III-nitrides for biosensor applications
215 Seiten
ISBN 978-3-941650-28-2

Vol. 129
Arne Laucht
Semiconductor quantum optics with tailored photonic nanostructures
232 Seiten
ISBN 978-3-941650-29-9

Vol. 130
Jia Chen
Compact laser-spectroscopic gas sensors using Vertical-Cavity Surface-Emitting Lasers
150 Seiten
ISBN 978-3-941650-30-5

Vol. 131
Hans Leonhard Prechtel
Ultrafast Photocurrents and Terahertz Radiation in Gallium Arsenide and Carbon Based Nanostructures
160 Seiten
ISBN 978-3-941650-31-2

Vol. 132
Roland Enzmann
Technologieentwicklung für eine Einzelphotonenquelle
142 Seiten
ISBN 978-3-941650-32-9

Vol. 133
Alexander Bachmann
Antimonide-Based Vertical-Cavity Surface-Emitting Lasers
144 Seiten
ISBN 978-3-941650-33-6

Vol. 134
Markus Andreas Mangold
Two-Dimensional Gold Nanoparticle Arrays – A Platform for Molecular Optoelectronics
140 Seiten
ISBN 978-3-941650-34-3

Vol. 135
Stefan Birner
Modeling of semiconductor nanostructures and semiconductor–electrolyte interfaces
227 Seiten
ISBN 978-3-941650-35-0

Vol. 136
Christian Claus Jäger
Polycrystalline Silicon Thin Films for Electronic Applications
202 Seiten
ISBN 978-3-941650-36-7

Vol. 137
Gunther Christian Jegert
Modeling of Leakage Currents in High-κ Dielectrics
170 Seiten
ISBN 978-3-941650-37-4

Vol. 138
Shamsul Arafin
Electrically-Pumped GaSb-Based Vertical-Cavity Surface-Emitting Lasers
126 Seiten
ISBN 978-3-941650-38-1

Vol. 139
Norman Hauke
Enhanced spontaneous emission from silicon-based photonic crystal nanostructures
208 Seiten
ISBN 978-3-941650-39-8

Vol. 140
Christoph Schindler
Quantum spin transport in semiconductor nanostructures
175 Seiten
ISBN 978-3-941650-40-4

Vol. 141
Narayan Sircar
Group IV all-semiconductor spin-tronics: Materials aspects and optical spin selection rules
163 Seiten
ISBN 978-3-941650-41-1

Vol. 142
Alaa Abdellah
Scalable Thin-Film Manufacturing Technologies for Organic Electronics
162 Seiten
ISBN 978-3-941650-42-8

Vol. 143
Roland Dietmüller
Hybrid organic-inorganic heterojunctions for photovoltaic applications
179 Seiten
ISBN 978-3-941650-43-5

Vol. 144
Simon Hertenberger
Growth and Properties of In(Ga)As Nanowires on Silicon
152 Seiten
ISBN 978-3-941650-44-2

Vol. 145
Thomas Zabel
Study on silicon-germanium nanoislands as emitters for a monolithic silicon light source
152 Seiten
ISBN 978-3-941650-45-9